

Characterization of small megavoltage photon beams for radiotherapy

By

Itumeleng Setilo

This dissertation is submitted in fulfilment of the requirements for the degree
MMedSc (Medical Physics) in the Faculty of Health Sciences, Department of
Medical Physics at the University of the Free State


July 2017

Supervisor: Dr. F.C.P. du Plessis

I, Itumeleng Setilo, declare that the dissertation which is hereby submitted for the MMedSc (Medical Physics) degree at the University of the Free State, is my own independent work and has not been handed in before for a degree at/in another university/faculty

Bloemfontein

July 2017

A handwritten signature in black ink, consisting of a stylized 'I' and 'S' intertwined, with a horizontal line extending to the right.

Itumeleng Setilo

Acknowledgements

I would like to thank, Dr F.C.P du Plessis for his guidance during my research. I would also like to thank the Free State Department of Health for allowing me to use their equipment.

This research project was funded by the South African Medical Research Council (MRC) with funds from National Treasury under its Economic Competitiveness and Support Package. This research and the publication thereof is the result of funding provided by the MRC of South Africa in terms of the MRC's Flagship Awards Project SAMRC-RFA-UFSP-01-2013/HARD.

Table of Contents

Abstract	VII
Abstrak	IX
Abbreviations	XII
Chapter 1: Introduction	1
Chapter 2: Theory	2
2.1 Photon interactions	2-1
2.2 Electron interactions	2-3
2.3 Dosimetry	2-4
2.4 Photon source and collimation	2-5
2.5 Radiation field	2-6
2.6 Detectors	2-8
2.6.1 CC01 ion chamber	2-8
2.6.2 Solid state detectors	2-9
2.6.2.1 EFD-3G Diode	2-10
2.6.2.2 PTW 60019 Microdiamond detector	2-12
2.6.3 Film	2-13
2.6.3.1 Radiochromic film (EBT2)	2-13
2.6.3.2 Radiographic film (Kodak X-Omat V/ Kodak EDR2)	2-14

2.7	Beam profile	2-16
2.8	Percentage depth dose curve	2-21
2.9	Relative output factors	2-22
2.9	References	2-24

Chapter 3: Materials and Methods 3

3.1	Linear accelerator	3-1
3.2	Phantoms and detectors	3-3
3.2.1	Blue water phantom	3-2
3.2.1.1	Electrometer CU500e	3-4
3.2.1.2	Detectors	3-6
3.2.1.3	Alignment	3-8
3.2.1.4	Voltage	3-9
3.2.1.5	Dose rate	3-9
3.2.2	RW3	3-9
3.2.2.1	Detectors	3-10
3.3	References	3-19

Chapter 4: Results and Discussions

4.1	Film analysis	4-1
4.1.1	EBT2	4-1
4.1.2	EDR2	4-4
4.2	Beam profiles	4-7
4.2.2	Beam profiles measured at an SSD of 90 cm	4-9

4.2.2	Beam profiles measured at an SSD of 95 cm	4-33
4.2.3	Beam profiles measured at an SSD of 100 cm	4-52
4.2.4	Beam profiles measured at an SSD of 110 cm	4-72
4.3	Percentage depth dose	4-95
4.3.1	PDDs measured at an SSD of 90 cm	4-96
4.3.2	PDDs measured at an SSD of 95 cm	4-106
4.3.3	PDDs measured at an SSD of 100 cm	4-116
4.3.4	PDDs measured at an SSD of 110 cm	4-128
4.4	Relative output factors	4-139
4.4.1	Output factors measured using a 6 MV photon beam at different SSDs	4-140
4.4.2	Output factors measured using a 10 MV photon beam at different SSDs	4-143
4.4.3	Output factors measured using a 15 MV photon beam at different SSDs	4-145
4.5	References	4-147
Chapter 5:	Conclusion	5-1
Appendix A:	Beam profiles	A-1
Appendix B:	Relative output factors	B-1

Abstract

Introduction

The landscape of radiation treatment techniques is ever evolving in pursuit of improved target coverage. The latest techniques such as IMRT, SBRT, SRS and VMAT, provide improved target coverage by controlling the intensity of the given dose through the use of multiple small fields in contrast to large fields in conventional treatments. The advantage of using these large fields is that, their characteristics are fully understood.

The introduction of small fields leads to improved coverage, but the physics of these fields are not fully understood. So, when used in patient treatment, it resulted in unaccounted radiation exposure due to inaccurate commissioning and inaccurate absolute dose calibration at these field sizes. The errors were due to incorrect detectors used for data collection, and incorrect application of factors when performing absolute dose calibration.

This report investigated the characteristics of these small fields using different detectors whilst varying the SSD and the incident photon beam energy. The measurements included beam profiles, percentage depth dose (PDD) curves as well as the relative output factors (ROF).

Materials and Methods

The photon energies, 6 MV, 10 MV and 15 MV were delivered using the Synergy LINAC, which is equipped with Agility multileaf collimators (MLCs). The detectors that were investigated were the CC01 ion chamber, EFD-3G diode, PTW60019 microdiamond, EBT2 radiochromic film and the EDR2 radiographic film. Measurements were carried out using water as a medium for the CC01 ion chamber, EFD-3G diode and the PTW60019. Films were placed in between water equivalent RW3 phantom slabs. These measurements were carried out at 90 cm, 95 cm, 100 cm and 110 cm source to surface distances (SSD). The field sizes that were investigated were $1\times 1\text{ cm}^2$, $2\times 2\text{ cm}^2$, $3\times 3\text{ cm}^2$, $4\times 4\text{ cm}^2$, $5\times 5\text{ cm}^2$ and $10\times 10\text{ cm}^2$, these fields sizes were set using Jaws and MLCs. The $10\times 10\text{ cm}^2$ field size was included as a reference field.

Results and Discussion

The results showed that the beam profiles were insignificantly different at the various SSDs for the detectors. The EBT2 film showed the sharpest penumbra, with the EDR2 and the CC01 showing broad penumbrae, but the difference was negligible.

The PDD measurements showed that the difference between the detectors after Depth of maximum dose (D_{max}) were insignificant. The films differed significantly at shallower depths, and this can be attributed to setup, as well as the artefacts that showed up when the films were being analyzed. The PDD measurements indicated that the setup used for the films was not adequate for measuring the 1 cm square field sizes and below.

D_{max} was used to compare the detectors, though it did not vary greatly for the detectors, it was shown that there is a change in the manner in which this factor changes with field size. Below a certain field size, 2 cm for the 6 MV and 10 MV and 3 cm for the 15 MV, the D_{max} would start shifting back to the surface instead of moving deeper as expected.

The relative output factor (ROF) increased with energy, and this is true for all the fields which had lateral electronic equilibrium (LEE). This relation broke down as the field sizes decreased due to the onset of lateral electronic disequilibrium (LED). The high-density detector, PTW60019 gave the highest ROF for the different energies, with the less dense CC01 giving the lowest ROFs. This showed that the density of the detector had an effect on the output factor measured.

Conclusion

The fields were characterized with the different detectors, barring the artefacts experienced with film measurements in some instances, these detectors can be used safely for the small fields. The ROFs can be measured at longer SSDs as they showed little variation due to increased SSDs.

Keywords

Small fields, PDD, D_{max} , Relative output factor, Lateral electronic equilibrium, microdiamond, three-channel dosimetry, RW3, beam profiles

Abstrak

Inleiding

Die aantal moderne beskikbare bestralingstegnieke is konstant besig om te vermeerder ter wille van beter teiken dekking. Die nuutste bestralingstegnieke soos IMRT, SBRT, SRS en VMAT bied beter teiken dekking deur die intensiteit van die gegewe dosis te verdeel in veelvuldige kleiner bestralingsvelde in plaas van die groot bestralings velde wat tydens konvensionele radioterapie gebruik word. Die voordeel van konvensionele radioterapie is dat die eienskappe van groot bestralingsvelde ten volle verstaan word.

Die bekendstelling van klein bestralingsvelde kan lei tot beter teiken dekking, maar die fisiese wette van klein veld bestraling word nog nie ten volle verstaan nie. Wanneer klein veld radioterapie dus in pasiënt behandeling toegepas word kan onbeplande bestralingsblootstelling plaasvind as 'n resultaat van onakkurate bundle karakterisering en die onakkuraatheid van absolute dosis kalibrasie vir klein velde. Hierdie foute is as gevolg van die feit dat die verkeerde bestralingsdetektore gebruik word en omdat faktore verkeerdelik toegepas word tydens absolute kalibrasie van bestralingsdosis.

Hierdie verslag ondersoek die eienskappe van hierdie klein velde met behulp van verskillende bestralingsdetektore terwyl die SSD en die intree foton bundel energie verander word. Die metings sluit bundel profiele, persentasie diepte dosis (PDD) kurwes en relatiewe opbrengs faktore (ROF) in.

Materiale en metodes

Foton energieë, 6 MV, 10 MV en 15 MV was gelever met behulp van die Synergy lineer versneller, wat toegerus is met Agility multipliet kollimators (MLCs). Die toerusting wat ondersoek was die CC01 ionisasie kamer, EFD-3G diode, PTW60019 mikro diamant detektor, EBT2 radiochromiese film en die EDR2 radiografiese film. Metings is geneem met water as medium vir die CC01 ionisasie kamer, EFD-3G diode en die PTW60019 mikro diamant detektor. Die films was geplaas tussen water ekwivalente RW3 fantoom vlakke. Metings is gemaak met 'n bron-oppervlak afstande (SSD) van 90 cm, 95 cm, 100 cm en 110 cm. Die groottes van die velde wat ondersoek

was, was $1 \times 1 \text{ cm}^2$, $2 \times 2 \text{ cm}^2$, $3 \times 3 \text{ cm}^2$, $4 \times 4 \text{ cm}^2$, $5 \times 5 \text{ cm}^2$ en $10 \times 10 \text{ cm}^2$. Die veldgrootte van die verwysingsveld was $10 \times 10 \text{ cm}^2$.

Resultate en bespreking

Die resultate het getoon dat die bundel profiele nie beduidend verander het tussen die onderskeie SSDs vir die detektore nie. Die EBT2 film het die skerpste penumbra getoon. Die EDR2 en die CC01 het breë penumbrae getoon, maar die verskil was nie so beduidend nie.

Die PDD metings het getoon dat die verskil tussen die detektore in die meting van diepte van maksimum dosis (D_{max}) nie beduidend was nie. Die films het aansienlik verskil by vlakke dieptes, en dit kan toegeskryf word aan die opstelling, asook die artefakte wat gepresenteer het toe die films geskandeer was. Die PDD metings dui daarop dat die opstelling wat gebruik was vir die films nie voldoende was vir die metings vir 1 vierkante cm en kleiner veld groottes.

D_{max} was gebruik om die toerusting te vergelyk, al was die intertoerusting variasie min, was daar getoon dat verandering was in die manier hoe die faktore verander met veldgrootte. Onder 'n sekere veld grootte het D_{max} vlakker begin beweeg in plaas daarvan om dieper te beweeg soos verwag word. Die veldgrootte waarteen die verskuiwing begin het verskil met die invallende foton energie, 2 cm vir die 6 MV en 10 MV en 3 cm vir die 15 MV.

Die ROF het toegeneem met foton energie, en dit is waar vir al die veldgroottes wat laterale elektroniese balans gehad het (LEE). Die verhouding het verval soos die groottes van die velde afgeneem het as gevolg van die ontstaan van laterale elektroniese onewewigtigheid (LED). Die hoë-digtheid detector, PTW60019 het die hoogste ROF gegee vir die verskillende energieë, met die minder digte CC01 wat die laagste ROFs getoon het. Dit het getoon dat die digtheid van die detector 'n uitwerking op die gemete opbrengs faktor het.

Gevolgtrekking

Die velde was gekarakteriseer met die verskillende detektore, behalwe die artefakte wat ondervind was met film metings in sekere gevalle, kan hierdie toerusting met veiligheid gebruik word vir die kleinveld metings. Die ROFs kan gemeet word by langer SSDs omdat hulle min variasie getoon het as 'n gevolg van verhoogde SSDs.

Sleutelwoorde

Kleinvelde, PDD, Dmax, relatiewe opbrengs faktore, laterale elektroniese onewewigtigheid, mikrodiamante, drie-kanaal dosimetrie, RW3, bundel profiele

Abbreviations

Ag	Silver
c	Speed of light
CAX	Central Axis
CC01	0.1 cubic centimeters ion chamber
cGy	CentiGray
CPE	Charge Particle Equilibrium
CV	Coefficient of Variation
d	General cavity theory weighting factor
ds	Source width
D	Absorbed dose
D_{det}	Dose in the detector
D_k	absolute dose measured by channel k
\dot{D}_k	First derivative of the absolute dose with respect to NOD of each colour channel
D_{max}	Depth of dose maximum
D_{medium}	Dose deposited in the medium
$D_{\text{dose detector}}$	Dose deposited in a detector
dp	Depth
dpi	Dots per inch
EFD	Electron Field Diode
F	Flatness
$h\nu'$	Final energy of the photon of interacting with the electron

$h\nu$	Initial energy of the incoming photon
I	Intensity
IDL	Interactive Data Language
IMRT	Intensity Modulated Radiotherapy
k	Different color channel: blue, red or green
KERMA	Kinetic Energy Released per Mass
LED	Lateral Electronic Disequilibrium
LEE	Lateral Electronic Equilibrium
LINAC	Linear Accelerator
LIPCDA	Lithium salt of Pentacosa-10,12-Diynoic Acid
m_e	Mass of an electron
MATLAB	Matrix Laboratory
MLC	Multi-Leaf Collimator
MM	Micke-Mayer
MV	MegaVoltage
NOD	Net Optical Density
OD	Optical Density
PDD	Percentage Depth Dose
RMSE	Root Mean Square Error
ROF	Relative Output Factor
ROI	Region of Interest
σ_D	Variance in the calculated absorbed dose

σ_k^2	Variance of dose in each colour channel
sw	Source width
S	Symmetry
SAD	Source to Axis Distance
SBRT	Stereotactic Body Radiotherapy
S_{col}	Collision stopping power
SDD	Source to Detector Distance
S_{det}	Stopping power of the detector
S_{med}	Stopping power of the medium
SNR	Signal to Noise Ratio
SRS	Stereotactic Radiosurgery
SSD	Source to Surface Distance
VMAT	Volumetric Arc Therapy
μ_{en}	Mass Energy-Absorption Coefficient
ρ_{cavity}	Density of a cavity
ρ_{medium}	Density of a medium
ϕ_{cavity}	Photon fluence in a cavity
ϕ_{medium}	Photon fluence in a medium
θ	Deflection angle of the photon from original direction
$\frac{S_{col}}{\rho_{(medium)}}$	Mass collision stopping power in a medium
$\frac{S_{col}}{\rho_{(cavity)}}$	Mass collision stopping power in a cavity

$\left(\frac{\mu_{en}}{\rho}\right)_{(medium)}$ Mass energy attenuation coefficient of a medium

$\left(\frac{\mu_{en}}{\rho}\right)_{(detector)}$ Mass energy attenuation coefficient of a detector

Chapter 1 – Introduction

Ionizing radiation was discovered in 1895 and soon after the discovery it was used as an imaging modality. The effects the ionizing radiation had on imaging patients consequently led to its use in treating cancers. Since then, advancements in treating the tumours have aimed to achieve better tumour coverage whilst decreasing the dose to the surrounding normal tissue. These advancements include techniques such as intensity modulated radiotherapy (IMRT), stereotactic body radiotherapy (SBRT) and stereotactic radiosurgery (SRS).

In, IMRT, a large field is converted into a number of small segments and these segments deliver doses with varying fluence intensities. In the SBRT and SRS techniques, the small fields are also used to control the early stage primary and the oligometastatic tumours¹ which have a diameter of less than 5 cm (Benedict et al., 2010). These techniques require a high level of confidence in the accuracy of the entire treatment as high doses are delivered to the target* (Godwin, Simpson, & Mugabe, 2012).

The small fields are usually defined to start from fields equal to and below 3x3 cm² field size (Das, Ding, & Ahnesjö, 2008) (Cranmer-Sargison, Weston, Sidhu, & Thwaites, 2011). These fields provide improved dose modulation due to sharper penumbrae, thus are essential in minimizing dose to normal surrounding tissue.

The issue with these fields is a loss of scatter, leading to a condition of lateral electronic disequilibrium (LED) (Das, Ding, et al., 2008), (Heydarian, Hoban, & Beddoe, 1996), (Gagnon et al., 2012). The LED indicates an absence of charged particle equilibrium (CPE) meaning that the number of electrons migrating from the central part of the field is more than the number of electrons migrating back into the central region**. Naturally under CPE conditions, the number of outflowing electrons is balanced by the number of inflowing electrons and the absorbed dose is equal to the collision KERMA (Gray, Gy) (Khan, 2010) (Mayles, Nahum, & Rosenwald, 2007).

¹ Oligometastatic tumours refer to cancers which have spread to one or small number of sites

* Sometimes lesions like arterial malformations in the brain are treated with only a single fraction

**This means that kinetic energy is flowing out of the central field with no replenishment from electrons in the outer regions of the field

When more electrons move out of the field, there will be less dose deposited within the field (Gagnon et al., 2012), particularly in small fields. The detector used within these small fields must not then disturb the existing LED state of the field (Scott, Nahum, & Fenwick, 2009), (Herrup, Chu, Cheung, & Pankuch, 2005), by either artificially increasing or decreasing the LED.

Photon beams interact via Raleigh, Photo-Electric, Compton Effect, pair-production and nuclear interactions with incident materials. The Compton Effect is more prevalent than photo-electric events. The Compton interaction intensity varies with the electron density in the material, which is proportional to the physical density of the material. Accordingly, the materials will decrease/increase interactions according to their physical density. Thus, the electrons from this interaction will move further away for a low-density medium, resulting in lower dose on the central axis. Thus, one characteristic a detector to be used for characterization of small fields should have, is that its physical density should be close to that of water ($\rho = 1 \text{ g/cm}^3$) so that LED state is not disturbed by its presence. Another characteristic a detector should have is a small sensitive area in order to accurately measure the sharp penumbrae of the small fields, such a small water-based detector does not exist at present.

The different detectors available are the radiographic films (EDR2), radio-chromic films (EBT2), ion chambers (CC01), diodes (EFD-3G) and micro-diamonds (PTW60019). Due to the small field size, most of the detectors employed in these fields provide differing outcomes for the same field. The values in table 1, indicate the various physical densities associated with different detectors.

Table 1. The density for the various detectors

Detector	EDR2	EBT2	CC01	EFD ^{3G}	PTW60019
Density	2.3 g/cm ² with effective thickness of 0.2 μ m	1.2 g/cm ³	0.0012 g/cm ³	2.3 g/cm ³	3.5 g/cm ³

Different publications advise the use of more than one type of detector for measurements of small fields such as beam profiles and relative output factors (ROF) (Sauer & Wilbert, 2007). Charles et al. stated that the ROF and the beam profile measured together would yield a better presentation of the output of that particular field (Charles et al., 2014).

The diode detectors have a higher atomic number and can be manufactured with very small sensitive volumes, Scanditronix-Wellhofer has introduced such a detector, called the electron field diode or the EFD-3G diode. The small sensitive volume leads to a better penumbra width resolution for beam profiles. These detectors have higher sensitivity compared to ion chambers due to their high density as well as high effective atomic number. They suffer from directional dependence, dose rate dependence and long-term irreversible ionizing radiation damage which alters their radiation sensitivity (Low et al., 2011).

The micro-diamond detector, PTW60019, is a high-density detector (Tyler, Liu, Lee, McKenzie, & Suchowerska, 2016), table 1. This is a synthetic diamond detector, which overcomes the dose rate dependence of natural diamond detectors. The diamond detector offers the same advantages of diodes without deterioration over time as experienced by the diodes.

The recommended ion chamber for small fields is the small volume ionization chamber, an example of which is the CC01. This chamber has a small volume of air compared to other ion chambers, and the signal it produces, if using the normal aluminium electrode will be low (Stasi, Baiotto, Barboni, & Scielzo, 2004). These small chambers use steel instead of aluminium to increase the signal to noise ratio (Sauer & Wilbert, 2007). The smaller volume results in better penumbra definition compared to larger ion chambers. The ion chambers offer good stability and linear response to absorbed dose compared to other types of detectors. The ion chamber response is relatively independent of ionizing radiation direction and independent of beam quality response and is traceable to a primary calibration standard (Low et al., 2011).

The radiographic films were mainly used in imaging, with the active particles being mostly silver bromide crystals, thus the films have more physical density compared to water. And due to the silver bromide, the films also have a higher effective atomic number compared to water. The EDR2 film is an example of a radiographic film but it has been modified to handle therapeutic doses. The EDR2 has high spatial resolution (Fuss, Sturtewagen, De_Wagter, & Georg, 2007) compared to diode detectors and ionization chambers due to its use of nanometre-sized small crystals of silver bromide. The film suffers from having a strong energy dependence (Das, Ding,

et al., 2008) due to its high effective atomic number and its physical density. The film is sensitive to light, as a consequence the handling and development of the film is carried out in a dark room.

A radio-chromic film is self-developing and is light insensitive. This film does not require the use of a dark room for processing as compared to the radiographic film. The EBT2 film introduced by the ISP Technologies INC in 2009 following the EBT series, with the EBT3 being the latest of the series. This film has a photon mass energy absorption coefficient as well as electron mass collision stopping power similar to water (water equivalent) (Andres, Del Castillo, Tortosa, Alonso, & Barquero, 2010) (Mayles et al., 2007). The film is relatively energy independent and has a high spatial resolution (small active particles). EBT2 film has needle-like active particles which are 1-2 μm in diameter and 15-25 μm in length (ISP, 2009). These small needle-like active particles are sandwiched between a polyester over-laminate (50 μm) and a polyester substrate (175 μm) (Aland, Kairn, & Kenny, 2011). The measurement side should be chosen and adhered to due to this difference in the thickness of overlays. The film is self-developing and therefore the results will not be influenced by developer temperature, as is the case with radiographic film (Pai et al., 2007). A waiting period of 24 hours post-irradiation is recommended, to allow for proper film development and stabilization due to post-irradiation polymerization.

The problems with the small fields are that the appropriate detector has not yet been established. The different detectors employed within these fields tend to provide varying information regarding the small field size in regards to the penumbrae of the field sizes as well as the measure dose output factor ratio of these fields.

The aim of this project is to measure beam parameters for small megavoltage photon beams, using different detectors. The following beam parameters will be used to characterize the small beams, namely: the output factor, beam profile and percentage depth dose using different detectors at different SSDs. These are the EBT2 film, CC01, EFD-3G, EDR2 and PTW60019 detectors. The measurements will be performed at different source to surface distances (SSDs).

References

- Aland, T., Kairn, T., & Kenny, J. (2011). Evaluation of a Gafchromic EBT2 film dosimetry system for radiotherapy quality assurance. *Australas Phys Eng Sci Med*, 34, 251–260.
- Andres, C., Del Castillo, A., Tortosa, R., Alonso, D., & Barquero, R. (2010). A comprehensive study of the Gafchromic EBT2 radiochromic film. A comparison with EBT. *Medical Physics*, 37, 6271–6278.
- Benedict, S. H., Yenice, K. M., Followill, D., Galvin, J. M., Hinson, W., Kavanagh, B., ... Yin, F.-F. (2010). Stereotactic body radiation therapy: The report of AAPM Task Group 101. *Medical Physics*, 37(8), 4078–4101. <http://doi.org/10.1118/1.3438081>
- Charles, P. H., Cranmer-Sargison, G., Thwaites, D. I., Crowe, S. B., Kairn, T., Knight, R. T., ... Trapp, J. V. (2014). A practical and theoretical definition of very small field size for radiotherapy output factor measurements. *Medical Physics*, 41(4), 041707. <http://doi.org/10.1118/1.4868461>
- Cranmer-Sargison, G., Weston, S., Sidhu, N. P., & Thwaites, D. I. (2011). Experimental small field 6 MV output ratio analysis for various diode detector and accelerator combinations. *Radiotherapy and Oncology*, 100(3), 429–435. <http://doi.org/10.1016/j.radonc.2011.09.002>
- Das, I. J., Ding, G. X., & Ahnesjö, A. (2008). Small fields: Nonequilibrium radiation dosimetry. *Medical Physics*, 35(1), 206. <http://doi.org/10.1118/1.2815356>
- Fuss, M., Sturtewagen, E., De_Wagter, C., & Georg, D. (2007). Dosimetric characterization of GafChromic EBT film and its implication on film dosimetry quality assurance. *Phys Med Biol*, 52, 4211–4225.
- Gagnon, J.-C., Thériault, D., Guillot, M., Archambault, L., Beddar, S., Gingras, L., & Beaulieu, L. (2012). Dosimetric performance and array assessment of plastic scintillation detectors for stereotactic radiosurgery quality assurance. *Medical Physics*, 39(1), 429. <http://doi.org/10.1118/1.3666765>
- Godwin, G. A., Simpson, J. B., & Mugabe, K. V. (2012). Characterization of a dynamic multi-leaf collimator for stereotactic radiotherapy applications. *Physics in Medicine and Biology*, 57(14), 4643–4654. <http://doi.org/10.1088/0031-9155/57/14/4643>
- Herrup, D., Chu, J., Cheung, H., & Pankuch, M. (2005). Determination of penumbral widths from ion chamber measurements. *Medical Physics*, 32, 3636–3640.
- Heydarian, M., Hoban, P. W., & Beddoe, a. H. (1996). A comparison of dosimetry techniques in stereotactic radiosurgery. *Physics in Medicine and Biology*, 41(1), 93–110. <http://doi.org/10.1088/0031-9155/41/1/008>

ISP. (n.d.). GAFCHROMIC(R) EBT2 SELF-DEVELOPING FILM FOR RADIOTHERAPY DOSIMETRY.

Khan, F. M. (2010). *The Physics of Radiation Therapy*. Lippincott Williams & Wilkins. Retrieved from <https://books.google.com/books?id=BaAJ4UFerxMC&pgis=1>

Mayles, P., Nahum, A., & Rosenwald, J. C. (Eds. . (2007). *Handbook of Radiotherapy Physics: Theory and Practice, 1st ed.* Taylor & Francis.

Pai, S., Das, I. J., Dempsey, J. F., Lam, K. L., Losasso, T. J., Olch, A. J., ... Wilcox, E. E. (2007). Radiographic film for megavoltage beam dosimetry. *Medical Physics*, 34(6), 2228–2258. <http://doi.org/10.1118/1.2736779>

Sauer, O. A., & Wilbert, J. (2007). Measurement of output factors for small photon beams. *Medical Physics*, 34.

Scott, A. J. D., Nahum, A. E., & Fenwick, J. D. (2009). Monte Carlo modeling of small photon fields: Quantifying the impact of focal spot size on source occlusion and output factors, and exploring miniphantom design for small-field measurements. *Medical Physics*, 36(7), 3132. <http://doi.org/10.1118/1.3152866>

Stasi, M., Baiotto, B., Barboni, G., & Scielzo, G. (2004). The behavior of several microionization chambers in small intensity modulated radiotherapy fields. *Medical Physics*, 31(10), 2792–2795. <http://doi.org/10.1118/1.1788911>

Chapter 2 Theory

2.1 Photon interactions	2-1
2.2 Electron interactions	2-3
2.3 Dosimetry	2-3
2.4 Photon source and collimation	2-5
2.5 Radiation field	2-6
2.6 Detectors	2-8
2.6.1 CC01 ion chamber.....	2-8
2.6.2 Solid state detectors.....	2-9
2.6.2.1 EFD ^{3G} Diode	2-9
2.6.2.2 PTW 60019 Microdiamond detector	2-12
2.6.3 Film	2-13
2.6.3.1 Radiochromic film (EBT2).....	2-13
2.6.3.2 Radiographic film (Kodak X-Omat V/ Kodak EDR2).....	2-14
2.7 Beam profile	2-16
2.8 Percentage depth dose curve	2-21
2.9 Relative output factors.....	2-22
2.9 References.....	2-22

2.1 Photon interactions

Photons are generated in a number of ways, but all methods boil down to production of either, bremsstrahlung x-rays or characteristic x-rays. Bremsstrahlung or braking radiation results from an electron passing near a nucleus. The path of the electron will be changed during this interaction, resulting in a photon being emitted. The range of photon energies produced via this process goes up to the maximum electron energy.

Meanwhile, the characteristic x-rays are produced in the event when an electron from one orbit moves to fill in a space left by an ejected electron from the lower orbit in an atom. These photons will have discrete energies. The Bremsstrahlung process produces more photons compared to the characteristic X-ray process, and it is via this process that a photon beam is produced on a linear accelerator.

There are five possible photon interactions that occur within a medium, and all are governed by the incident photon energy: Rayleigh scattering, photoelectric effect, Compton Effect, pair production and photon disintegration. Rayleigh scattering, photoelectric effect and Compton Effect involve interactions of a photon with an electron. Pair production and photon disintegration involves photon interactions with the nucleus of the atom.

The Compton Effect has a higher probability of this occurring at the energies of interest within this dissertation. The energy of an interacting photon during the Compton Effect is such that the photon acts as a particle thus it cannot be absorbed by an electron. The interaction therefore results in the transfer of energy via collision resulting in the incident photon changing its initial direction. The resulting transfer of energy from the photon to an electron is called Kinetic Energy Released per Mass unit, or KERMA. KERMA can be divided into collision KERMA as explained above and into radiative KERMA which results in bremsstrahlung production.

The final energy gained via collision KERMA, will result in an electron having its final kinetic energy being the difference in energy between the absorbed energy and the electron-atom binding energy.

The resulting energy of the scattered photon will then be given by equation 2-1 (eq. 2-1):

$$h\nu' = \frac{h\nu}{1 + \frac{h\nu(1 - \cos\theta)}{m_e c^2}} \quad (2-1)$$

Where $h\nu'$ is the final energy of the photon of interacting with the electron, $h\nu$ is the initial energy of the incoming photon, θ is the deflection angle of the photon from original direction, m_e is the mass of an electron and c is the speed of light. Equation 2-1 indicates that the final energy of the photon is dependent on the angle of incidence between the photon and the electron. A head-on collision, i.e θ equal 0° , will result in a photon transferring its maximum energy to the electron.

This interaction explains the energy transfer of the photon to electrons within a medium, thus a denser medium (increase in electron density) will result in more of these process occurring. The ejected electron, or the recoil electron will then travel and deposit dose within the medium, as seen in figure 1.

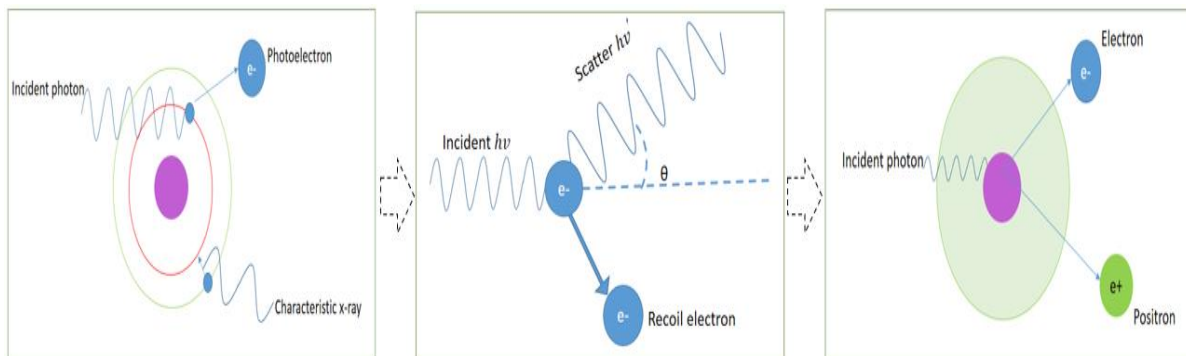


Figure 1. Photon interactions: (1) Photo-electric effect, (2) Compton Effect and (3) Pair production

2.2 Electron interactions

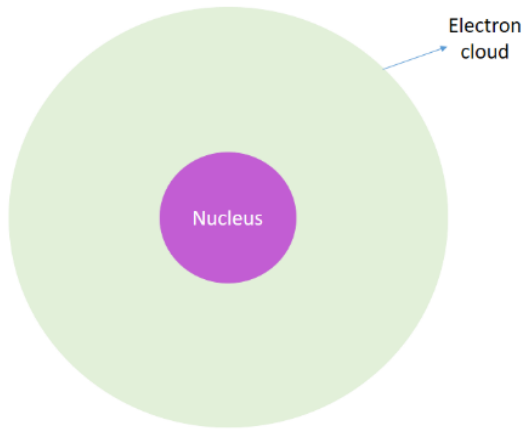


Figure 2 Structure of an atom showing an electron cloud around the nucleus

When traversing matter, electrons undergo either soft (excitation of atoms) or hard (ionization of atoms) interactions. The soft collisions result in an excitement of an orbital electron to a higher state, the space left is then filled by another orbital electron in a lower state, resulting in an emission of a characteristic x-ray. In case of ionization process, the incident electron passes energy to the orbital electron, these orbital electrons will then escape the atom, ionizing the atom.

The released electron will travel a certain distance while depositing its energy within the medium before coming to a halt. The distance changes from one medium to the next and is governed by the density of the medium. The factor which describes this loss of energy in a material is the stopping power. The mass collision stopping power is defined as the ratio of the medium collision stopping power and the density of the medium, to remove the influence of density (eq. 2-2).

$$\frac{S_{col}}{\rho} = \frac{d\bar{E}}{\rho dl} \quad (2-2)$$

where the S_{col} , is the collision stopping power of the medium, ρ is the physical density of the medium, \bar{E} is the energy transferred to the medium via collision KERMA and l is the length the electron travels before coming to a halt.

2.3 Dosimetry

Dosimetry is the measurement of the absorbed dose deposited by ionizing radiation. The resulting measurement will be the amount of energy deposited per mass of the medium. This is usually carried out using a detector which is placed within the medium of interest.

Bragg-Gray theory introduced the idea that dose measured by the detector in one medium can be related to another medium provided the following conditions are met:

- The detector should not disturb the charge particle equilibrium that would exist without its presence within the medium
- The absorbed dose within the cavity should be due to the charged particles that are crossing the cavity of the detector

When these conditions are met, dose is calculated within the medium as:

$$Dose_{detector} = \Phi_{detector} \times \frac{S_{col}}{\rho_{detector}} \quad (2-3)$$

$$Dose_{medium} = \Phi_{medium} \times \frac{S_{col}}{\rho_{medium}} \quad (2-4)$$

$$Dose_{medium} = Dose_{detector} \times \frac{\frac{S_{col}}{\rho_{(medium)}}}{\frac{S_{col}}{\rho_{(detector)}}} \quad (2-5)$$

Where $Dose_{cavity}$ is, the dose calculated within the detector, and as the fluence is not disturbed then the fluence in the detector ($\Phi_{detector}$) and that of the medium (Φ_{medium}) is equal. Thus the $Dose_{medium}$ can be related to $Dose_{cavity}$ via the ratio of the mass collision stopping power of the medium $\frac{S_{col}}{\rho_{(medium)}}$ and that of the detector $\frac{S_{col}}{\rho_{(detector)}}$.

The Bragg-Gray theory does not account for secondary electrons (delta rays) produced within the sensitive volume due to primary electrons. Spencer-Attix theory added the influence of secondary electrons or delta rays by introducing a cut-off energy, Δ . The theory shows that if these particles have an energy below 10 keV, they will have an influence on the dose measured,

if delta rays have an energy higher than the cut-off, then that energy will be enough to escape the cavity of the detector.

$$Dose_{medium} = Dose_{detector} \frac{\frac{S_{col}}{\rho} (medium, \Delta)}{\frac{S_{col}}{\rho} (detector, \Delta)} \quad (2-6)$$

A much more general cavity theory was then developed by Burlin, to account for all other detectors which have large cavities. This is where the general cavity theory is used, this theory is an extension on the above Spencer-Attix theory

$$\overline{Dose_{medium}} = \overline{Dose_{detector}} \left(d \frac{\frac{S_{col}}{\rho} (medium)}{\frac{S_{col}}{\rho} (detector)} + (1 - d) \frac{\left(\frac{\mu_{en}}{\rho}\right)_{med}}{\left(\frac{\mu_{en}}{\rho}\right)_{detector}} \right) \quad (2-7)$$

Where $\overline{Dose_{medium}}$ and $\overline{Dose_{detector}}$ are the average doses to the medium and the detector respectively, the weighting factor, d , changes from one for a small cavity to zero for a large cavity. When, $d = 1$, then second term becomes zero, then eq. 2-7 reverts back to eq. 2-6. And, $\left(\frac{\mu_{en}}{\rho}\right)_{med}$ and $\left(\frac{\mu_{en}}{\rho}\right)_{detector}$ are the mass energy attenuation coefficients of the medium and detector, respectively.

2.4 Photon source and collimation

A linear accelerator produces photon beams for treatment. These photons are produced via Bremsstrahlung at the target as the electrons from the electron gun are accelerated through the waveguide, and interact with the target. The size of beam at the target is defined by the electron beam hitting the target, that defines the size of the photon source and its typically in millimetres (Mayles et al., 2007). The size of this source will differ with linear accelerators.

The beam produced is collimated to a desired size for treatment. The collimation of the beam is achieved through use of collimators located within the treatment head i.e. the jaws and MLCs. MLCs were introduced to allow complex fields to be formed. Literature has shown that when forming small fields, sometimes these collimators will over travel resulting in occlusion of the photon source thereby influence the size of the visible source (Charles et al., 2014).

2.5 Radiation field

The radiation field consists of two photon spectra; primary and secondary (figure 3). The primary spectrum consists of the photons produced within the target. These are predominant on the central axis of the required field. The secondary spectrum consists of all the photons that were scattered away from the CAX, due to interactions within the head of the LINAC thus are referred to as scatter.

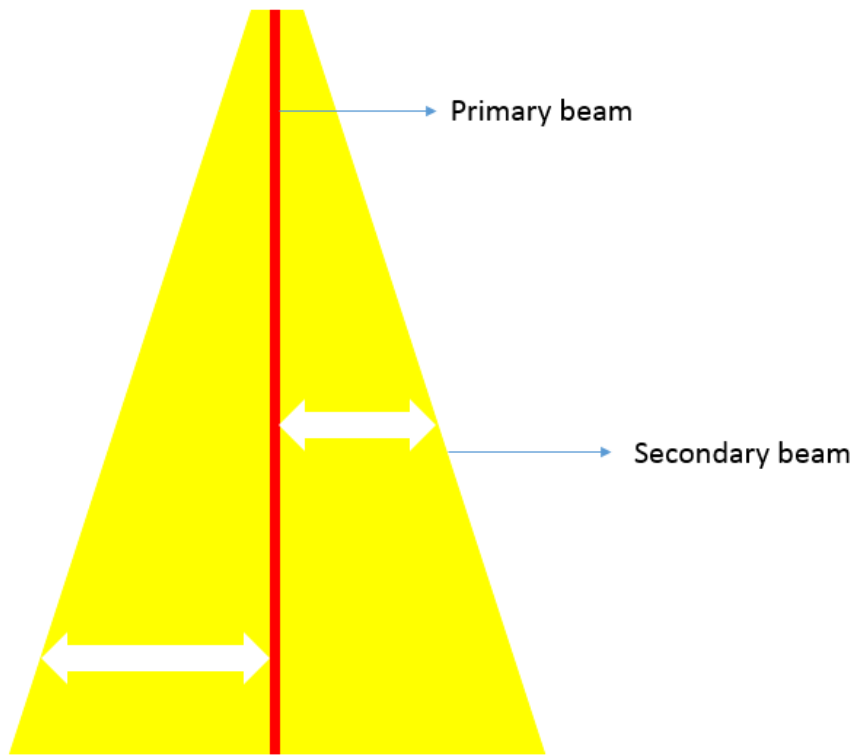


Figure 3 Primary and scattered areas of a radiation beam

Scatter contributes to the dose on the at the edges and the CAX. The contribution at the CAX increases with field size up until a certain field size is reached. The contribution of these photons to the primary spectrum, tends to decrease the average energy of the beam since these photons have lower energy than the primary spectrum. This energy change leads to an insignificant change in the stopping power ratios due to the dependence of stopping power on energy. Ding et al. 2012 (Ding & Ding, 2012) showed that the water-to-air stopping-power-ratios changed by 0.5% even though the mean photon energy changed by more than 20% for field sizes between $4 \times 4 \text{ mm}^2$ and $10 \times 10 \text{ cm}^2$, thus the reference field should have nearly the same conditions as the

fields being investigated. This change in energy will affect the dosimetry accuracy of energy dependent detectors.

When detectors are placed within a field, they will perturb the fluence due to their higher/lower density, when compared to water. The high density material tends to stop electrons over shorter distances, thus the signal obtained from such a higher density sensitive volume will be higher when compared to water; likewise low density material in the sensitive volume would lead to lower signal when compared to water (Bouchard, Seuntjens, Duane, Kamio, & Palmans, 2015). This poses a problem as centres around the world do not necessarily use the same detectors to obtain a signal within water.

The electronic equilibrium is achieved at a certain distance from the CAX depending on the density of the medium. The lateral range of the electrons that are produced on the CAX increases with an increase in incident photon energy and the radius of which increases with higher photon energies. Li et al. (Li, Soubra, Szanto, & Gerig, 1995) showed this relation of energy and radius of CPE is explained using the tissue phantom ratios at 10 cm and 20 cm depths for a particular energy on the CAX. The relationship was determined empirically from Monte Carlo simulations.

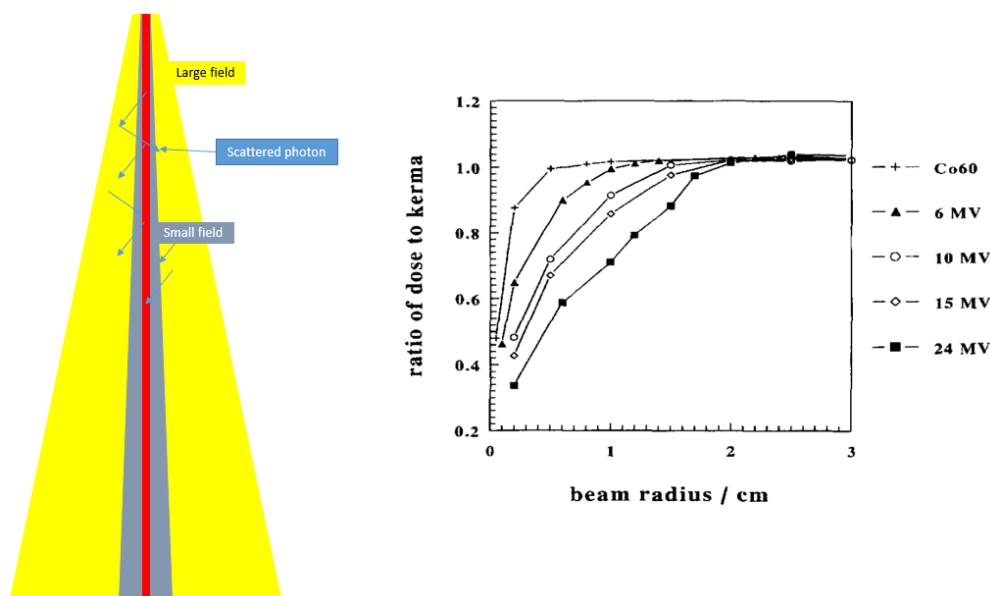


Figure 4 Lateral charge particle equilibrium (LCPE) establishment in different fields, and energy influence in LCPE (Li et al., 1995)

The change in this electronic equilibrium will result in a change of dose being detected, resulting in differences amongst the various detectors. Thus, small fields are those fields which exhibit the lack of lateral charge particle equilibrium, Figure 4, it is at these field sizes that the variation of field information is observed.

2.6 Detectors

There were five different detectors available for this study: ion chamber (CC01), solid state detectors (EFD and PTW600019 microdiamond) and films: radiographic (X-OMAT V/ EDR2), radiochromic film (EBT2).

2.6.1 CC01 ion chamber

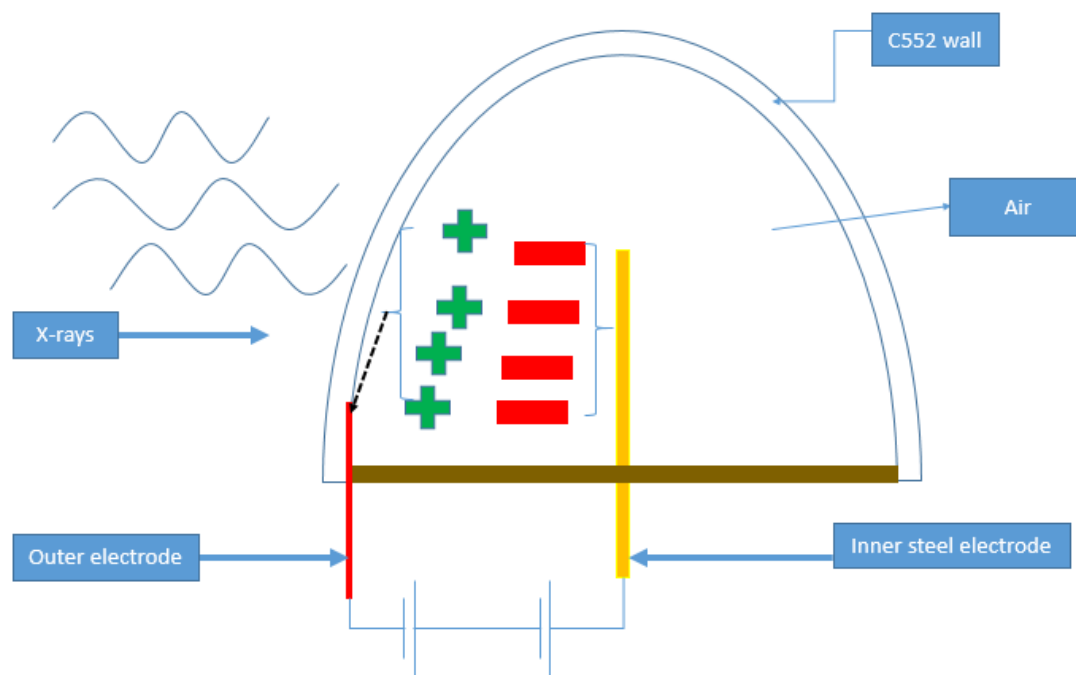


Figure 5 Schematic of an ion chamber, courtesy of ion chamber manufacturer PTW (PTW Freiburg, 2013)

Ionization chambers detect the ionizations that are created within its volume; when an electron/ion pair is created by the local electron fluence traversing its cavity. An external voltage is applied to this system to collect the electrons at the positively charged central electrode and the positive ions are collected at the outer electrode as shown in Figure 5. The signal generated from the electron/ion pair collection can then be related to the dose deposited within the medium.

The CC01, ion chamber, is a small cavity ionization chamber. The CC01 is manufactured by IBA or Scanditronix-Wellhofer, it has an air cavity with a volume of 0.01 cm³.

The volume of the chamber has been decreased as it was seen that the larger air volume ion chambers presented inaccuracies at these field sizes due to volume averaging. Volume averaging occurs as a signal is averaged across the sensitive volume of the detector (Das, Cheng, et al., 2008; Low, Moran, Dempsey, Dong, & Oldham, 2011), as a result the dose measured at the small fields is underestimated and the penumbra is broadened.

The CC01 uses a steel electrode instead of graphite. This inclusion of steel was to improve the signal to noise ratio value due to the small volume of the detector as explained by Low et al (Low et al., 2011).

The overall shape of the detector is such the ratio of the length and diameter is closer to one compared to other ion chambers produced by IBA. This means that the CC01 can be used either in the perpendicular or parallel orientation without losing too much resolution in either direction (Fox et al., 2010).

2.6.2 Solid state detectors

2.6.2.1 EFD^{3G} Diode

The first solid state detector investigated, Electron Field Detector (EFD^{3G}) diode from IBA is a highly-doped p-type silicon diode. The doping increases linear response of the detector in radiation fields (Grusell & Rikner, 1993). A diode is a semiconductor which allows the flow of charges in one direction. The silicon diode is composed of a p-type semiconductor and an n-type semiconductor.

N-type silicon semiconductors are formed by adding pentavalent impurities to silicon. Atoms bond together by filling energy levels. Pentavalent elements have five free valence electrons, silicon requires four additional valence electrons to complete its energy level. Thus, addition of each pentavalent atom will result in a free valence electron within the N-type material, N-type materials thus contribute electrons, and are then referred to as donors, Figure 6.

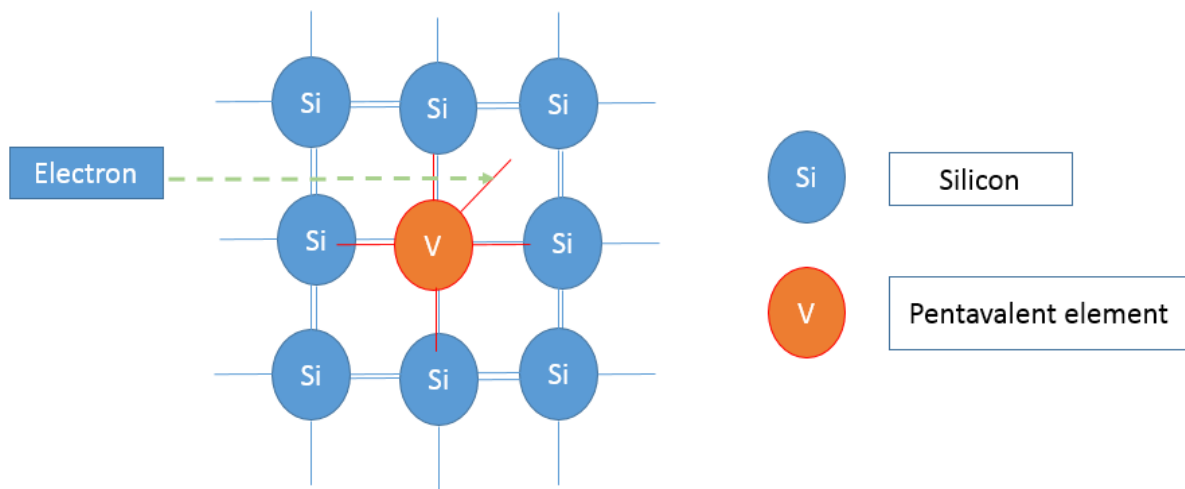


Figure 6 atomic structure of an N-type material

P-type silicon semiconductors are manufactured by adding trivalent impurities to silicon, since silicon requires four free valence electrons and trivalent elements have only three free valence electrons. Three of the four holes of silicon will be filled by the valence electrons leaving a space for an electron to fill. P-type silicon semiconductors are then referred to as acceptors, Figure 7.

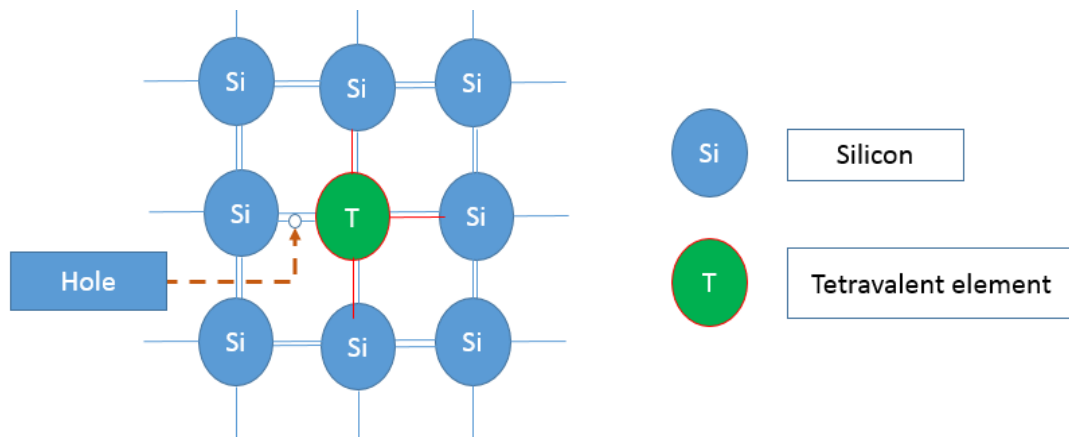


Figure 7 atomic structure of a P-type material

When a P-N junction is formed, holes will travel across towards the N-type semiconductor whereas the electrons move towards the P-type semiconductors creating a depletion region where there are no free charges, figure 8. The N-type semiconductor will become positive at the junction, and the P-type semiconductor will become negative. A potential barrier is established

at this junction, thus if a charge is created within this junction it will require a certain energy to cross the depletion region. The voltage is 0.7 V for silicon diodes.

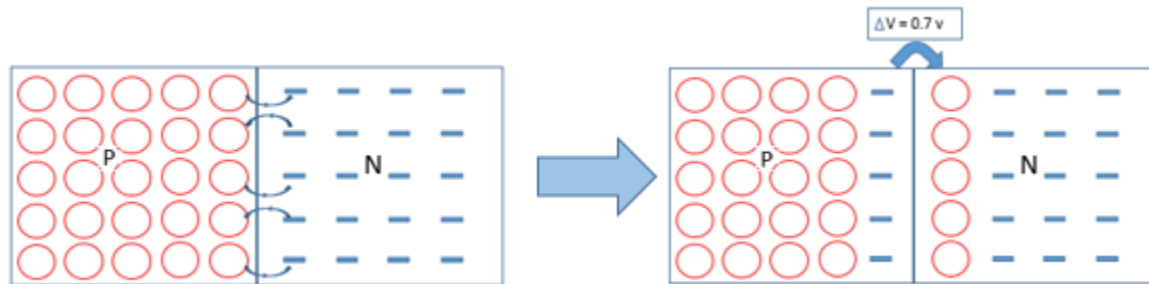


Figure 8 Depletion region of a semiconductor at the PN junction

Most semiconductor radiation detectors are p-type due to a high sensitivity loss of n-type material due to irradiation (Seco, Clasie, & Partridge, 2014).

When radiation interacts with a EFD-3G diode, it creates electron-hole pairs within the depletion region. Under the electric field established within the depletion region the electrons formed will accelerate towards the p-type region whilst the holes move toward the n-type region.

2.6.2.2 PTW 60019 Microdiamond detector

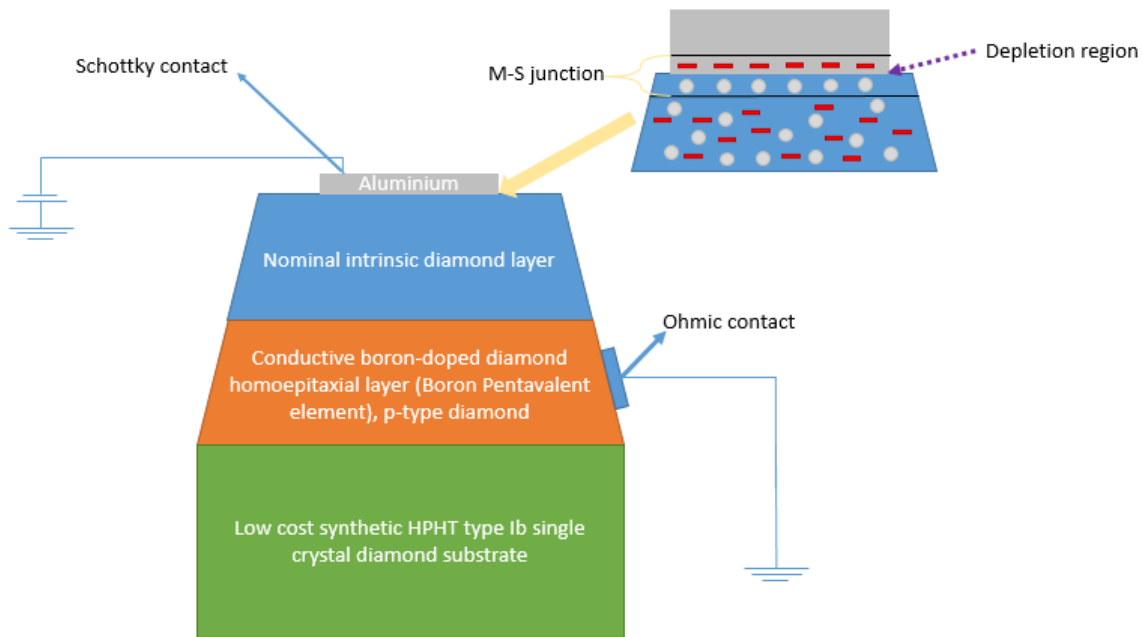


Figure 9 PTW60019 structure (Almaviva et al., 2009)

PTW60019 microdiamond detector, is a single crystal diamond diode which was developed at the Rome “Tor Vergata” University. Figure 9, which has been adapted from that shown by Almaviva et al. (Almaviva et al., 2009) shows the structure of this detector. The cell shown is built within the detector thus the detector does not need external voltage. Almaviva et al. (Almaviva et al., 2009) showed that the detector has a barrier junction at the metal contact and the nominally intrinsic layer, thus it acts as a sandwich-type metal/p/p⁺-doped Schottky barrier diode. The total photocurrent is contributed by electron-hole pairs generated in the depletion region and charges generated within the neutral zone. Charges created in the neutral region partly diffuse toward the depletion region. Almaviva et al also showed that the signal generation for the PTW60019 requires 3.5 times less current than the silicon diode.

2.6.3 Film

2.6.3.1 Radiochromic film (EBT2)

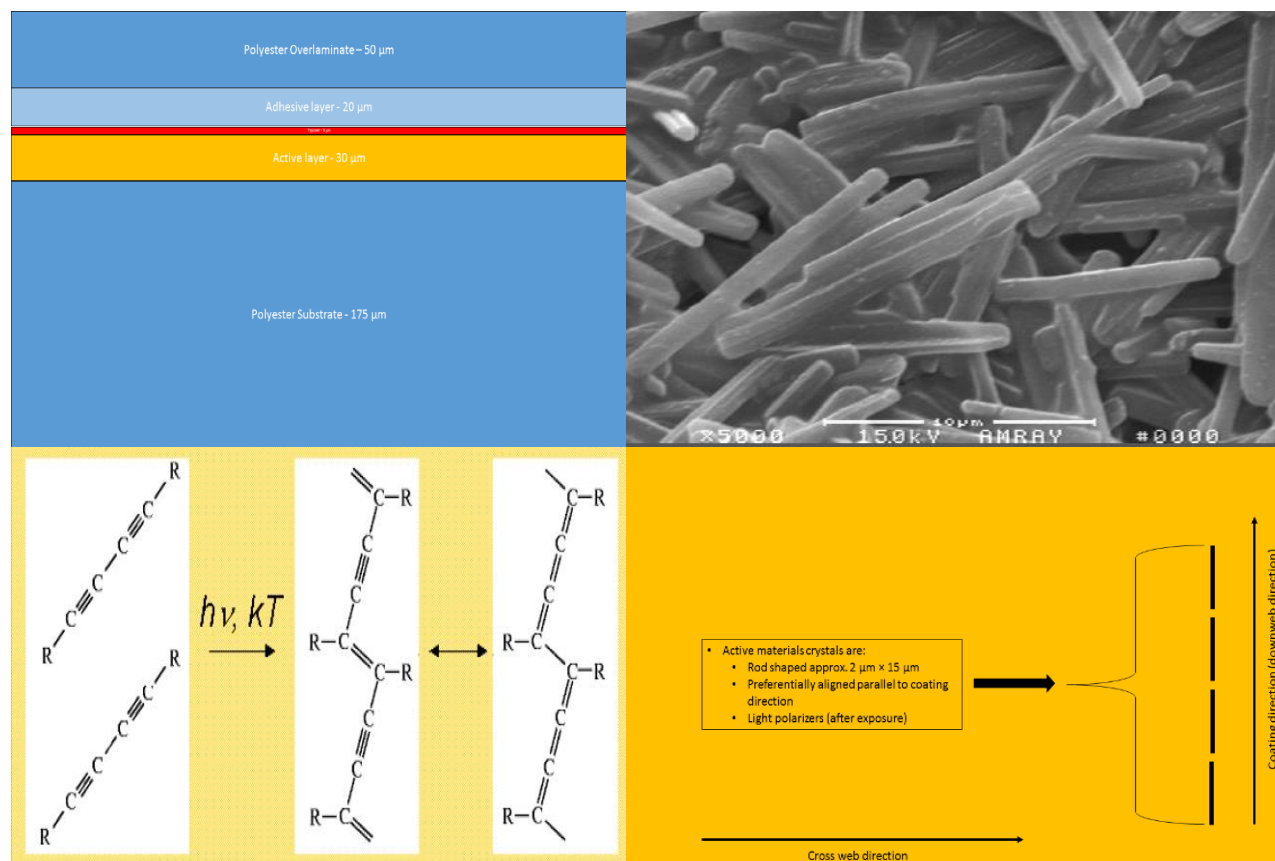


Figure 10. The structural layers of the EBT2 are shown top left); the size of the rod shaped active particles (Top right), the chemical reaction that occurs after the active particles interact with radiation (bottom left) and the structural arrangement of rod shaped active particles (bottom right)

Radiochromic film is a self-developing film. The active particles (rod shaped particles) are made of polyacetylene lithium salt (LIPCDA) (Rink, Lewis, Varma, Vitkin, & Jaffray, 2008) contained within a gel. These undergo chemical changes when exposed to radiation, the change is shown as a colour change. This colour change is brought on by polymerization of monomeric polyacetylene compound. In figure 10, the polymers are dyed yellow and after irradiation the dye turns blue and it shows as green due to the yellow hue of the film. It is during this process that the active particles rearrange to form lines within the film. The long side of the particles will re-assemble to be parallel to the short side of the film. This reaction stabilizes after a 24-hour period. The yellow dye of the film allows for the film to be less sensitive to room light compared to previous generations of this film.

The amount of dose deposited on the film is determined from a calibration curve. It is set up to show how the darkening of the film (optical density) changes with absorbed dose. The optical density is obtained by either digitally scanning the film (Vidar or flatbed scanner) or using a densitometer. The flatbed scanner is the most used for film evaluation due to its convenience.

The resolution of the scanned image is the important parameter. The number of pixels/dots per inch will determine the quality of scanning, the larger the number of the pixels per inch the more representative the scanned image (better the resolution), is to reality, but the resulting image will be very large in size. Lewis et al. (Lewis, Micke, Yu, & Chan, 2012) showed 72 dpi scanning resolution to be the optimum resolution. The scanned image represents the actual film being scanned, thus if there are dust, oil or finger prints these will be included within the image, resulting in misrepresentation of data. Proper handling of film is then advised to ensure reproducibility.

The resulting scanned image is composed of three 16-bit channels: red, green and blue. Literature has shown that the red channel is the most stable at the low doses and is often used with film investigation. The manufacturer has shown that all 3 channels (Micke, Lewis, & Yu, 2011; van Hoof, Granton, Landry, Podesta, & Verhaegen, 2012) can be used to obtain a final dose which has been corrected for artefacts such as variation of the active layer thickness, nonlinearity of the scanner and noise. The triple channel method will be used due to the above advantages.

2.6.3.2 Radiographic film (Kodak X-Omat V/ Kodak EDR2)

Radiographic film has been in use for imaging and dosimetric purposes. The film of interest in this investigation is produced by Kodak. The EDR2 is composed of similar sized grains which contain silver halide crystals placed within gelatin. Kodak EDR2 is latest radiographic film used in radiotherapy, and its crystals are nearly uniform in size as well as 10 times smaller than the Kodak XV model (higher resolution), and is less sensitive to low X-ray energies (Marcu, Bezak, & Allen, 2012, p. 77).

When radiation interacts with this section of the film, it releases electrons from Bromide ion. The free formed electrons drift toward the centre of the grain made of sulphide impurities, this region is known as the speck. As more electrons drift towards the speck, it will then start attracting

positively charged Ag ions. An increase in radiation will result in more Ag ion being attracted to the specks (figure 11).

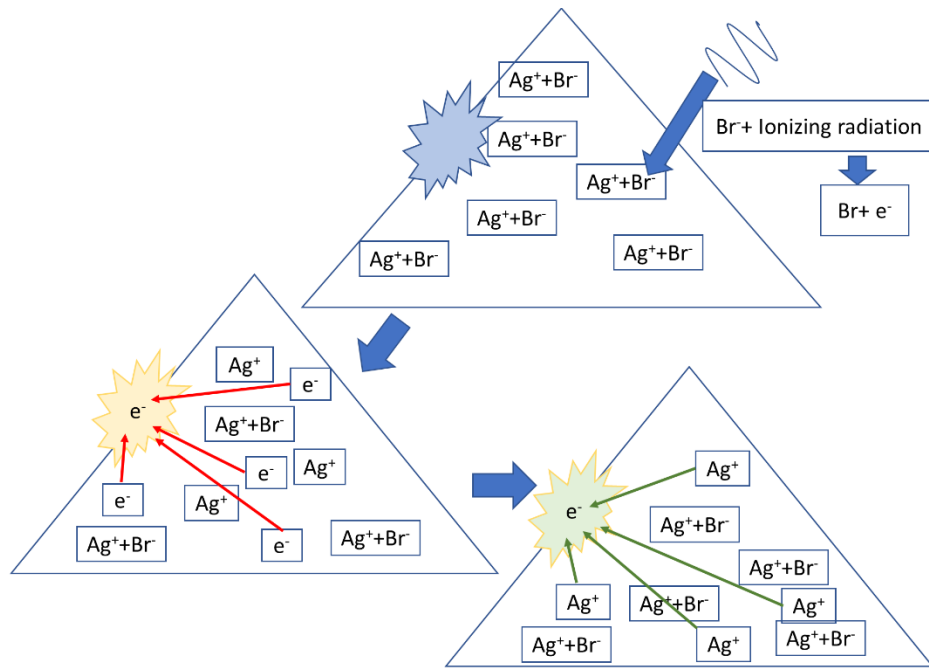


Figure 11 Gurney and Mott concentration theory graphic representation

Developing the film leads to the grains with the latent image being converted to metallic silver which is shown as a dark region on a developed film. After development, the film can either be analysed with a transmission densitometer or a specialized film scanner, such as a Vidar scanner.

Optical density (OD) factor is then calculated to establish the level of darkening of the film with dose (Pai et al., 2007). OD is obtained by taking a logarithmic ratio between the light intensity detected of an optical densitometer with an unexposed film, I_0 and an exposed film I , respectively.

$$OD = \log_{10}(I_0/I) \quad (2-8)$$

The calibration curve, eq 2-9, will then be determined to relate the observed optical density to dose.

$$Dose = aOD^2 + bOD + c \quad (2-9)$$

Where a , b and c are fitting parameters, OD is the optical density. The EDR2 film is dose rate independent (Shi, Papanikolaou, Yan, Weng, & Jiang, 2006), but is energy dependent due to the high atomic number silver bromide.

2.7 Field characteristics

The field characteristics that are to be measured are the beam profiles, percentage depth dose and output factors.

2.7.1 Beam profile

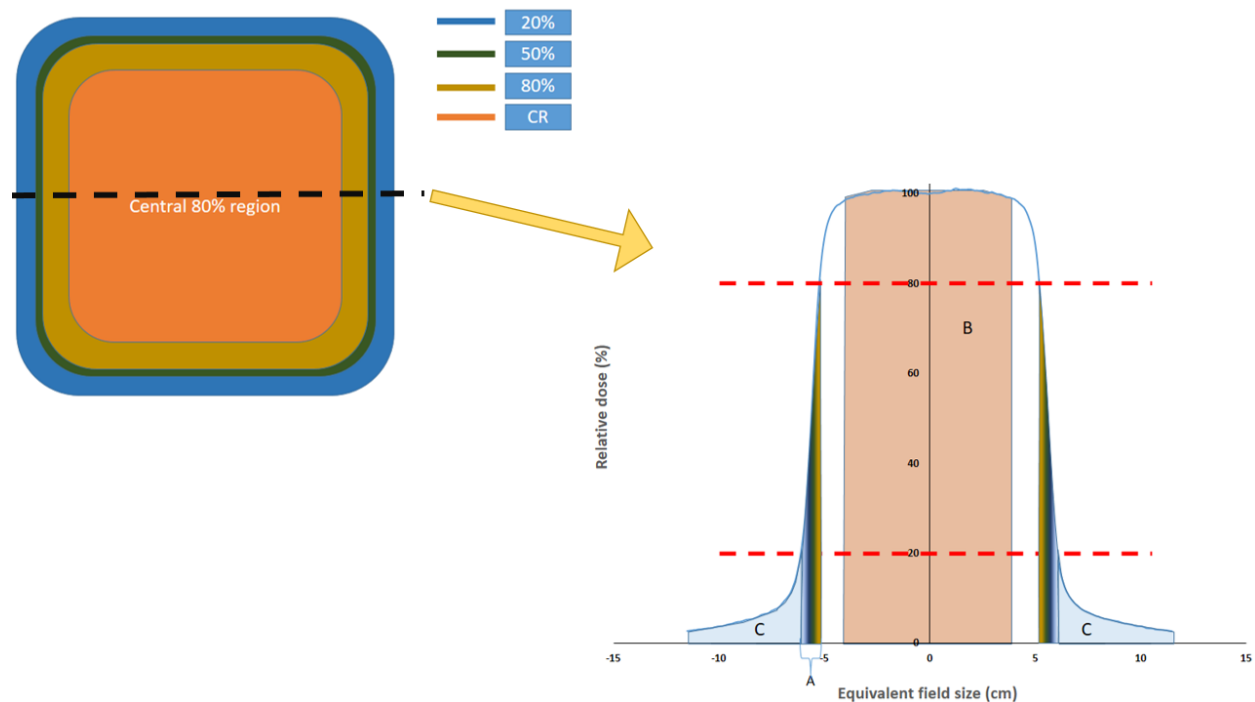


Figure 12 penumbra shown on beam profile

A beam profile indicates the change in dose distribution laterally at a certain specified field size and depth in a medium, as seen in figure 12. A beam profile provides the following characteristics of the field: central region of the field (region B), penumbra (region A), field size and umbra (region C). Central region of the field gives information regarding the flatness (within region B) and symmetry of the incident radiation.

Flatness (F) (eq. 2-9), indicates the uniformity of radiation across the central region of the set field size, as seen in Figure 13. Symmetry (S) (eq. 11) indicates the symmetry about the central axis of the set field size, as seen in Figure 13.

The central region is broad at larger field sizes, and decreases to a sharp peak at small fields. It is advised to measure within the central region of a field, as there is lateral electronic equilibrium (LEE) in large fields. This loss of LEE is assumed to become significant below a $3 \times 3 \text{ cm}^2$ field size.

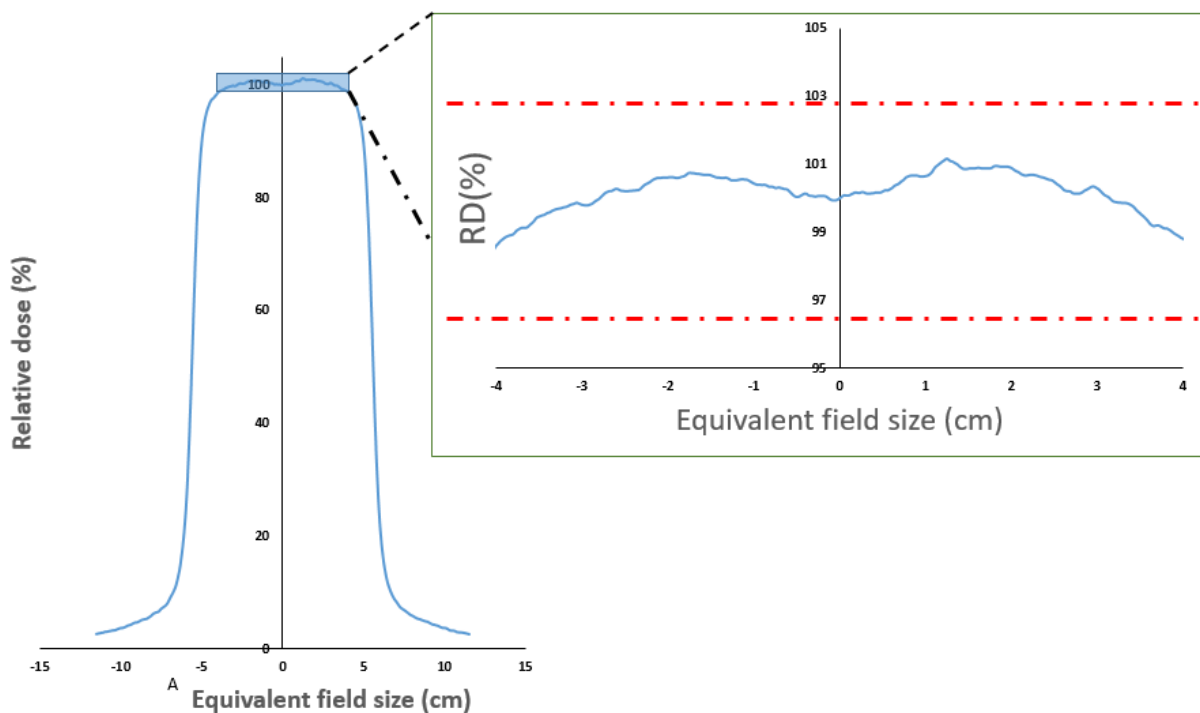


Figure 13 Flatness is calculated within 80% of central field

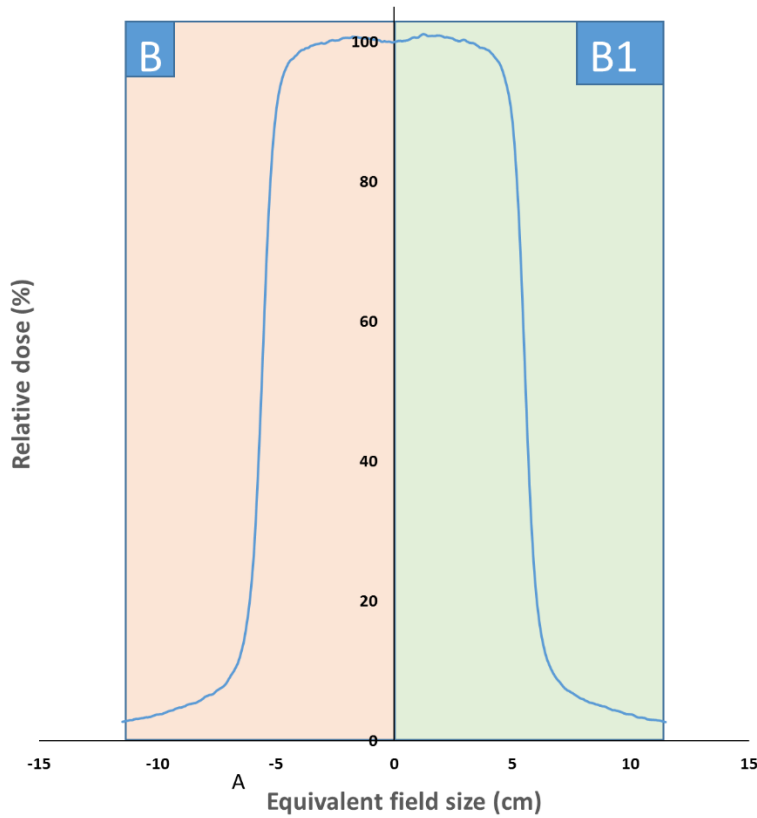


Figure 14. Symmetry of a beam profile

$$F = 100 \times \frac{Max - Min}{Max + Min} \quad (2-10)$$

$$S = 100 \times \frac{Area B - Area B1}{Area B + Area B1} \quad (2-11)$$

Where F , is the flatness of the beam profile, with the Max referring to the maximum dose deposited within the central 80%, and the Min being the minimum dose within the central 80% as seen in figure 13. S , is the symmetry of the beam profile, with Area B being the total beam profile area on the left of the CAX and Area B1 being the total beam profile area on the right of the CAX (figure 14).

Penumbra is the dose fall off region (Figure 15), it is defined as the distance of which the relative dose fall from 80% of CAX to 20% of the CAX at a certain depth. There are four contributors to

the physical penumbra: transmission penumbra, geometric penumbra, lateral electronic disequilibrium and side scatter.

Transmission penumbra results from radiation passing through edges of the collimation blocks and has a small contribution to the overall penumbra.

The geometric penumbra shows how the penumbra changes with the source width (sw), source to surface distance (SSD), depth (dp) and source to diaphragm distance (SDD). SDD is the main factor which will influence the geometric penumbra, change in field size has no impact on the geometric penumbra. The lateral electronic disequilibrium is indicated by the broadening of the beam profile with increase in energy as the range of electrons scattered laterally increases with energy.

$$\text{Geometric penumbra} = \frac{sw(SSD + dp - SDD)}{SDD} \quad (2-12)$$

The umbra region represents the region where the dose is less than 20% of the central region. The dose within this region is due to the radiation transmission through the collimators and head shielding.

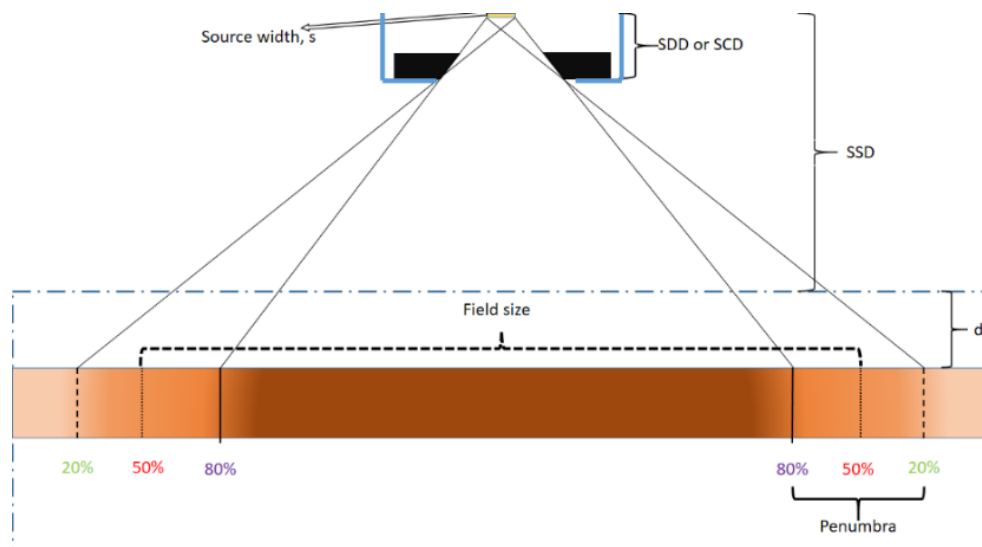


Figure 15 Geometric penumbra

The field size of a beam is determined by using the distance between 50% dose points of the beam profile (figure 15). This definition is invalid when the beam profile becomes peaked as seen with physically small fields.

2.7.2 Percentage depth dose curve

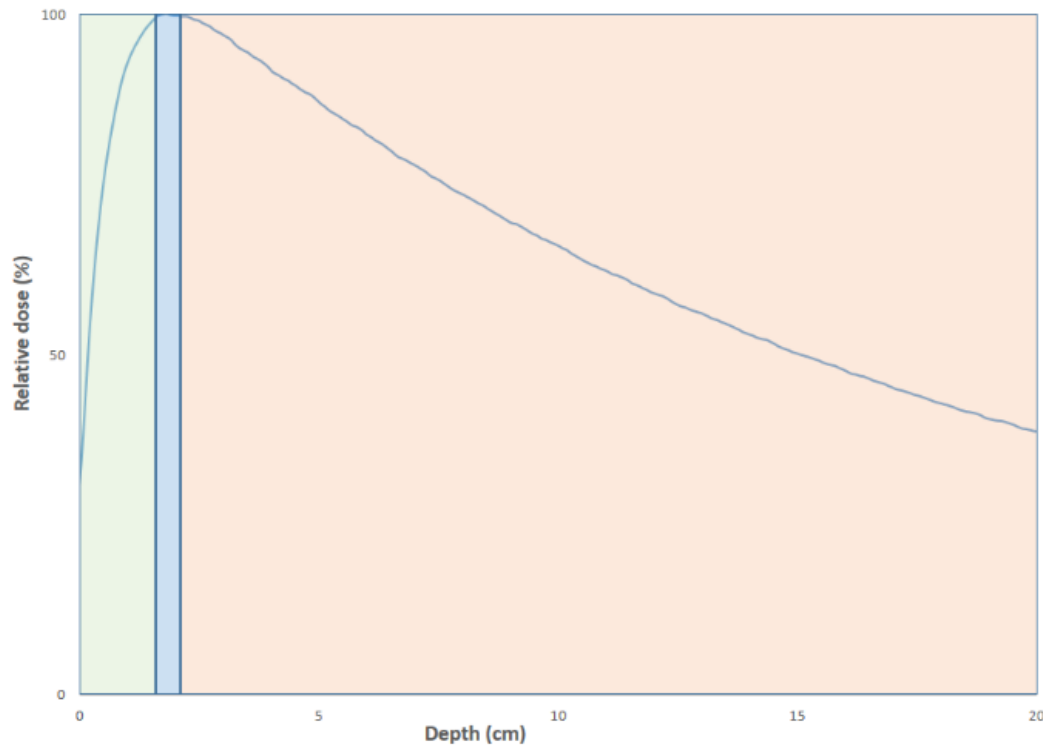


Figure 16 PDD regions of interest

The figure above shows the PDD (figure 16), which describes the change in dose deposition as radiation travels through a medium along the CAX.

$$PDD = 100 \times \frac{\text{Dose at depth}}{\text{Dose of reference depth}} \quad (2-13)$$

The curve can be divided into three regions; build up (green region), depth of dose maximum (D_{\max}) (blue region) and depth below D_{\max} (orange region).

The build-up region represents the region from the surface to the depth at which maximum dose is deposited. This occurs as the electrons that are liberated at the surface travel within the medium and deposit energy along the way until a certain depth. The distance from the surface an electron can travel is dependent on the incident photon energy, high photon energies have deeper build-up regions. High photon energies have a depth of maximum dose further into the medium, thus less dose is deposited at the surface compared to lower photon energies.

D_{max} represents the depth to which the most energetic electron ejected from the surface can travel. It is also the depth where electronic equilibrium exists. D_{max} is both field size and energy dependent. The increase in the field size increases the scatter towards the central axis of the field size. Scatter that is reaching the central axis, is of lower energy, thus will contribute dose closer the surface. This leads to the D_{max} shifting towards the surface. D_{max} moves deeper from the surface as the energy transferred to electrons is increased, thus the electrons will travel deeper before depositing dose.

When photons travel through the medium they are attenuated exponentially so there is less energy transferred to the electrons, KERMA (Kinetic Energy Released per Mass), at deeper depths. Therefore, the deposited dose will decrease with increasing depth. The exponential attenuation decreases with increasing incident photon energies, i.e. at the same depth the higher photon energy beam will deposit more dose compared to the lower energy photon beam.

2.7.2 Relative output factors

A relative output factor (ROF) relates the dose rate for a certain field to that from a reference field (standard reference field is a $10 \times 10 \text{ cm}^2$ field) at the same depth as shown in eq. 2-14. The ratio is expected to be more than unity for field sizes greater than the reference field, due to more scatter being able to reach the beam central axis, and is less than unity for fields less than the reference. The ROF is measured at depth, d and is not corrected for D_{max} .

$$ROF = \frac{\text{Dose rate}(\text{chosen field, depth})}{\text{Dose rate}(\text{reference field, depth})} \quad (2 - 14)$$

This chapter showed that photons deposit energy in two stages. The first stage is the photon-electron interaction, in this case via the Compton Effect, this results in a release of a Compton electron and the incident photon losing energy depending on the angle of collision. This Compton electron will travel through the medium before coming to a halt, the distance travelled was shown to be dependent on the electronic density of the medium. The theories which describe mathematically the process of determining the dose to the medium using a detector also showed that the stopping of electrons plays a major role in the dose that is being deposited.

As the field size decreases the electronic equilibrium found in large fields tends to decline in the lateral direction as more electrons move out of the CAX than electrons scattering back into the CAX. This decline is energy dependent, and was shown that the lower energy photon field will reach this state of LED slower than a high-energy megavoltage photon field. The detectors listed here, have varying densities, thus will behave differently under LED conditions. The high-density materials will stop more electrons from exiting the CAX at point of measurement resulting in an over response of the detector.

The characteristics that will be measured in the next section are the beam profiles, PDD and ROF. The beam profiles which show the alteration of dose laterally, as the electronic equilibrium decreases the penumbra of the field should broaden.

The PDD is measured on the CAX, from the entrance of the medium to its exit. As this is directly measured on the CAX, the differences between the detectors should be deductible.

The ROF is shown to also be affected under non-equilibrium conditions, as the reference field chosen is a large field size which has electronic equilibrium. The high-density detectors should then have a higher output at small fields, thus a higher ROF due to the stopping power.

2.9 References

Almaviva, S., Ciancaglioni, I., Consorti, R., De Notaristefani, F., Manfredotti, C., Marinelli, M., ... Verona-Rinati, G. (2009). Synthetic single crystal diamond dosimeters for Intensity Modulated Radiation Therapy applications. *Nuclear Instruments and Methods in Physics Research, Section A: Accelerators, Spectrometers, Detectors and Associated Equipment*, 608(1), 191–194. <http://doi.org/10.1016/j.nima.2009.07.004>

Bouchard, H., Seuntjens, J., Duane, S., Kamio, Y., & Palmans, H. (2015). Detector dose response in megavoltage small photon beams . I . Theoretical concepts Detector dose response in megavoltage small photon beams . I . Theoretical concepts, 6033. <http://doi.org/10.1118/1.4930053>

Charles, P. H., Cranmer-Sargison, G., Thwaites, D. I., Crowe, S. B., Kairn, T., Knight, R. T., ... Trapp, J. V. (2014). A practical and theoretical definition of very small field size for radiotherapy output factor measurements. *Medical Physics*, 41(4), 41707. <http://doi.org/10.1118/1.4868461>

Das, I. J., Cheng, C.-W., Watts, R. J., Ahnesjö, A., Gibbons, J., Li, X. A., ... Zhu, T. C. (2008). Accelerator beam data commissioning equipment and procedures: Report of the TG-106 of the Therapy Physics Committee of the AAPM. *Medical Physics*, 35(9), 4186–4215. <http://doi.org/10.1118/1.2969070>

Ding, G. X., & Ding, F. (2012). Geometric penumbra= $s(\text{SSD}+d-\text{SDD})/\text{SDD}$ (8). *Physics in Medicine and Biology*, 57(17), 5509–5521. <http://doi.org/10.1088/0031-9155/57/17/5509>

Fox, C., Simon, T., Simon, B., Dempsey, J. F., Kahler, D., Palta, J. R., ... Yan, G. (2010). Assessment of the setup dependence of detector response functions for mega-voltage linear accelerators. *Medical Physics*, 37(2), 477–484. <http://doi.org/10.1118/1.3284529>

Grusell, E., & Rikner, G. (1993). Linearity with dose rate of low resistivity p-type silicon semiconductor detectors. *Physics in Medicine and Biology*, 38(6), 785–792. <http://doi.org/10.1088/0031-9155/38/6/011>

Kehwar, T. S., Bhardwaj, A. K., & Chakarvarti, S. K. (2006). Evaluation of dosimetric effect of leaf position in a radition field of an 80-leaf multileaf collimator fitted to the LINAC head as tertiary collimator. *Journal of Applied Clinical Medical Physics*, 7(3), 43–54. <http://doi.org/10.1120/jacmp.v7i3.2310>

Lewis, D., Micke, A., Yu, X., & Chan, M. F. (2012). An efficient protocol for radiochromic film dosimetry combining calibration and measurement in a single scan. *Medical Physics*, 39(10), 6339. <http://doi.org/10.1118/1.4754797>

Li, X. a, Soubra, M., Szanto, J., & Gerig, L. H. (1995). Lateral electron equilibrium and electron contamination in measurements of head-scatter factors using miniphantoms and brass caps. *Medical Physics*, 22(7), 1167–1170. <http://doi.org/10.1118/1.597508>

Low, D. A., Moran, J. M., Dempsey, J. F., Dong, L., & Oldham, M. (2011). Dosimetry tools and techniques for IMRT. *Medical Physics*, 38(3), 1313–1338. <http://doi.org/10.1118/1.3514120>

Marcu, L., Bezak, E., & Allen, B. J. (2012). *Biomedical Physics in Radiotherapy for Cancer*. Csiro Publishing. Retrieved from <https://books.google.com/books?id=BGXsqplYoDEC&pgis=1>

Mayles, P., Nahum, A., & Rosenwald, J. C. (Eds. . (2007). *Handbook of Radiotherapy Physics: Theory and Practice, 1st ed.* Taylor & Francis.

Micke, A., Lewis, D. F., & Yu, X. (2011). Multichannel film dosimetry with nonuniformity correction. *Medical Physics*, 38(5), 2523. <http://doi.org/10.1118/1.3576105>

Pai, S., Das, I. J., Dempsey, J. F., Lam, K. L., Losasso, T. J., Olch, A. J., ... Wilcox, E. E. (2007). Radiographic film for megavoltage beam dosimetry. *Medical Physics*, 34(6), 2228–2258. <http://doi.org/10.1118/1.2736779>

PTW Freiburg. (2013). *IONIZING RADIATION DETECTORS: Including Codes of Practice*. Retrieved from http://www.ptw.de/online_brochures.html

Rink, A., Lewis, D. F., Varma, S., Vitkin, I. A., & Jaffray, D. a. (2008). Temperature and hydration effects on absorbance spectra and radiation sensitivity of a radiochromic medium. *Medical Physics*, 35(10), 4545–4555. <http://doi.org/10.1118/1.2975483>

Seco, J., Clasié, B., & Partridge, M. (2014). Review on the characteristics of radiation detectors for dosimetry and imaging. *Physics in Medicine and Biology*, 59(20), R303–R347. <http://doi.org/10.1088/0031-9155/59/20/R303>

Shi, C., Papanikolaou, N., Yan, Y., Weng, X., & Jiang, H. (2006). Analysis of the sources of uncertainty for EDR2 film-based IMRT quality assurance. *Journal of Applied Clinical Medical Physics*, 7(2), 1–8. <http://doi.org/10.1120/jacmp.v7i2.2230>

van Hoof, S. J., Granton, P. V, Landry, G., Podesta, M., & Verhaegen, F. (2012). Evaluation of a novel triple-channel radiochromic film analysis procedure using EBT2. *Physics in Medicine and Biology*, 57(13), 4353–68. <http://doi.org/10.1088/0031-9155/57/13/4353>

Chapter 3 – Materials and Methods

3.1	Linear accelerator.....	3-1
3.2	Phantoms and detectors	3-3
3.2.1	Blue water phantom.....	3-3
3.2.1.1	Electrometer CU500e.....	3-4
3.2.1.2	Detectors.....	3-6
3.2.1.4	Alignment.....	3-8
3.2.1.5	Voltage	3-9
3.2.1.6	Dose rate	3-9
3.2.2	RW3	3-9
3.2.2.1	Detectors.....	3-10
3.3	References.....	3-19

This section will cover the material and methods needed to establish the characteristics of the small fields. The measurements were carried out at the Synergy bunker at Universitas Annex. This facility is equipped with a Synergy S linear accelerator.

3.1 Linear accelerator



Figure 17. Elekta Synergy S LINAC with Agility MLC

The Elekta Synergy S LINAC (figure 17) produced the 6, 10, and 15 MV photon beams for measurements and is capable of delivering 4, 6, 8, 10, 12 and 15 MeV electron beams.

The field definition of this accelerator is achieved by using the primary collimators and MLCs. This unit does not have secondary collimators. It is fitted with Agility MLCs that have 5 mm resolution

at the isocenter compared to the 10 mm resolution of the previous MLCs (Kantz et al., 2015; Thompson, Weston, Cosgrove, & Thwaites, 2014). The MLCs have increased length resulting in less transmission. The accuracy of the resulting field is within 2 mm.

Quality assurance was carried out monthly to ensure the LINAC response does not vary from the commissioning data (CPQR, 2013). The LINAC has been calibrated to 100 cGy/monitor unit (MU) at D_{\max} for a 10×10 cm². Output measurements were done to ensure that the LINAC operated within the $\pm 3\%$ dose output limit (Andreo et al., 2006).

3.2 Phantoms and detectors

The measurements should be clinically relevant, to achieve this, soft tissue equivalent or water equivalent materials should be used as a medium in which the results are collected. Water was used for measurements with IBA CC01, IBA EFD-3G diode and the PTW60019 microDiamond. Whereas, solid water (RW3, Goettingen white water) was used for the films, see section 3.2.2 for further details.

3.2.1 Blue water phantom



Figure 18 Scanditronix-Wellhofer water phantom

The water-tank measurements were collected using a water filled Blue water phantom (48x48x41 cm³) using the aforementioned detectors, figure 18. The phantom is fitted with detector holder and the holder is attached to motors that can be controlled remotely. The motors were used to position the detector at a chosen position during data collection. The maintenance was carried out to ensure that the motors positional accuracy was still within limits.

The rails which are used for positioning were cleaned and lubricated to ensure no stuttering during scanning. The positioning accuracy of the motors was assessed in all three directions, X, Y and Z. The OmniPro-Accept software was used to move the motors to a number of positions as displayed on the software: 100 mm, 200 mm, -200 mm, -100 mm and 0.0 mm, for the different directions. The distance travelled was then checked physically using a measuring tape, and compared to that displayed on the software. The differences were within ± 1 mm.

3.2.1.1 Electrometer CU500e



Figure 19. The dual processor based CU500E electrometer used to measure signals

The detectors were connected to the CU500e electrometer (figure 19) for power and measurements. The manufacturer advises that the unit be warmed up and allowed to stabilize for 30 minutes prior to taking measurements and also recommends calibration of the unit every year, for absolute dosimetry mode, but in this study, it is used for the relative measurements.

The measurements are normally collected using two detectors; reference and field detector. The field detector is used to collect the actual data, whilst the reference is used to correct for the pulsed dose rate of the linac. In this study, the use of the reference detector was not employed due to the reference being too close to the field at these field sizes thus influencing the collected the data. Instead, the measurements were collected using the step-by-step mode which allows for use of one detector. The time in between the steps needs to be optimized in order to achieve the same results as scanning with two detectors.

The Omni-Pro software was used to set the required voltage for a particular detector and background measurements. The full setup of the water phantom with the electrometer is shown below in figure 20.

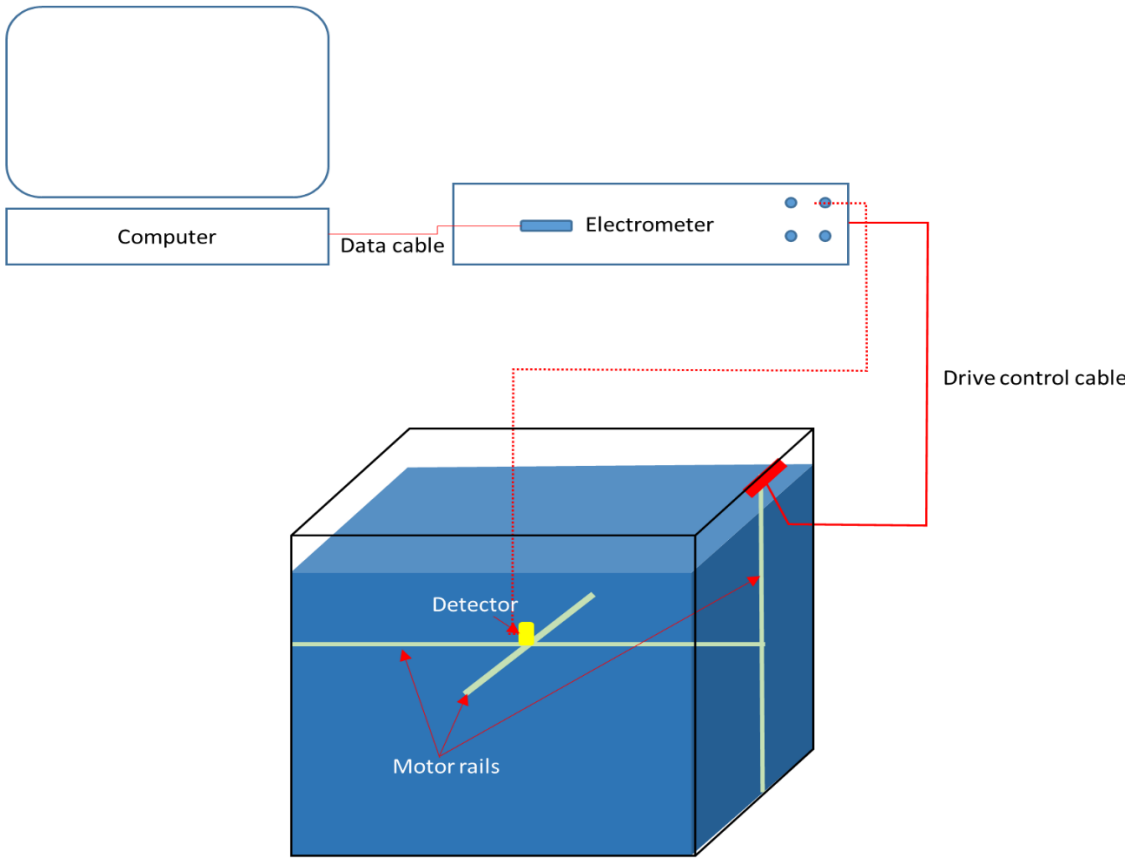


Figure 20 Complete blue water phantom connection

3.2.1.2 Detectors

IBA CC01 ion chamber



Figure 21. IBA-CC01 (top), mammography image (bottom)

The IBA-CC01 (figure 21) is a small volume air ion chamber manufactured by IBA, IBA has designed the chamber for use in small fields and for use in either in-air, in solid or in water phantoms to produce high reproducible measurements. The small volume improves the spatial resolution compared to larger volume ion chambers. The chamber is fitted with a steel electrode to improve the signal to noise ratio due to the small air volume enclosed by a 0.088 g/cm^2 thick C552 water-proof wall material. As the name suggests, the volume is 0.01 cm^3 with the cylindrical cavity length of 3.6 mm and a radius of 1.0 mm.

IBA Electron field diode-3G

The EFD-3G (figure 22) is a solid-state detector (diode) manufactured by IBA Dosimetry. The diode is a highly-doped p-type silicon (*pSi*) detector, this is a 3rd generation *pSi* semiconductor. The diode has a small circular active diameter of 2.0 mm with 0.06 mm thickness, and this is placed less than 0.9 mm from the surface. Though, the volume is small, the high density of Silicon as well as the small energy needed to create ion pairs, greatly improves the signal to noise ratio (SNR) of the detector due to the diode being 1800 times denser than air, or IBA-CC01. The detector is energy independent and dose rate independent according to the manufacturer. It does not require warm-up time prior collecting measurements.

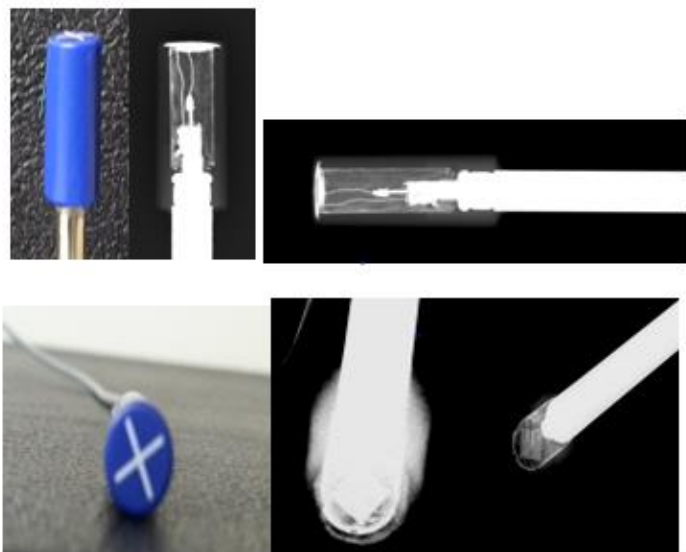


Figure 22 IBA EFD-3G diode with mammography images to view the active area

PTW 60019 microDiamond

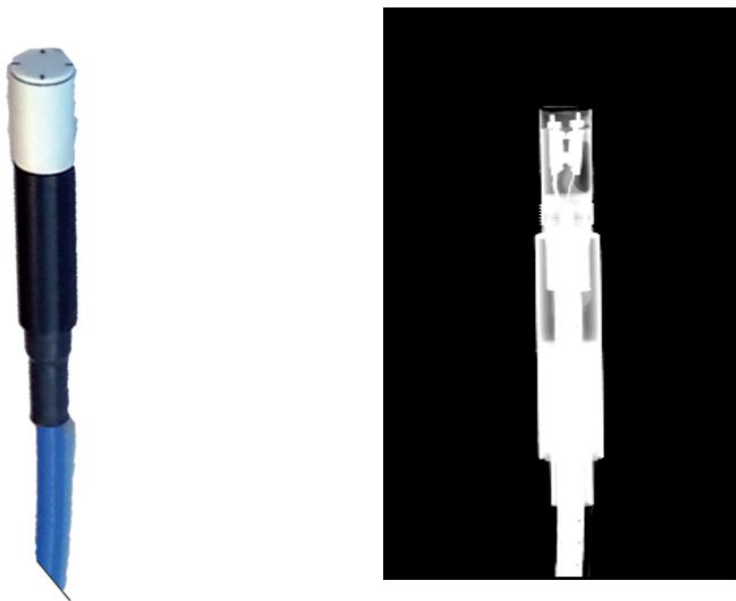


Figure 23. PTW60019 microdiamond detector, with its mammography image

The diamond detector (figure 23) manufactured by PTW, is a synthetic diamond detector. The detector has a sensitive volume of 0.004 mm^3 , with a radius of 1.1 mm and a thickness of 0.001 mm. The reference point is placed 1 mm below the detector tip. The small sensitive volume

makes this a good detector for use in small fields. This detector has shown minimal energy, dose rate, temperature and directional dependence, thus changes within these factors will not have an influence on the measured signal according to the manufacturer.

3.2.1.4 Alignment

The alignment of the detector along the beam central axis is important in characterizing a field. The active volume of the detector is not always symmetrical around the central axis; thus, resolution of data alters with direction of alignment. Figure 24 shows the different orientations for the ion chamber, diode, and the diamond detector. Orientation A will provide better resolution of the penumbra due to the high lateral spatial resolution, whereas, orientation B, will be better used for measuring PDDs. However, the effect decreases as the ratio of the length and width of the sensitive volume becomes one (Martens, De Wagter, & De Neve, 2000). The CC01 was aligned according to orientation A for all measurements. The IBA EFD-3G diode and PTW600019 micro-diamond were both aligned according to orientation B according to the manufacturer's specifications.

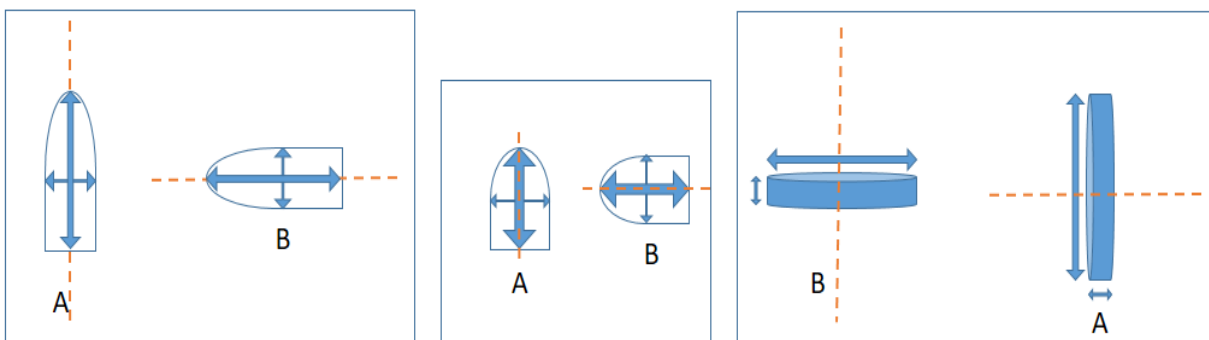


Figure 24 Sensitive volume orientations, left and centre shows the sensitive volume of ion chambers with large and small cavity. The right image shows the sensitive volume of a diode or diamond detector

The detectors were aligned visually with the cross hairs (centre of the beam, CAX), and then the OmniPro software is used to correct the positioning of the detector. The servo measured a depth dose curve to find the position of Dmax and 40% of a maximum dose. Then in-line and cross-lines profiles are measured at these depths, and the position of the 50% level was determined for these profiles. The positions of the 50% for the profiles are compared and the offsets are then displayed.

3.2.1.5 Voltage

Diode and micro-diamond detectors are semiconductor detectors thus no voltage is applied, CC01 required 300 volts to allow for optimal data collection.

3.2.1.6 Dose rate

Dose rate or dose per pulse was kept at 400 cGy/min. The detectors used have been reported to exhibit low to no dose rate dependence, that is the reading will not change as the dose rate from the LINAC is altered.

3.2.1.7 Field characteristics

The beam profile measurements were measured in both inline and crossline direction. These were measured 10 cm below water surface, for the 90 cm, 95 cm, 100 cm and 110 cm SSDs. The PDD was measured on the CAX, with the detector moving from 20 cm depth towards the surface. A depth of 20 cm was chosen as this is the limiting depth for the film because of the dimensions of the RW3 slabs. The chamber was then placed on the CAX at 10 cm depth, and 100 MU were delivered to obtain the output factors for the different field sizes.

The water based detectors were placed with their centres on the CAX. This was achieved by use of Omnipro[®] software, up to the 2×2 cm² field size. The 1×1 cm² field size profiles indicated that the centre of the detector had to be adjusted to ensure alignment with CAX. These steps are important in ensuring the signals are from the CAX otherwise the measured signal will be measured off axis, resulting in a decrease of the relative output factor.

3.2.2 RW3

The RW3 is a solid water phantom (figure 25) that has a water equivalent physical density of 1.045 g/cm³. The elemental composition by relative weight: Hydrogen (7.59%), Carbon (90.41%), Oxygen (0.8%) and Titanium (1.2%). The phantom is water-equivalent in the energy range from C0-60 to 25 MV photons (Hill, Brown, & Baldock, 2008). The plate thickness has a tolerance of ±0.1 mm.



Figure 25 RW3 (Goettingen white water), shown here is the 5 cm arrangement (left) and 10 cm (right).

3.2.2.1 Detectors

EDR2 film

The EDR2 film is a radiographic film produced by Kodak. It is the only film currently available as the X-OMAT V2 is discontinued. The film uses silver bromide crystals of uniform size with effective silver thickness of $0.2 \mu\text{m}$, the base thickness is $180 \mu\text{m}$, gelatin coating thickness 5 g/cm^2 . The total silver density is 2.3 g/cm^2 . The recommended dose to the film is 500 cGy . The film has been shown to have 5% reductions in the OD when the dose rate was decreased, thus it is important to consider this when considering potential errors in film dosimetry, to avoid this error the films were exposed at a constant dose rate of 400 cGy/min for all the measurements.

The radiographic film is light sensitive; hence it is enclosed in a light tight envelope (figure 26). The envelope creates air bubbles when sandwiched between plastic phantoms, thus a hole should be pricked to let the air bubbles escape. This setup arrangement led to an over response of 10%, but this was remedied by placing the films horizontally to allow gravity to compress the films with the gantry laterally rotated for irradiation with the gantry tilted (figure 28). This arrangement will not influence the measurements except at very small field sizes at deeper depths, this will be indicated by the percentage depth dose curves (Pai et al., 2007). The CAX of the beam will be diverted away from the film resulting in decreased dose deposition.



Figure 26 Kodak EDR2 radiographic film



Figure 27 LINAC setup for measuring calibration curves, beam profiles and ROFs. This image shows an example of the setup for $10 \times 10 \text{ cm}^2$ field at an SSD of 95 cm with 10 cm build-up of the RW3 phantom.

Calibration curve

The radiographic EDR2 films which were used for measurement of percentage depth dose (PDD), beam profile, and ROFs, were cut into $5 \text{ cm} \times 20 \text{ cm}$ film pieces and sealed within a light-tight envelope. The cutting process was performed in the dark room as this film is sensitive to light. The film response versus dose calibration curves (Pai et al., 2007) were established for the photon beams using $10 \times 10 \text{ cm}^2$ field size, with film pieces placed at 10 cm depth in an RW3 phantom with a source to surface distance (SSD) of 100 cm and gantry angle of 0° . The dose given was 0, 30, 60, 90, 120, and 150 cGy at 400 cGy/min for all measurements (Chetty & Charland, 2002).

The films were developed using a PROTEC OPTIMAX processor and scanned using a VIDAR VXR-12 plus scanner (Figure 29) with a resolution of 75 dots per inch, at 12 bits depth, greyscale. Regions of interest were drawn at the centre of the film image using ImageJ® software to obtain the average pixel value. The radiation dose given to the film was corrected using PDD values at 10 cm depth for 6, 10 and 15 MV taken as 67.5%, 72.0%, and 76.5% respectively. The average pixel values along with the corrected doses at 10 cm depth were used to establish calibration curves (Shi et al., 2006).

The resulting dose and optical density (OD) were used to establish a fitting curve, which will allow the dose to be determined at any OD within the maximum range. The fitting parameters in equation 2-9, are then determined using the CURVEFIT function within the Interactive Data Language (IDL) software.

Beam profiles, ROFs and PDD

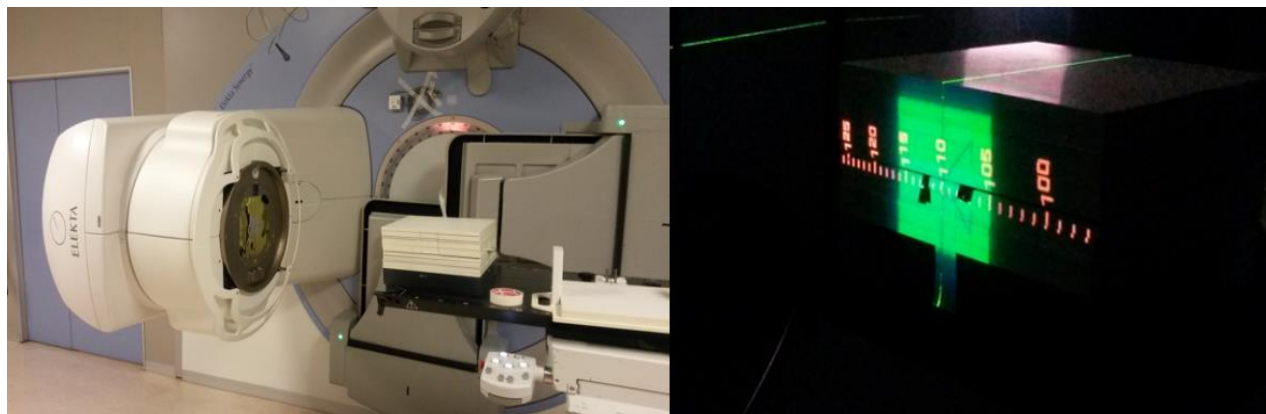


Figure 28 PDD measurement example for a $10 \times 10 \text{ cm}^2$ field size at an SSD of 110 cm, with a 10 cm build-up of RW3 phantom

The films that were used for investigation of beam profiles and ROFs were exposed to 120 MU for the different field sizes with gantry at 0° . The beam profiles were measured using two pieces of film for each field. The one film was aligned in the crossline direction and the other in the inline direction. These films were then placed at a 10 cm below the RW3 slabs. A total of 120 MU was then delivered for each investigation. Each field size was repeated twice.

The ROFs were determined from the resulting beam profiles, as the setup is similar compared to beam profiles measurements. The average pixel value of the central 80% of the field size for both

films to obtain an average OD for the field. This average was obtained using beam profile images without any smoothing. The central pixel value can be influenced by the scanner and other non-uniformities which require smoothing; thus, it is not accurate to just use this pixel value.



Figure 29 Optec film processor and VIDAR film scanner

The PDD (figure 30) was measured using a film piece sandwiched between slabs of RW3 and the gantry placed at 88° for the different field sizes and SSDs. The measurements were done for the $1 \times 1 \text{ cm}^2$, $2 \times 2 \text{ cm}^2$, $3 \times 3 \text{ cm}^2$, $4 \times 4 \text{ cm}^2$, $5 \times 5 \text{ cm}^2$ and $10 \times 10 \text{ cm}^2$ field sizes, each field was repeated for the following SSDs: 90 cm, 95 cm, 100 cm and 110 cm. Gantry angle of 2° from the normal, was used (Suchowerska, Hoban, Butson, Davison, & Metcalfe, 2001), to avoid penetration of un-attenuated primary beams between the slabs and also to minimize the effect of air pockets (Chetty & Charland, 2002).

These were developed, scanned and then converted to dose using the different calibration curve equations one for each energy. A line profile (5 pixel wide, translates to 1.8 mm thick) was drawn across the beam profile film to determine the field size and penumbra. Also, from this line profile, the average pixel value across the central 80% of the field was used as for determination of ROFs. The use of the central region provides better averages when compared to using just the CAX pixel which tends to deviate due to the erratic nature of film development and scanning. The ROF was

obtained from the same film that was used to obtain the beam profile. This method was applied to all fields except the $1 \times 1 \text{ cm}^2$, this field does not have a broad central region, and thus a 2 mm wide profile across the centre was drawn to obtain the average pixel value for the $1 \times 1 \text{ cm}^2$ field as shown in Figure 30. The PDD curve was obtained by drawing the same thick line profile across the films that were used for measuring PDD.

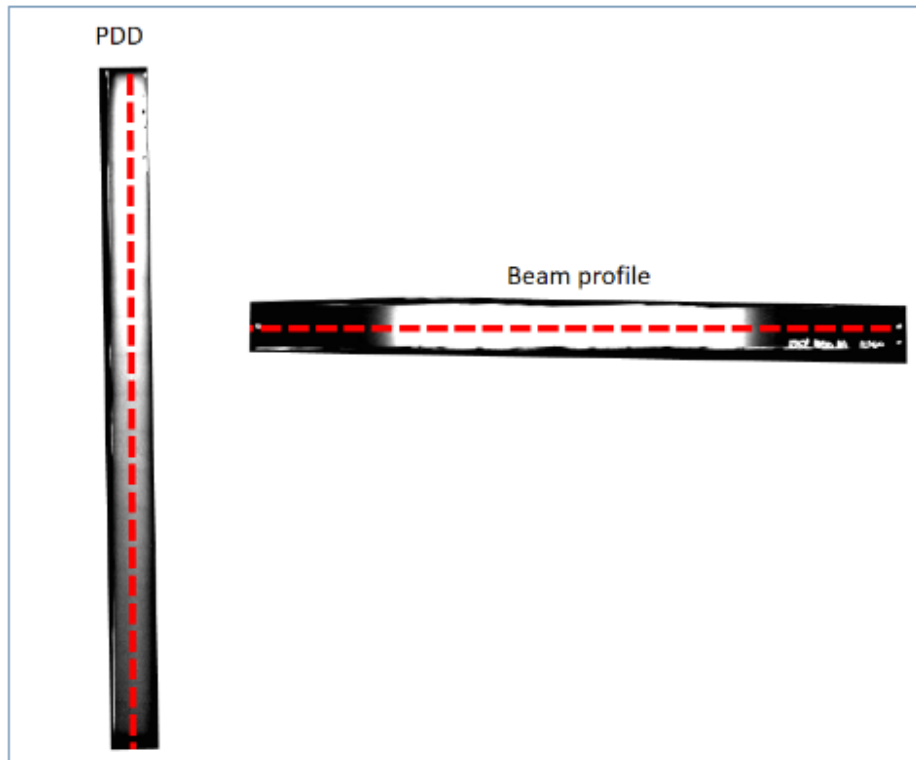


Figure 30 Line profile measurement of beam PDD (left) and beam profile (right).

Gafchromic film EBT2

The EBT2 that was used was always kept within light tight envelopes and was stored at room temperature ≈ 25 °c. The different lots were used for measurements thus, calibration curves were established in each measurement session. This needed to be performed as the response of the film changes according to lots and also is dependent on the storage environment, thus calibrating for each session decreased this potential error.

Calibration curve

The calibration film pieces (2×2.5 cm²) were exposed to 0, 75, 150, 300 and 350 MU. These film pieces were placed in the centre of a 10×10 cm² field, with 10 cm RW3 build-up (Lewis et al., 2012), (Alfonso et al., 2008; Wang, 2005) and the gantry angle of 0° at an SSD of 100 cm.

The 24-hour waiting period was observed after which the films were scanned using the Epson V330 document scanner. The films were scanned ten times, and keeping only the last scan, the repeats done to warm up the scanner. The scanning parameters that were used: 72 dots per inch (dpi), 48-bit colour depth (Hu, Wang, Fogarty, & Liu, 2013) and all scanner enhancements were deactivated.

The ROIs were drawn at the centre of the exposed film pieces to obtain the average pixel value. The dose given was also corrected for depth as described above for the EDR2 radiographic film. The calibration curve was then determined for each colour (Micke et al. 2010 and 2011; Méndez et al. 2014), the triple channel calibration method improves the flatness and symmetry response of the film, and allows the entire sensitive range of the film to be used in measurements. It also corrects for variations in the thickness of the active layer, the scanner nonlinearity and noise.

Lewis et al. 2012 found that the rational function (equation 3- 1) fitted well with the response seen from the film, and equation 2-8 is used to convert the pixel values obtained from ROI's drawn at the centre of the exposed film to OD,

$$OD = a + \frac{b}{Dose - c} \quad (3-1)$$

Where a , b and c being the fitting parameters, $Dose$ is the dose given to the film. The parameters as well as the root-mean-square errors were determined for each of the three colour channels. These values were used to convert the scanned image to a dose image using a matrix laboratory (MATLAB) works code.

The MATLAB code implemented the Micke-Mayer method as written in literature (Méndez et al., 2014). The absorbed dose, D , employed was given as:

$$D = \frac{(\sum_{k=1}^n \dot{D}_k)(\sum_{k=1}^n D_k \dot{D}_k) - (\sum_{k=1}^n \dot{D}_k^2)(\sum_{k=1}^n D_k)}{(\sum_{k=1}^n \dot{D}_k)^2 - n(\sum_{k=1}^n \dot{D}_k^2)} \quad (3-2)$$

Where D_k , is the absolute dose measured by channel k , this has been determined using the following equation,

$$D_k = c + \frac{b}{OD - a} \quad (3-3)$$

And \dot{D}_k , is the first derivative of the dose (eq. 3-4) with respect to the net optical density (NOD),

$$\dot{D}_k = \frac{-b}{(OD - a)^2} \quad (3-4)$$

The error in the dose, σ_D , was given by,

$$\sigma_D = \sigma_k \sqrt{\frac{\sum_{k=1}^n \dot{D}_k^2}{n(\sum_{k=1}^n \dot{D}_k^2) - (\sum_{k=1}^n \dot{D}_k)^2}} \quad (3-5)$$

And the variance of dose in each colour channel (RMSE), σ_k^2 . The Micke-Mayer (MM) method is considered equal for all channels and also the probability density functions are assumed to be uniformly distributed.

Beam profile, ROFs and PDD

The EBT2 film was cut into $2 \times 20 \text{ cm}^2$ strips to measure PDD's for 6, 10 and 15 MV photon beams (Arjomandy, Tailor, Zhao, & Devic, 2012), and the films were also cut into 1 cm by twice the field side length to obtain beam profiles. The length ensures that the full penumbra fitted onto the film strip. The beam profiles, ROFs, and PDD were determined as in the above case using radiographic film.

3.3 References

Alfonso, R, P Andreo, R Capote, M Saiful Huq, W Kilby, P Kjäll, T R Mackie, et al. "A New Formalism for Reference Dosimetry of Small and Nonstandard Fields." *Medical Physics* 35, no. 11 (2008): 5179–86. doi:10.1118/1.3005481.

Andreo, P, D Burns, K Hohlfield, M S Huq, T Kanai, F Laitano, V G Smyth, and S Vynckier. "Absorbed Dose Determination in External Beam Radiotherapy: An International Code of Practice for Dosimetry Based on Absorbed Dose to Water" IAEA Tech., no. June (2006): 183. http://www-naweb.iaea.org/nahu/DMRP/documents/CoP_V12_2006-06-05.pdf.

Arjomandy, Bijan, Ramesh Tailor, Li Zhao, and Slobodan Devic. "EBT2 Film as a Depth-Dose Measurement Tool for Radiotherapy Beams over a Wide Range of Energies and Modalities." *Medical Physics* 39, no. 2 (2012): 912. doi:10.1118/1.3678989.

Chetty, Indrin J, and Paule M Charland. "Investigation of Kodak Extended Dose Range (EDR) Film for Megavoltage Photon Beam Dosimetry." *Physics in Medicine and Biology* 47, no. 20 (2002): 3629–41. doi:10.1088/0031-9155/47/20/305.

CPQR. "Canadian Partnership for Quality Radiotherapy Technical Quality Control Guidelines for Canadian Radiation Treatment Centres Medical Linear Accelerators and Multileaf Collimators A Guidance Document on Behalf of : Canadian Association of Radiation Oncology," 2013, 1–23.

Hill, R F, S Brown, and C Baldock. "Evaluation of the Water Equivalence of Solid Phantoms Using Gamma Ray Transmission Measurements" 43 (2008): 1258–64. doi:10.1016/j.radmeas.2008.01.019.

Hu, Yunfei, Yang Wang, Gerald Fogarty, and Guilin Liu. "Developing a Novel Method to Analyse Gafchromic EBT2 Films in Intensity Modulated Radiation Therapy Quality Assurance." *Australasian Physical & Engineering Sciences in Medicine / Supported by the Australasian College of Physical Scientists in Medicine and the Australasian Association of Physical Sciences in Medicine* 36, no. 4 (2013): 487–94. doi:10.1007/s13246-013-0232-y.

Kantz, Steffi, Matthias Söhn, Almut Troeller, Michael Reiner, Helmut Weingandt, Markus Alber, Claus Belka, and Ute Ganswindt. "Impact of MLC Properties and IMRT Technique in Meningioma and Head-and-Neck Treatments." *Radiation Oncology* 10, no. 1 (2015): 184. doi:10.1186/s13014-015-0447-z.

Lewis, David, Andre Micke, Xiang Yu, and Maria F. Chan. "An Efficient Protocol for Radiochromic Film Dosimetry Combining Calibration and Measurement in a Single Scan." *Medical Physics* 39, no. 10 (2012): 6339. doi:10.1118/1.4754797.

Martens, C, C De Wagter, and W De Neve. "The Value of the PinPoint Ion Chamber for Characterization of Small Field Segments Used in Intensity-Modulated Radiotherapy." *Physics in Medicine and Biology* 45 (2000): 2519–30. doi:10.1088/0031-9155/45/9/306.

Méndez, I, P Peterlin, R Hudej, a Strojnik, and B Casar. "On Multichannel Film Dosimetry with Channel-Independent Perturbations." *Medical Physics* 41, no. 1 (2014): 11705. doi:10.1118/1.4845095.

Micke, a, D Lewis, and X Yu. "Triple Channel Technique Film Dosimetry Single Channel Film Dosimetry Calibration Curve $X = R$." *Isp*, no. January (2010).

Micke, Andre, David F. Lewis, and Xiang Yu. "Multichannel Film Dosimetry with Nonuniformity Correction." *Medical Physics* 38, no. 5 (2011): 2523. doi:10.1118/1.3576105.

Pai, Sujatha, Indra J Das, James F Dempsey, Kwok L Lam, Thomas J Losasso, Arthur J Olch, Jatinder R Palta, Lawrence E Reinstein, Dan Ritt, and Ellen E Wilcox. "Radiographic Film for Megavoltage Beam Dosimetry." *Medical Physics* 34, no. 6 (2007): 2228–58. doi:10.1118/1.2736779.

Shi, Chengyu, Nikos Papanikolaou, Yulong Yan, Xuejun Weng, and Hongyu Jiang. "Analysis of the Sources of Uncertainty for EDR2 Film-Based IMRT Quality Assurance." *Journal of Applied Clinical Medical Physics* 7, no. 2 (2006): 1–8. doi:10.1120/jacmp.v7i2.2230.

Suchowerska, Nataalka, Peter Hoban, Martin Butson, Alastair Davison, and Peter Metcalfe. "Directional Dependence in Film Dosimetry: Radiographic and Radiochromic Film." *Physics in Medicine and Biology* 46, no. 5 (May 1, 2001): 1391–97. doi:10.1088/0031-9155/46/5/305.

Thompson, C M, S J Weston, V C Cosgrove, and D I Thwaites. "A Dosimetric Characterization of a Novel Linear Accelerator Collimator." *Medical Physics* 41, no. 3 (2014): 31713. doi:10.1118/1.4866228.

Wang, Yang. "filmdosimetry02Whole.pdf," 2005.

Chapter 4 Results and Discussion

4.1.1	EBT2	4-1
4.1.2	EDR2	4-4
4.2	Beam profiles	4-7
4.2.2	Beam profiles measured at an SSD of 95 cm	4-28
4.2.3	Beam profiles measured at an SSD of 100 cm	4-46
4.2.4	Beam profiles measured at an SSD of 110 cm	4-64
4.3	Percentage depth dose	4-82
4.3.1	PDDs measured at an SSD of 90 cm	4-87
4.3.2	PDDs measured at an SSD of 95 cm	4-98
4.3.3	PDDs measured at an SSD of 100 cm	4-109
4.3.4	PDDs measured at an SSD of 110 cm	4-120
4.4	Relative output factors	4-131
4.4.1	Output factors measured using a 6 MV photon beam at different SSDs	4-132
4.4.2	Output factors measured using a 10 MV photon beam at different SSDs	4-135
4.4.3	Output factors measured using a 15 MV photon beam at different SSDs	4-137
4.5	References	4-139

4.1 Film analysis

4.1.1 EBT2

The calibration films were exposed, scanned and the appropriate fitting variables were then determined using the IDL software.

The calibration curve for the EBT2 film was obtained using the 15 MV photon beam at an SSD of 100 cm and this was repeated five times. The resulting curve is displayed in figure 31 with the fitting parameters shown in table 2. The y-axis represents the OD determined from the films that were scanned, and the x-axis represents the dose given to the films. The fit functions for each channel are shown below, red channel (equation 4-1), green channel (equation 4-2) and blue channel (equation 4-3).

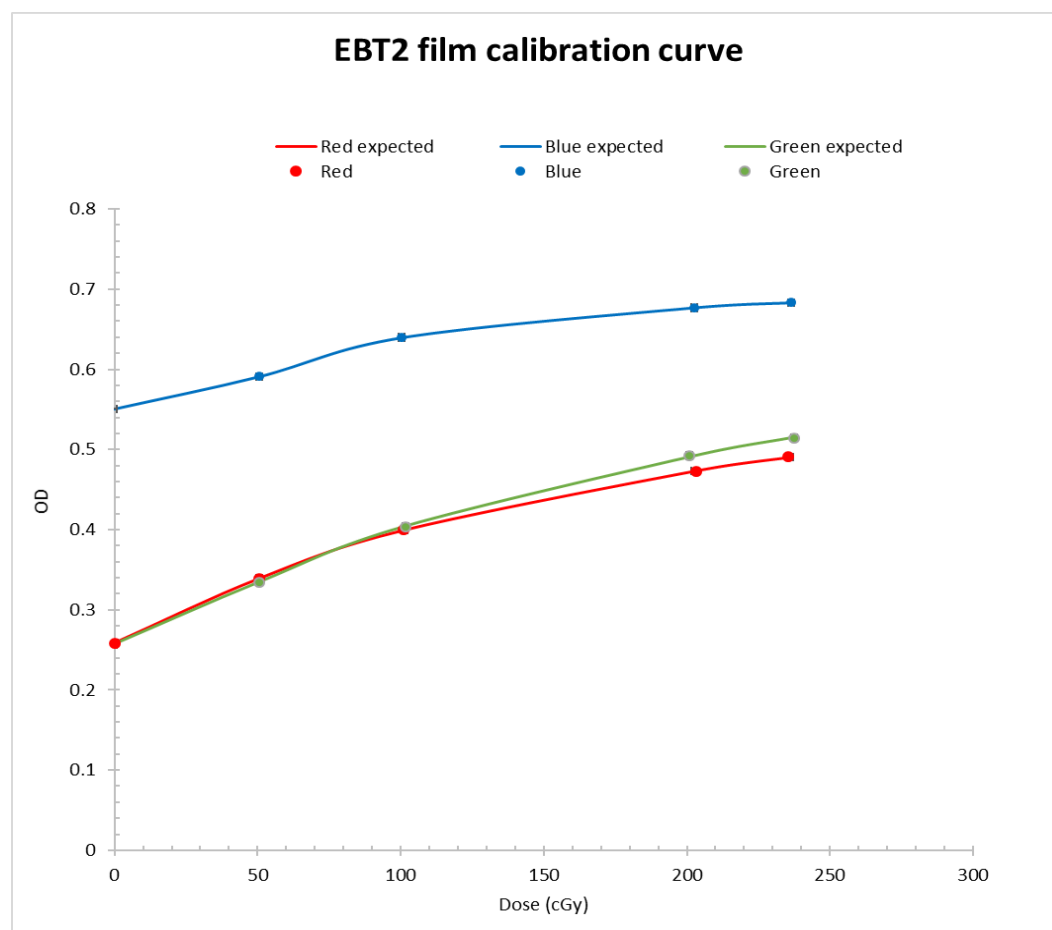


Figure 31. EBT2 film calibration curve

Table 2. EBT2 gafchromic film average *a*, *b* and *c*, for eq 3-3 where RMSE is the variance in the Dose for each channel

EBT2		a	b	c	RMSE
Red	Avg	0.743	-116.363	-245.568	1.599
	Stdev	0.027	18.112	29.127	1.234
Green	Avg	1.146	-444.995	-503.638	1.722
	Stdev	0.112	145.882	99.776	0.896
Blue	Avg	1.080	-248.857	-477.264	2.485
	Stdev	0.078	92.135	114.436	1.186

The calibration was carried out as mentioned in chapter 3. The resulting root mean square (RMSE) values obtained from fitting the calibration curves from the measurements, indicate that the errors in the Dose calculated using the EBT2 film are acceptable, thus the fitted data is not spread out from the measured data.

The coefficient of variation (CV) describes the variation of each variable from the mean of the acquired data. A lower CV value indicates less variation, thus a good fit. The red channel CV is lower compared to the other channels as shown in table 3. Though, the red channel seems to offer higher accuracy compared to other channels, Micke et al. has shown that the incorporation of other channels improves the overall accuracy of dose determined from the film (Micke et al., 2011).

Table 3. CV for the different colour channels

	a	b	C
Red	3.6%	-15.6%	-11.9%
Green	9.8%	-32.8%	-19.8%
Blue	7.2%	-37.0%	-24.0%

The fitting functions of these curves are indicated below, the dose curve function for the red channel is shown in equation 4-1, with green channel fitting function shown in equation 4-2 and lastly the blue channel dose curve fitting function shown in equation 4-3. The associated RMSE values are indicated in table 1.

$$Dose_{red} = -245.57 + \left(\frac{-116.36}{\log\left(\frac{65535}{PixelValue_{red}}\right) - 0.743} \right) \quad (4-1)$$

$$Dose_{green} = -503.64 + \left(\frac{-445.00}{\log\left(\frac{65535}{PixelValue_{green}}\right) - 1.146} \right) \quad (4-2)$$

$$Dose_{blue} = -477.26 + \left(\frac{-248.86}{\log\left(\frac{65535}{PixelValue_{blue}}\right) - 1.08} \right) \quad (4-3)$$

4.1.2 EDR2

The calibration curves for the EDR2 film were measured in a similar manner to that used for the EBT2 film but each energy had its own curve as shown in figure 32. The curves were determined for every measuring session. The y-axis represents the OD determined from the films that were scanned, and the x-axis represents the dose given to the films. The average pixel value of the unexposed film (base + fog) was 342 units for this processor.

The curves shown below differ with energy as suggested by Indrin et al. (Chetty & Charland, 2002).

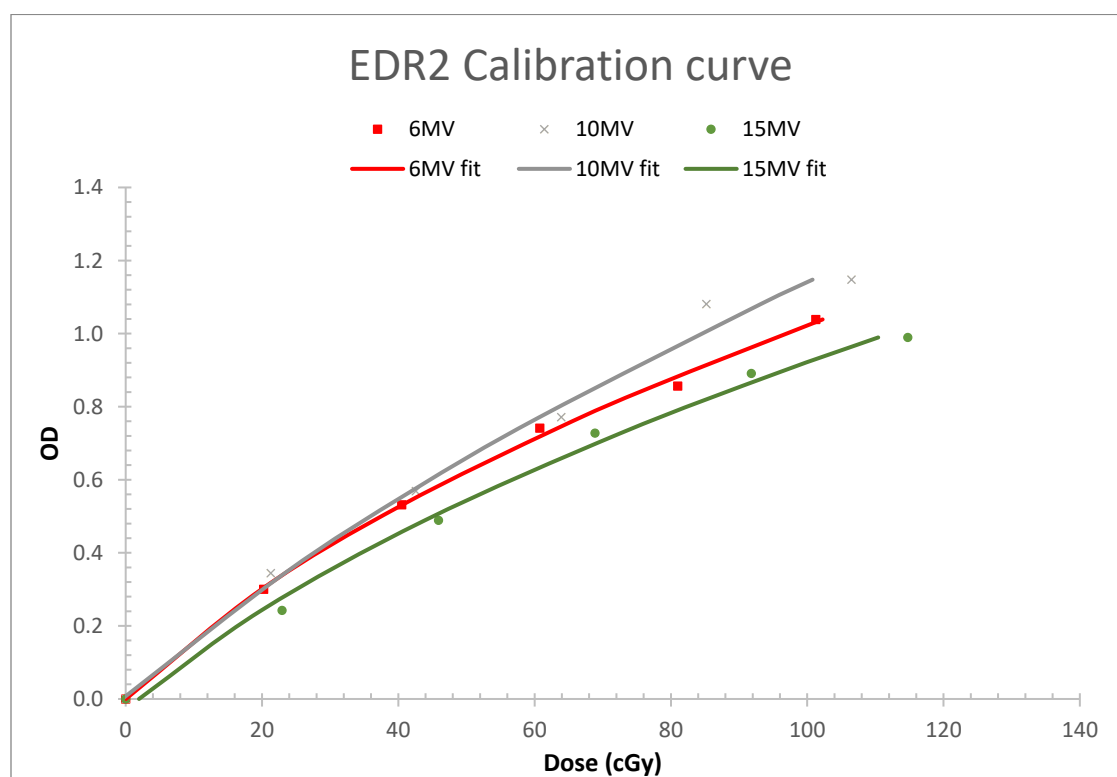


Figure 32. The EDR2 calibration curve with associated curve fitting functions for the different energies employed in the study

The curves above show the calibration data as well as their fitting functions. A method of least square fitting using a polynomial function was used to determine the fit functions for the different energies at an SSD of 100 cm with a 10×10 cm² field. The resulting equations describing the data are listed below:

$$Dose (6MV) = 43.50D^2 + 53.20D + 0.023 \quad (4-4)$$

$$Dose (10MV) = 23.60D^2 + 61.180D - 0.52 \quad (4-5)$$

$$Dose (15MV) = 47.60D^2 + 62.50D + 1.95 \quad (4-6)$$

Where OD is the optical density. The fitting parameters for the 6 MV, 10 MV and 15 MV are shown in table 4, table 5 and table 6, respectively with their associated RMSE values. The results show that the RMSE varies from one session to the next, thus the need to repeat the calibration curve for each session. The variation is due to the different film batches during data collection, this was impossible to overcome due to the number of films required to complete the collection.

The processor conditions such as the change in temperature will influence the development of the film (Pai et al., 2007)(Hsu, Kulasekere, & Roberson, 2010). The linac output variation was within the acceptable limit of $\pm 3\%$ (Klein et al., 2009), thus this did not strongly influence the data. The time between the last film being exposed and developed was at least 3 hours, Childress et al. (Childress & Rosen, 2004) showed at least 1-hour gap is needed between exposure and development for the EDR2 film, as this allows the chemical processes taking place to stabilize after radiation exposure.

Table 4. EDR2 radiographic film a, b and c values for a 6 MV photon beam at different SSD (eq 2-9)

6MV					
SSD	Repetition	a	b	c	RMSE
90 cm	1	36.084	58.610	2.801	6.476
	2	-0.220	123.195	-0.697	3.930
95 cm	1	32.317	66.077	-0.719	1.690
	2	38.077	78.197	1.225	1.370
100 cm	1	43.489	53.243	0.023	1.829
	2	43.131	65.492	1.128	1.285
110 cm	1	11.113	94.629	-0.252	2.462
	2	27.764	78.749	0.092	0.176

Table 5. EDR2 radiographic film *a*, *b* and *c* values for a 10 MV photon beam at different SSD (eq 2-9)

10MV					
SSD	Repetition	a	b	c	RMSE
90 cm	1	23.607	61.177	-0.520	4.328
	2	105.470	-1.547	0.339	4.570
95 cm	1	30.728	58.878	0.379	2.113
	2	51.149	87.152	-0.809	6.317
100 cm	1	42.039	53.381	0.042	2.814
	2	26.489	83.013	-0.149	0.926
110 cm	1	41.847	56.223	1.638	1.814
	2	27.523	75.320	0.418	1.407

Table 6. EDR2 radiographic film *a*, *b* and *c* values for a 15 MV photon beam at different SSD (eq 2-9)

15MV					
SSD	Repetition	a	b	c	RMSE
90 cm	1	20.479	76.648	2.313	4.960
	2	55.421	73.347	1.265	2.944
95 cm	1	10.777	104.972	0.909	2.483
	2	25.464	84.453	-0.769	1.306
100 cm	1	49.845	47.323	-0.120	0.877
	2	31.098	77.406	0.462	1.591
110 cm	1	47.605	62.513	1.953	3.259
	2	99.620	32.962	2.330	4.102

The resulting parameters were used to converted the scanned images to dose using IDL®.

4.2 Beam profiles

A beam profile indicates the change of dose across a field, details such as the field size, penumbra, flatness and symmetry of the field can be extracted from the beam profile. Of interest in this section are the field size and the penumbra. The field size is the distance between the 50% relative dose points on the curve, and the penumbra is the distance between 80% relative dose point and the 20% relative dose point on the curve. The penumbra measured is composed of three penumbrae namely: geometric, transmission and scatter contributions. The resulting penumbra is influenced by the beam energy, source size, source to surface distance, source to collimator distance, field size and the depth in a phantom.

The profiles were collected using the Omnipro[®] software for the water-based detectors, whereas the film data had to be converted to dose using the above calibration curves. The dose was then imported into Omnipro[®] using an in-house IDL code.

The data obtained from the film were noisy, this was addressed using the available smoothing functions within Omnipro[®] software. The optimised smoothing parameters were first determined prior to finally smoothing out the noise of the collected data, the optimisation was done to ensure that the slope of the profile was not altered in order to achieve the desired smoothness (Das et al., 2008). There are a number algorithms available in the software, the manufacturer has advised the use of a spline interpolation algorithm (SPA) and a median smoothing filter (MSF) when smoothing profiles, as these algorithms conserve the slope of the profile. The slope is used to determine the penumbra and the field size of the set field size. An example is shown below in figure 33. The applied smoothing was able to correct for the noise seen on the raw profile whilst conserving the slope.

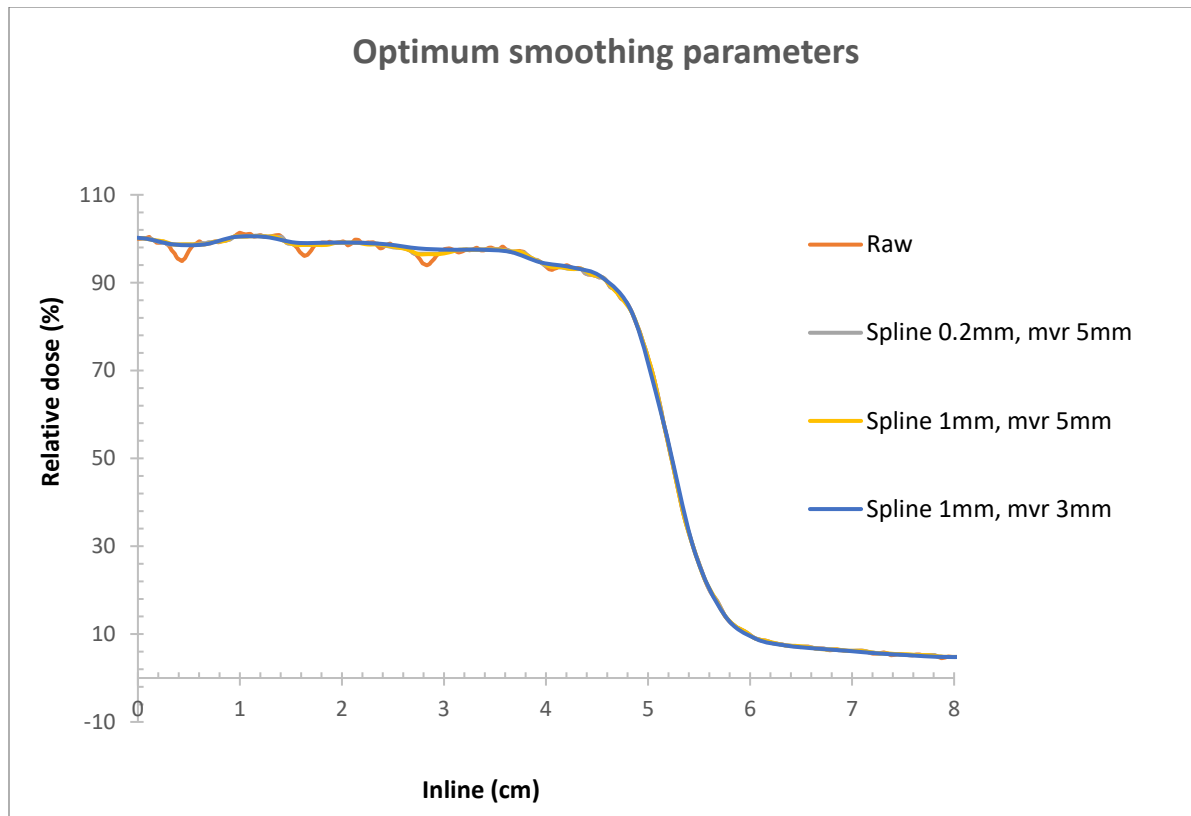


Figure 33. Optimum smoothing parameters for profiles using a EDR2 measured beam profile as an example

The discussion which follows below indicates the relation of the measured graphs between the detectors at each field size. The details concerning the penumbrae and field sizes measured by each detector in each direction at the different SSDs are listed in Appendix 1.

Appendix 1 shows the numerical values of the penumbrae on the left (PenL), penumbrae on the right (PenR) and the field sizes (FS) as measured by each detector at each SSD. The results show that penumbrae are sharper when measured in the Inline direction compared to the Crossline, this is due to the collimation being carried out at different source to diaphragm distances.

The increase in SSD shows that both the penumbrae and field size increase. The increase in the penumbrae is due to the increase in the geometric penumbrae, whereas, the field size changes based on the inverse square law.

The results also show the influence of the photon energy, in that the penumbrae are sharper for the 6 MV as compared to the 10 MV and the 15 MV. This is attributed to the increase in the transmission penumbra as the energy increases.

4.2.1 Beam profiles measured at an SSD of 90 cm

90 cm 6 MV Crossline

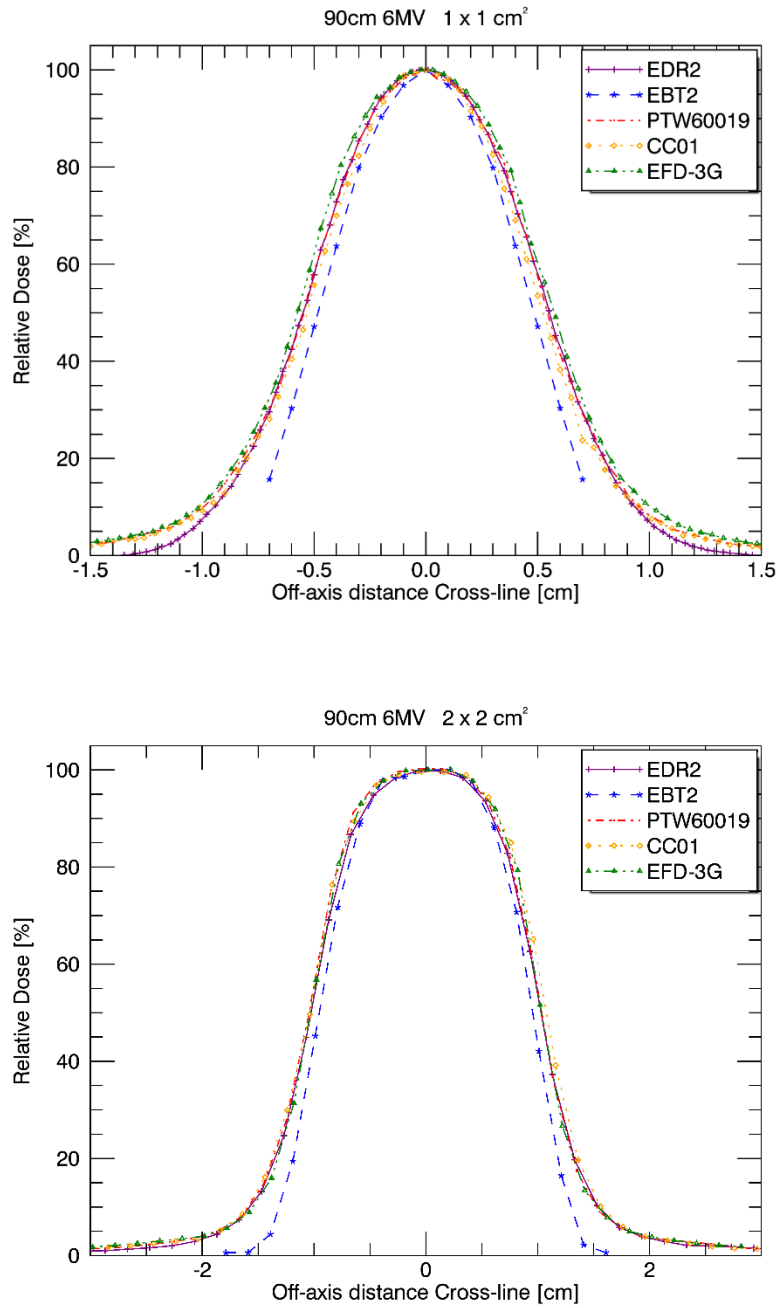


Figure 34. Crossline profiles for the 1x1 cm² and 2x2 cm² measured at an SSD of 90 cm and 10 cm depth in water using a 6 MV photon beam

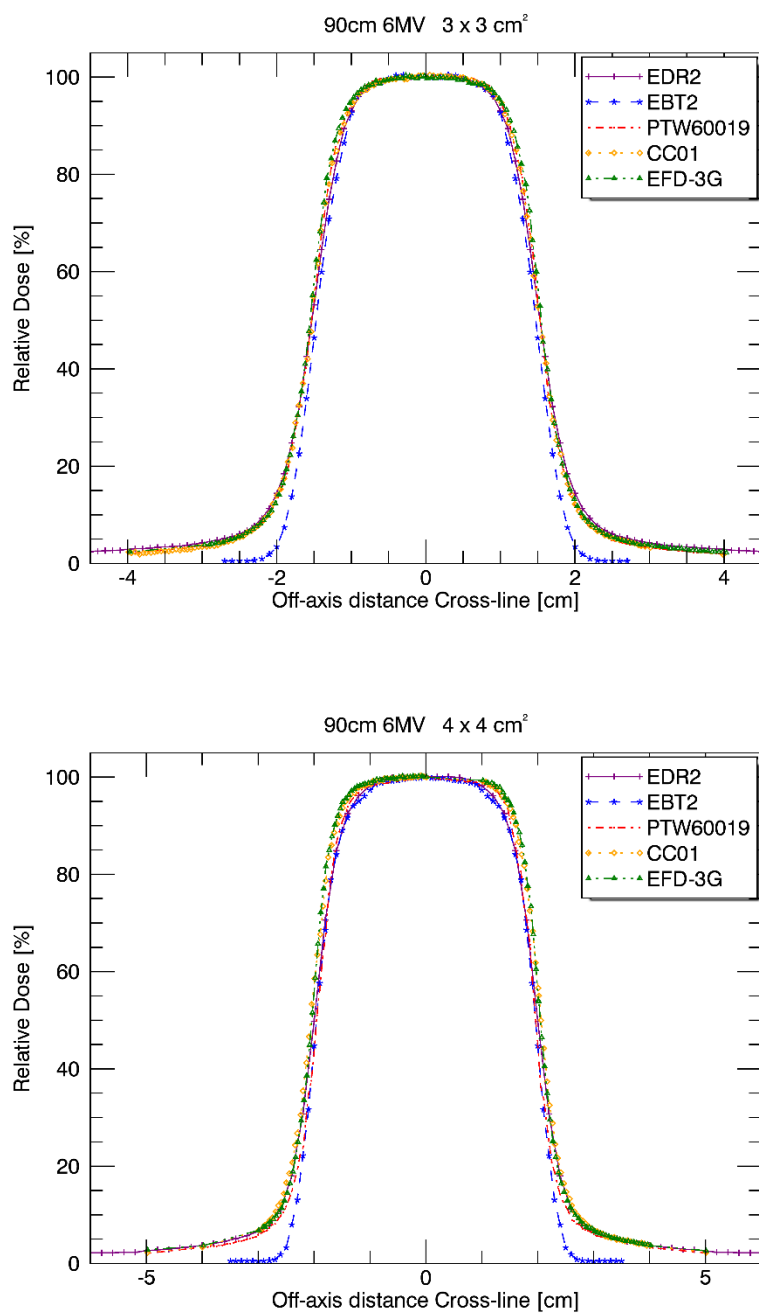


Figure 35. Crossline profiles for the $3 \times 3 \text{ cm}^2$ and $4 \times 4 \text{ cm}^2$ measured at an SSD of 90 cm and 10 cm depth in water using a 6 MV photon beam

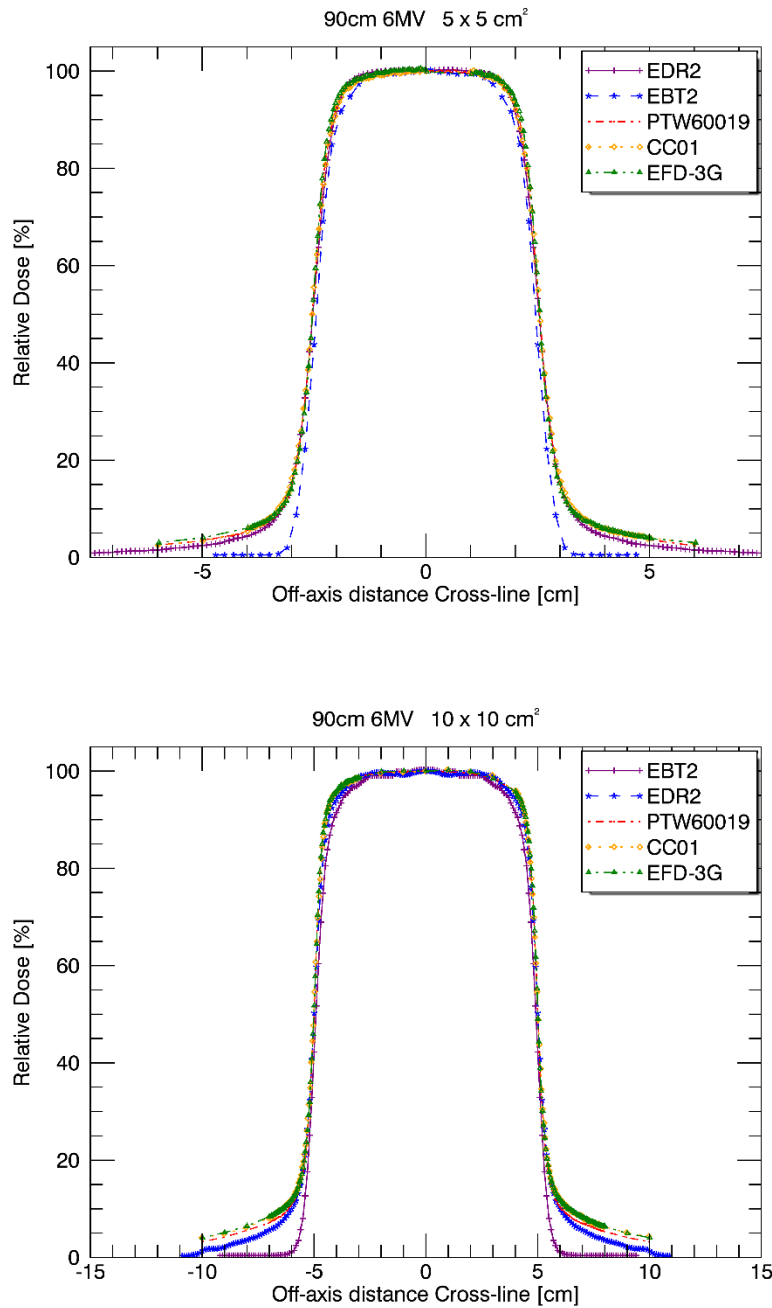


Figure 36. Crossline profiles for the 5x5 cm² and 10x10 cm² measured at an SSD of 90 cm and 10 cm depth in water using a 6 MV photon beam

Figure 34 shows that for the 1x1 cm² field size EBT2 film has a different curve compared to other detectors. However, the field sizes of the detectors for the above Crossline profiles do not show any noticeable differences except for the EBT2 film which measures smaller field sizes compared

to other detectors. The variation between the detectors is mostly seen in the jaw direction, this is prone to instabilities over time as mentioned by Das (Das, Cheng, et al., 2008)

This EBT2 film was cut short to only measure the beam profile up until at least 10% of the central axis to determine the penumbra. This was done to maximise film use, due to it being expensive.

The penumbrae changes by at least 3 mm from $1 \times 1 \text{ cm}^2$ to $10 \times 10 \text{ cm}^2$ field size (Appendix 1). The dome shape of the $5 \times 5 \text{ cm}^2$ and $10 \times 10 \text{ cm}^2$, see figure 35, field size were caused by the films not lying flat (Lewis & Devic, 2015) due to incessant Newton ring artefacts which resulted from the clean film clinging to the cleaned scanner glass. This resulted in central dose being higher than the off-axis dose. And since the profile were normalized to the central dose, it meant that the shoulders would sink resulting in the differences seen as they had a lower dose. This shows up for the longer films used to measure the $10 \times 10 \text{ cm}^2$ field size, as it was at these fields the artefact was apparent.

The penumbrae measured with the different detectors showed that the EBT2 film has a sharper penumbra, followed by the EFD-3G and the PTW60019, then both the CC01 and the EDR2 have broader penumbrae. This can be explained by the volumes of each detector the CC01 has the largest sensitive volume compared to other detectors, the EFD-3G and PTW60019 have the same sensitive radius of 2 mm, the EBT2 active particles have a size of 1-2 μm in diameter and 15-25 μm in length and with the EDR2 having grain sizes less than 1-3 μm . Based on these specifications, EDR2 should give a sharper penumbra based on the fact that its active particles are smaller, but due to its energy dependence it spreads out the penumbra (Cheung, Butson, & Yu, 2006).

The EDR2 results are questionable, as literature has shown that the EDR2 resolution closely correlates to that of the EBT2 film (Cheung et al., 2006), this results agree more with those shown by Patrick et al. (Cadman, McNutt, & Bzdusek, 2005). The EFD-3G, as well as the PTW60019, were expected to give similar penumbra as the detectors have similar sizes when their sensitive 2 mm wide active region is placed perpendicularly to the incoming beam (Bucciolini et al., 2003). The CC01 was expected to perform poorly in comparison to the others as it is the largest detector and thus it should experience more of the volume averaging effect resulting in a wider penumbra (Low et al., 2011).

90 cm 6 MV Inline

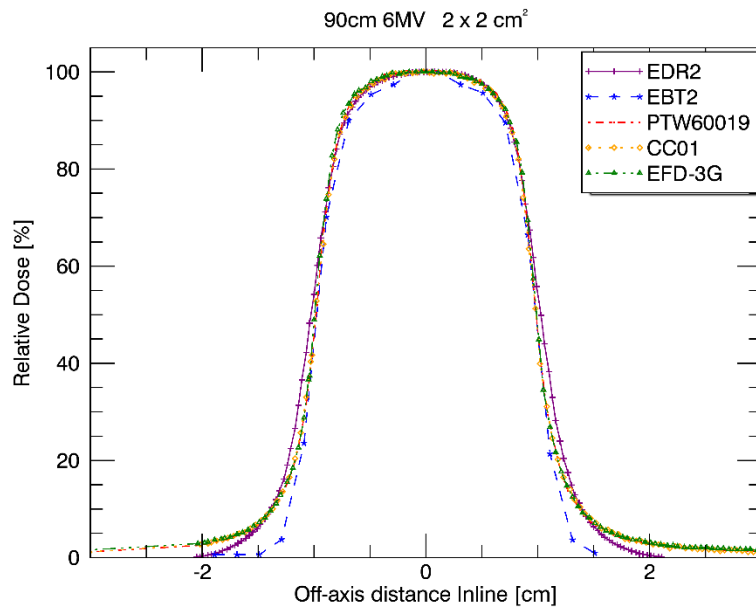
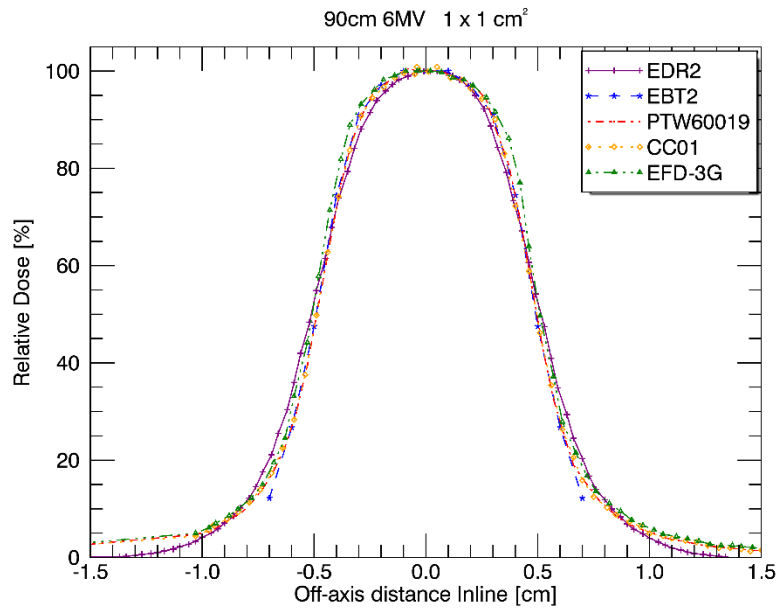


Figure 37. Inline profiles for the 1×1 cm² and 2×2 cm² measured at an SSD of 90 cm and 10 cm depth in water using a 6 MV photon beam

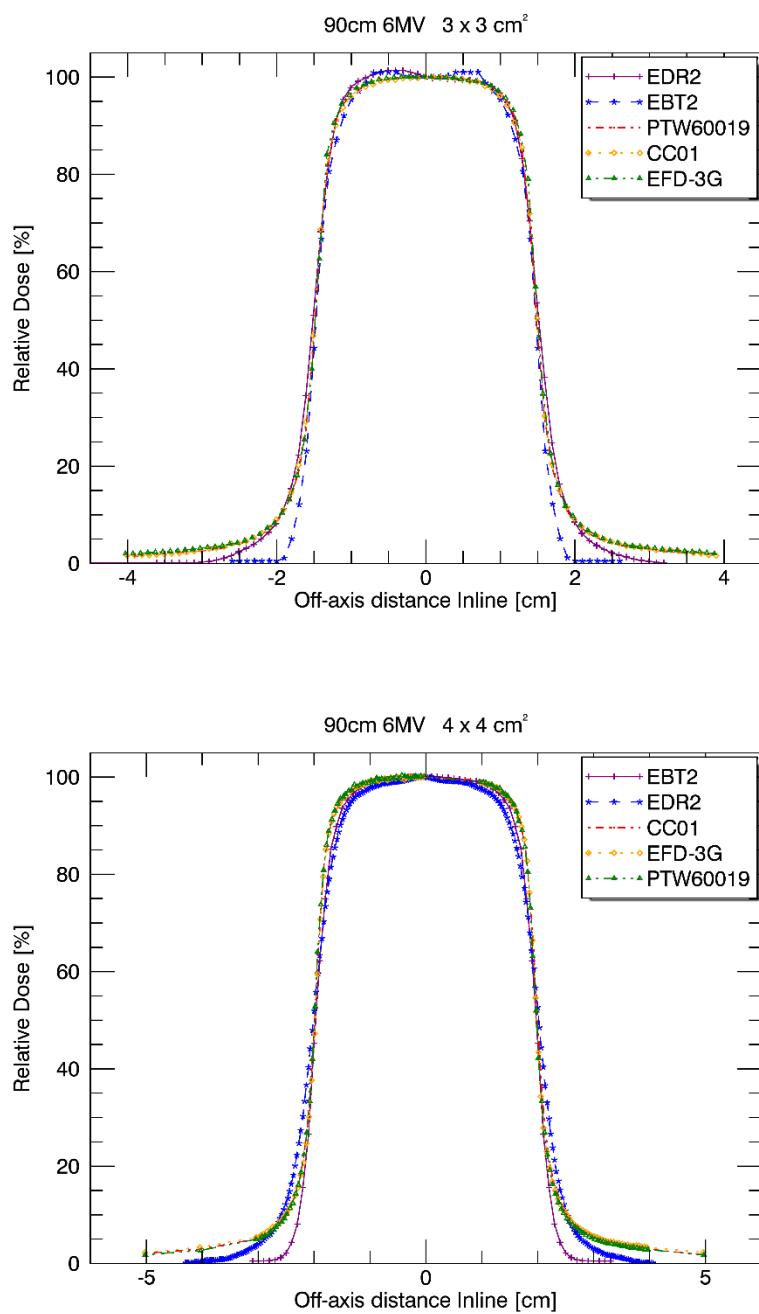


Figure 38. Inline profiles for the 3x3 cm² and 4x4 cm² measured at an SSD of 90 cm and 10 cm depth in water using a 6 MV photon beam

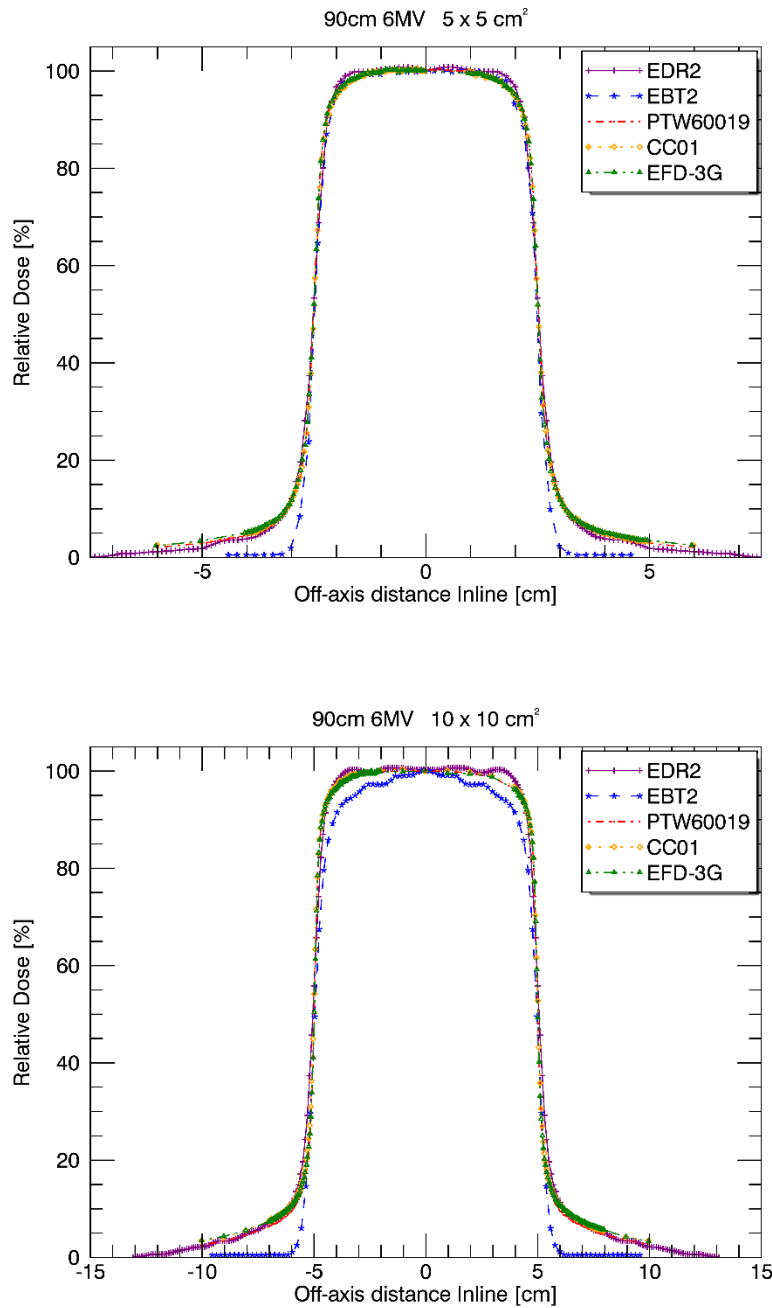


Figure 39. Inline profiles for the 5x5 cm² and 10x10 cm² measured at an SSD of 90 cm and 10 cm depth in water using a 6 MV photon beam

Figure 37 and figure 39 show that profiles measured between the detectors were similar for all the field sizes. However, the 10x10 cm² field size for the EBT2 film clearly shows the results of the artefact that was previously described (figure 39).

90 cm 10 MV Crossline

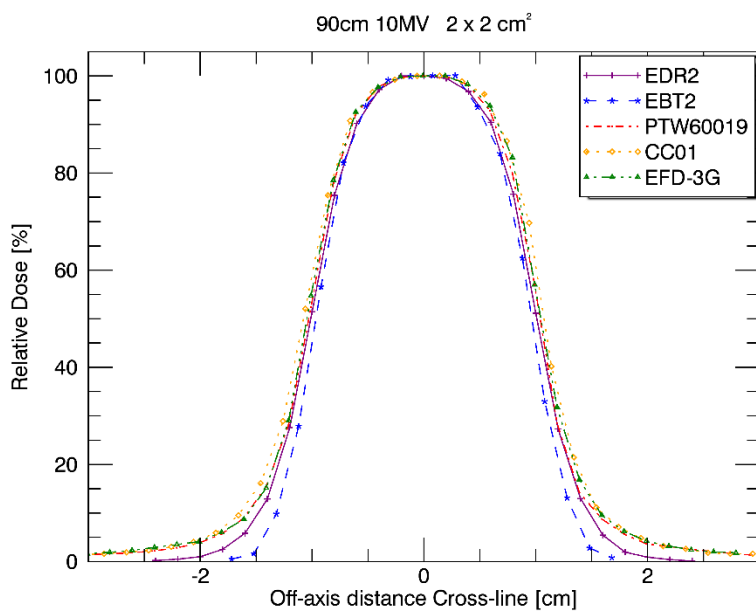
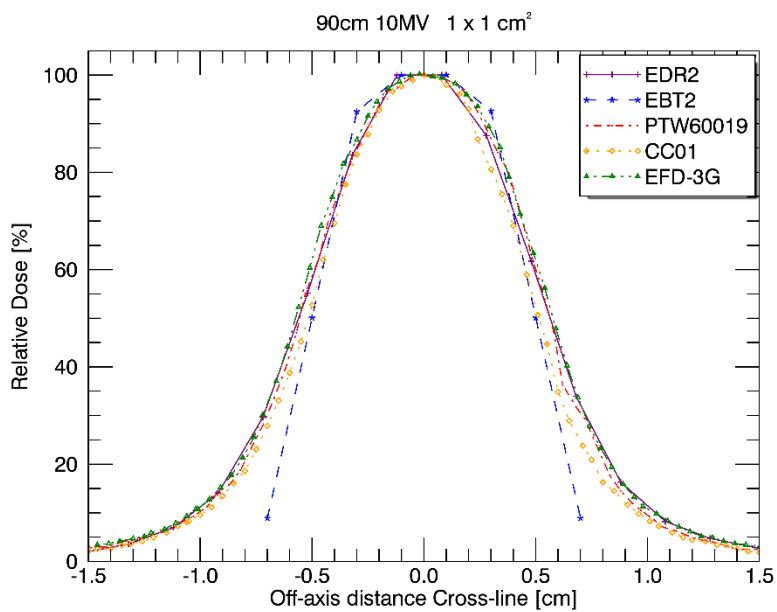


Figure 40. Crossline profiles for the 1x1 cm² and 2x2 cm² measured at an SSD of 90 cm and 10 cm depth in water using a 10 MV photon beam

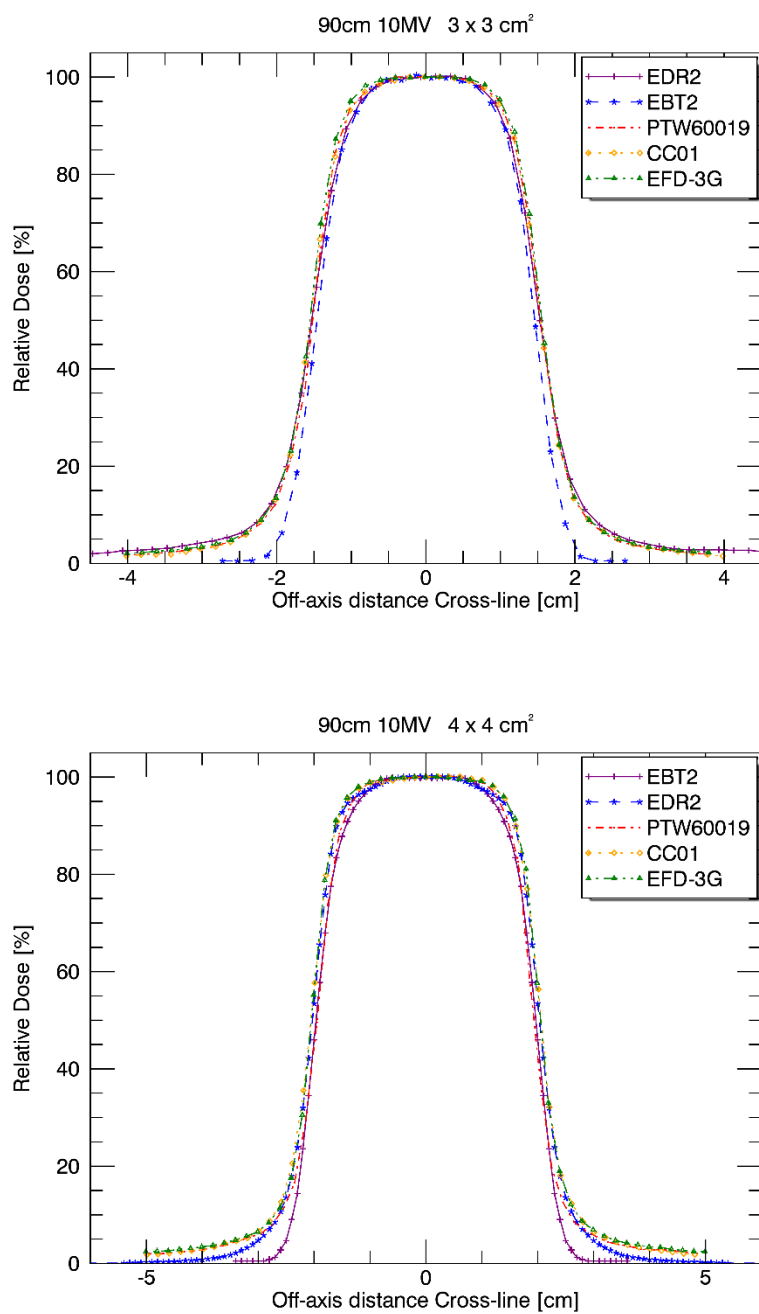


Figure 41. Crossline profiles for the 3x3 cm² and 4x4 cm² measured at an SSD of 90 cm and 10 cm depth in water using a 10 MV photon beam

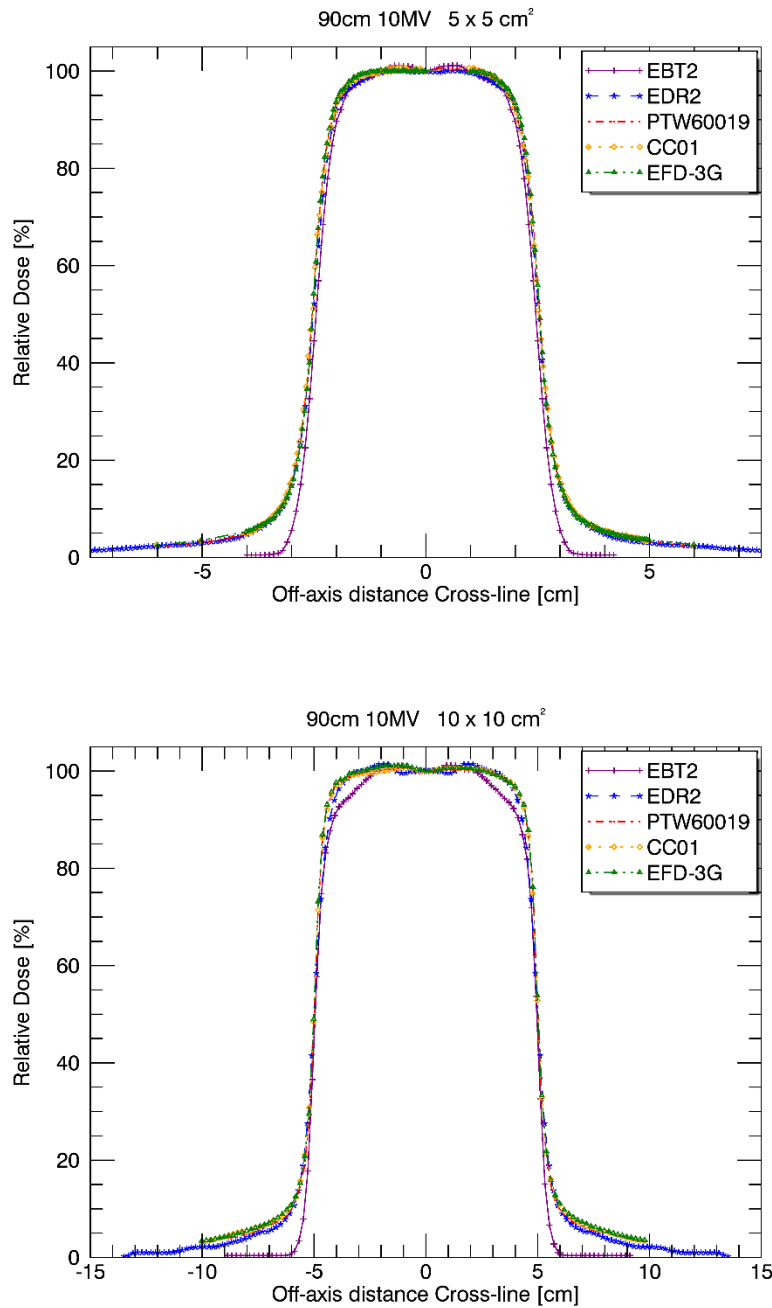


Figure 42. Crossline profiles for the 5x5 cm² and 10x10 cm² measured at an SSD of 90 cm and 10 cm depth in water using a 10 MV photon beam

The 1x1 cm² field size shows large variations in measuring the penumbra between the detectors (figure 40), but the calculated field sizes are within the action limit of 2 mm. The 10x10 cm² field size for the EBT2 film shows the same artefact as previously encountered (figure 42).

90 cm 10 MV Inline

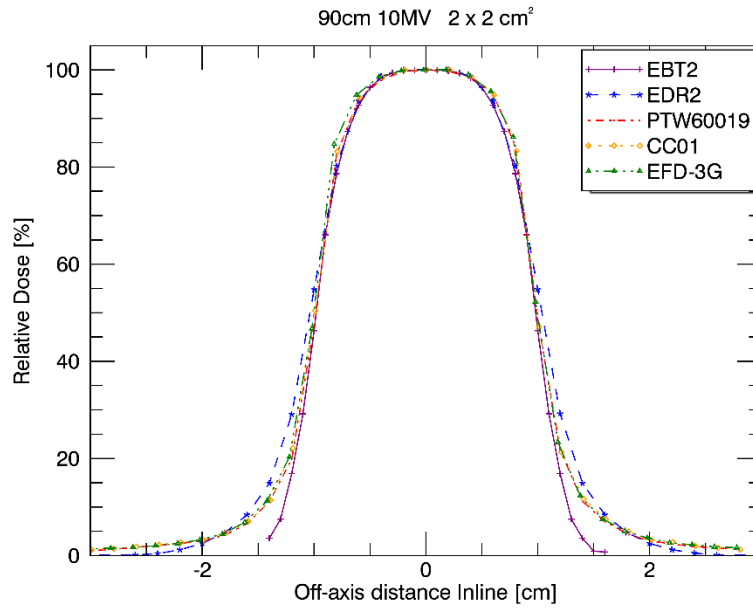
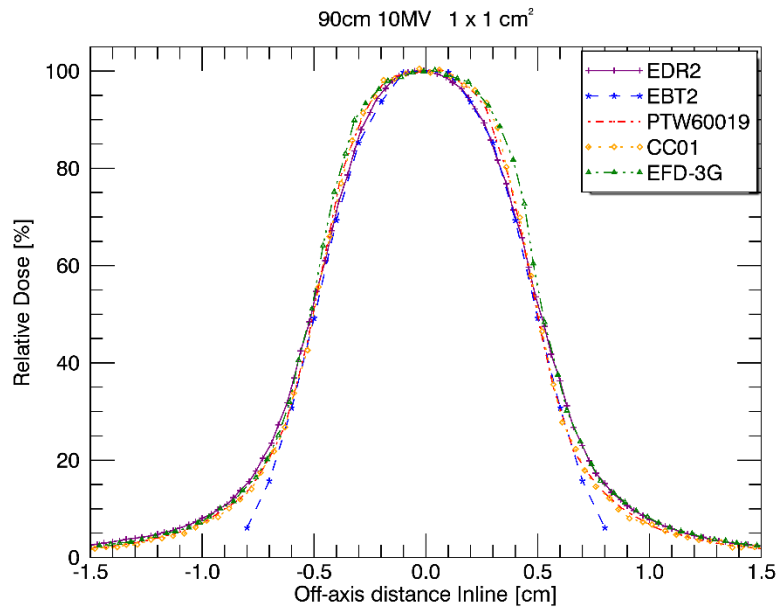


Figure 43. Inline profiles for the 1x1 cm² and 2x2 cm² measured at an SSD of 90 cm and 10 cm depth in water using a 10 MV photon beam

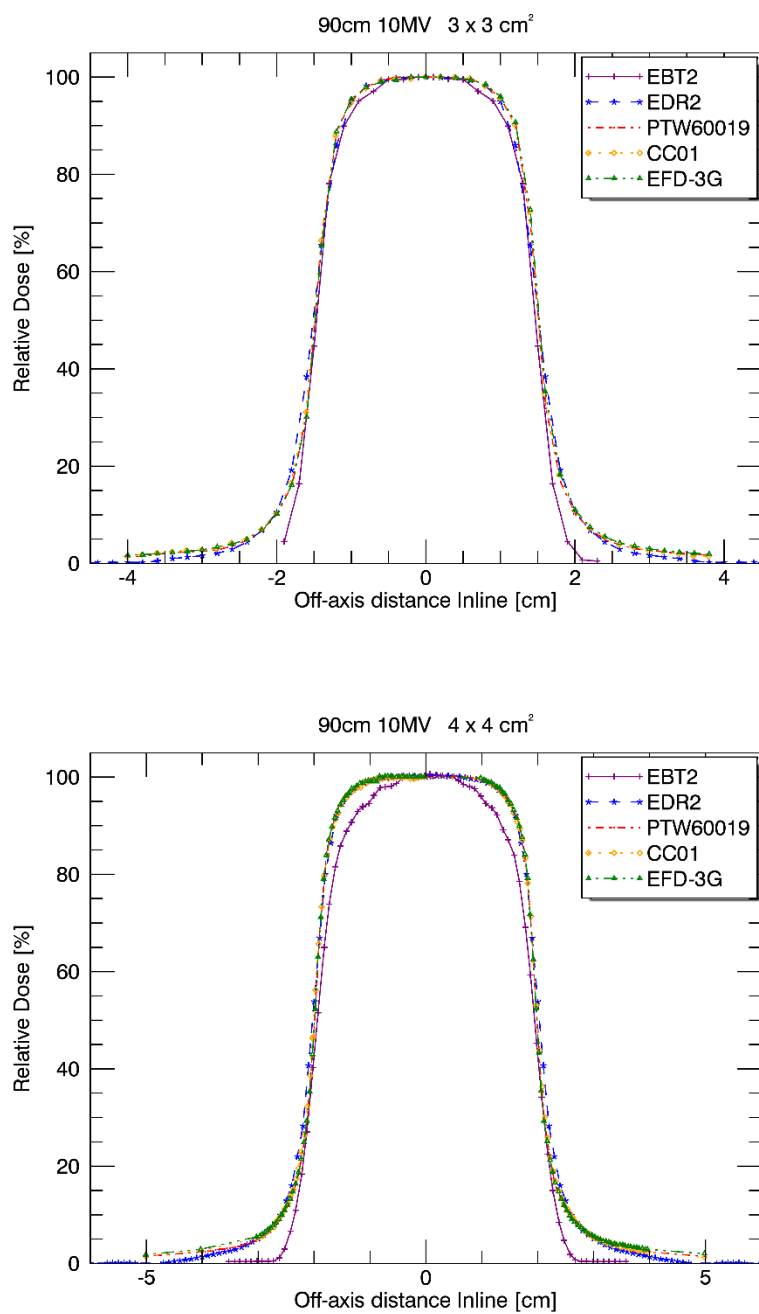


Figure 44. Inline profiles for the 3x3 cm² and 4x4 cm² measured at an SSD of 90 cm and 10 cm depth in water using a 10 MV photon beam

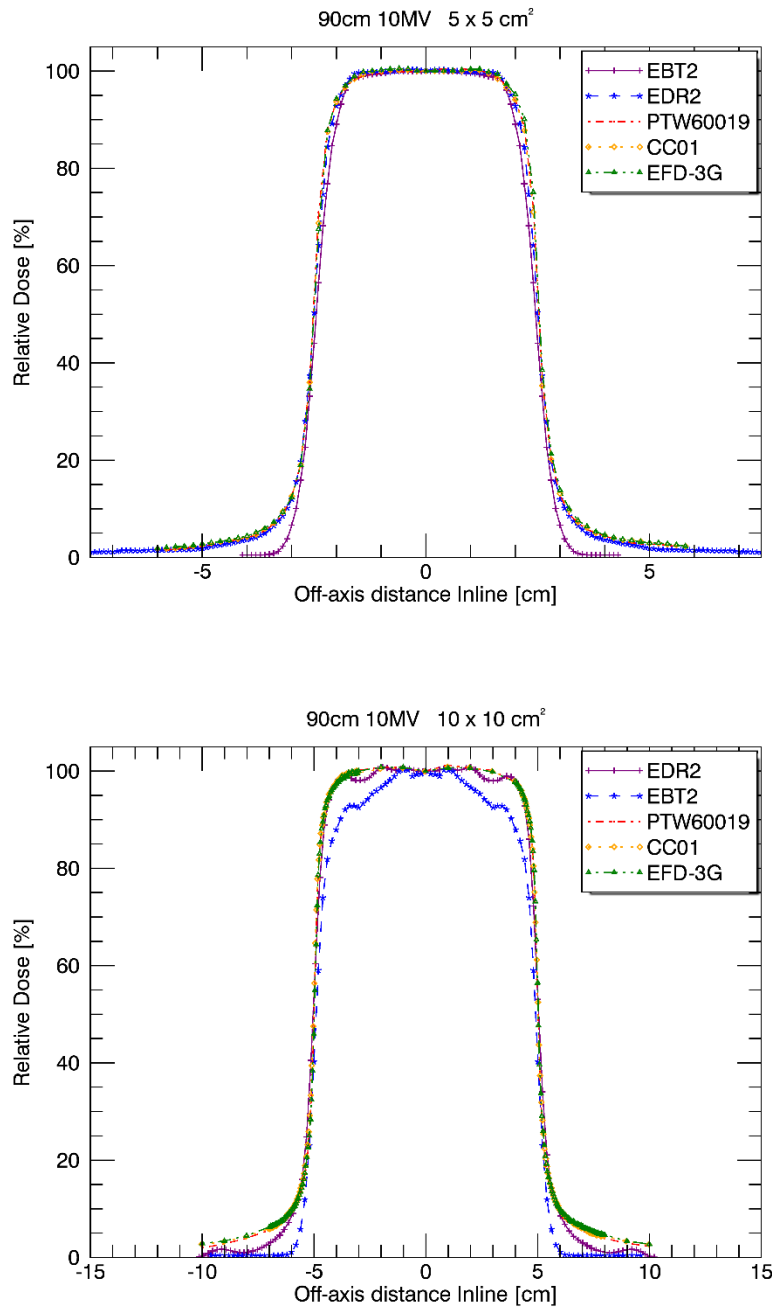


Figure 45. Inline profiles for the $5 \times 5 \text{ cm}^2$ and $10 \times 10 \text{ cm}^2$ measured at an SSD of 90 cm and 10 cm depth in water using a 10 MV photon beam

The EBT2 artefact is again shown at the $10 \times 10 \text{ cm}^2$ field size (figure 45), and the EDR2 experiences artefacts at this field size.

90 cm 15 MV Crossline

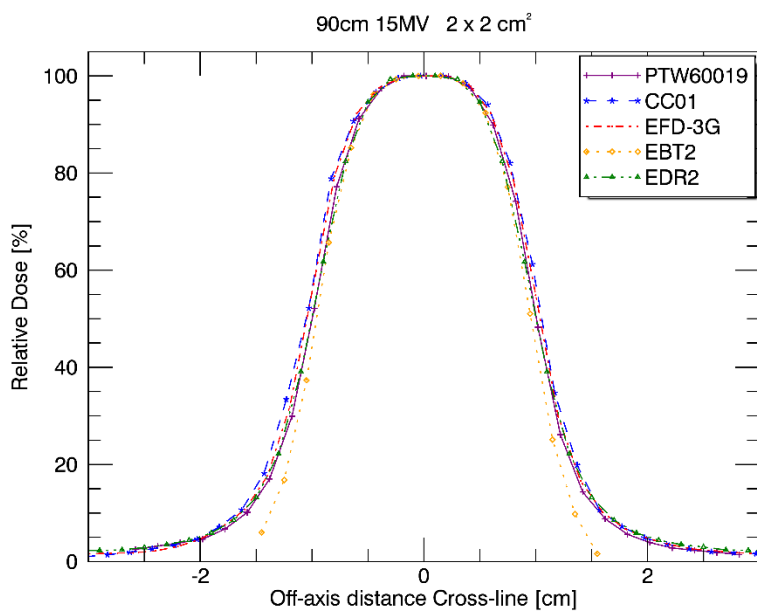
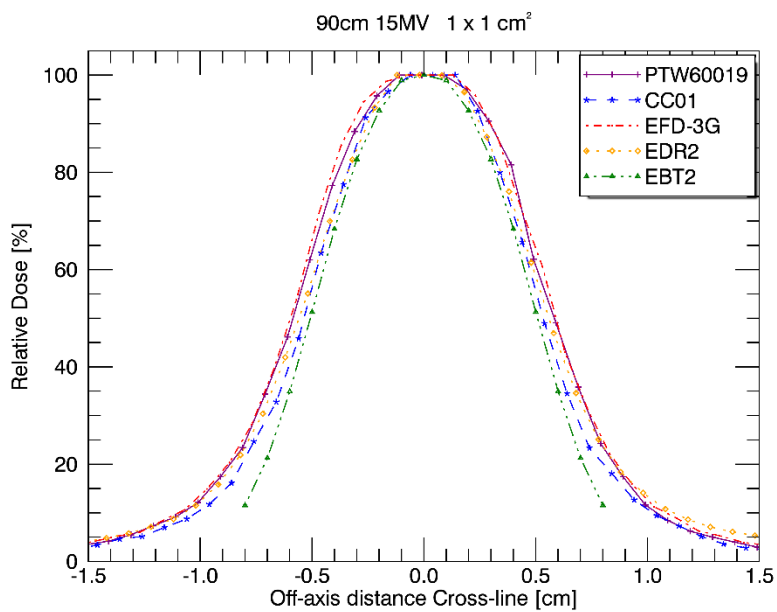


Figure 46. Crossline profiles for the 1x1 cm² and 2x2 cm² measured at an SSD of 90 cm and 10 cm depth in water using a 15 MV photon beam

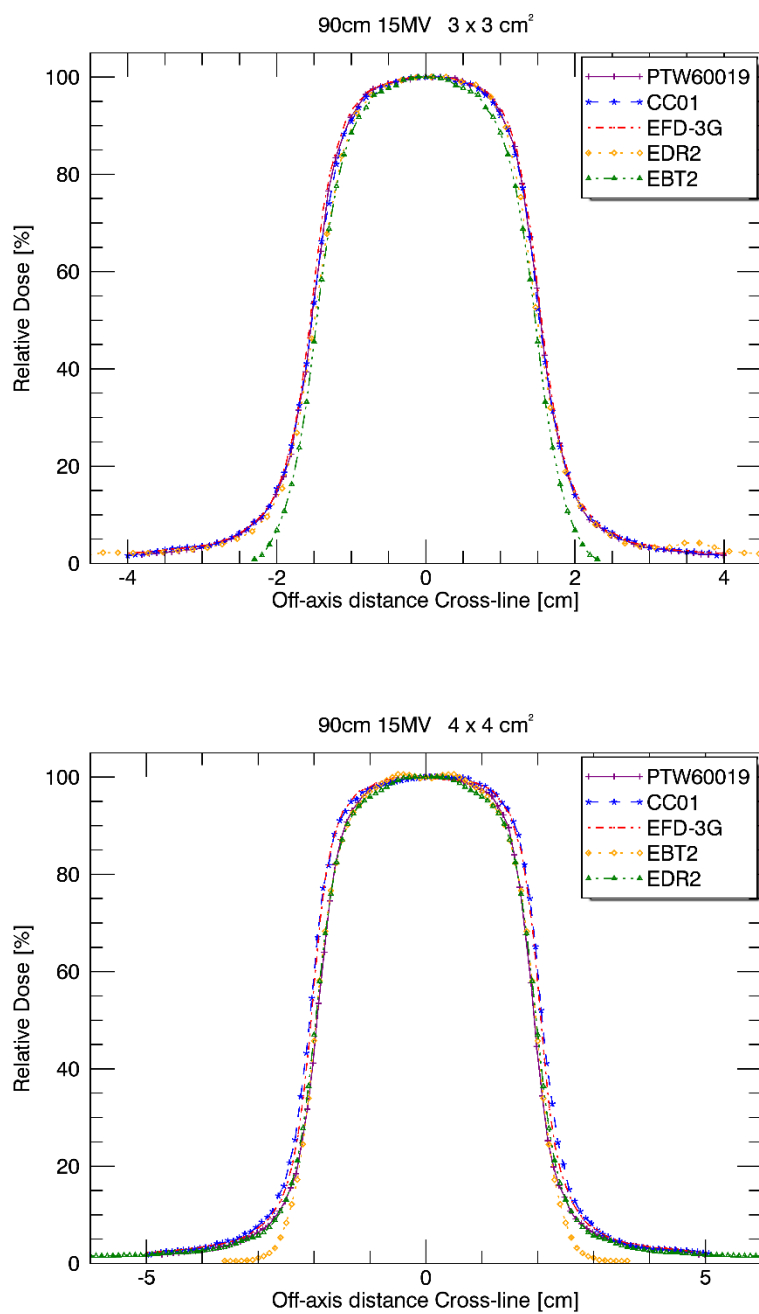


Figure 47. Crossline profiles for the $3 \times 3 \text{ cm}^2$ and $4 \times 4 \text{ cm}^2$ measured at an SSD of 90 cm and 10 cm depth in water using a 15 MV photon beam

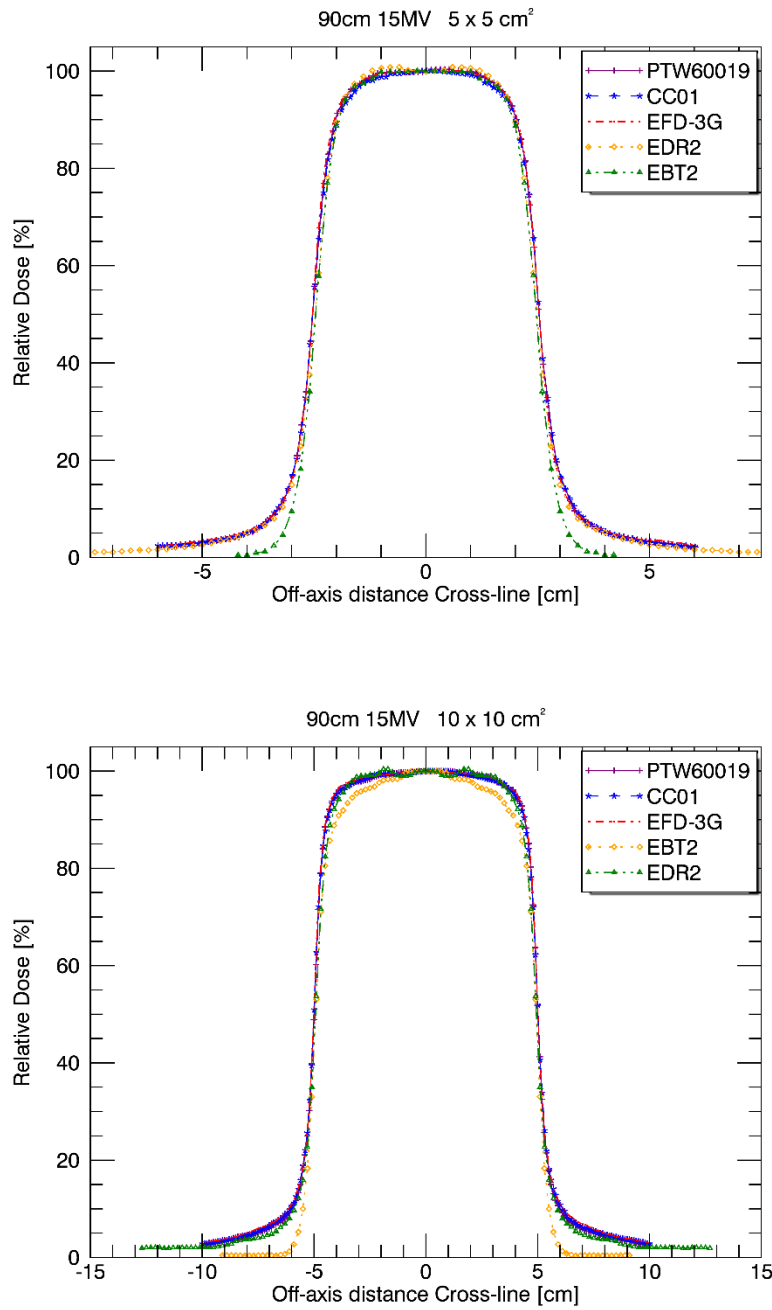


Figure 48. Crossline profiles for the $5 \times 5 \text{ cm}^2$ and $10 \times 10 \text{ cm}^2$ measured at an SSD of 90 cm and 10 cm depth in water using a 15 MV photon beam

In figure 46 there is a variation of the field size set using the linac at the $1 \times 1 \text{ cm}^2$ field size, this variation has been described previously in section 4.2.1.

90 cm 15 MV Inline

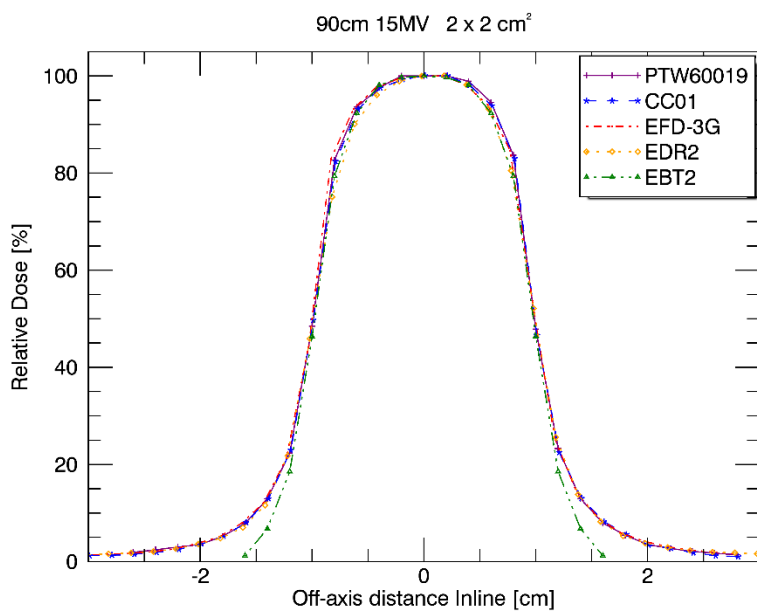
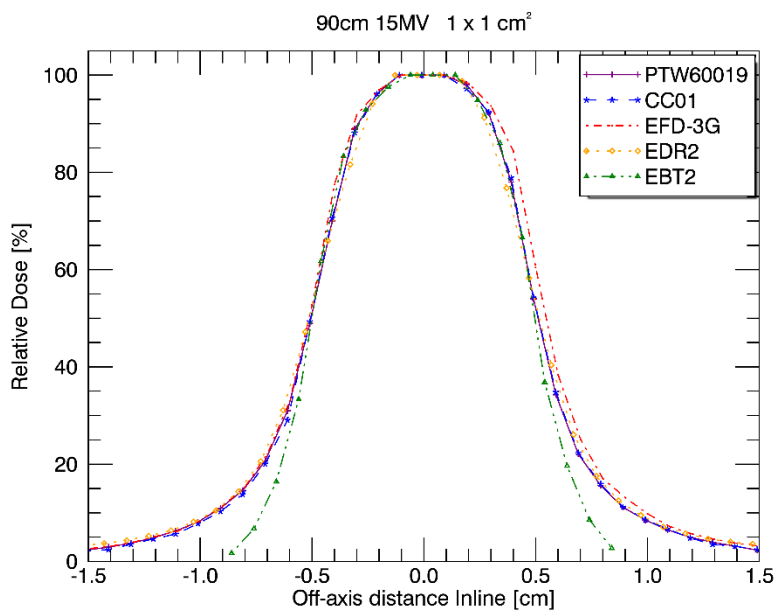


Figure 49. Inline profiles for the 1x1 cm² and 2x2 cm² measured at an SSD of 90 cm and 10 cm depth in water using a 15 MV photon beam

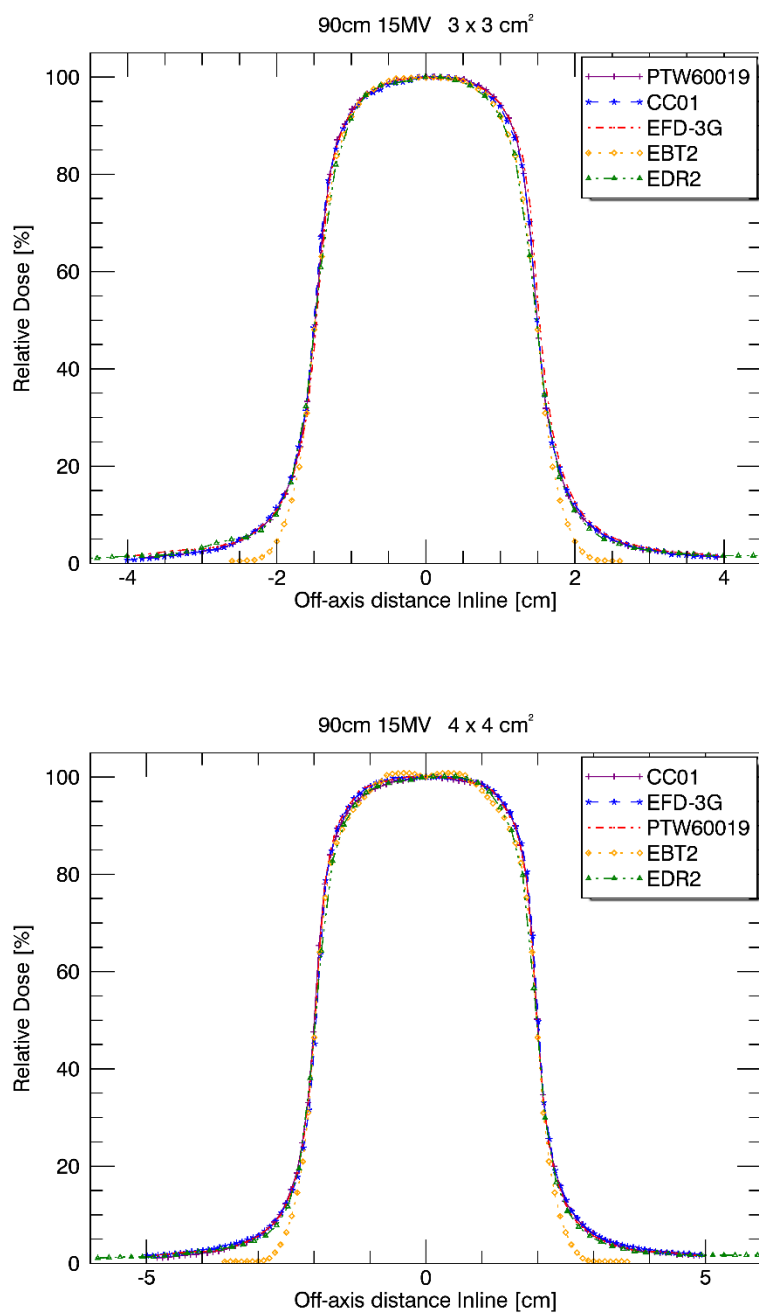


Figure 50. Inline profiles for the 3x3 cm² and 4x4 cm² measured at an SSD of 90 cm and 10 cm depth in water using a 15 MV photon beam

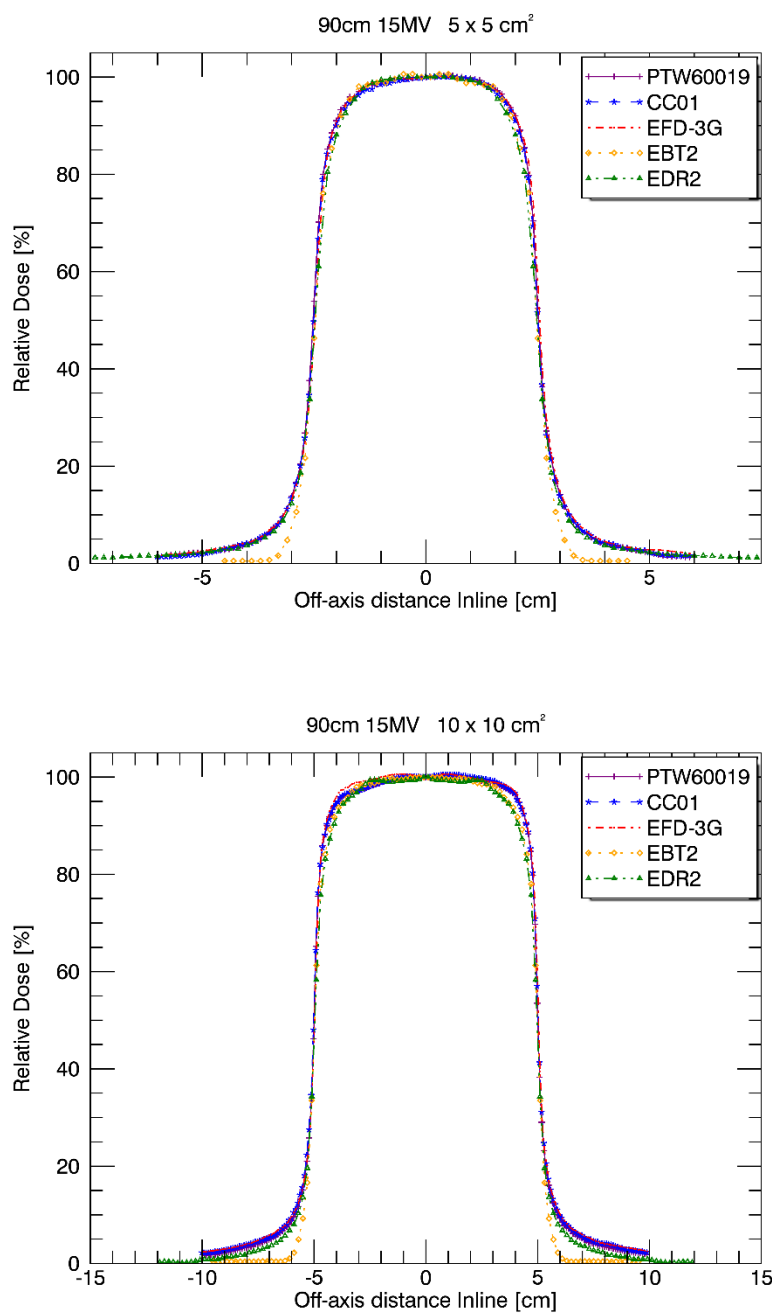


Figure 51. Inline profiles for the 5x5 cm² and 10x10 cm² measured at an SSD of 90 cm and 10 cm depth in water using a 15 MV photon beam

There are no artefacts seen in the above figures (Figure 49 – 51).

4.2.2 Beam profiles measured at an SSD of 95 cm

95 cm 6 MV Crossline

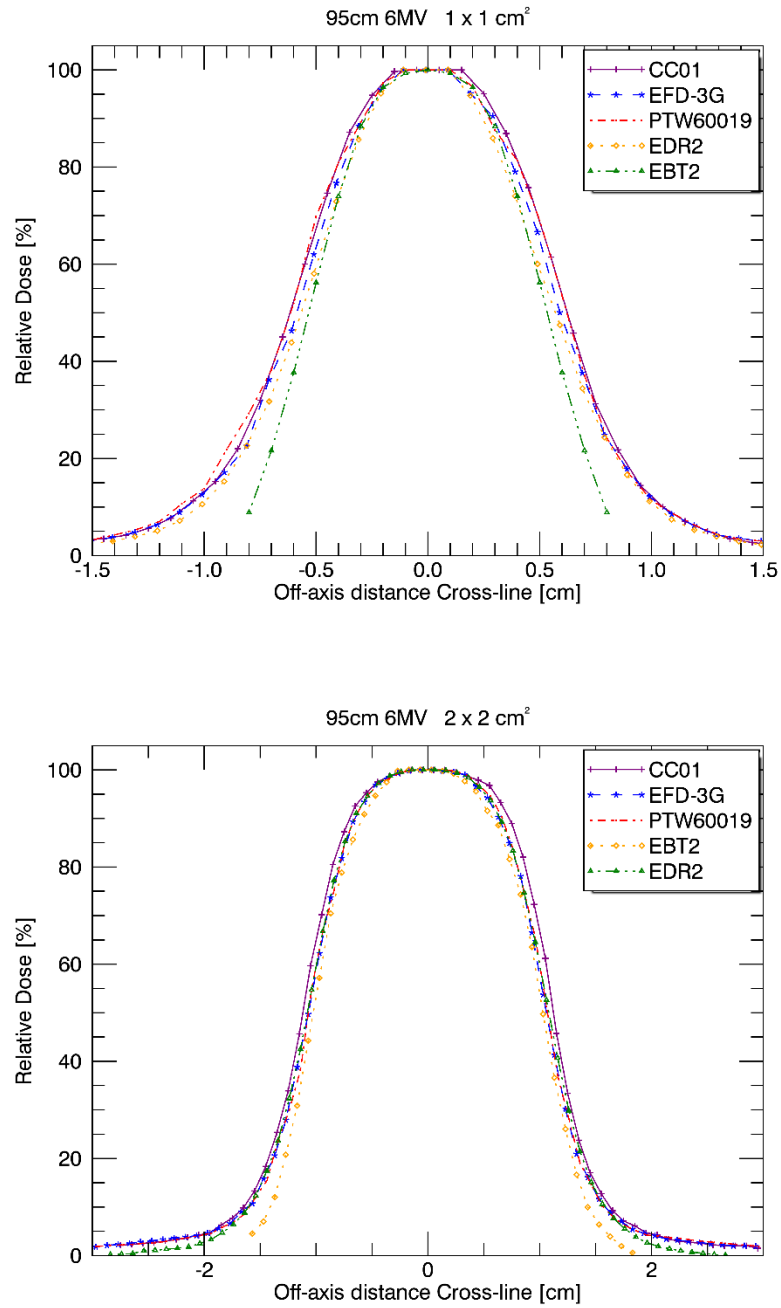


Figure 52. Crossline profiles for the 1x1 cm² and 2x2 cm² measured at an SSD of 95 cm and 10 cm depth in water using a 6 MV photon beam

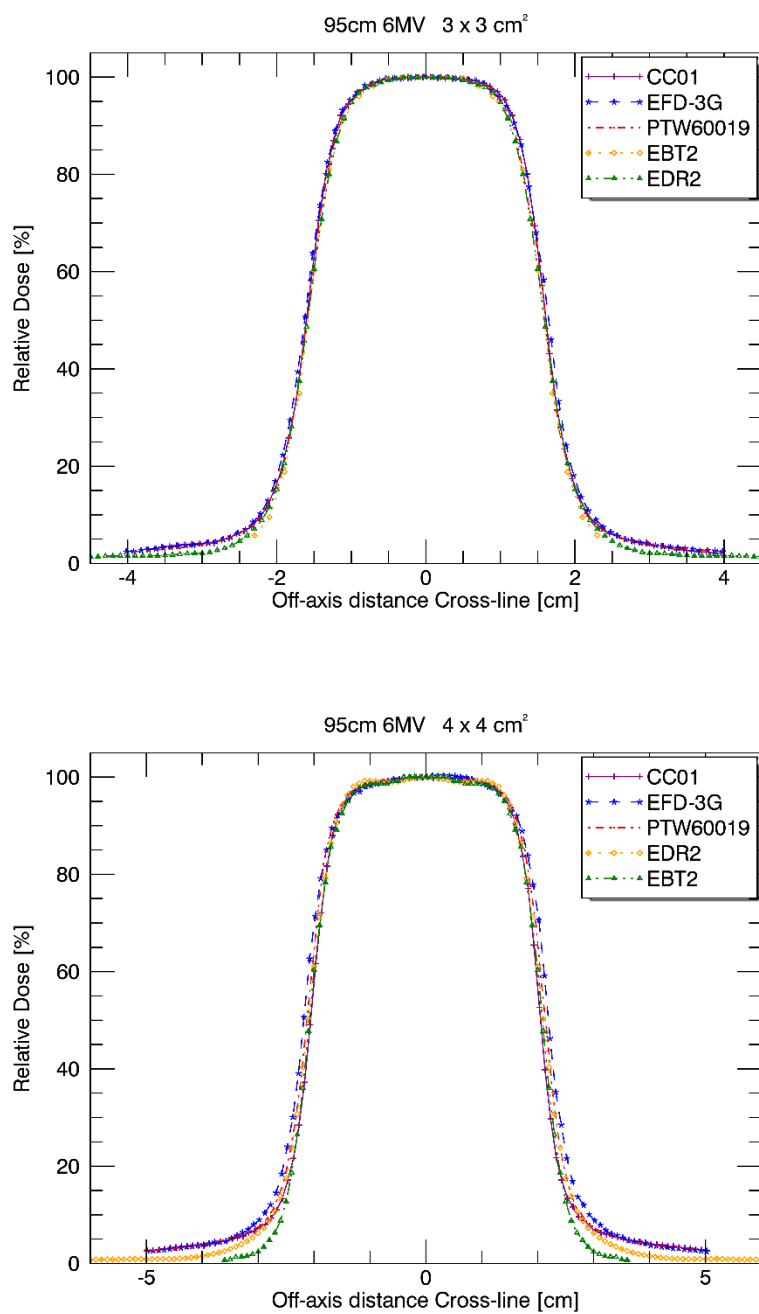


Figure 53. Crossline profiles for the $3 \times 3 \text{ cm}^2$ and $4 \times 4 \text{ cm}^2$ measured at an SSD of 95 cm and 10 cm depth in water using a 6 MV photon beam

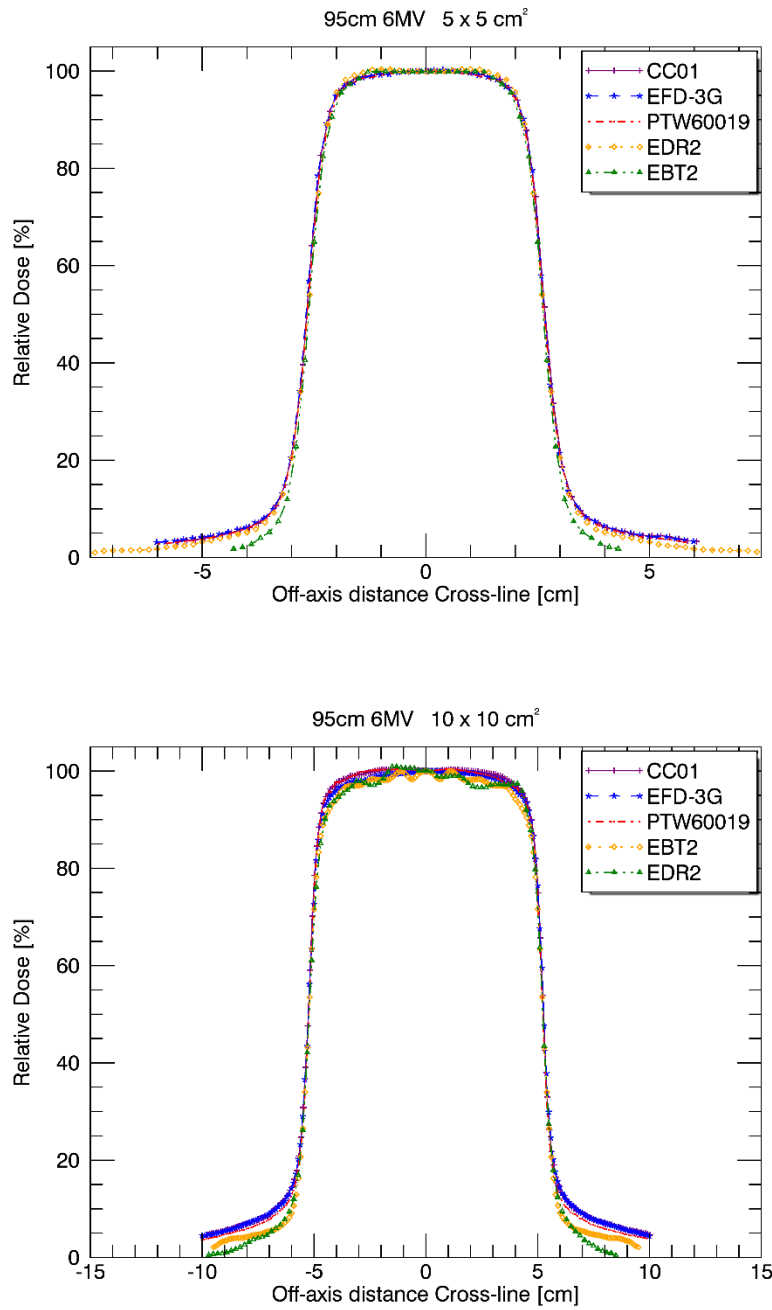


Figure 54. Crossline profiles for the $5 \times 5 \text{ cm}^2$ and $10 \times 10 \text{ cm}^2$ measured at an SSD of 95 cm and 10 cm depth in water using a 6 MV photon beam

The fluctuation of the field seen at $1 \times 1 \text{ cm}^2$ (figure 52) and $10 \times 10 \text{ cm}^2$ (figure 54) field sizes were explained in section 4.2.1.

95 cm 6 MV Inline

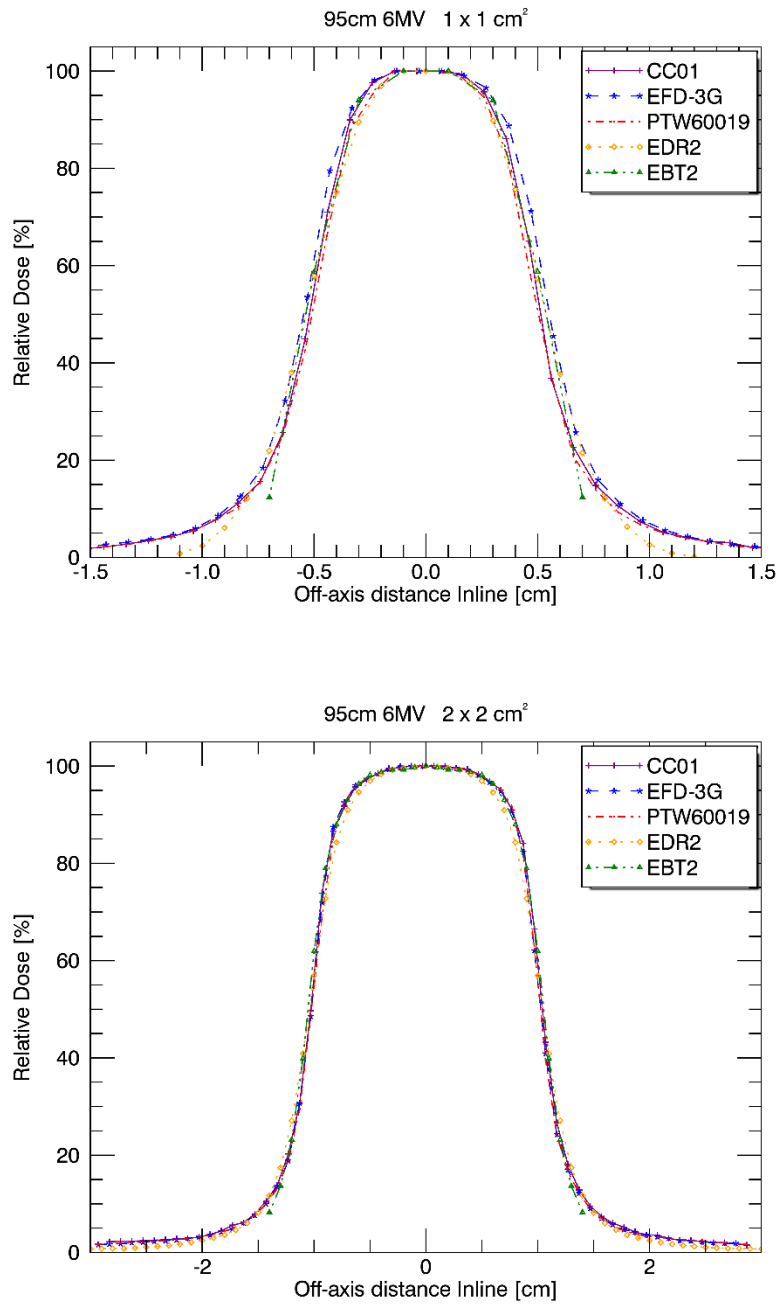


Figure 55. Inline profiles for the 1x1 cm² and 2x2 cm² measured at an SSD of 95 cm and 10 cm depth in water using a 6 MV photon beam

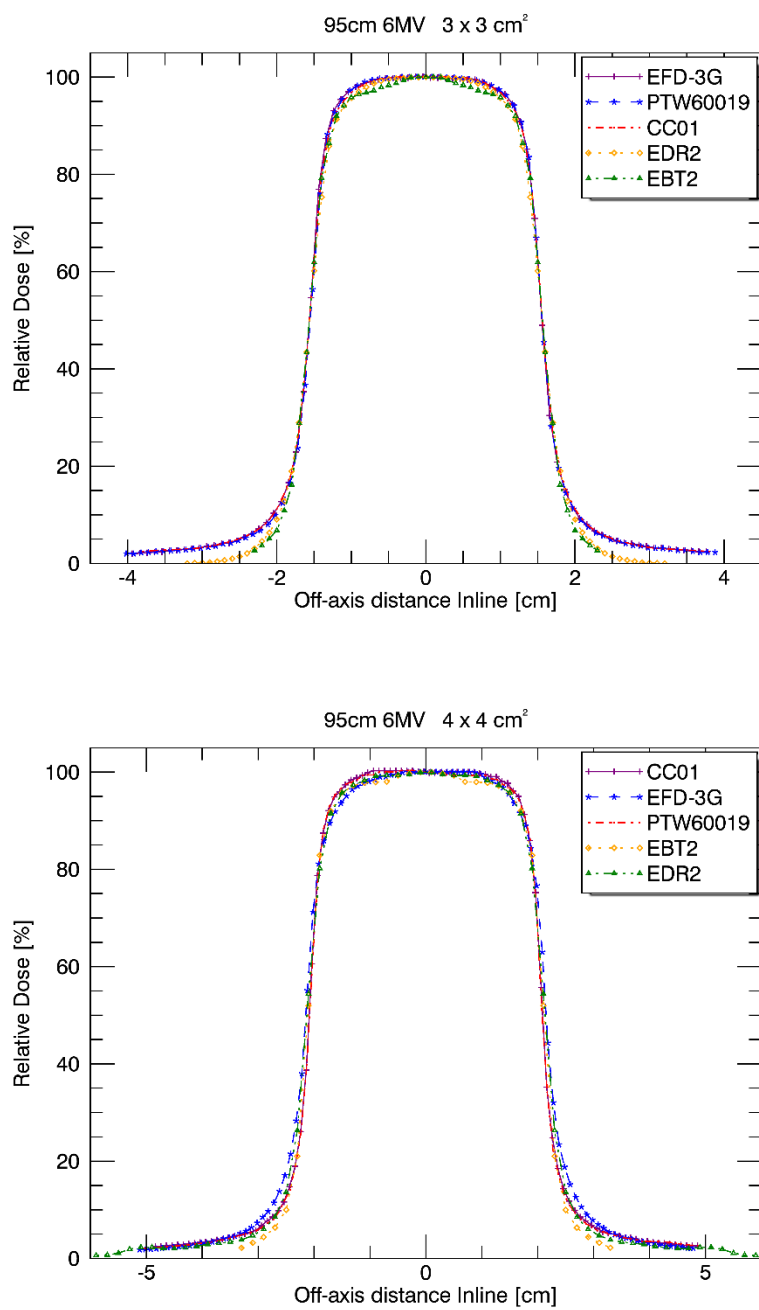


Figure 56. Inline profiles for the 3x3 cm² and 4x4 cm² measured at an SSD of 95 cm and 10 cm depth in water using a 6 MV photon beam

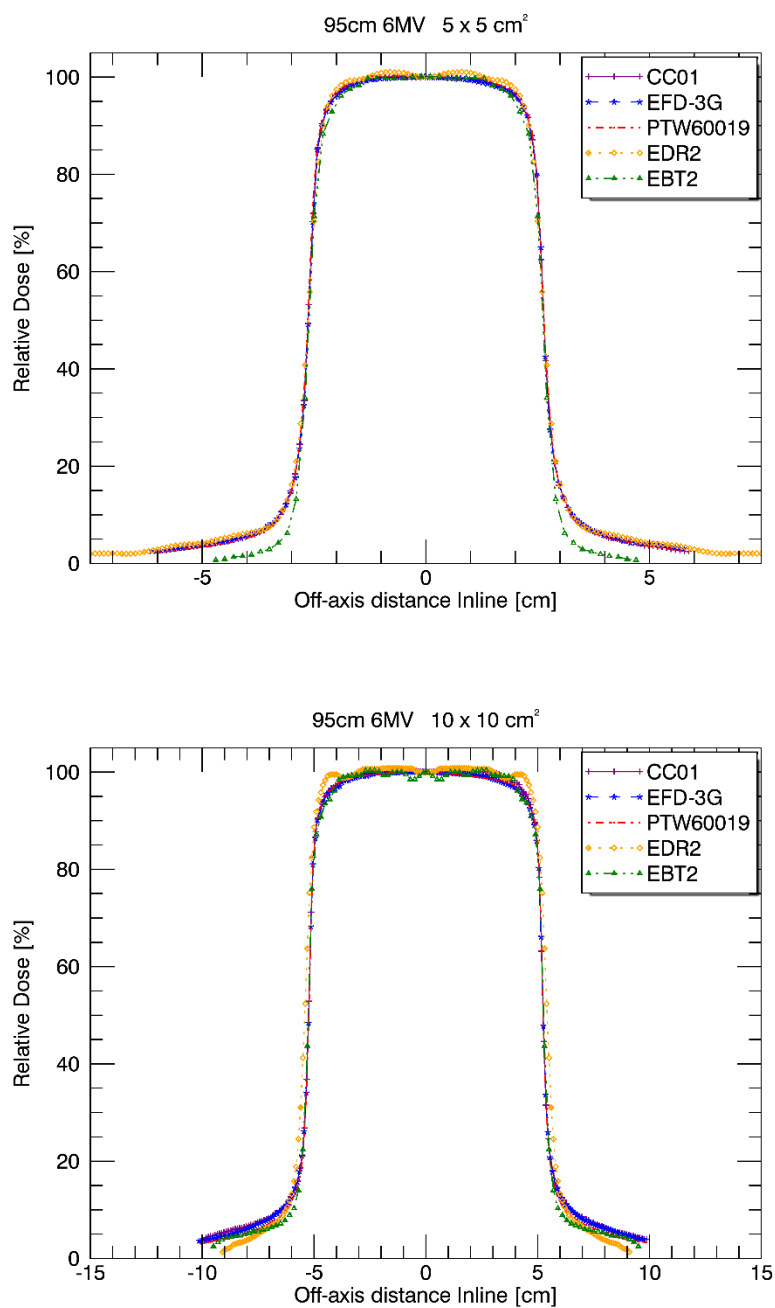


Figure 57. Inline profiles for the 5x5 cm² and 10x10 cm² measured at an SSD of 95 cm and 10 cm depth in water using a 6 MV photon beam

95 cm 10 MV Crossline

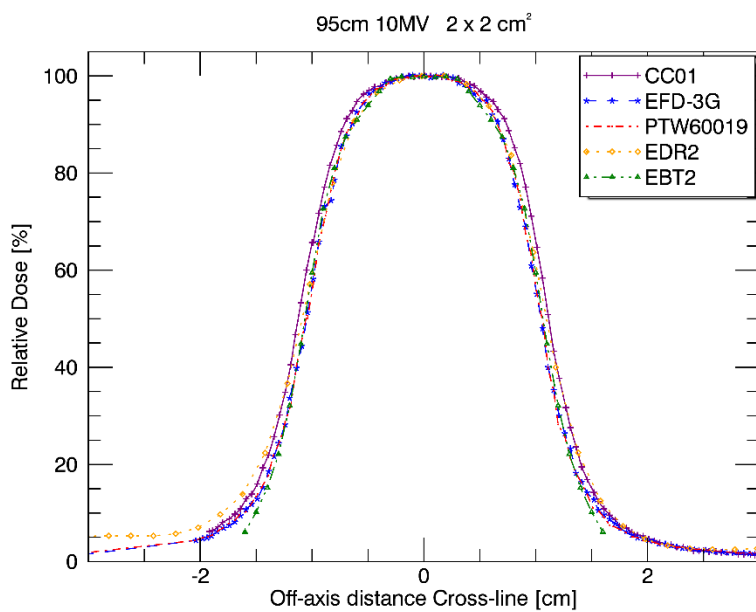
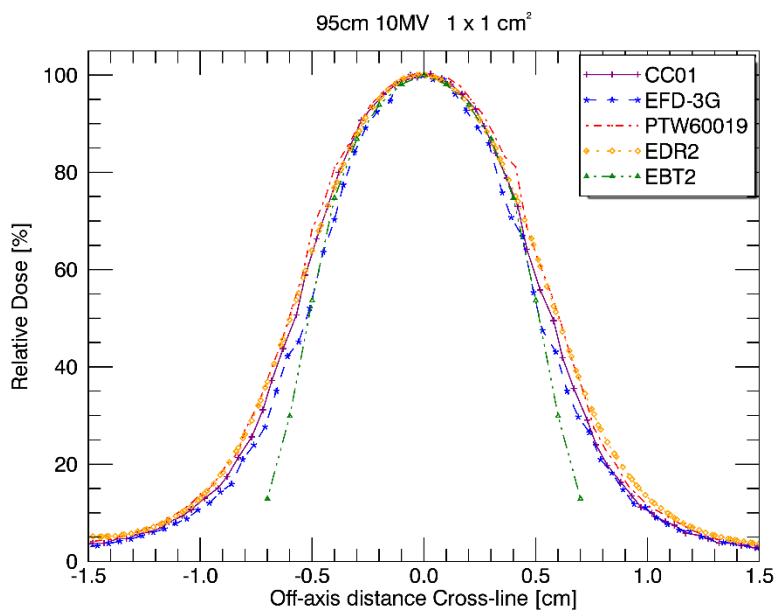


Figure 58. Crossline profiles for the 1x1 cm² and 2x2 cm² measured at an SSD of 95 cm and 10 cm depth in water using a 10 MV photon beam

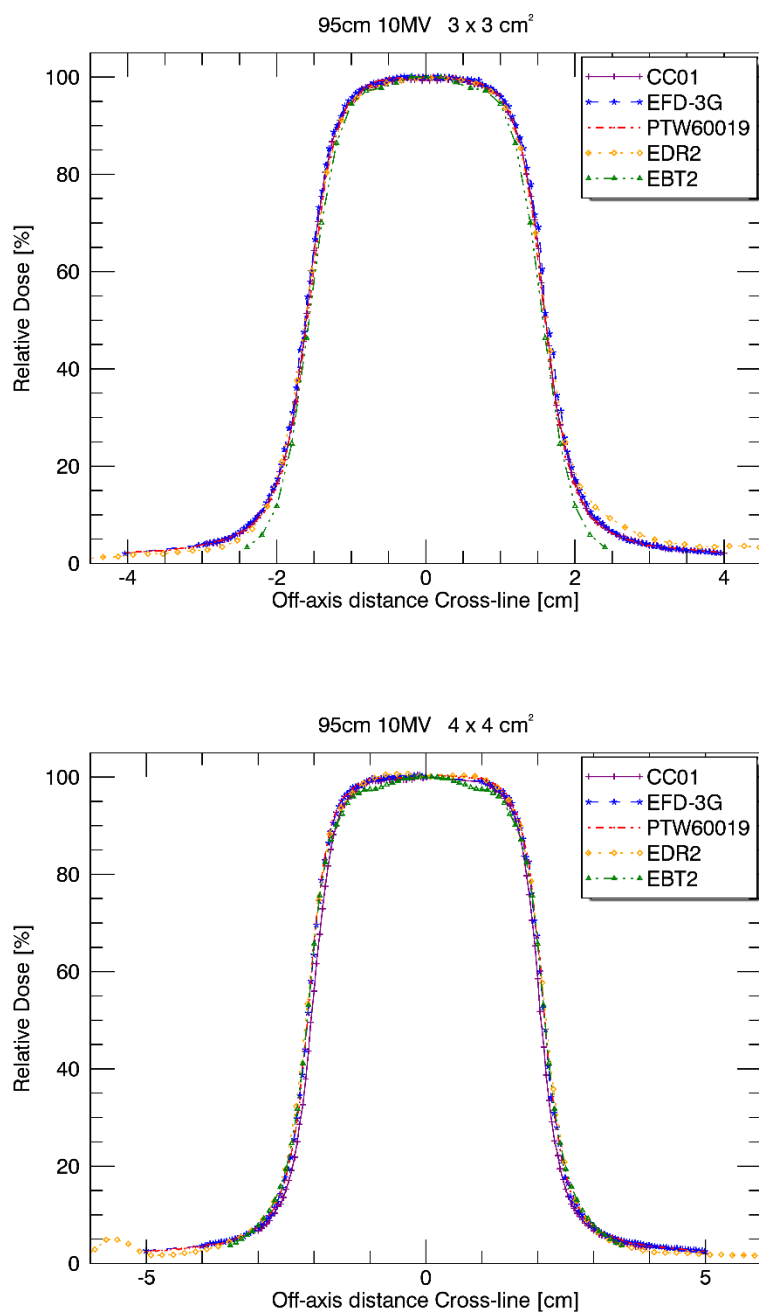


Figure 59. Crossline profiles for the 3x3 cm² and 4x4 cm² measured at an SSD of 95 cm and 10 cm depth in water using a 10 MV photon beam

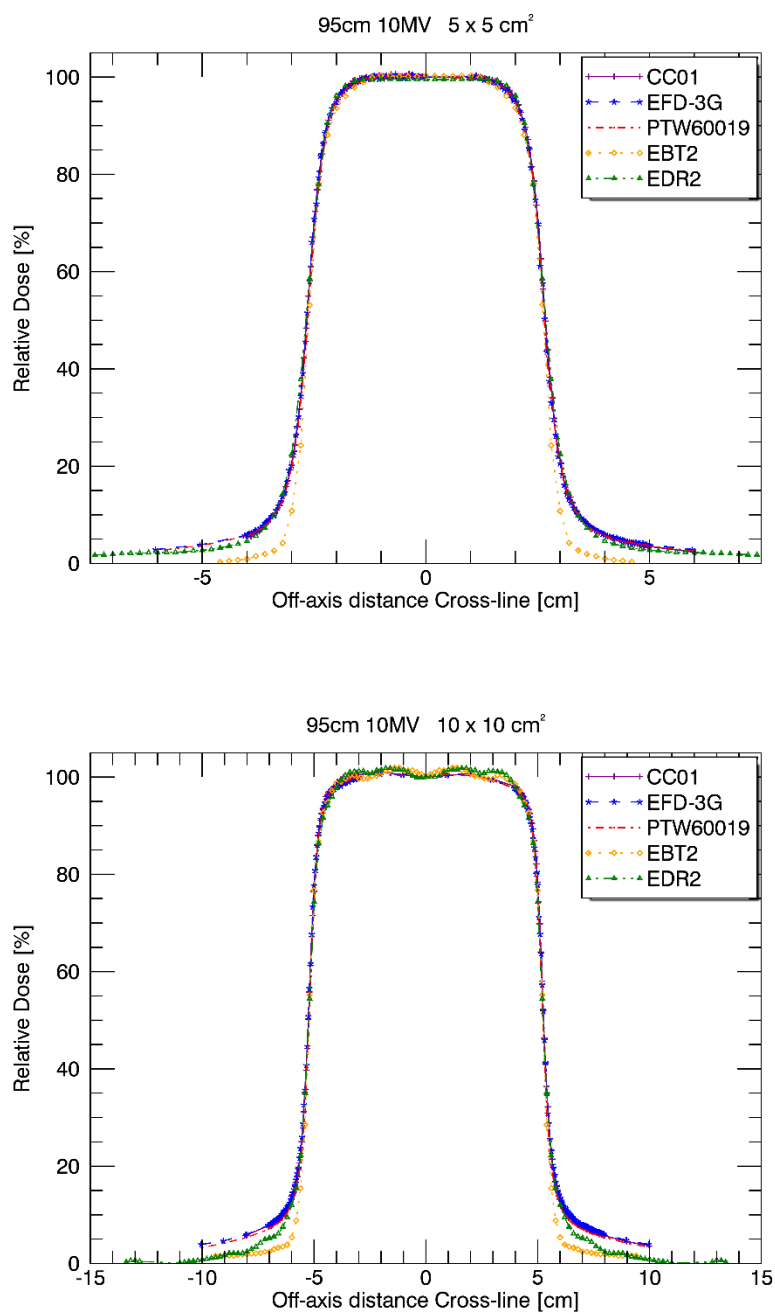


Figure 60. Crossline profiles for the 5x5 cm² and 10x10 cm² measured at an SSD of 95 cm and 10 cm depth in water using a 10 MV photon beam

95 cm 10 MV Inline

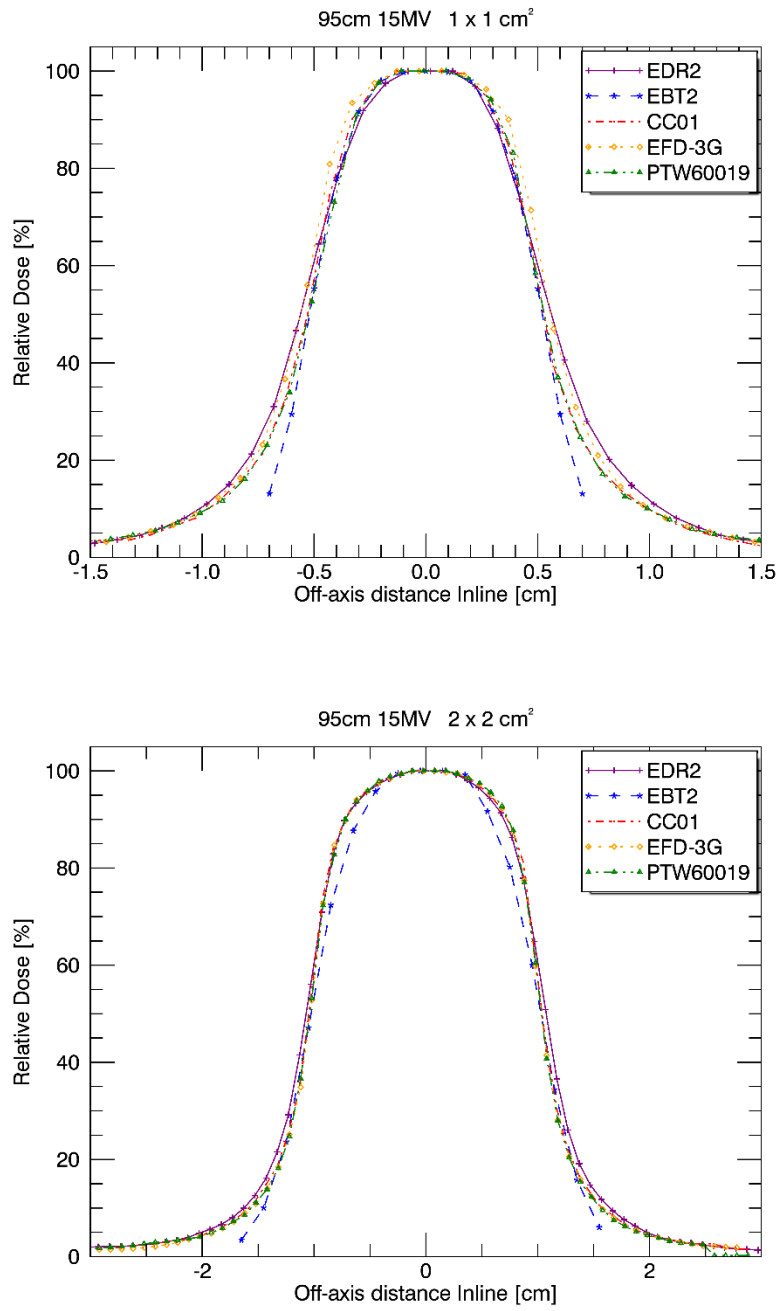


Figure 61. Inline profiles for the $1 \times 1 \text{ cm}^2$ and $2 \times 2 \text{ cm}^2$ measured at an SSD of 95 cm and 10 cm depth in water using a 10 MV photon beam

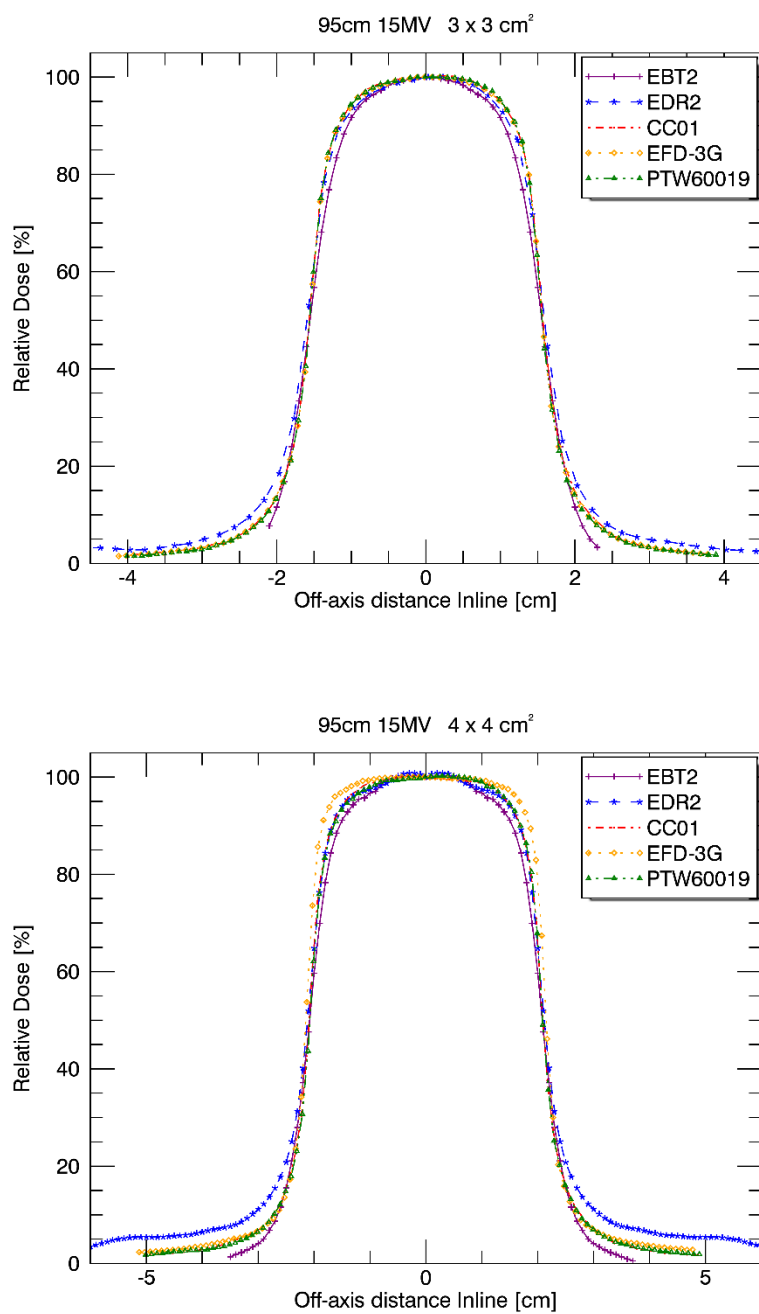


Figure 62. Inline profiles for the 3x3 cm² and 4x4 cm² measured at an SSD of 95 cm and 10 cm depth in water using a 10 MV photon beam

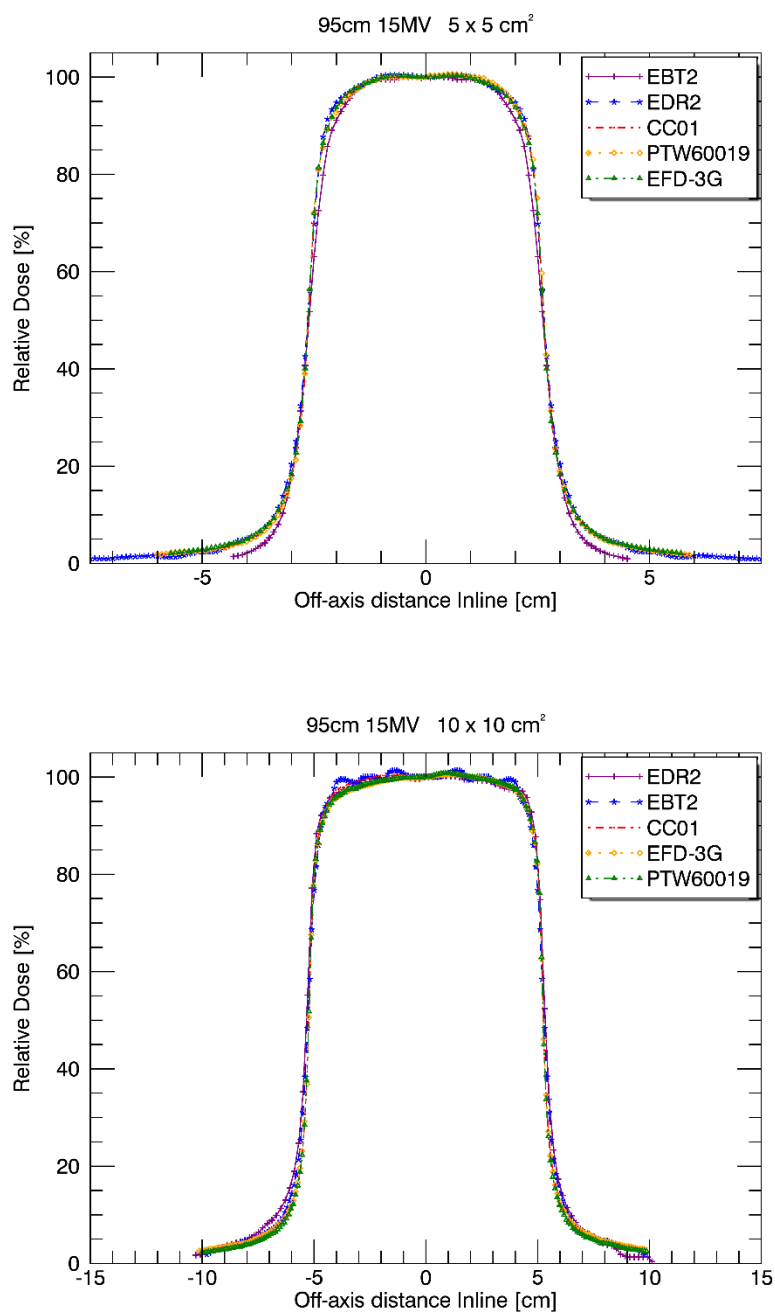


Figure 63. Inline profiles for the 5x5 cm² and 10x10 cm² measured at an SSD of 95 cm and 10 cm depth in water using a 10 MV photon beam

95 cm 15 MV Crossline

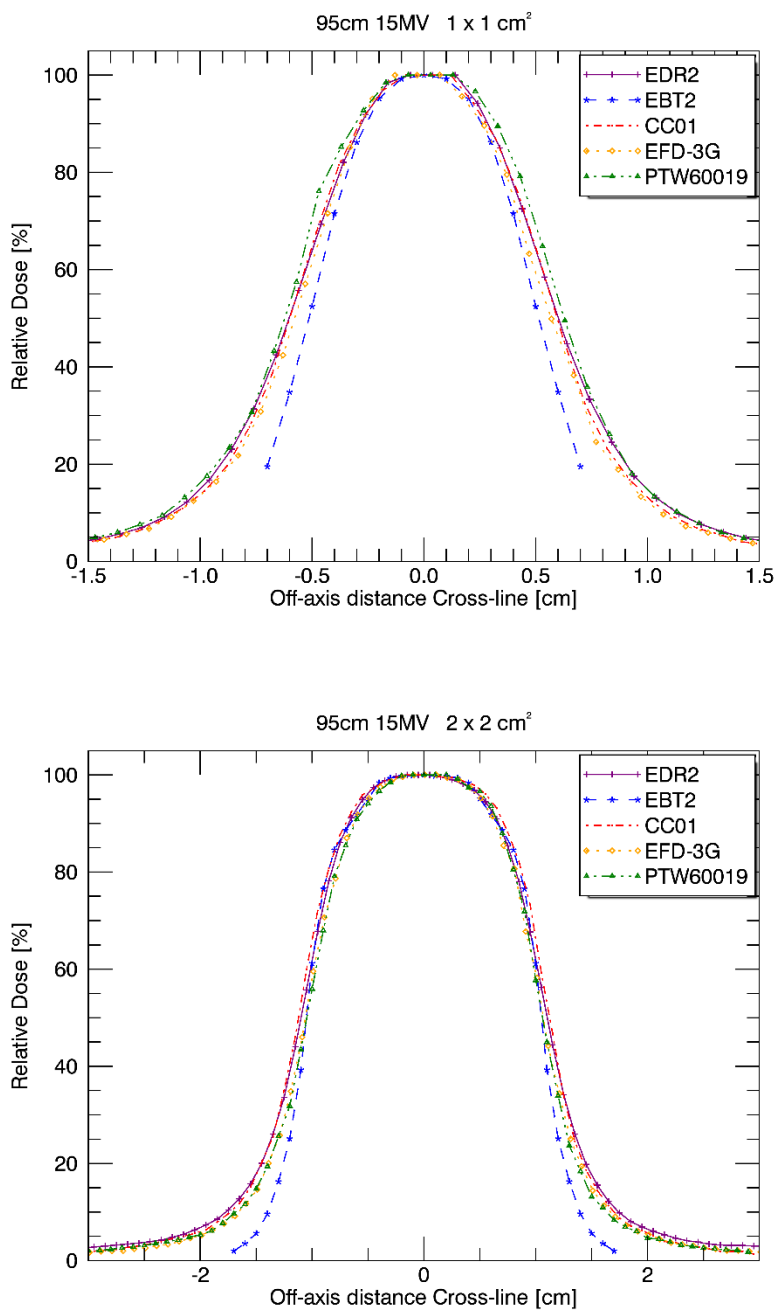


Figure 64. Crossline profiles for the 1×1 cm² and 2×2 cm² measured at an SSD of 95 cm and 10 cm depth in water using a 15 MV photon beam

The figure above shows the 1×1 cm² field size variation which was discussed earlier in section 4.2.1 (figure 64).

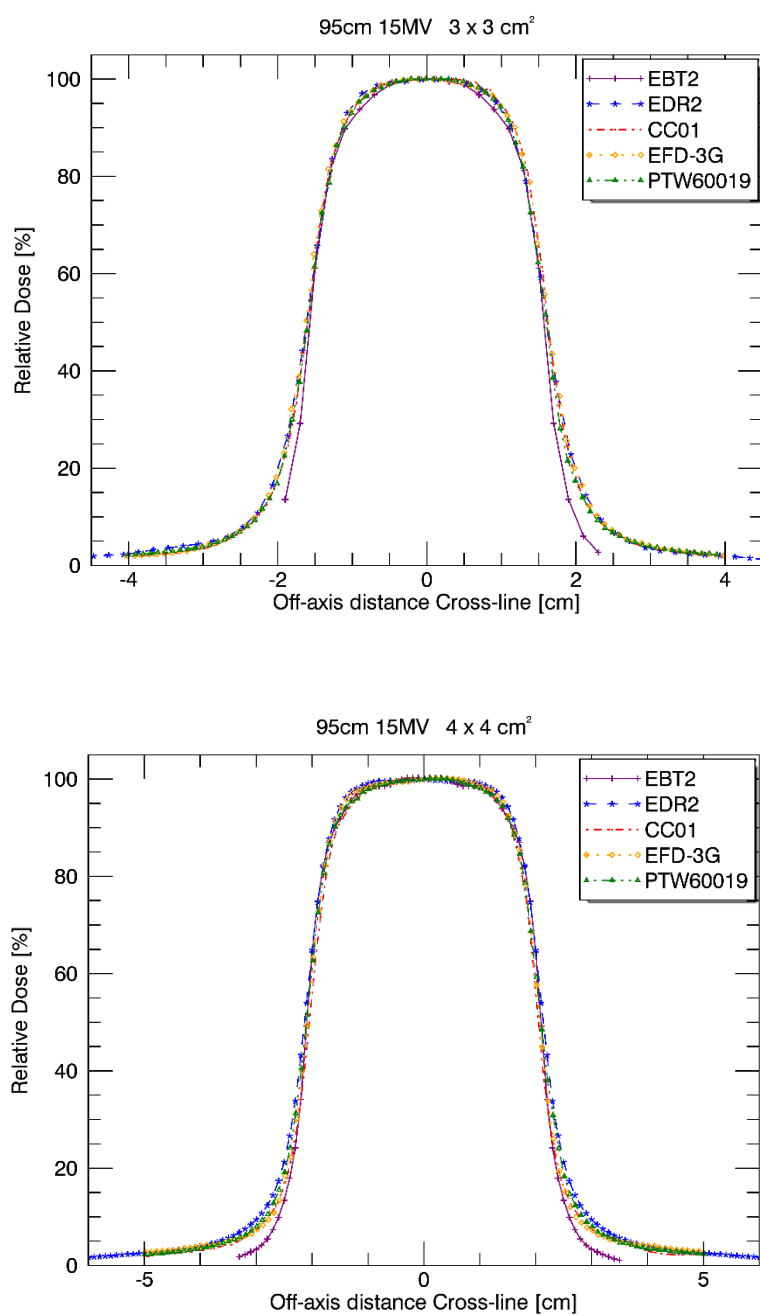


Figure 65. Crossline profiles for the 3x3 cm² and 4x4 cm² measured at an SSD of 95 cm and 10 cm depth in water using a 15 MV photon beam

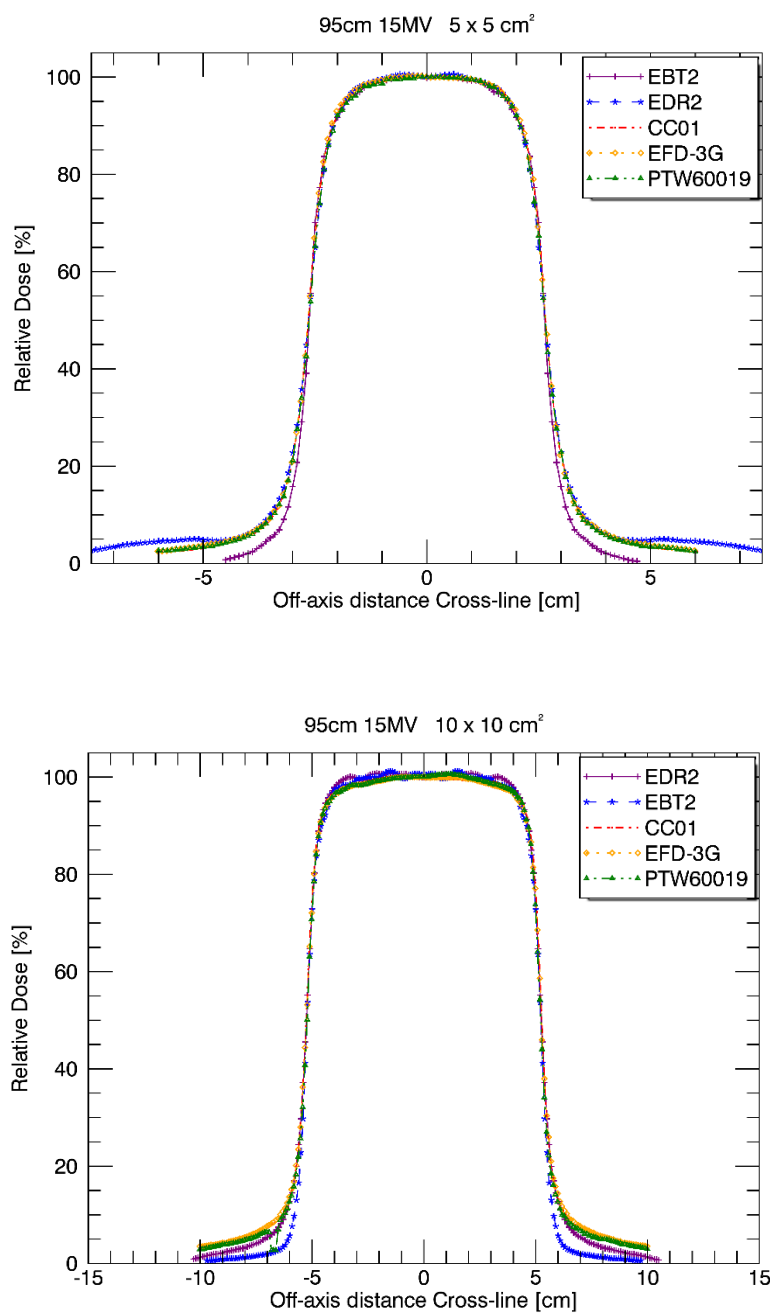


Figure 66. Crossline profiles for the 5x5 cm² and 10x10 cm² measured at an SSD of 95 cm and 10 cm depth in water using a 15 MV photon beam

95 cm 15 MV Inline

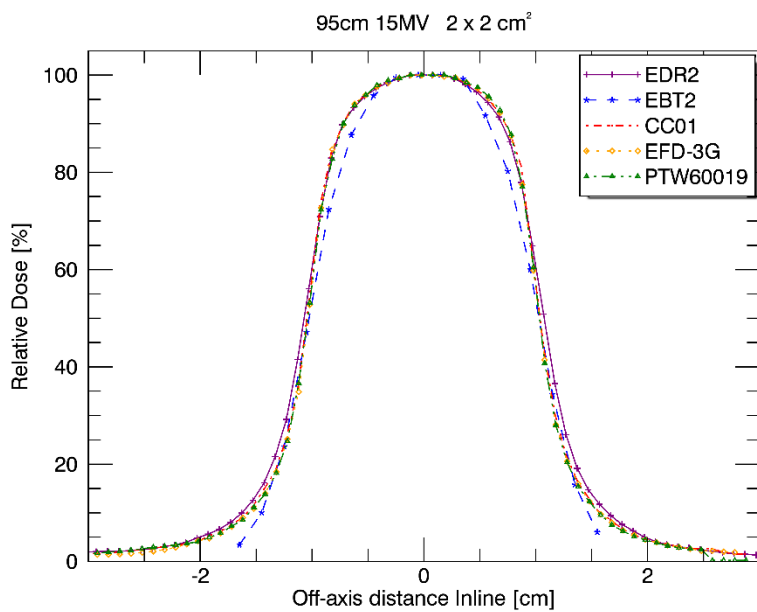
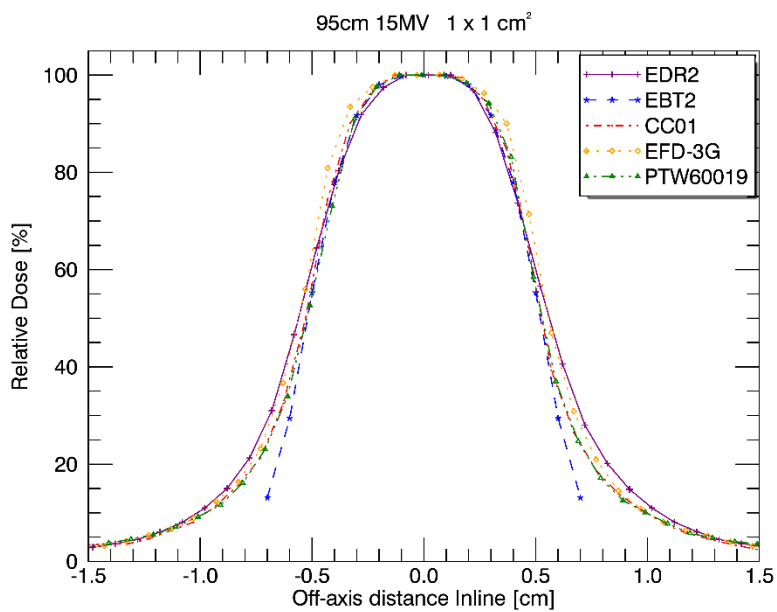


Figure 67. Inline profiles for the 1x1 cm² and 2x2 cm² measured at an SSD of 95 cm and 10 cm depth in water using a 15 MV photon beam

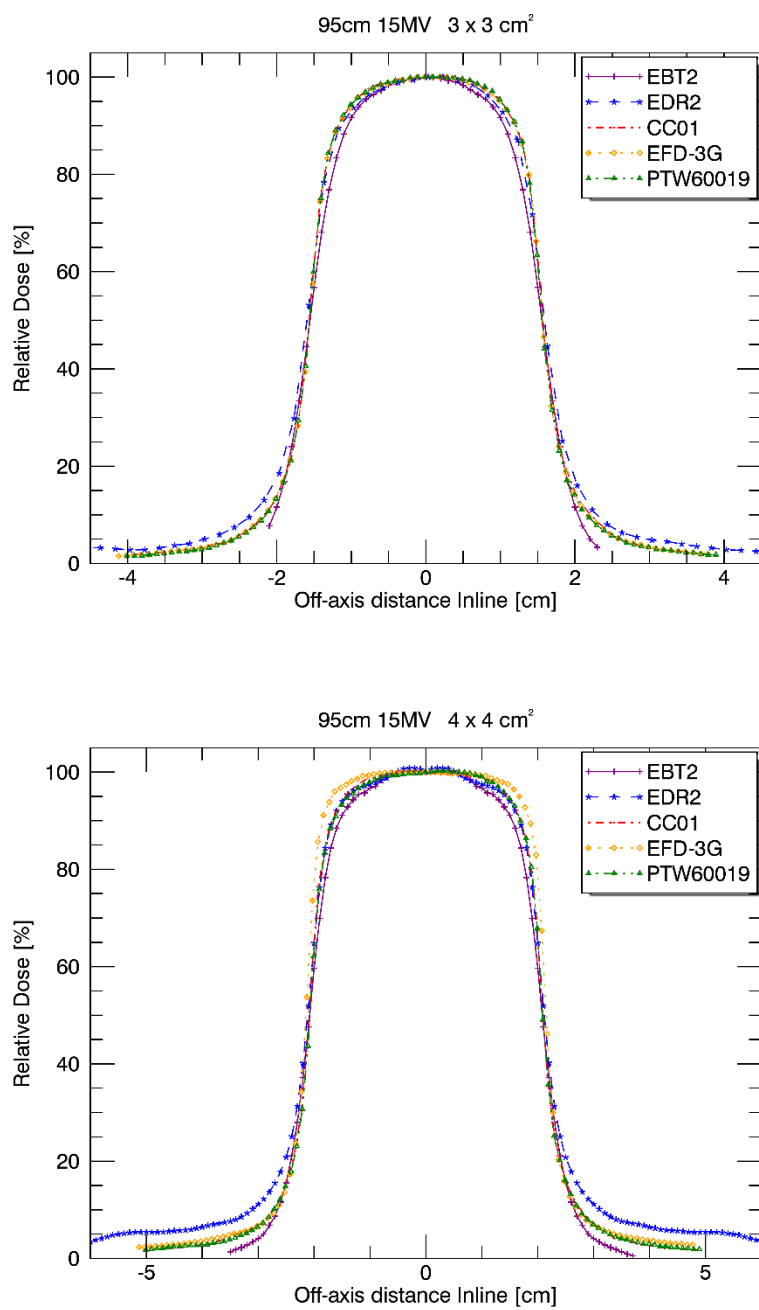


Figure 68. Inline profiles for the 3x3 cm² and 4x4 cm² measured at an SSD of 95 cm and 10 cm depth in water using a 15 MV photon beam

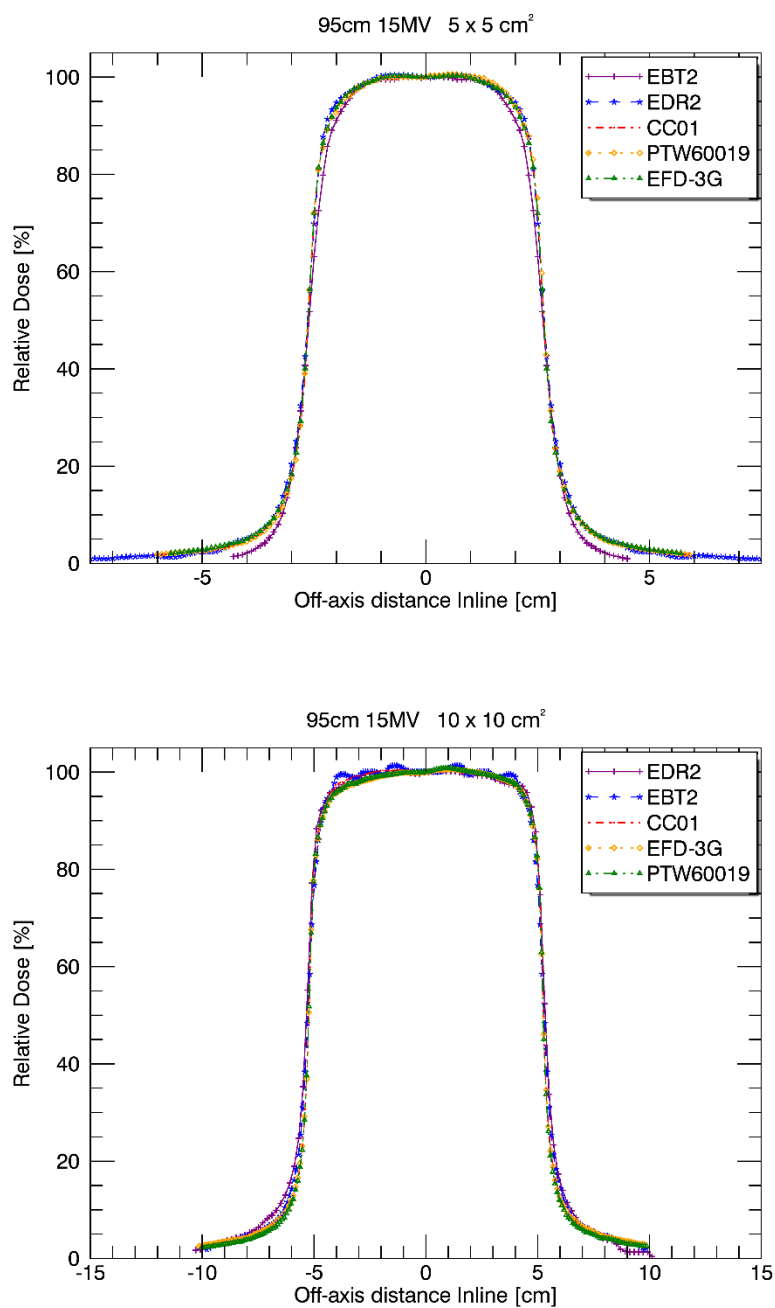


Figure 69. Inline profiles for the 5x5 cm² and 10x10 cm² measured at an SSD of 95 cm and 10 cm depth in water using a 15 MV photon beam

4.2.3 Beam profiles measured at an SSD of 100 cm

100 cm 6 MV Crossline

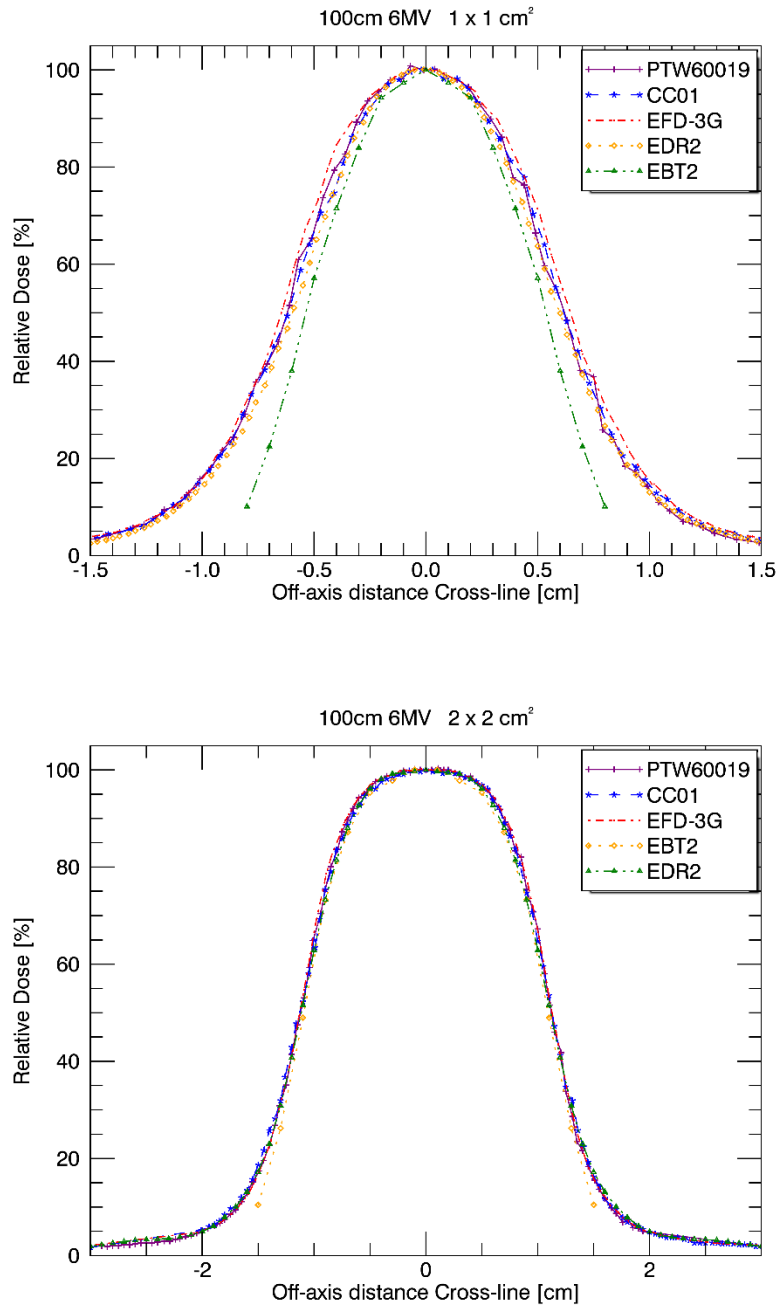


Figure 70. Crossline profiles for the $1 \times 1 \text{ cm}^2$ and $2 \times 2 \text{ cm}^2$ measured at an SSD of 100 cm and 10 cm depth in water using a 6 MV photon beam

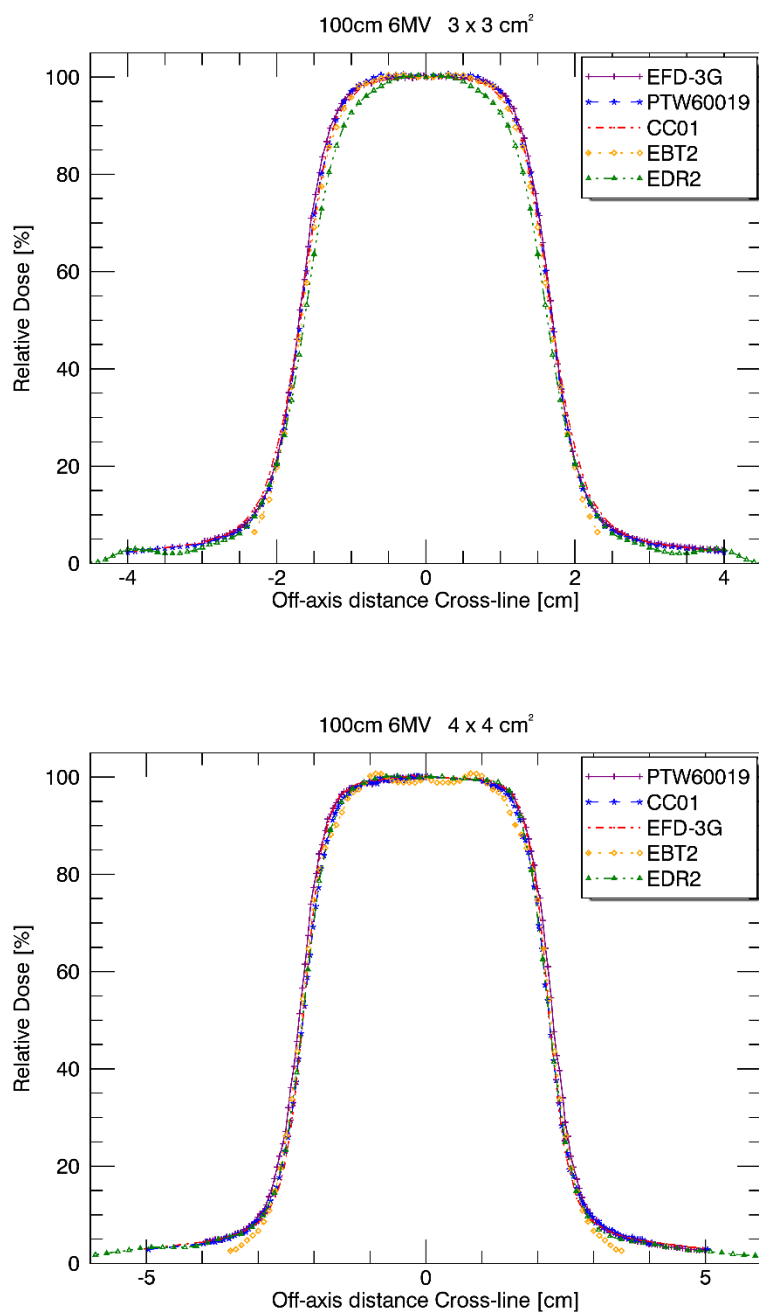


Figure 71. Crossline profiles for the $3 \times 3 \text{ cm}^2$ and $4 \times 4 \text{ cm}^2$ measured at an SSD of 100 cm and 10 cm depth in water using a 6 MV photon beam

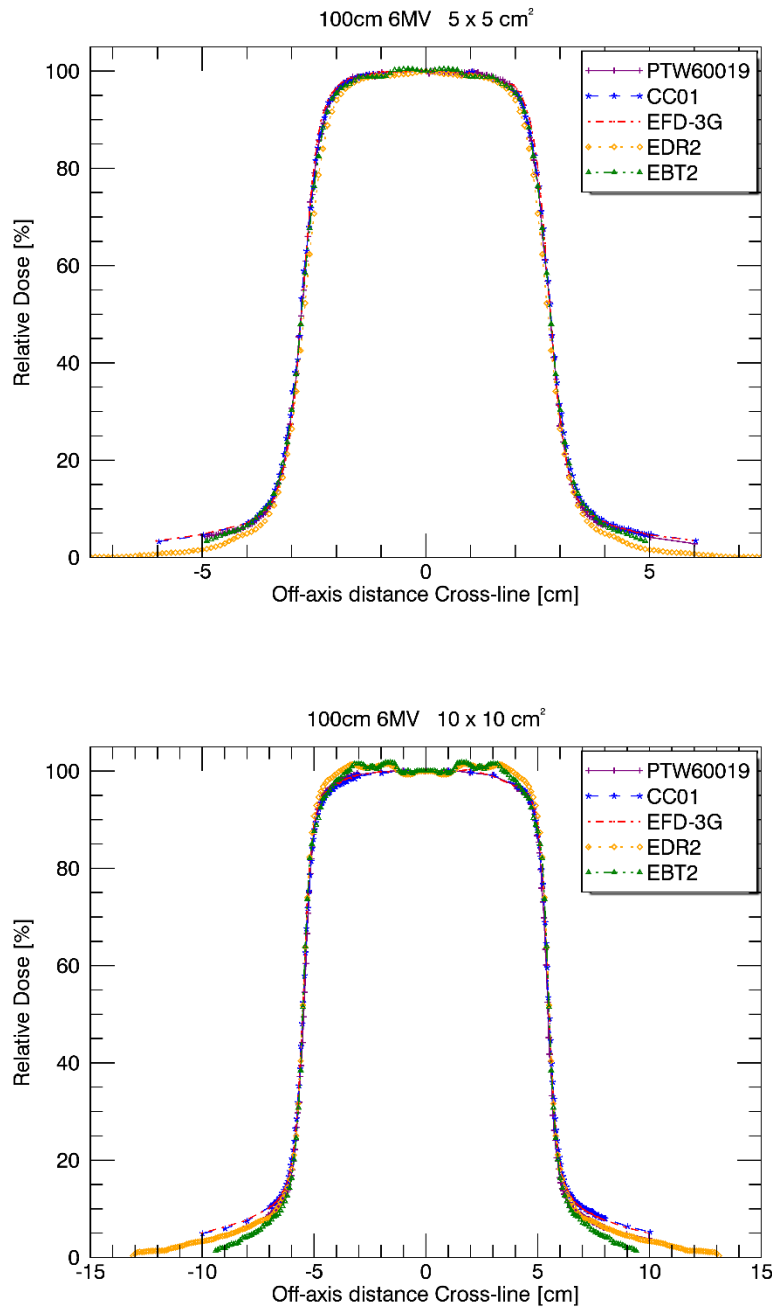


Figure 72. Crossline profiles for the 5x5 cm² and 10x10 cm² measured at an SSD of 100 cm and 10 cm depth in water using a 6 MV photon beam

The trend of high variation in measuring the field size in the Crossline direction continues at the 1x1 cm² field size (figure 70).

100 cm 6 MV Inline

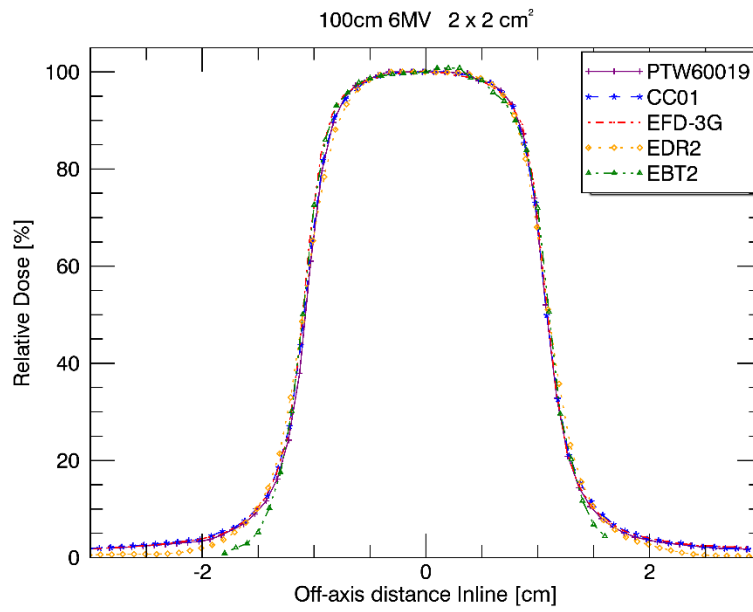
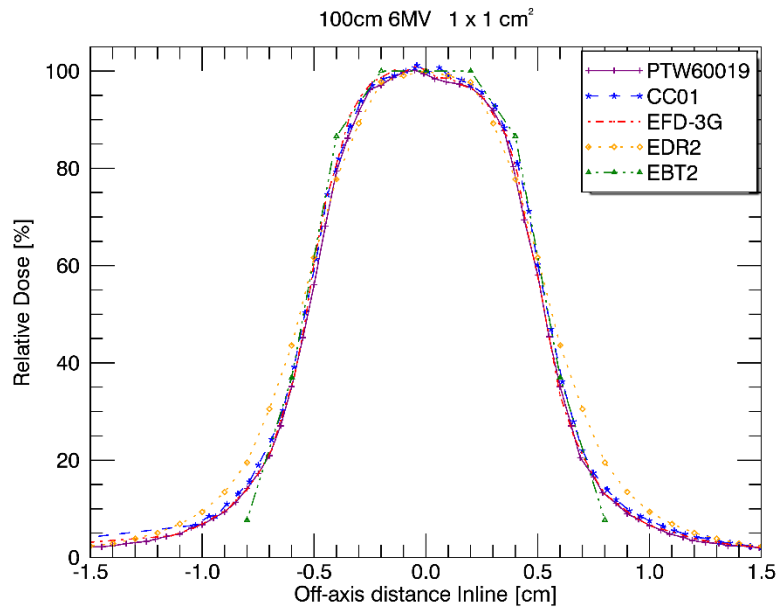


Figure 73. Inline profiles for the 1x1 cm² and 2x2 cm² measured at an SSD of 100 cm and 10 cm depth in water using a 6 MV photon beams

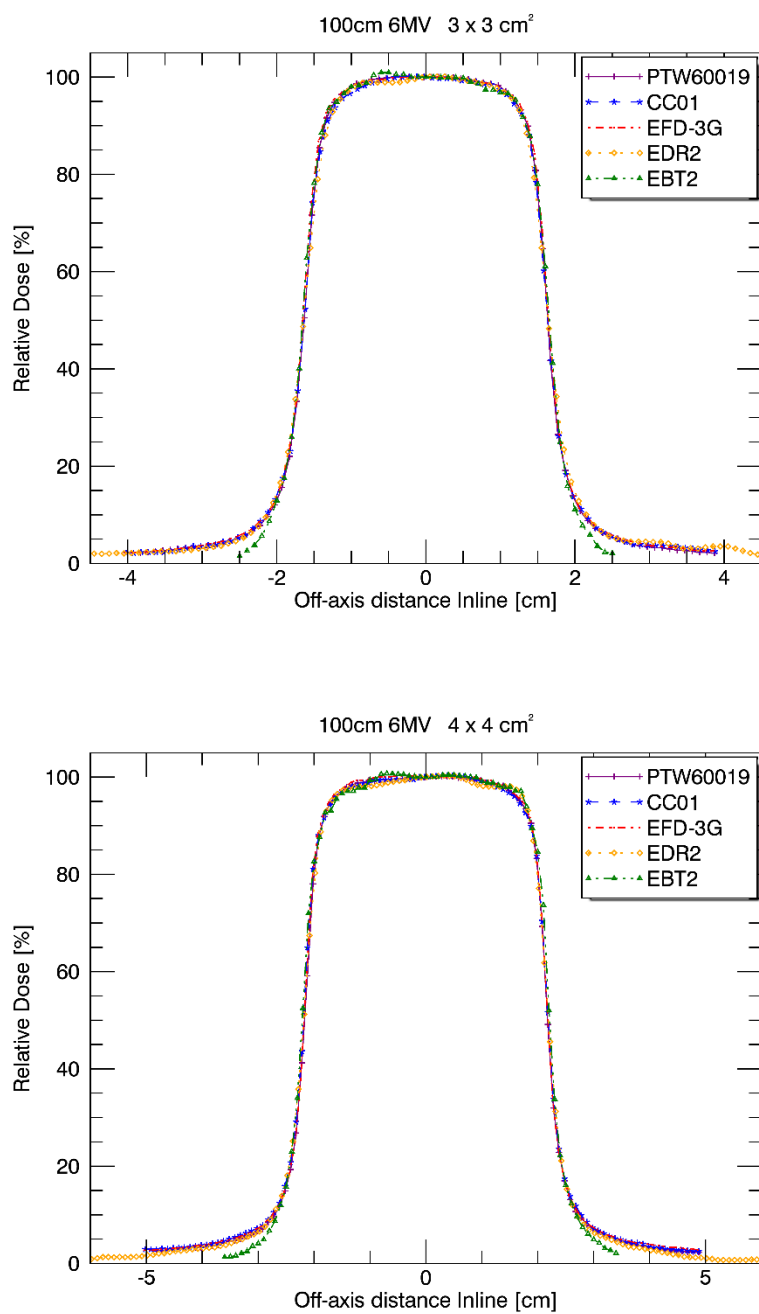


Figure 74. Inline profiles for the 3x3 cm² and 4x4 cm² measured at an SSD of 100 cm and 10 cm depth in water using a 6 MV photon beams

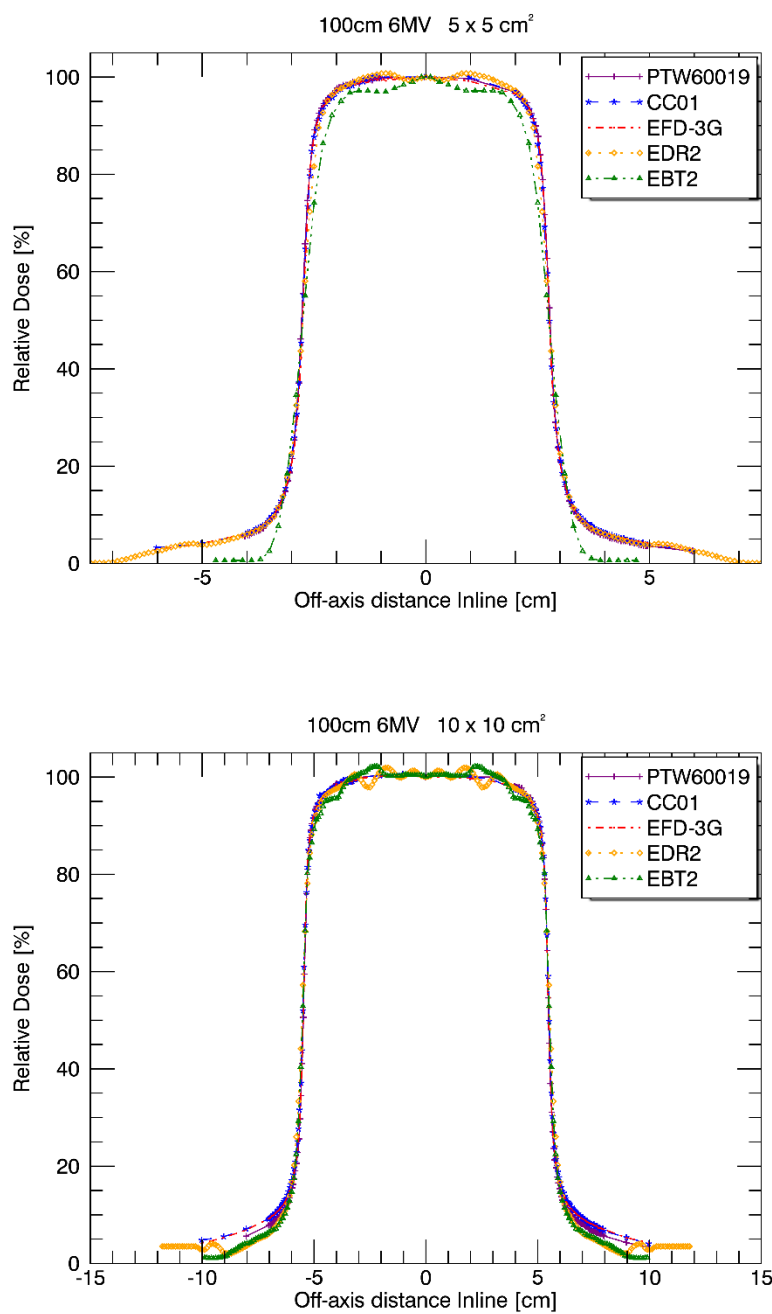


Figure 75. Inline profiles for the 5x5 cm² and 10x10 cm² measured at an SSD of 100 cm and 10 cm depth in water using a 6 MV photon beams

100 cm 10 MV Crossline

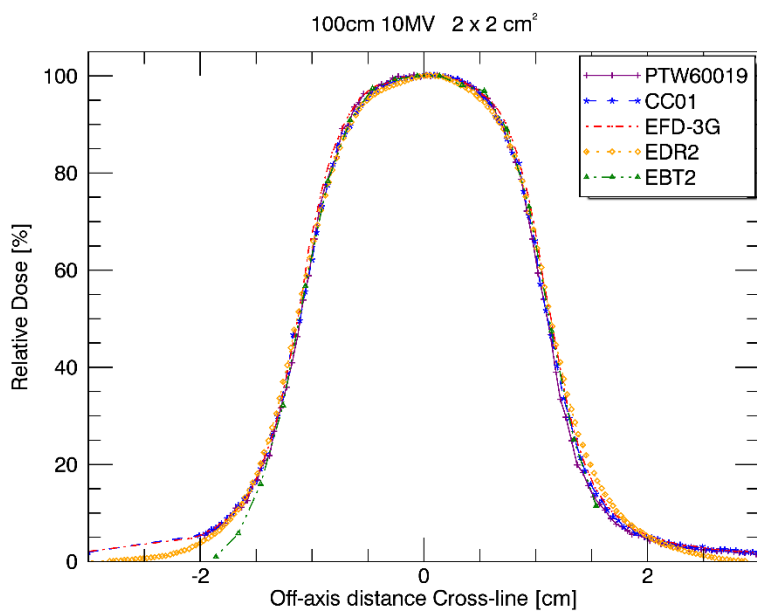
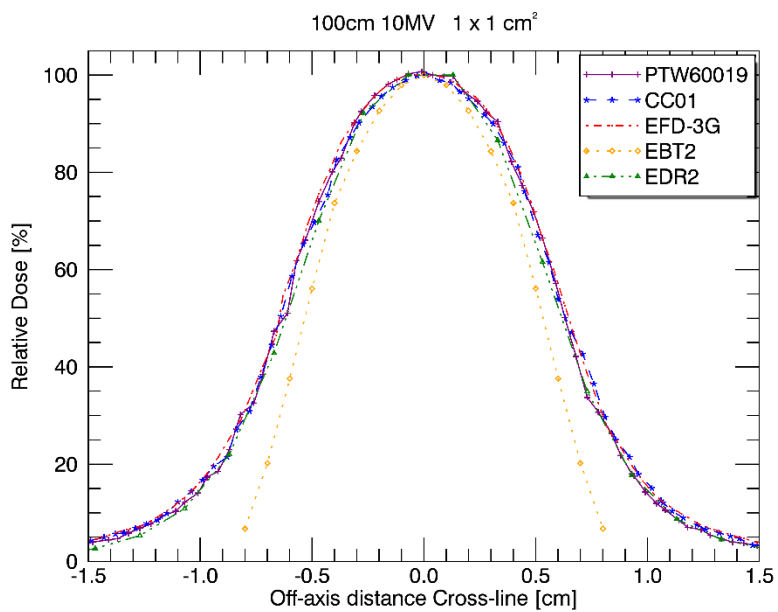


Figure 76. Crossline profiles for the 1x1 cm² and 2x2 cm² measured at an SSD of 100 cm and 10 cm depth in water using a 10 MV photon beam

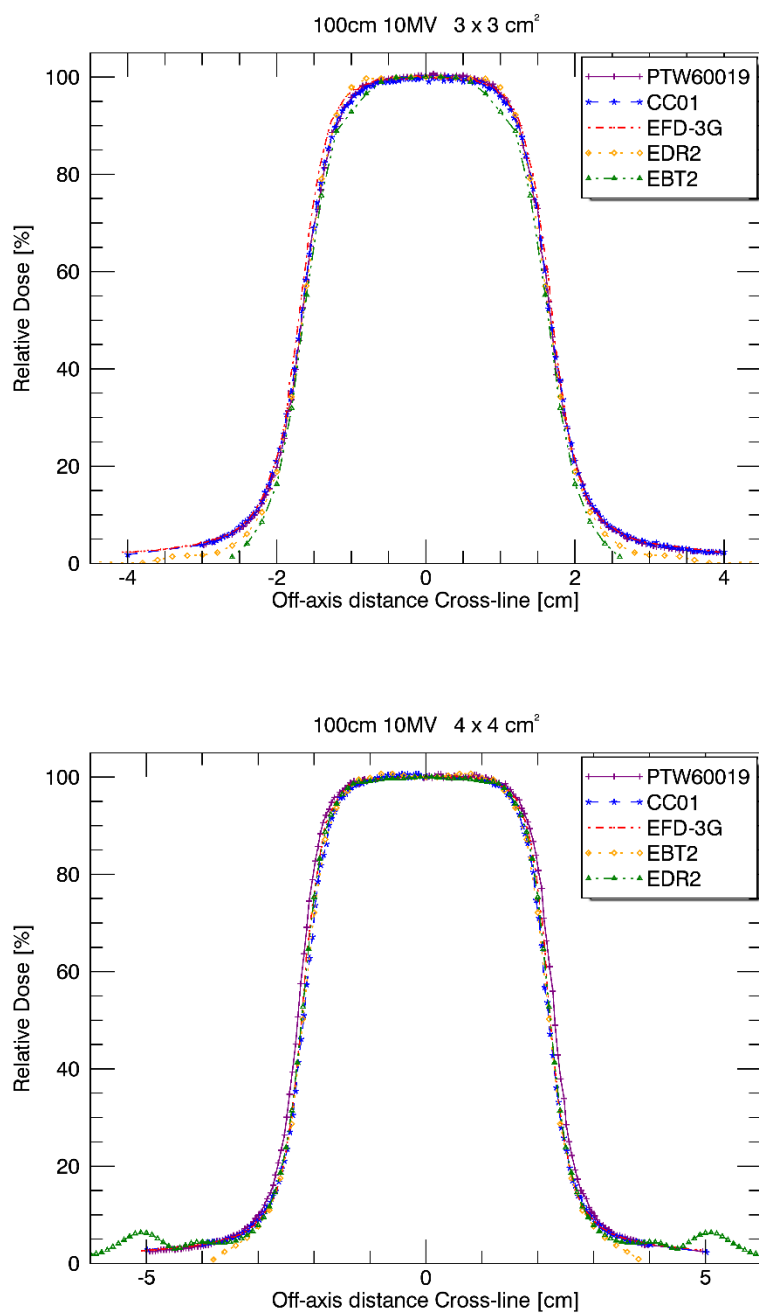


Figure 77. Crossline profiles for the 3x3 cm² and 4x4 cm² measured at an SSD of 100 cm and 10 cm depth in water using a 10 MV photon beam

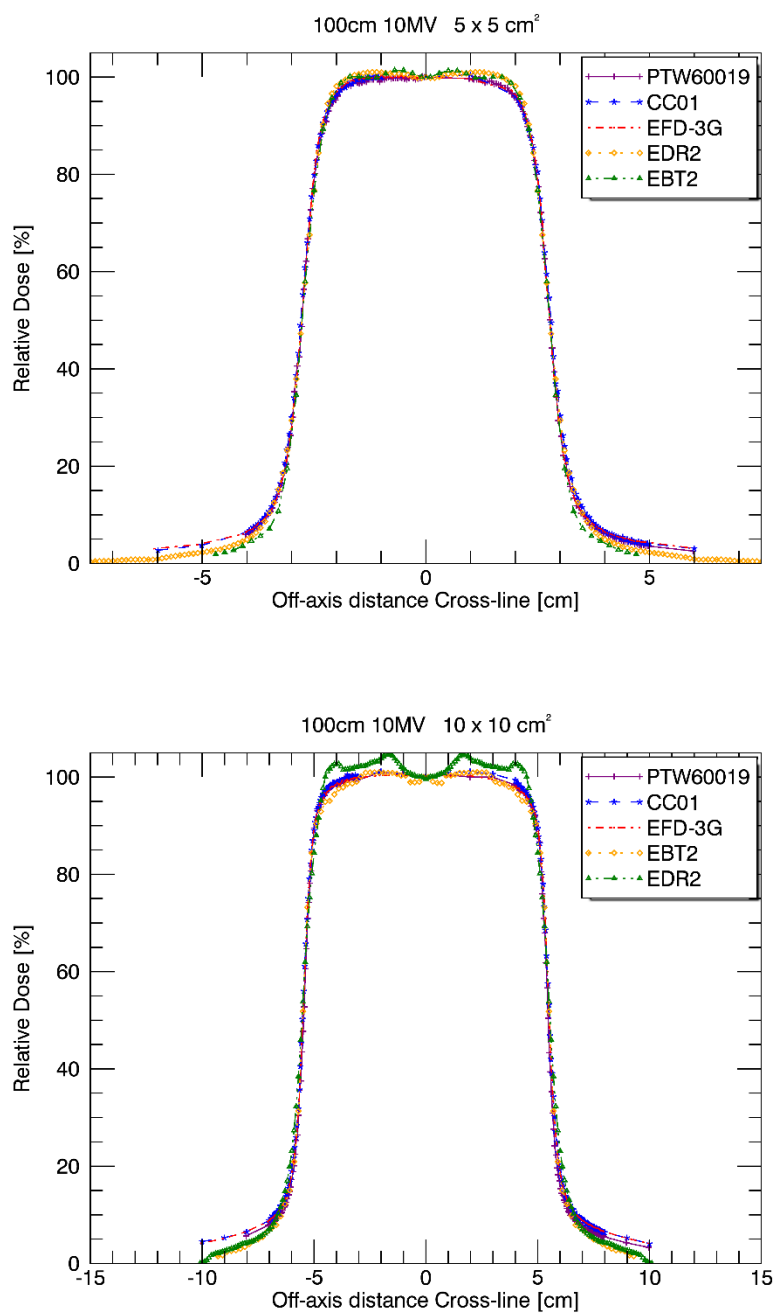


Figure 78. Crossline profiles for the 5x5 cm² and 10x10 cm² measured at an SSD of 100 cm and 10 cm depth in water using a 10 MV photon beam

The EDR2 artefact is shown again for the 10x10 cm² field size, in figure 78.

100 cm 10 MV Inline

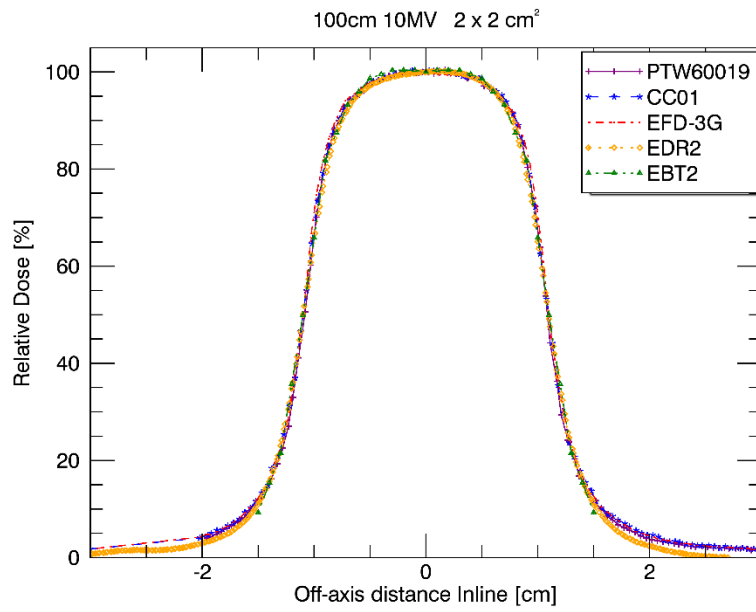
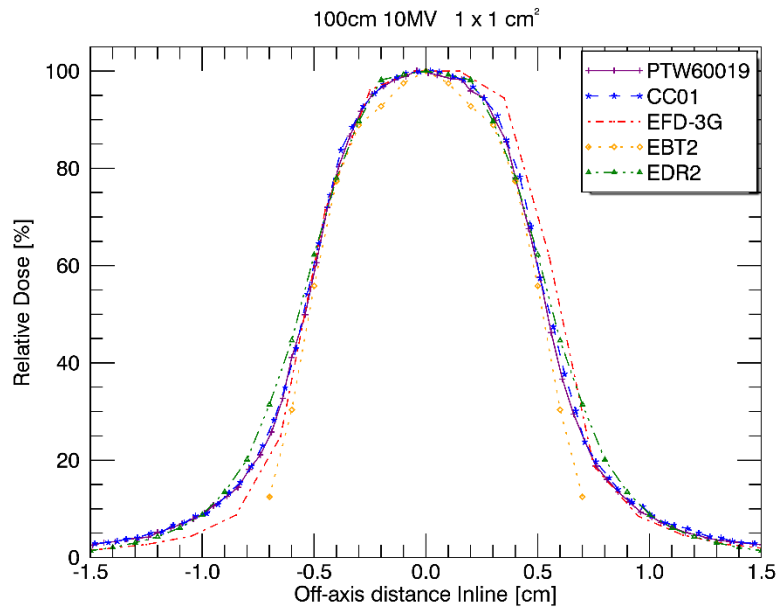


Figure 79. Inline profiles for the 1x1 cm² and 2x2 cm² measured at an SSD of 100 cm and 10 cm depth in water using a 10 MV photon beam

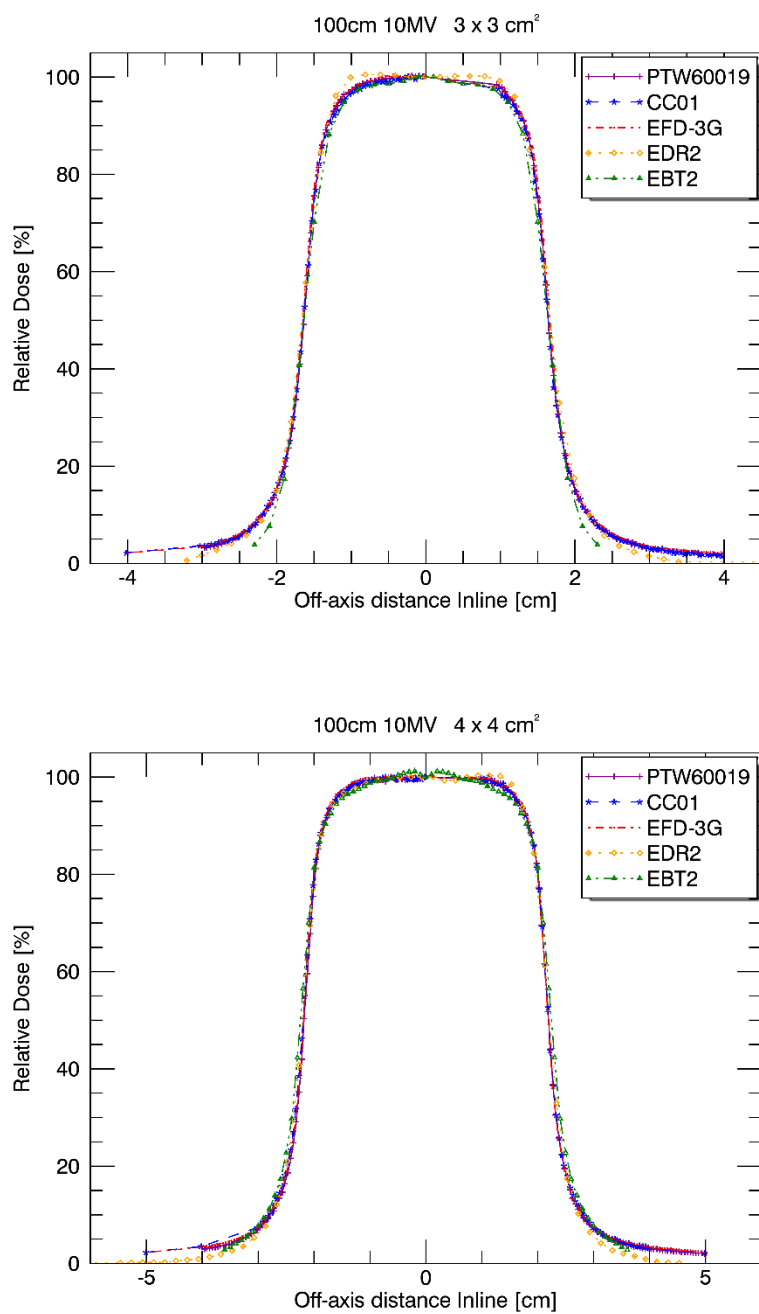


Figure 80. Inline profiles for the 3x3 cm² and 4x4 cm² measured at an SSD of 100 cm and 10 cm depth in water using a 10 MV photon beam

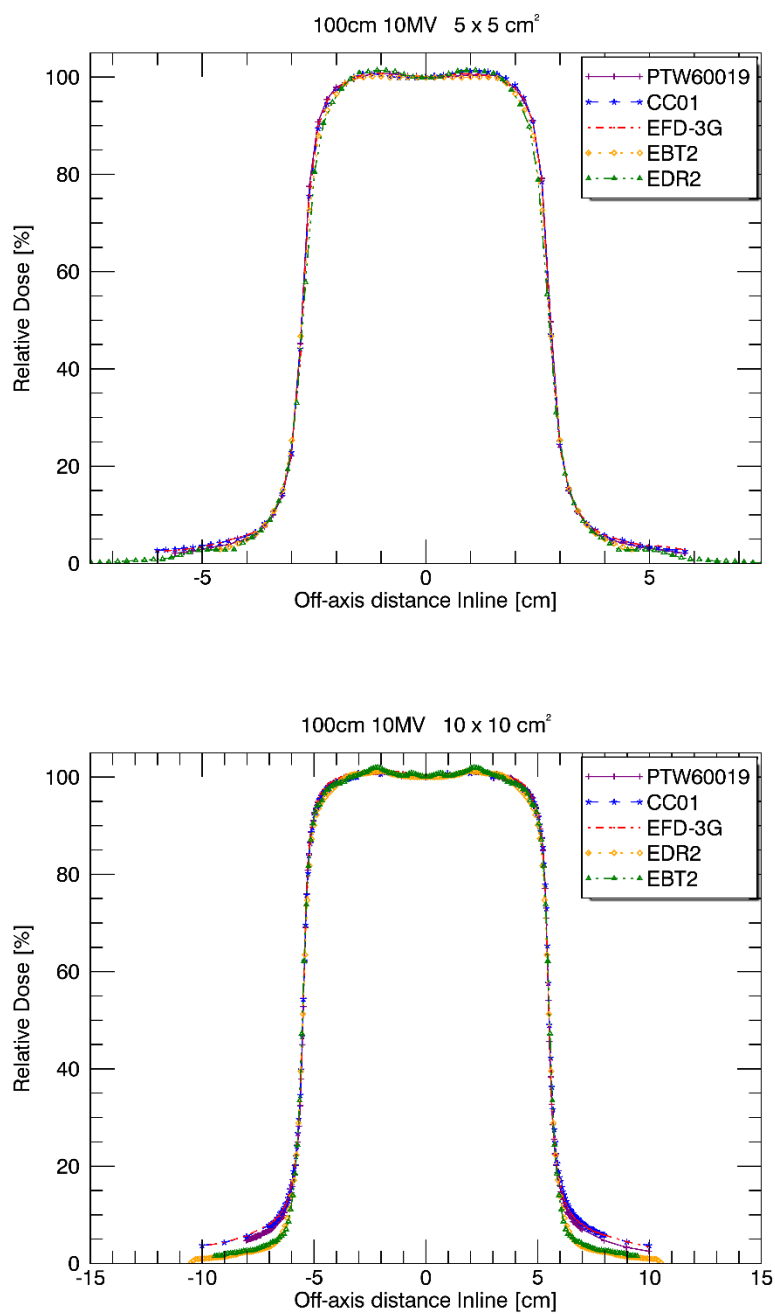


Figure 81. Inline profiles for the 5x5 cm² and 10x10 cm² measured at an SSD of 100 cm and 10 cm depth in water using a 10 MV photon beam

100 cm 15 MV Crossline

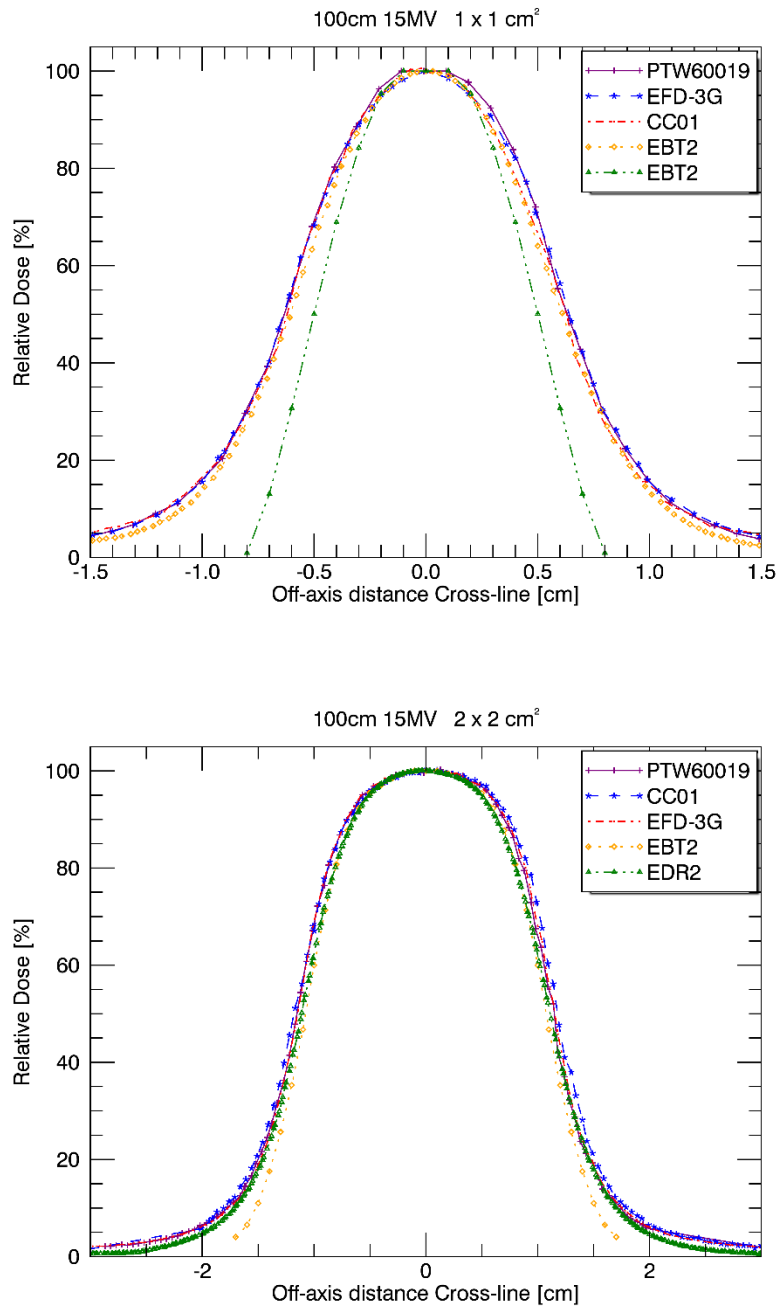


Figure 82. Crossline profiles for the 1x1 cm² and 2x2 cm² measured at an SSD of 100 cm and 10 cm depth in water using a 15 MV photon beam

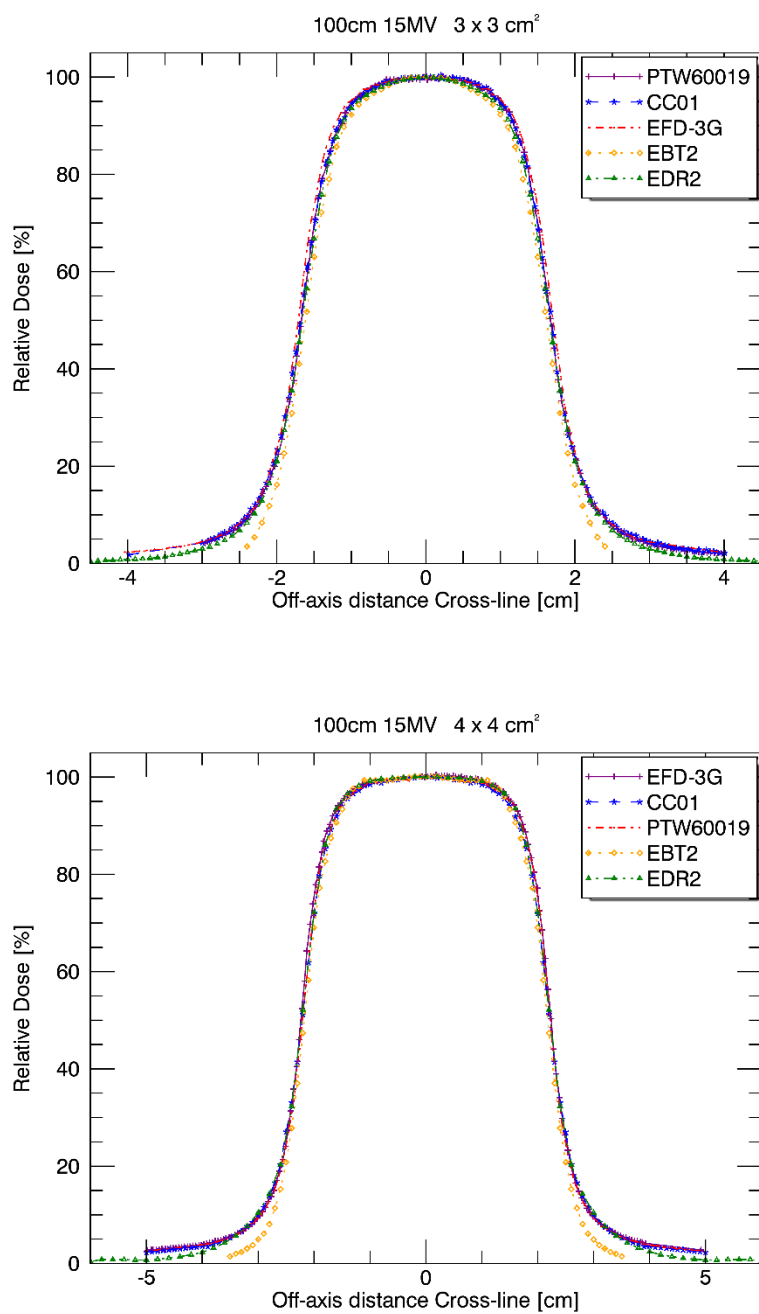


Figure 83. Crossline profiles for the 3x3 cm² and 4x4 cm² measured at an SSD of 100 cm and 10 cm depth in water using a 15 MV photon beam

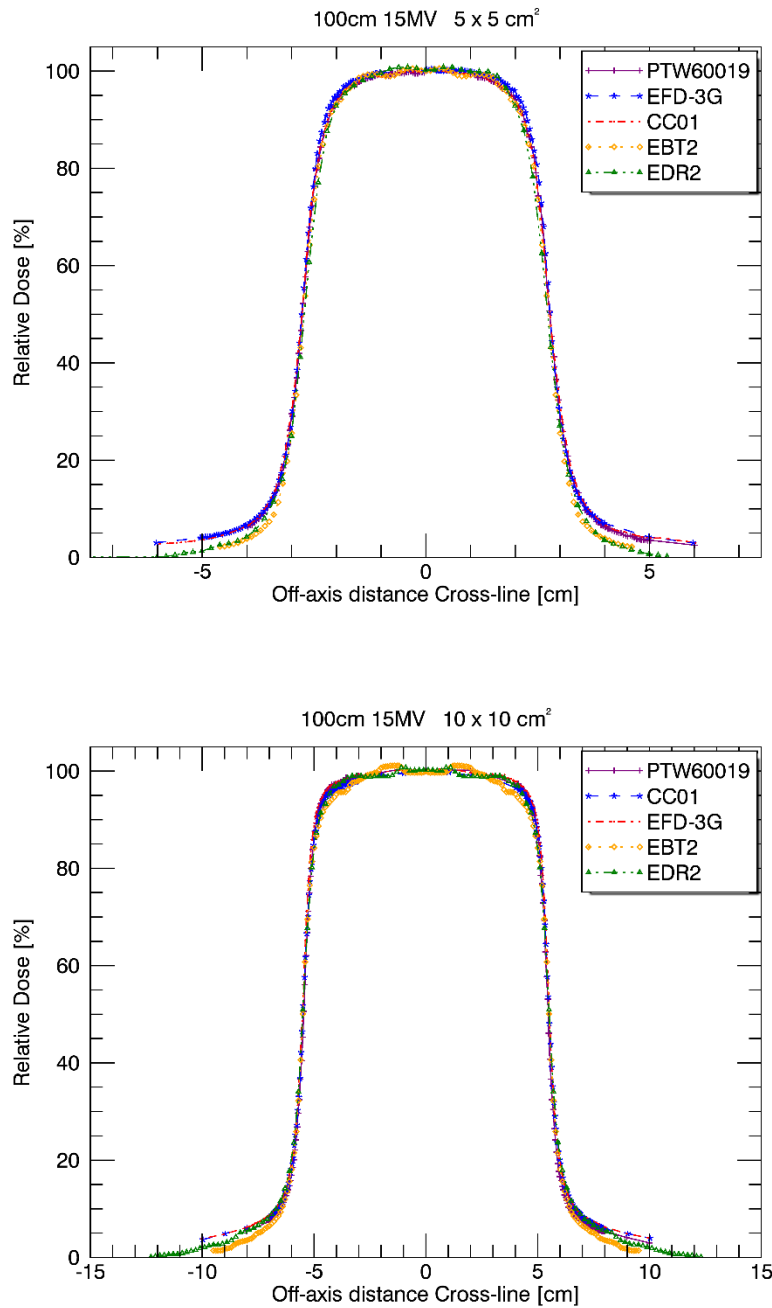


Figure 84. Crossline profiles for the 5x5 cm² and 10x10 cm² measured at an SSD of 100 cm and 10 cm depth in water using a 15 MV photon beam

The inconsistencies of field formation in this direction are again shown in Figure 81 to Figure 83. The film artefacts are visible for both types of film used. The EDR2 artefact is well outside the field of interest when looking at 10x10 cm² field size (figure 84), whereas the EBT2 has artefacts within the field of interest, but these are not detrimental to obtaining the required quantities.

100 cm 15 MV Inline

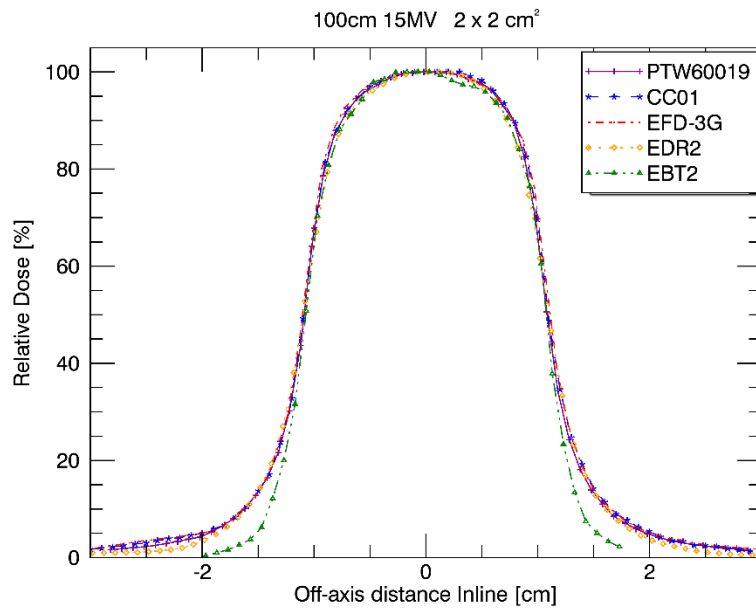
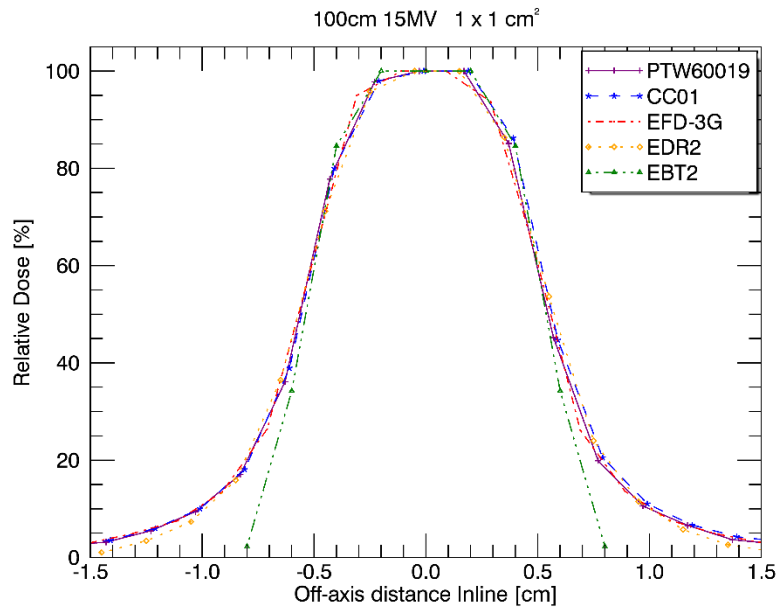


Figure 85. Inline profiles for the 1x1 cm² and 2x2 cm² measured at an SSD of 100 cm and 10 cm depth in water using a 15 MV photon beam

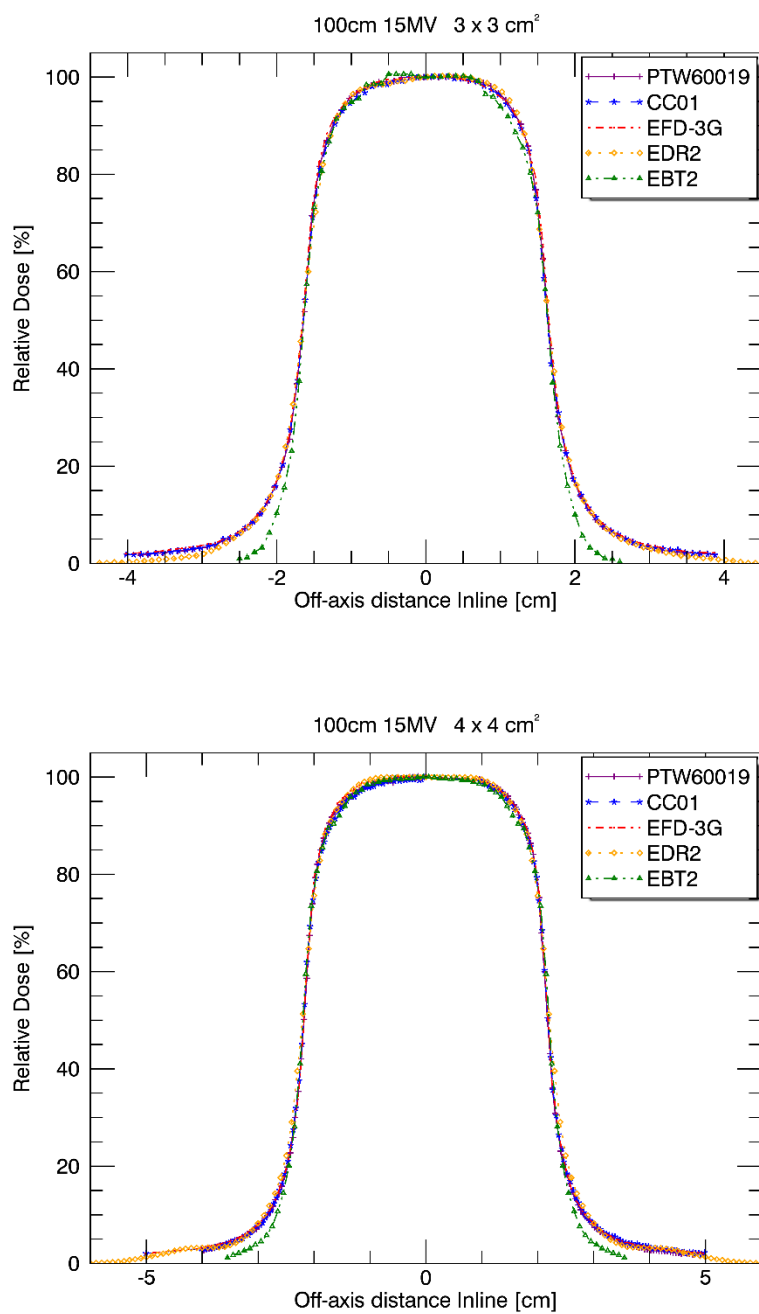


Figure 86. Inline profiles for the 3x3 cm² and 4x4 cm² measured at an SSD of 100 cm and 10 cm depth in water using a 15 MV photon beam

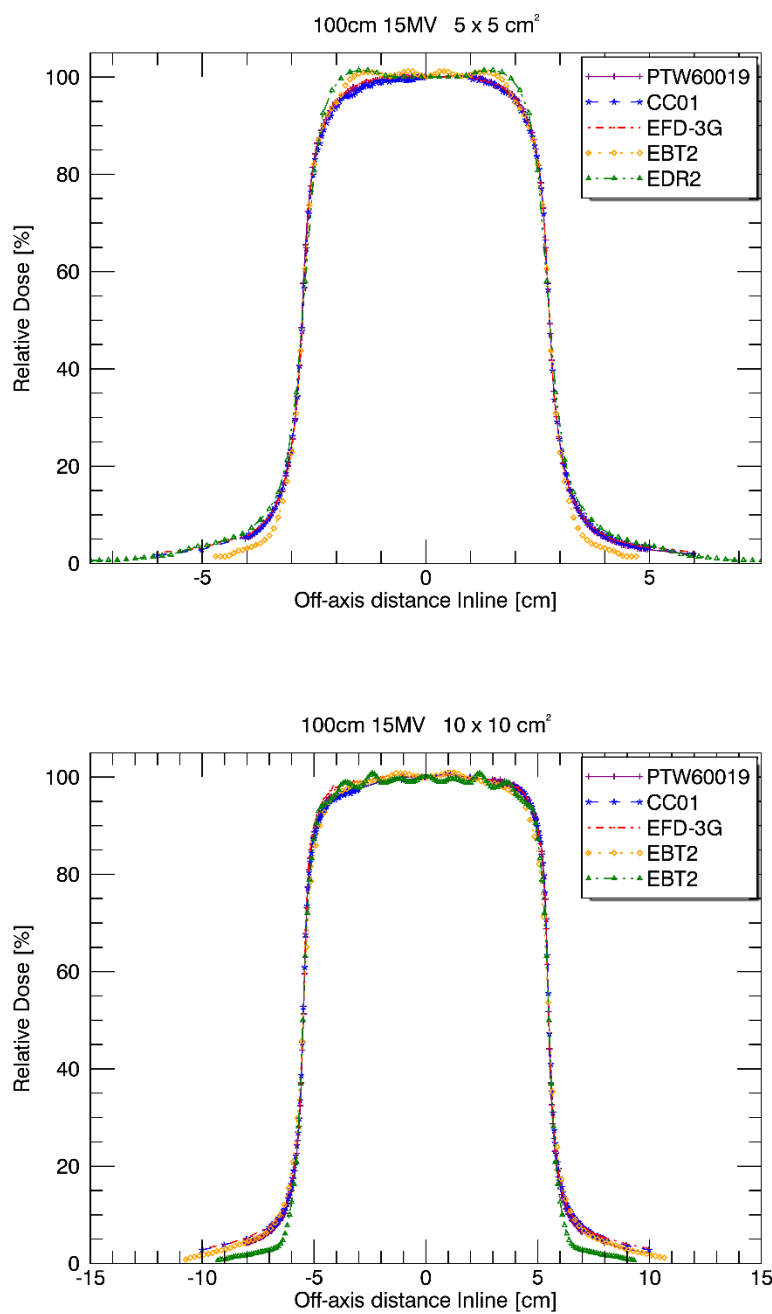


Figure 87. Inline profiles for the 5x5 cm² and 10x10 cm² measured at an SSD of 100 cm and 10 cm depth in water using a 15 MV photon beam

4.2.4 Beam profiles measured at an SSD of 110 cm

110 cm 6 MV Crossline

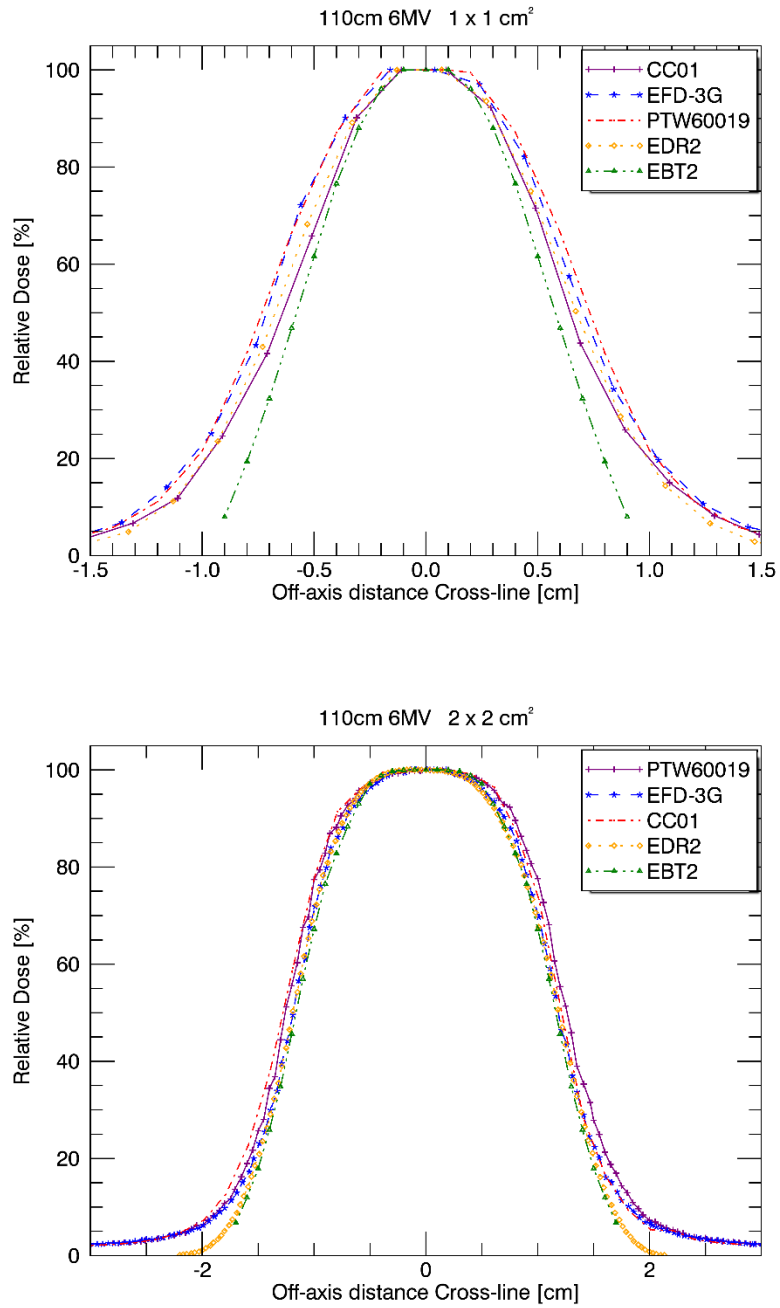


Figure 88. Crossline profiles for the 1x1 cm² and 2x2 cm² measured at an SSD of 110 cm and 10 cm depth in water using a 6 MV photon beam

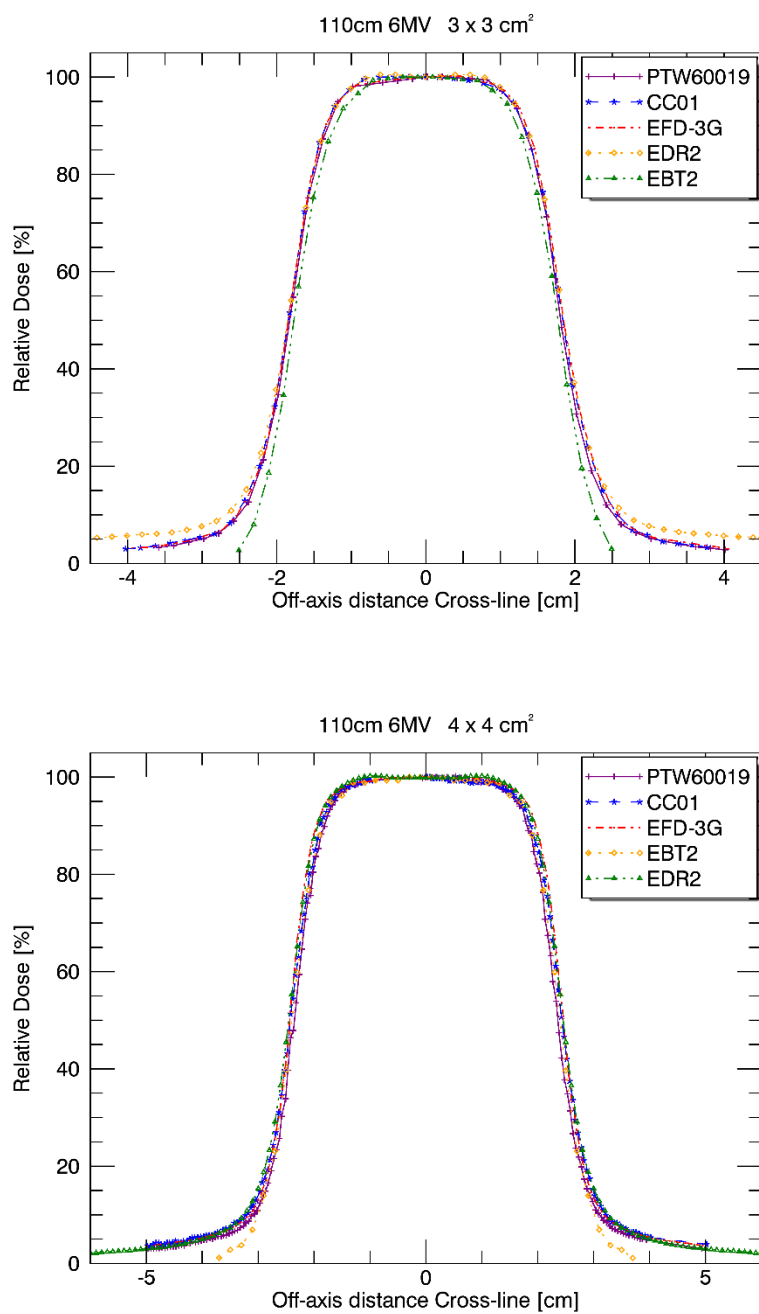


Figure 89. Crossline profiles for the 3x3 cm² and 4x4 cm² measured at an SSD of 110 cm and 10 cm depth in water using a 6 MV photon beam

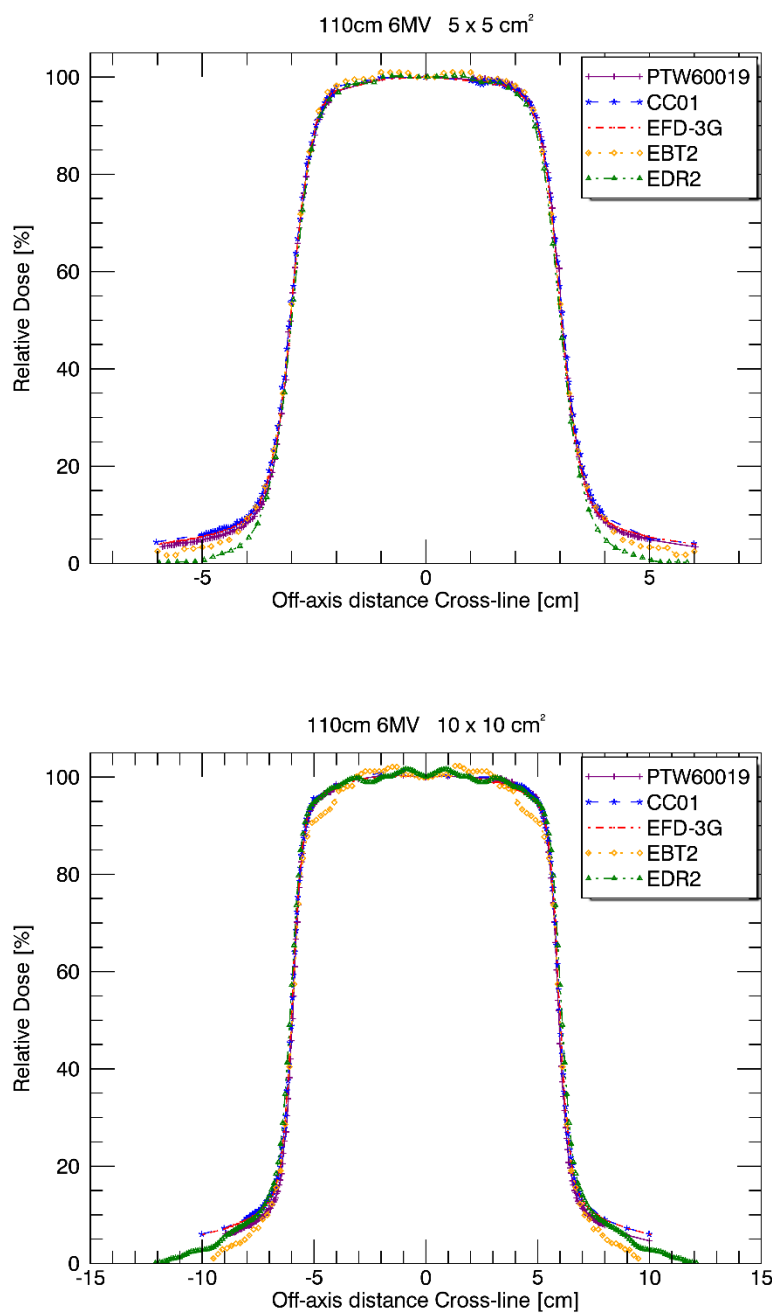


Figure 90. Crossline profiles for the 5x5 cm² and 10x10 cm² measured at an SSD of 110 cm and 10 cm depth in water using a 6 MV photon beam

110 cm 6 MV Inline

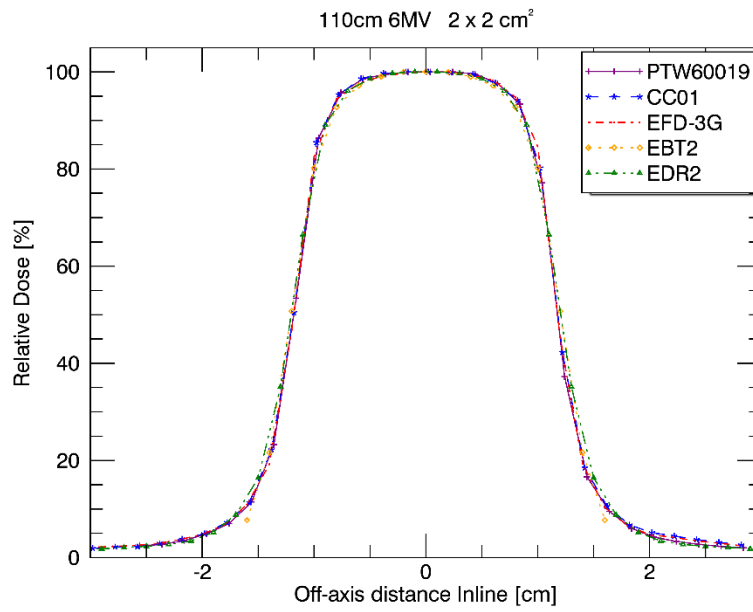
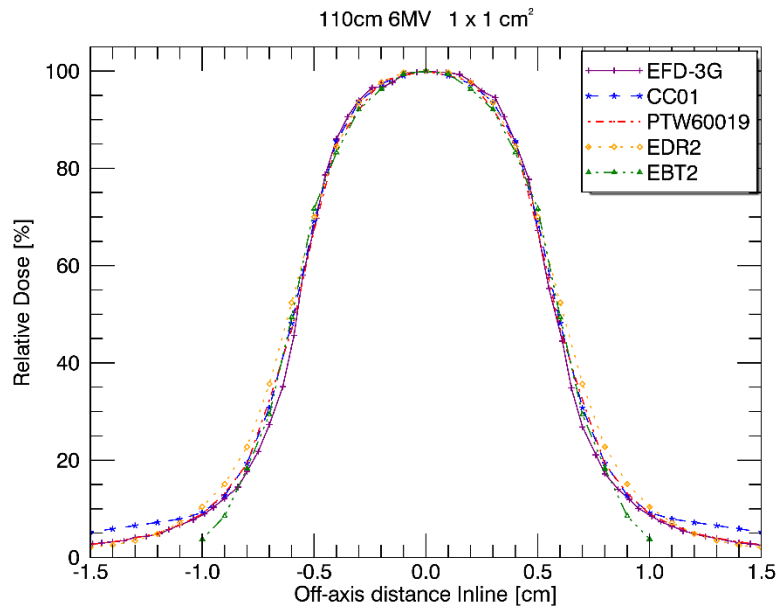


Figure 91. Inline profiles for the 1x1 cm² and 2x2 cm² measured at an SSD of 110 cm and 10 cm depth in water using a 6 MV photon beam

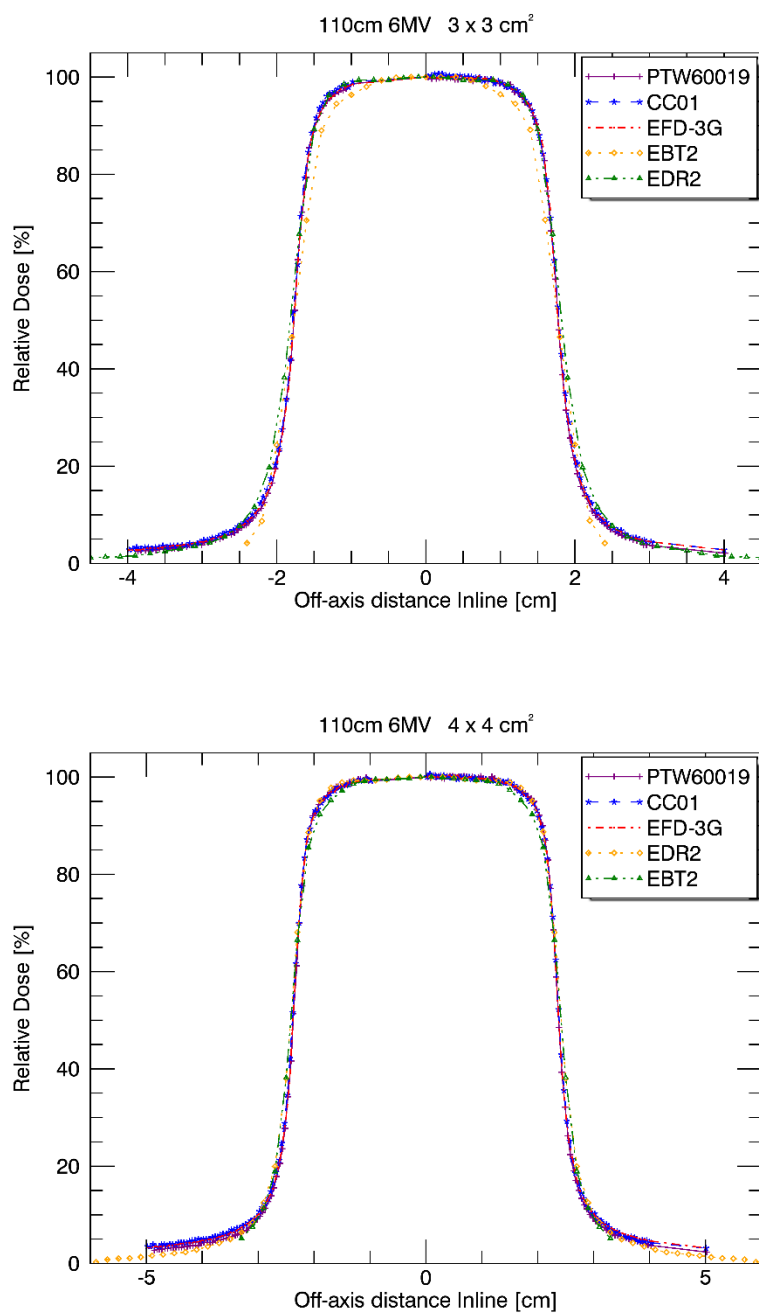


Figure 92. Inline profiles for the $3 \times 3 \text{ cm}^2$ and $4 \times 4 \text{ cm}^2$ measured at an SSD of 110 cm and 10 cm depth in water using a 6 MV photon beam

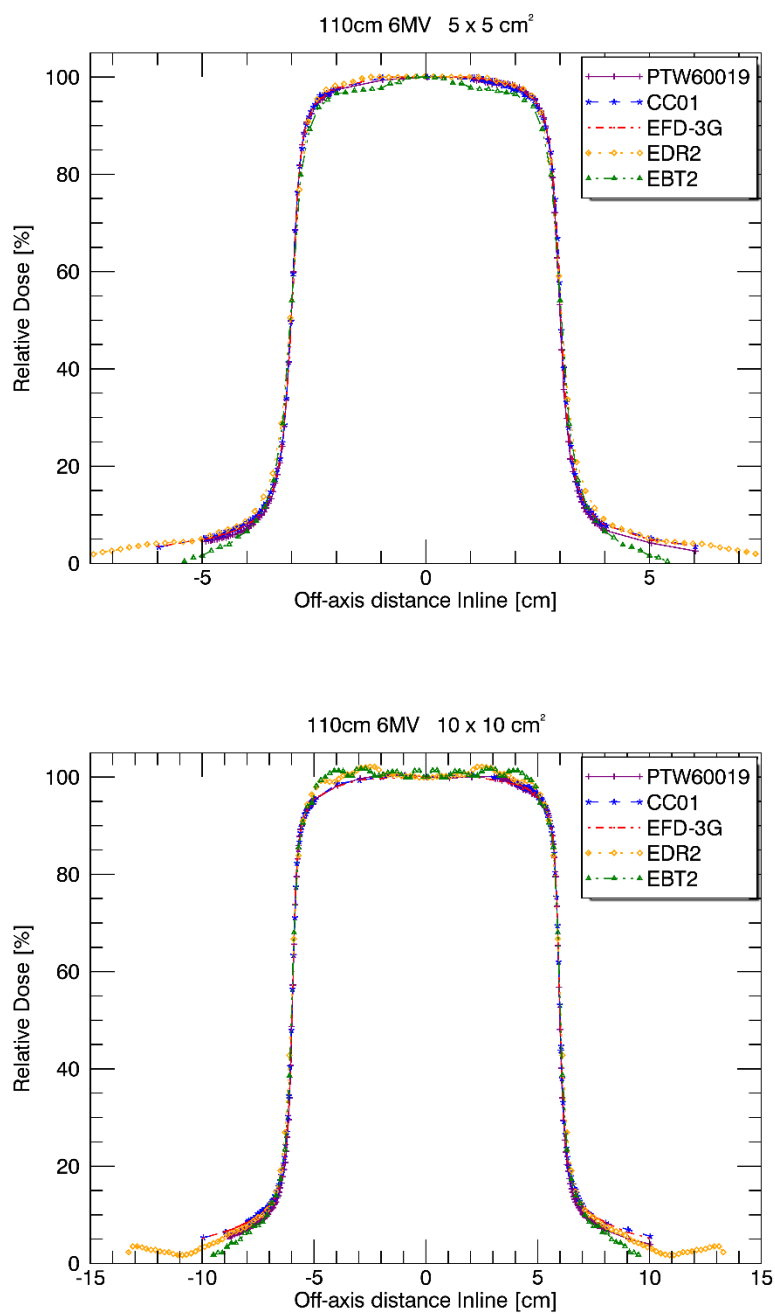


Figure 93. Inline profiles for the 5x5 cm² and 10x10 cm² measured at an SSD of 110 cm and 10 cm depth in water using a 6 MV photon beam

110 cm 10 MV Crossline

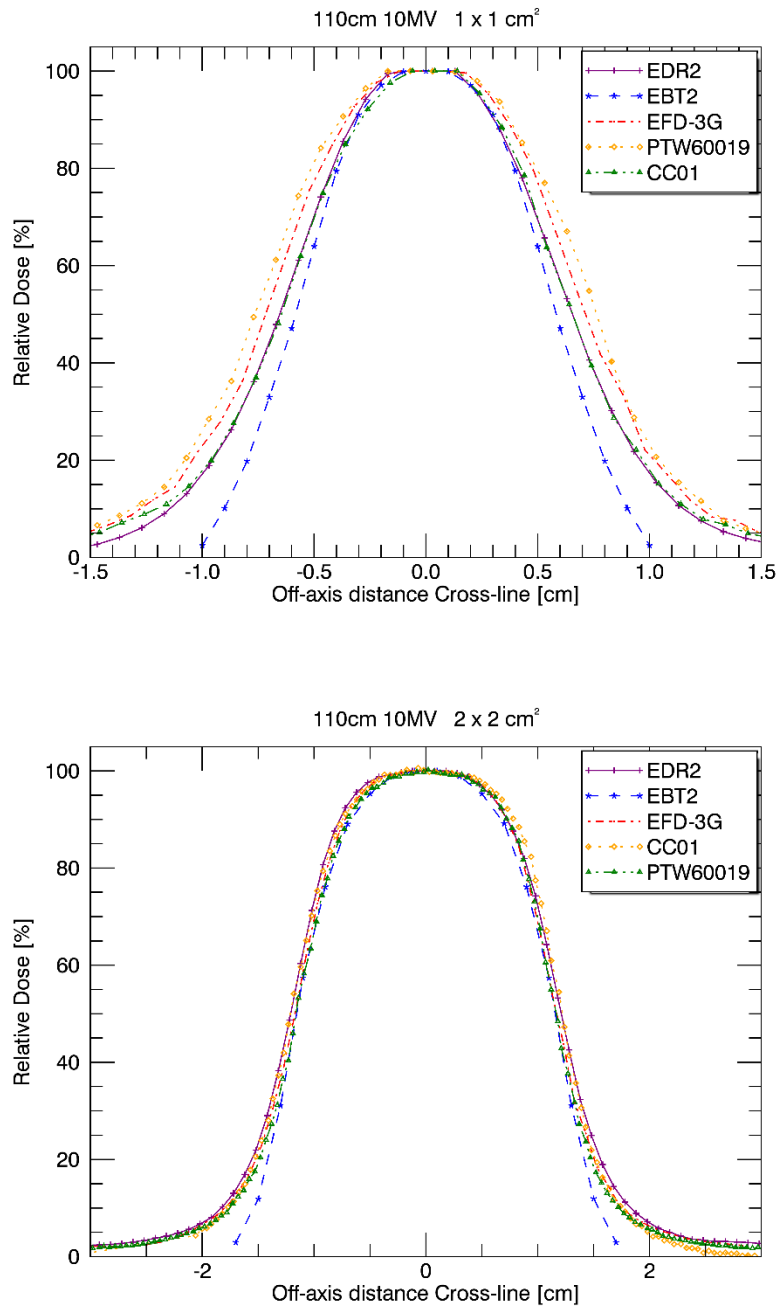


Figure 94. Crossline profiles for the $1 \times 1 \text{ cm}^2$ and $2 \times 2 \text{ cm}^2$ measured at an SSD of 110 cm and 10 cm depth in water using a 10 MV photon beam

In figure 94, the $1 \times 1 \text{ cm}^2$ field sizes are again showing a lot of variation compared to other field sizes.

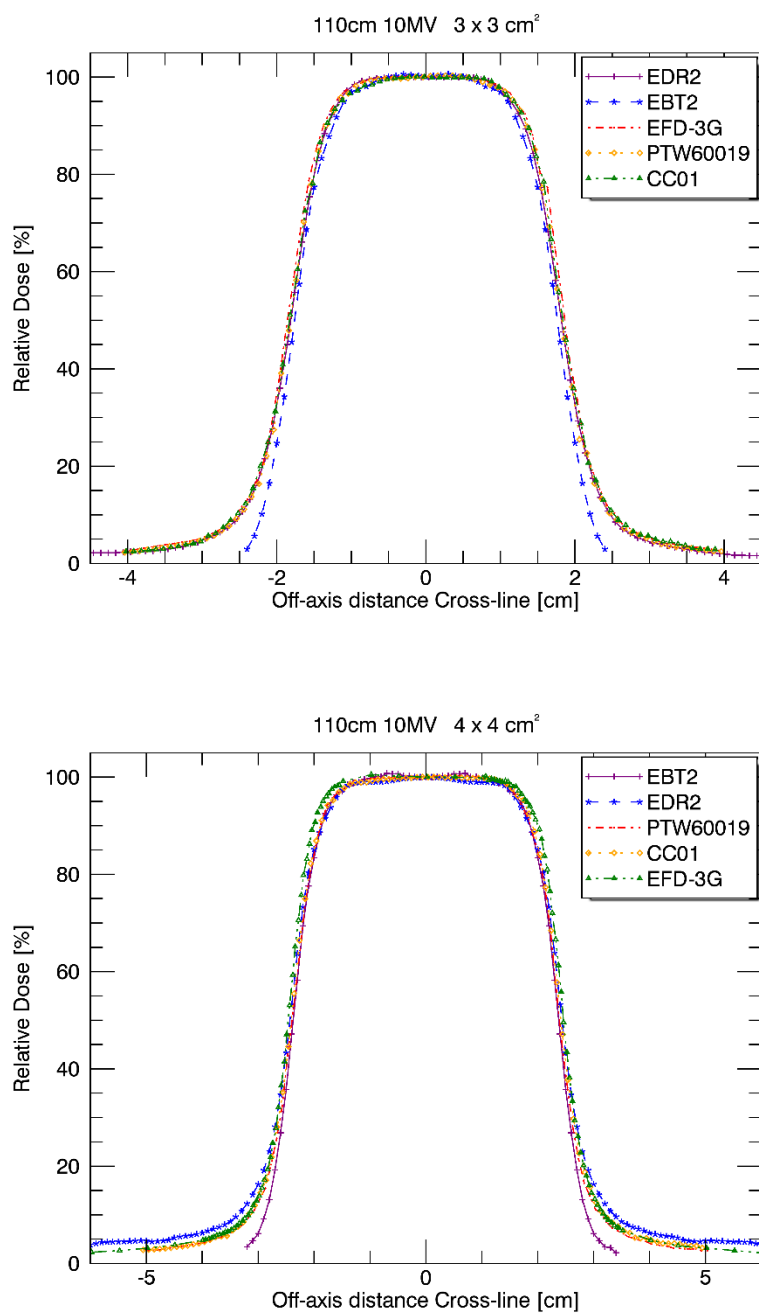


Figure 95. Crossline profiles for the 3x3 cm² and 4x4 cm² measured at an SSD of 110 cm and 10 cm depth in water using a 10 MV photon beam

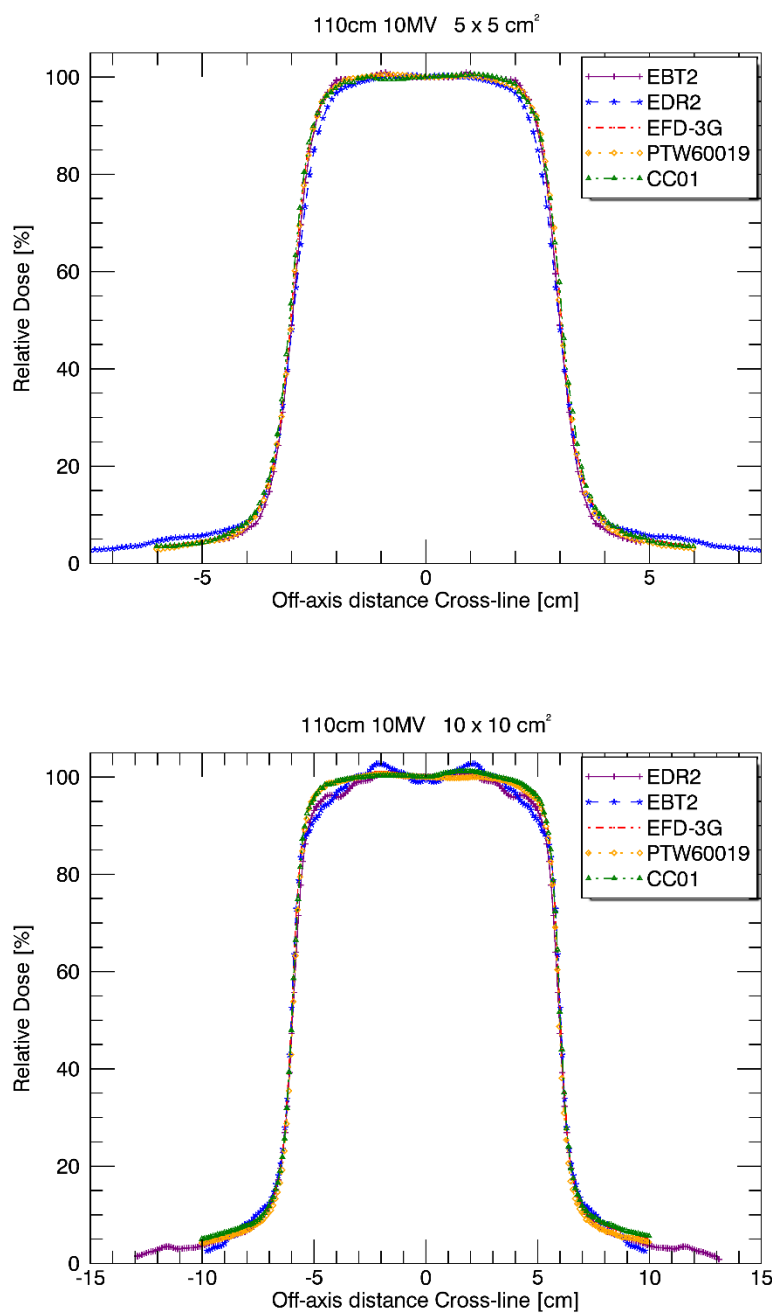


Figure 96. Crossline profiles for the 5x5 cm² and 10x10 cm² measured at an SSD of 110 cm and 10 cm depth in water using a 10 MV photon beam

The EBT2 displays scanner artefacts at the 10x10 cm² field size (figure 96).

110 cm 10 MV Inline

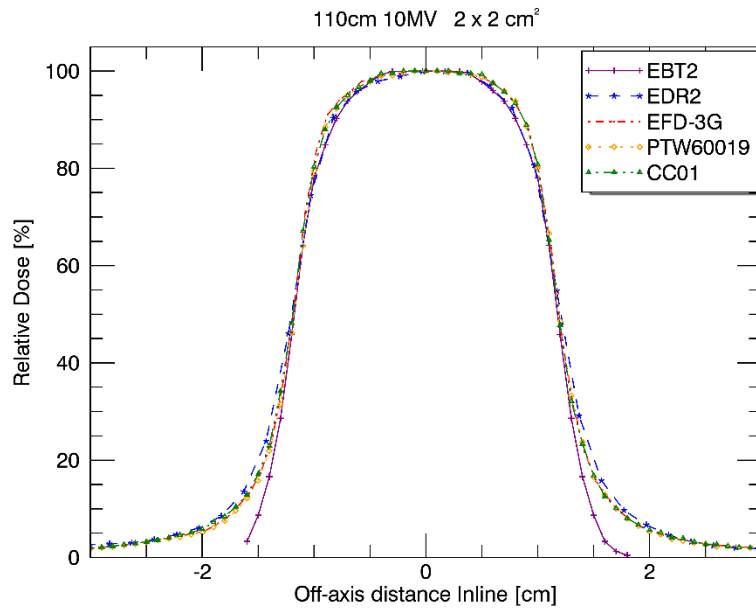
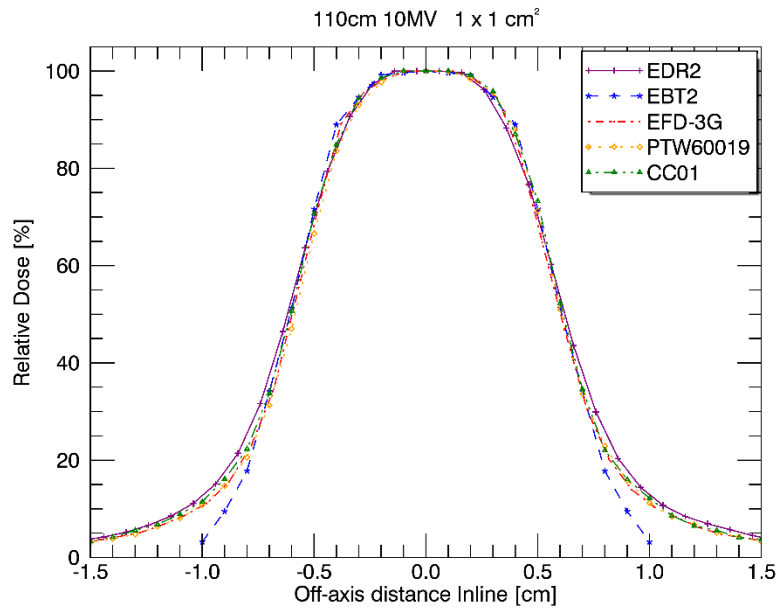


Figure 97. Inline profiles for the 1x1 cm² and 2x2 cm² measured at an SSD of 110 cm and 10 cm depth in water using a 10 MV photon beam

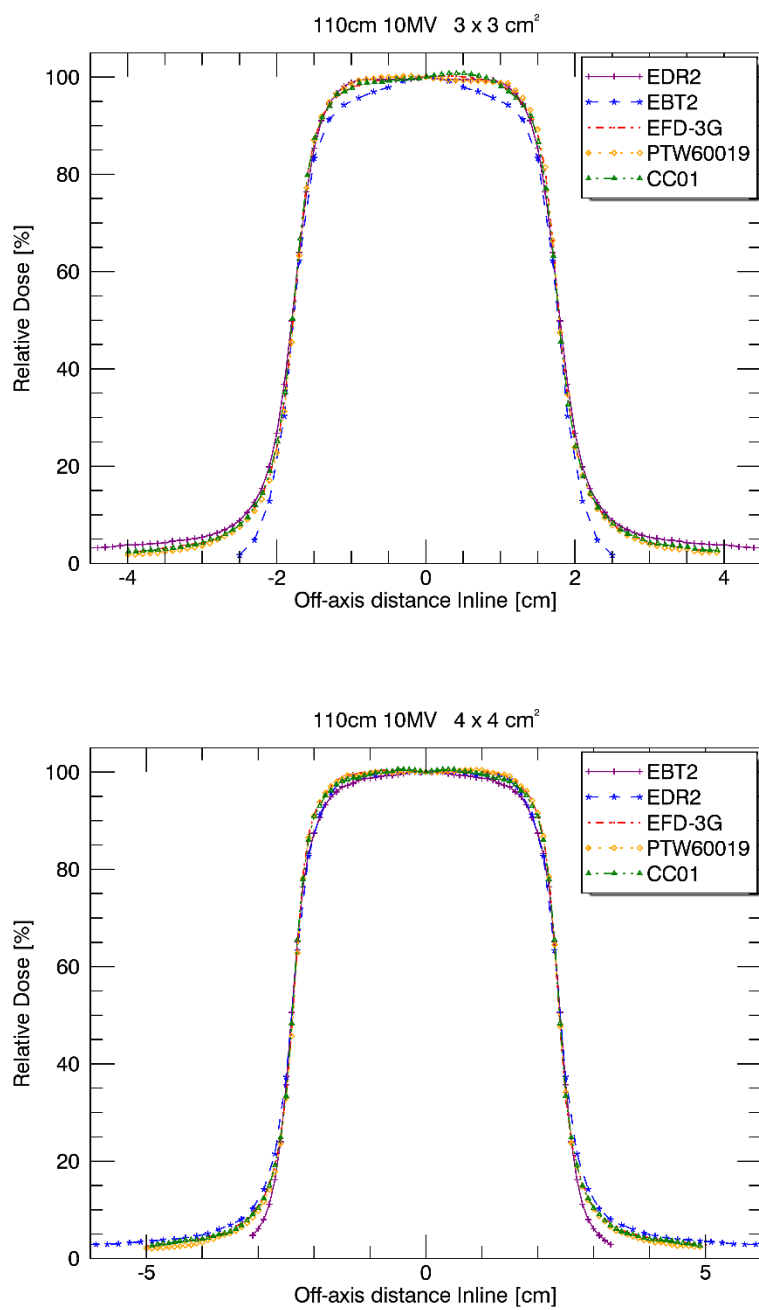


Figure 98. Inline profiles for the 3x3 cm² and 4x4 cm² measured at an SSD of 110 cm and 10 cm depth in water using a 10 MV photon beam

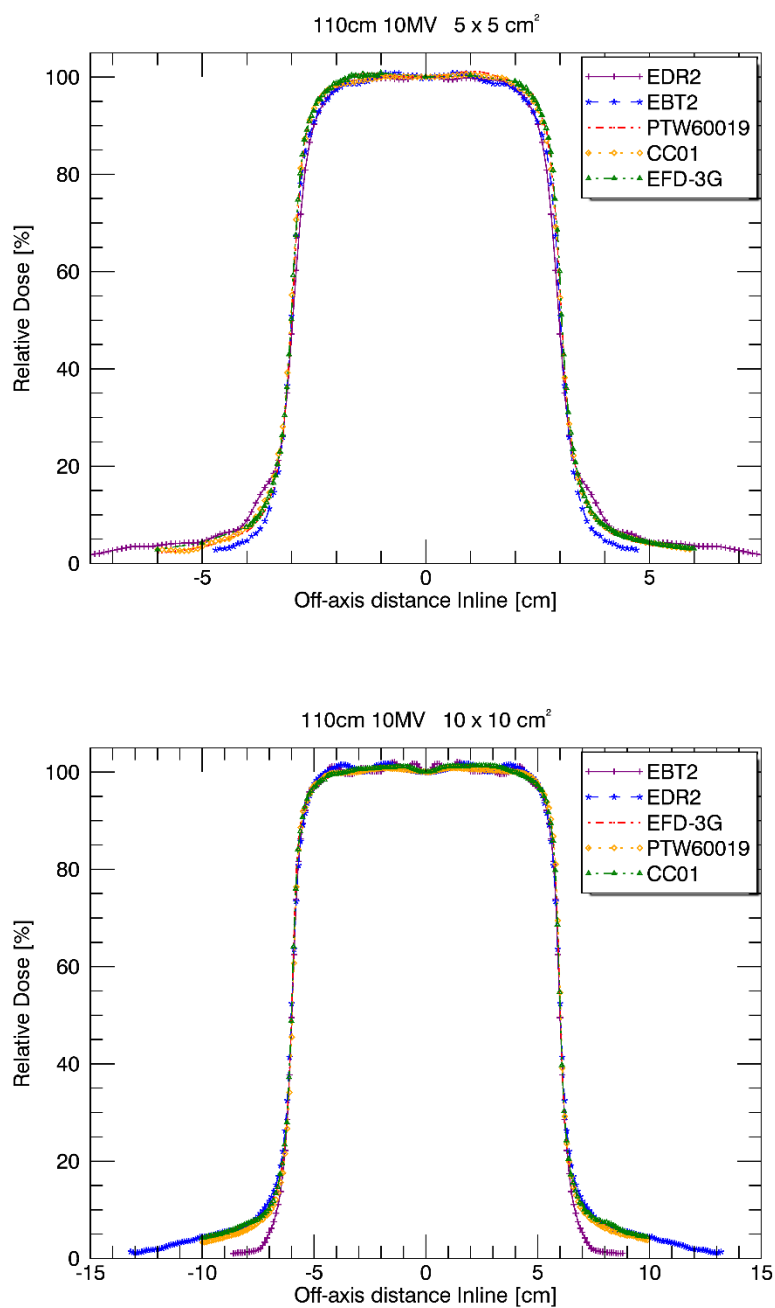


Figure 99. Inline profiles for the 5x5 cm² and 10x10 cm² measured at an SSD of 110 cm and 10 cm depth in water using a 10 MV photon beam

110 cm 15 MV Crossline

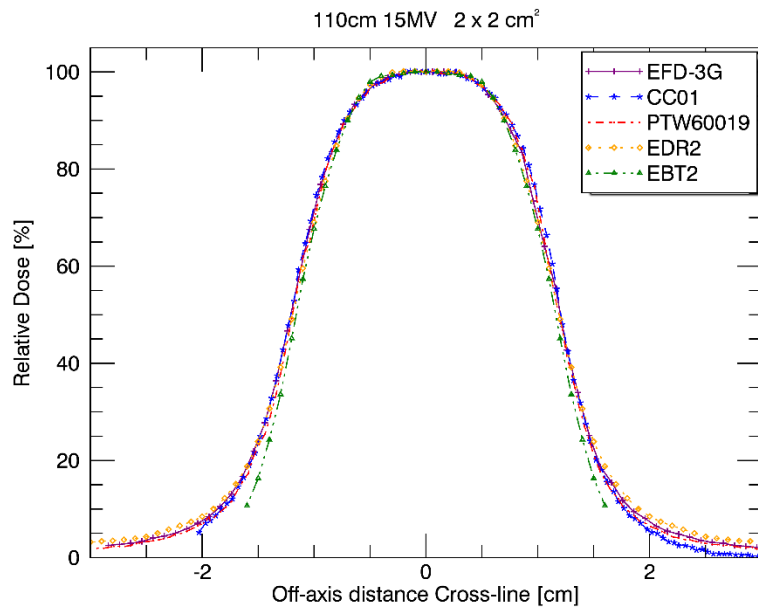
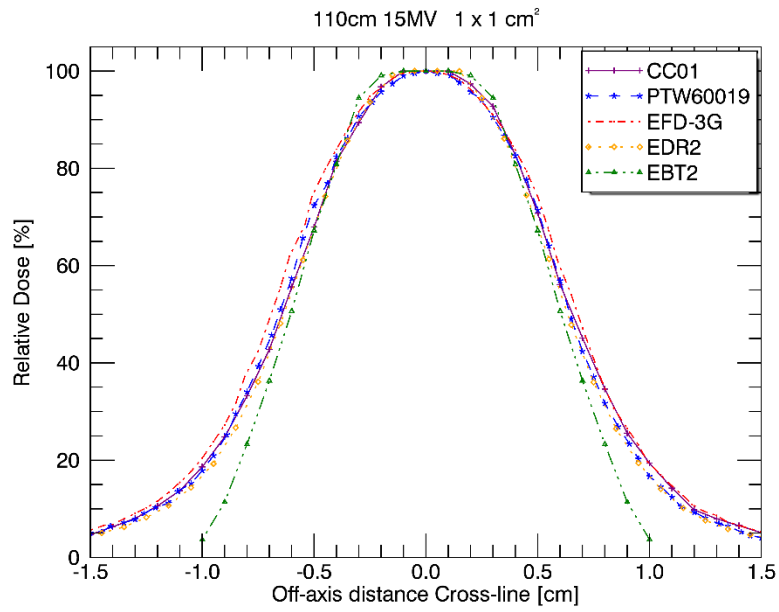


Figure 100. Crossline profiles for the 1x1 cm² and 2x2 cm² measured at an SSD of 110 cm and 10 cm depth in water using a 15 MV photon beam

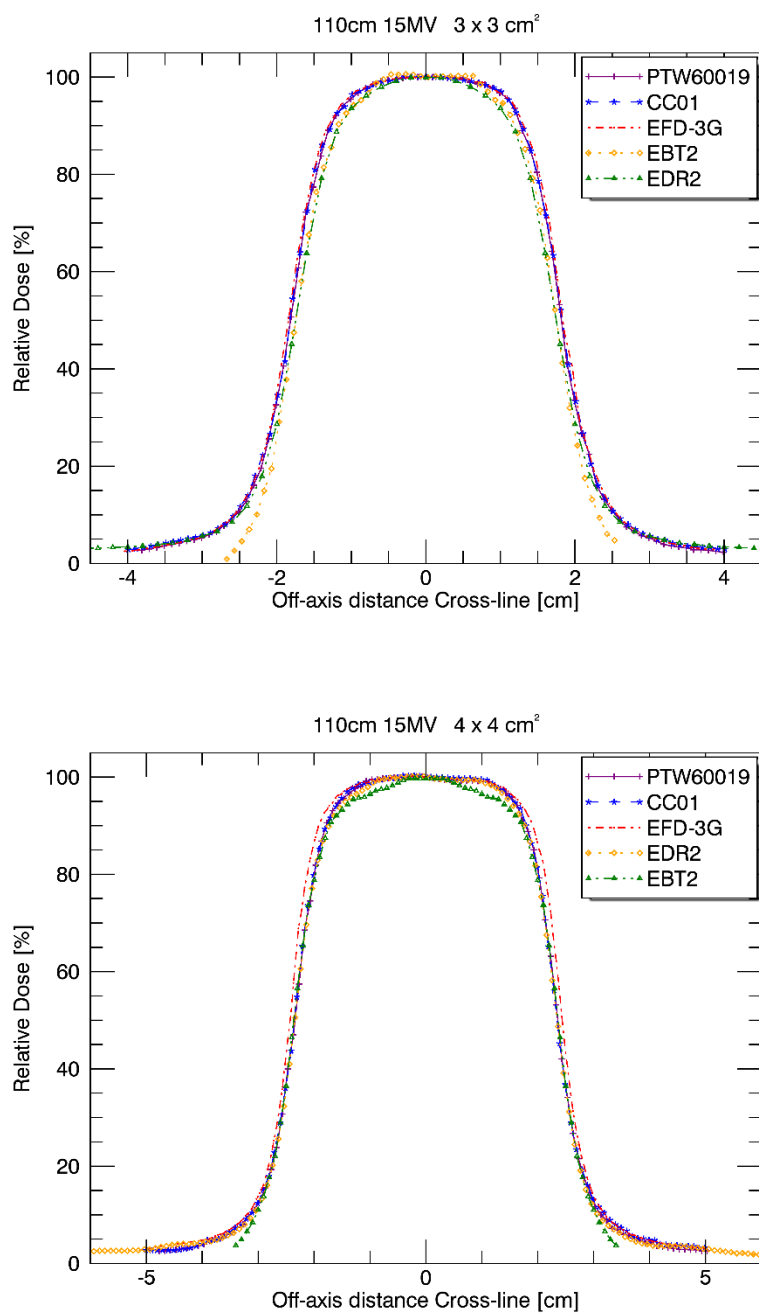


Figure 101. Crossline profiles for the $3 \times 3 \text{ cm}^2$ and $4 \times 4 \text{ cm}^2$ measured at an SSD of 110 cm and 10 cm depth in water using a 15 MV photon beam

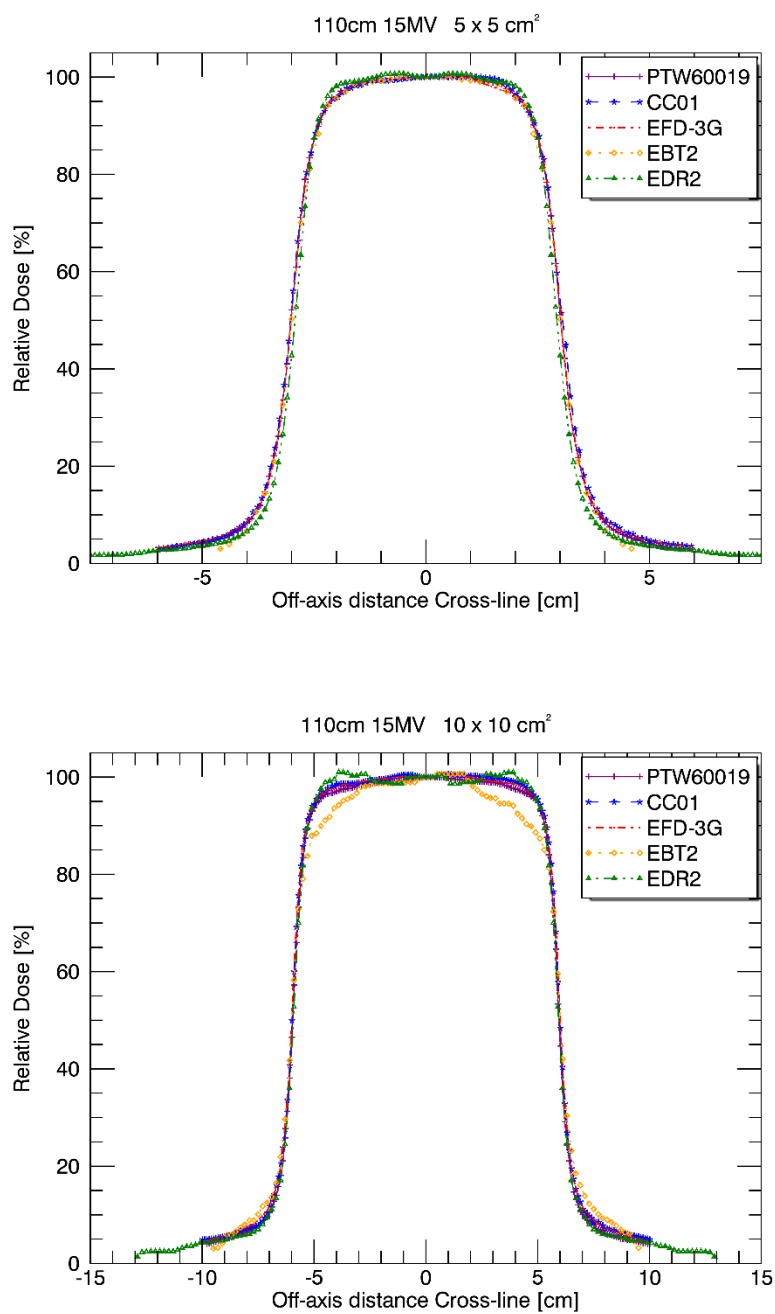


Figure 102. Crossline profiles for the $5 \times 5 \text{ cm}^2$ and $10 \times 10 \text{ cm}^2$ measured at an SSD of 110 cm and 10 cm depth in water using a 15 MV photon beam

110 cm 15 MV Inline

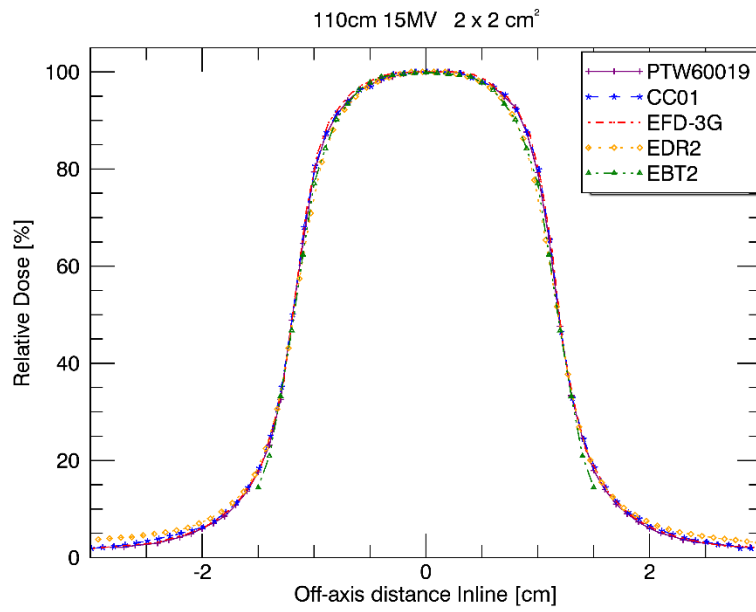
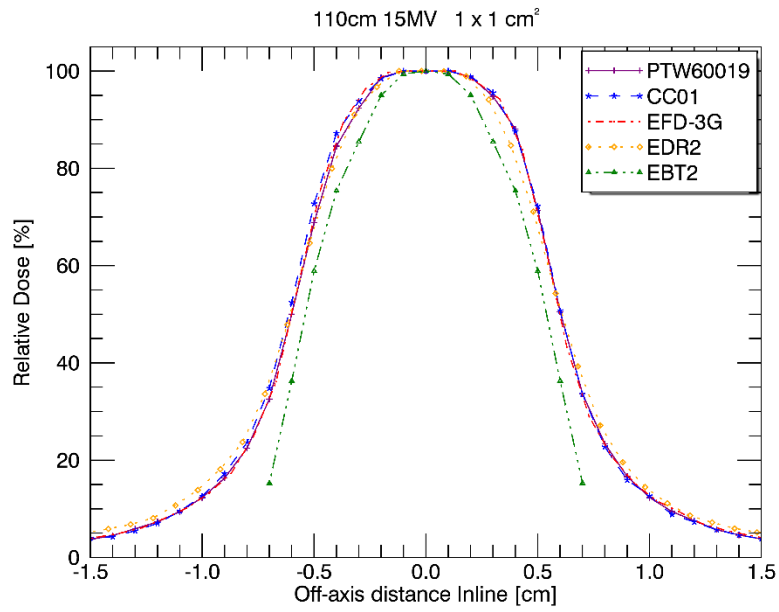


Figure 103. Inline profiles for the 1x1 cm² and 2x2 cm² measured at an SSD of 110 cm and 10 cm depth in water using a 15 MV photon beam

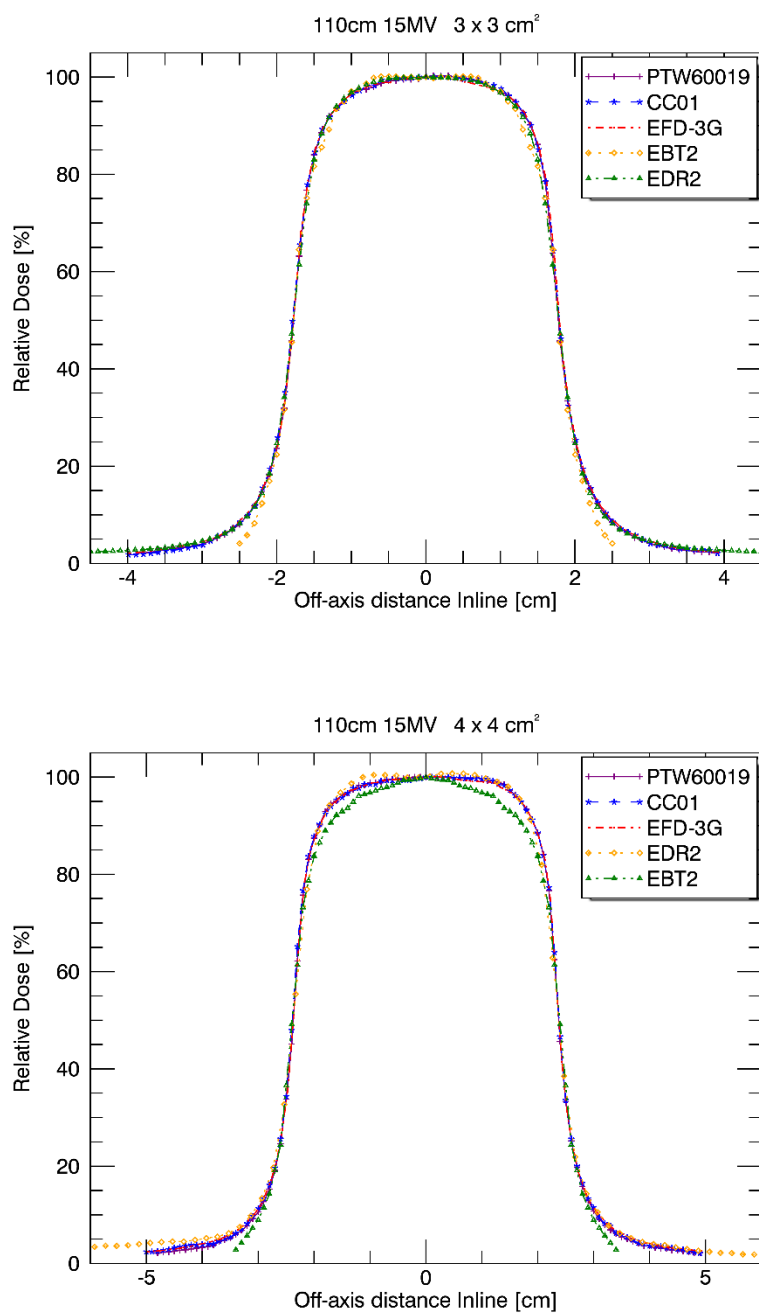


Figure 104. Inline profiles for the $3 \times 3 \text{ cm}^2$ and $4 \times 4 \text{ cm}^2$ measured at an SSD of 110 cm and 10 cm depth in water using a 15 MV photon beam

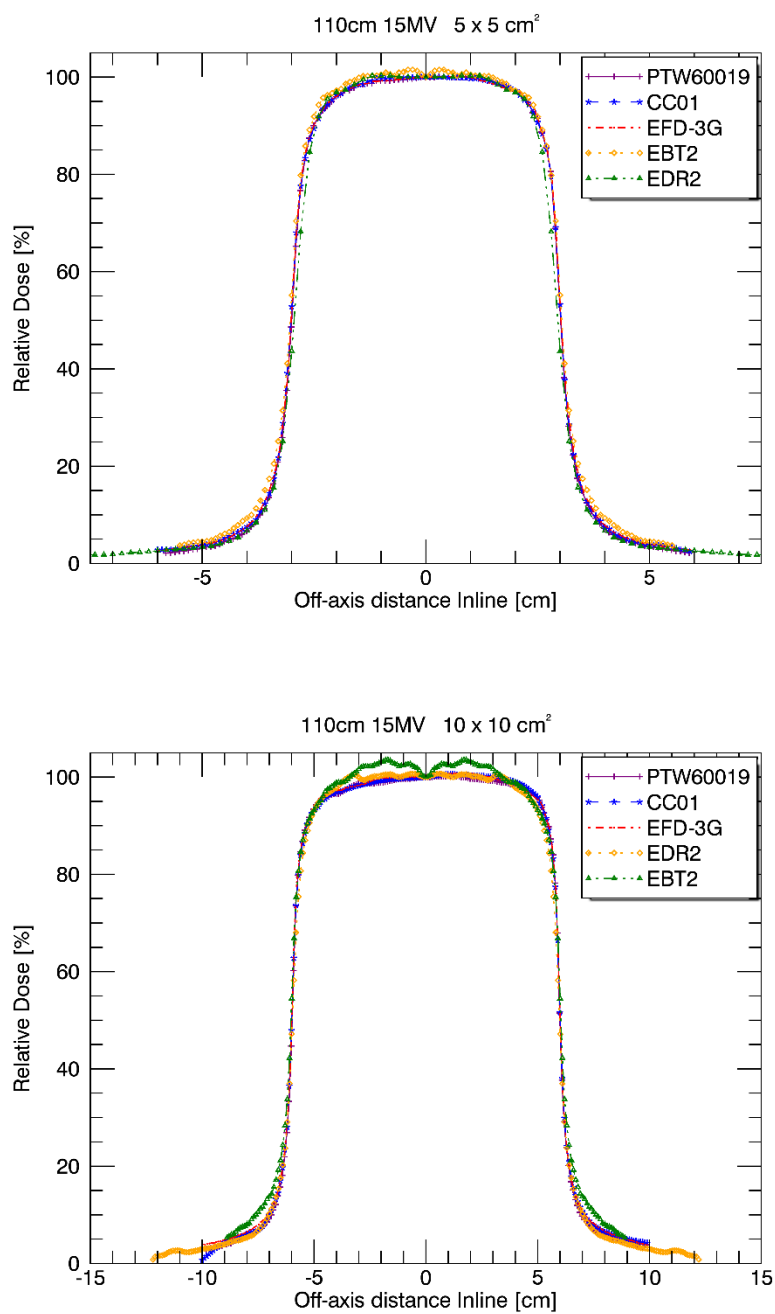


Figure 105. Inline profiles for the 5x5 cm² and 10x10 cm² measured at an SSD of 110 cm and 10 cm depth in water using a 15 MV photon beam

4.3 Percentage depth dose

The PDD as mentioned in chapter 2, indicates the change in the deposited dose on the CAX within the medium from the surface until the beam exits the medium. The measured dose is a contribution from the primary beam, and the radiation scattering back into the central axis. The scatter will decrease as the field size decreases. As a result, the depth dose curve will fall at a higher rate compared to larger fields.

The films were scanned and converted to dose using their respective calibration curves as explained in section 4.1. The results were then imported into the OmniPro® software, to merge with the other detectors.

The data smoothing was carried out using the spline algorithm available within the Omnipro® software. The interpolation was carried out using the above-mentioned spline algorithm with an interpolation step width of 0.5 mm. The step width chosen was the same as that used for the water-based detectors. The least squares smoothing was used as it does not change the depth of maximum dose (D_{max}) and also does not influence the slope of the PDD curve.

The scanning artefacts for the EBT2 film, are either due to the film not lying flat on the glass panel or due to the smooth surface, since the film will start to attach itself to the glass panel resulting in Newton ring artefacts. The dust or fingerprints on the film decrease the Newton ring artefacts. The influence of dust or fingerprints can be mediated through use of a multichannel dosimetry (Lewis et al., 2012).

In the case of the EDR2, the present artefacts are the processor added roller marks during development and water stains were left on the films, these affected the results of artificial increasing the OD which resulted in the bumps seen in some of the scans (Roberson, Moran, & Kulasekere, 2008) as seen in figure 106 and figure 107, and this can only be fixed by manually developing the films instead of using an automatic processor. The manual processing was not considered due to the number of films. At the end smoothing of data was chosen as it decreased handling time of the films.

The option of developing the film in the other direction was not available due to the thickness being shorter than the gaps in between rollers. Thus, would not roll fully through the developer. Another problem that could arise is that the pressure artefact might be along the length of the film instead of being across.

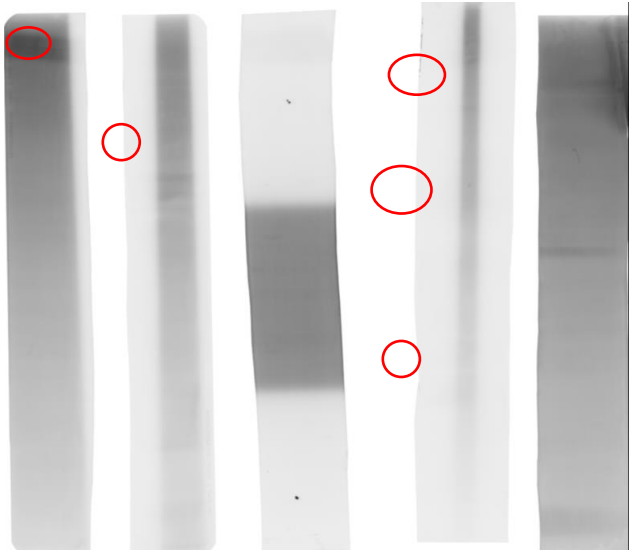


Figure 106. EDR2 film, encircled ROI illustrates the roller marks artefact

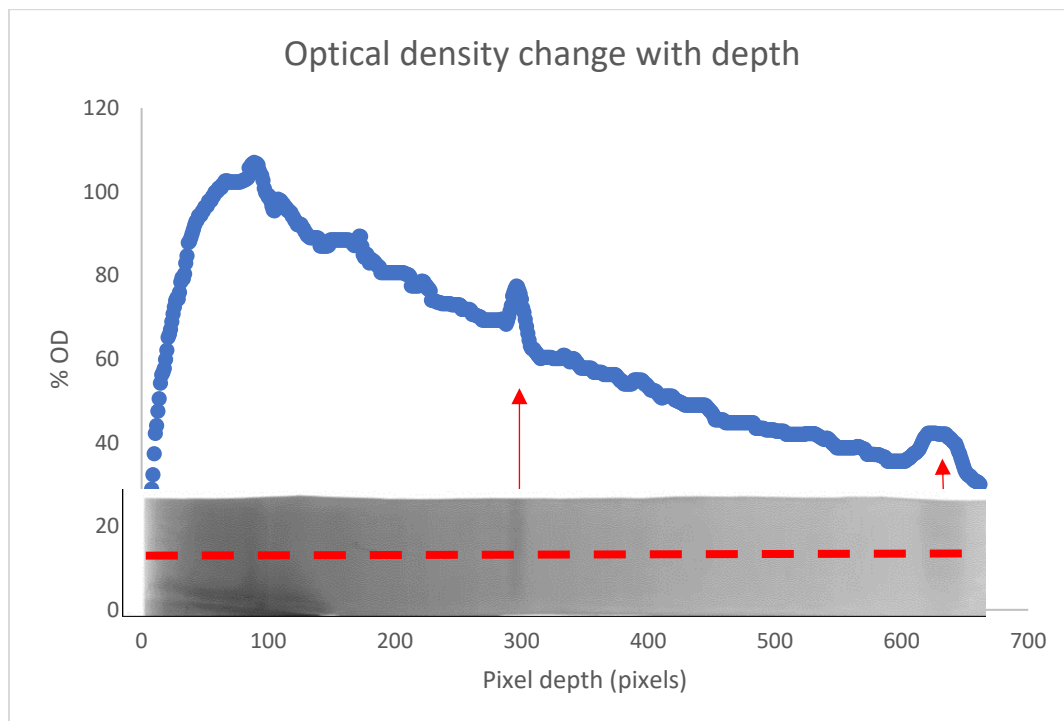


Figure 107. The influence of the processor artefact on the OD

The curves were normalised at 5 cm depth, most of the artefacts seen above were at 10 cm depth but these were present at other depths. Figures 110- 144 represent the PDD's measured with different detectors at each field size. There are two ways in which the data could have been presented and these are shown as examples, Figure 108, shows the comparison of PDD with changing energy for a 10×10 cm² field size measured with a PTW60019 microdiamond detector for a certain SSD, and figure 60 indicates the shift in the PDD as the SSD is increased for the same detector as well as the same energy.

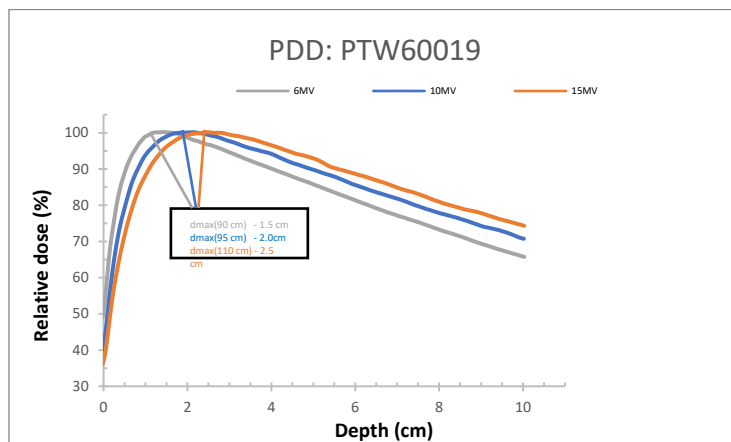


Figure 108. PDD change with energy

The Dmax is influenced by the incoming fluence, be it photons or scattered electrons as well as the field size. This position points to the deepest depth where the most energetic electron ejected from the surface can travel, this distance increases as the initial kinetic energy of the ejected electron increases, i.e. when the energy of the incident photons increases as seen from the results in figure 109.

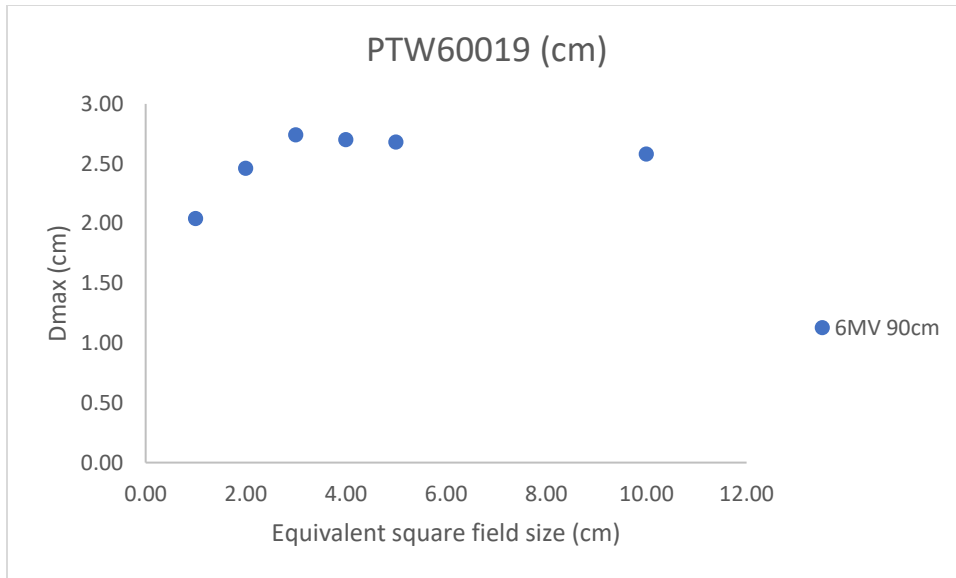


Figure 109. Dmax change with field size

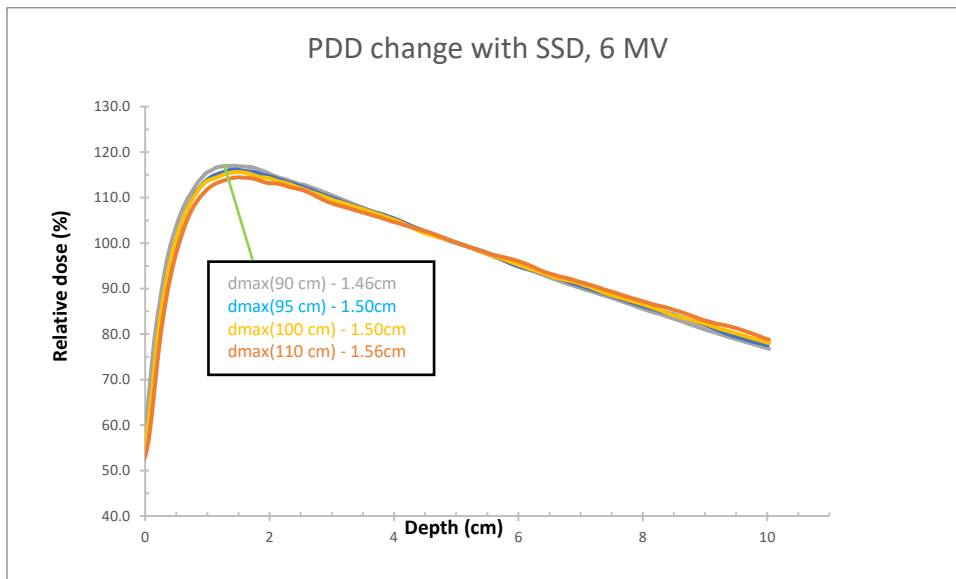


Figure 110. PDD change with SSD

The above figure shows that as the SSD increases the Dmax increases as expected for a 6 MV photon beam, the increase for the different is estimated by equation 4-8,

$$d_{max} = \left(\frac{\log(FS) + d(FS = 1)}{\sqrt[3]{FS}} \right) \quad (4-7)$$

Where, FS is the field size, and d is the d_{max} for the $1 \times 1 \text{ cm}^2$ field size. The

There is a 7% increase in D_{max} as the SSD shifts from 90 cm to 110 cm. The decrease of peak is due to the increase of the reference dose at deeper depths due to the inverse square law.

4.3.1 PDDs measured at an SSD of 90 cm

Figures 110- 119 show the PDD curves obtained at an SSD of 90 cm. The $1 \times 1 \text{ cm}^2$ field size shows that the curves for the different detectors are similar up to a depth of 7cm, then the PDD curves measured using films deviate from those measured using the water tank. The difference arises due to the difference in the setup, as the gantry is tilted 2° for the film measurements, and is placed at 0° for the water phantom measurements, the difference is accentuated at the $1 \times 1 \text{ cm}^2$ field. The smaller field size deviates away from the film due to the tilt, thus dose is not deposited further down on the films.

90 cm 6 MV PDD

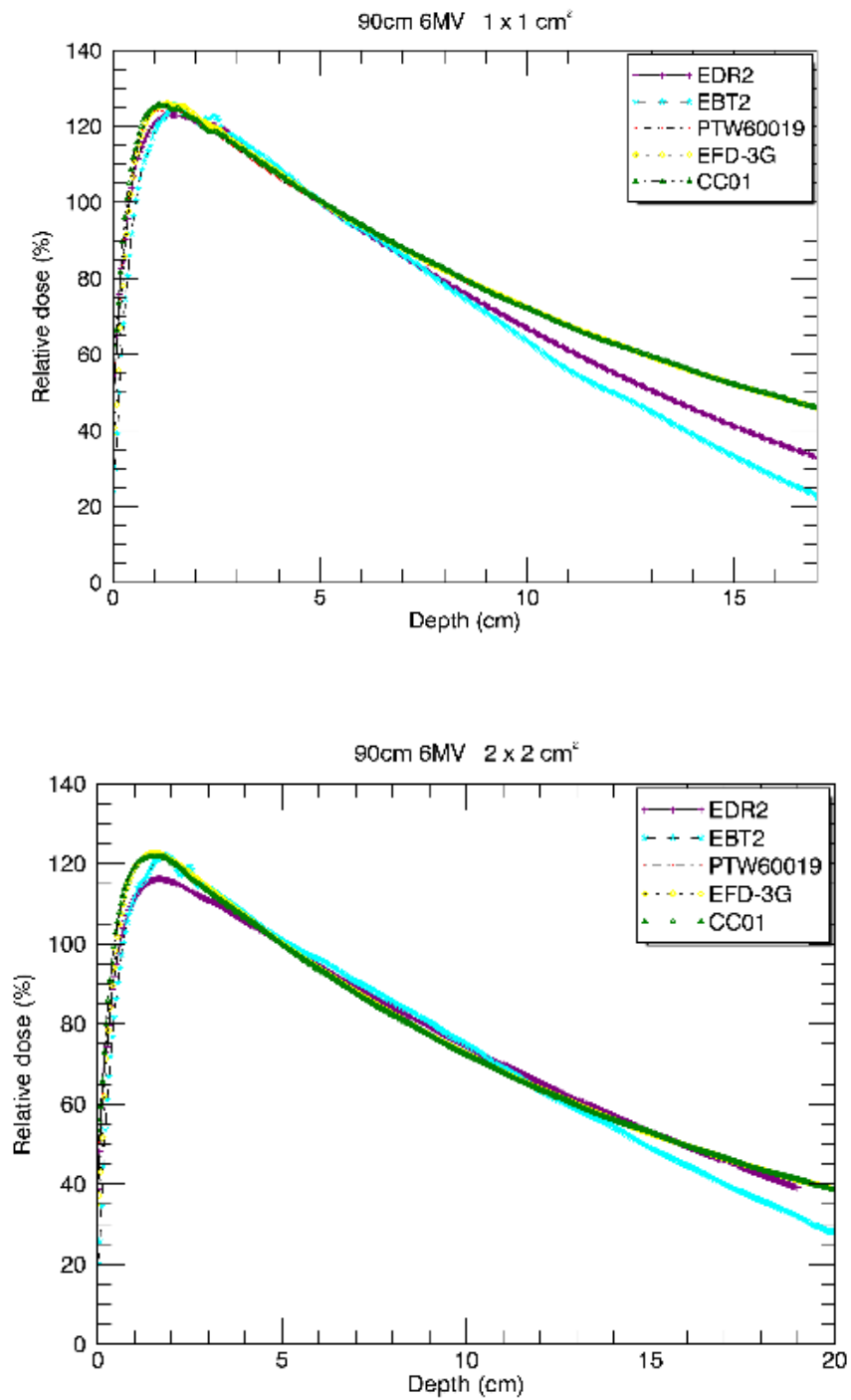


Figure 111. PDD curves for the different detectors measured at an SSD of 90 cm using a 6 MV photon beam for 1x1 cm² and 2x2 cm² field sizes

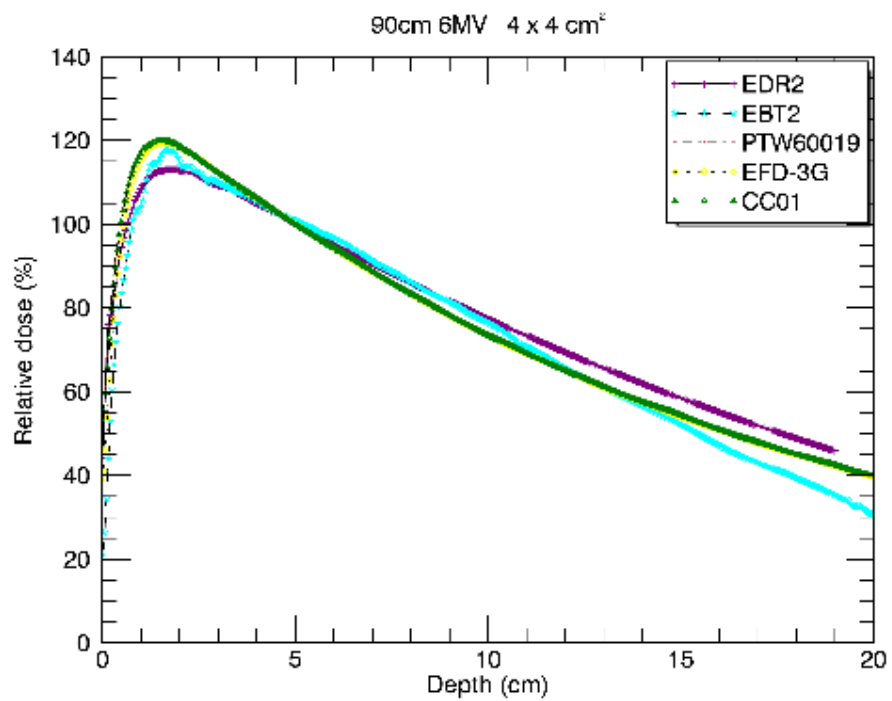
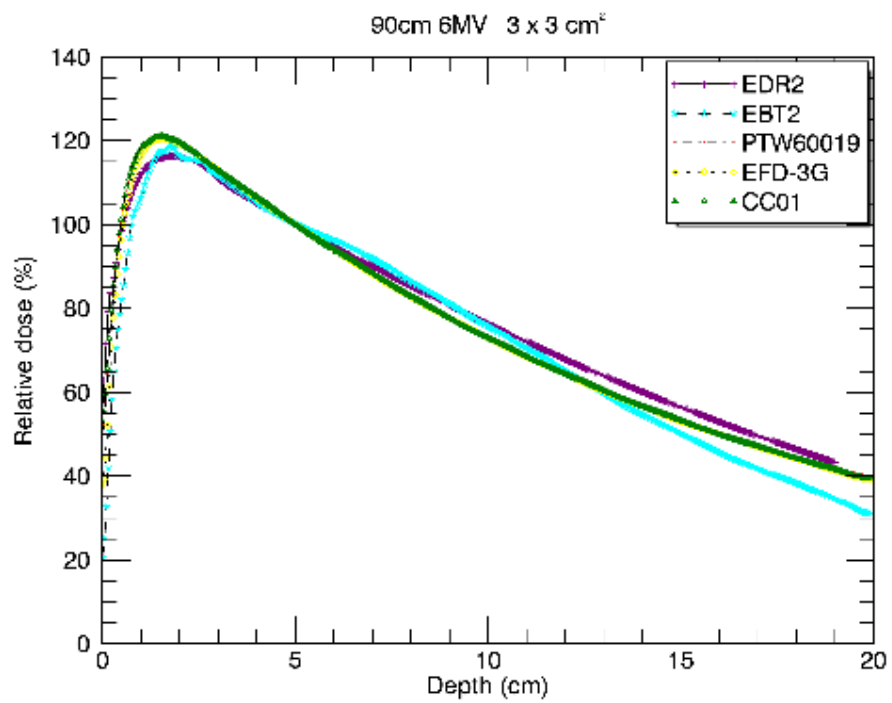


Figure 112. PDD curves for the different detectors measured at an SSD of 90 cm using a 6 MV photon beam for 3x3 cm² and 4x4 cm² field sizes

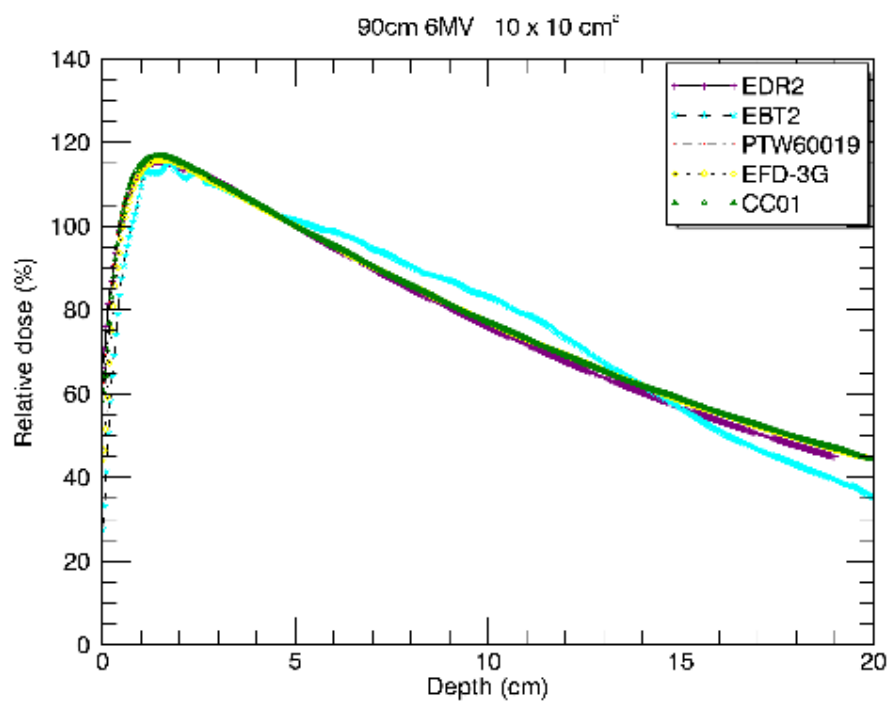
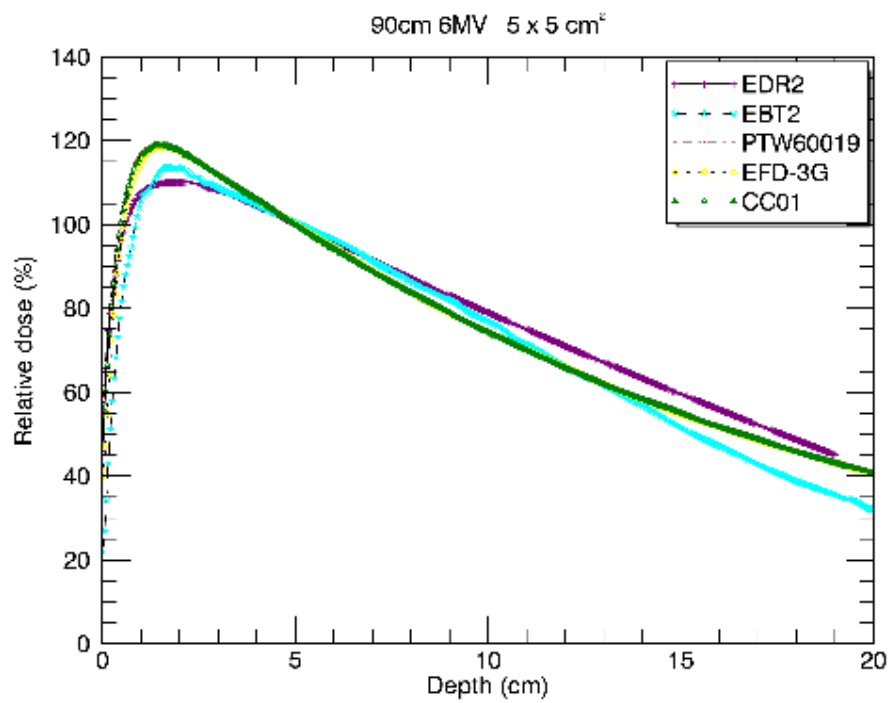


Figure 113 PDD curves for the different detectors measured at an SSD of 90 cm using a 6 MV photon beam for 5x5 cm² and 10x10 cm² field sizes

90 cm 10 MV PDD

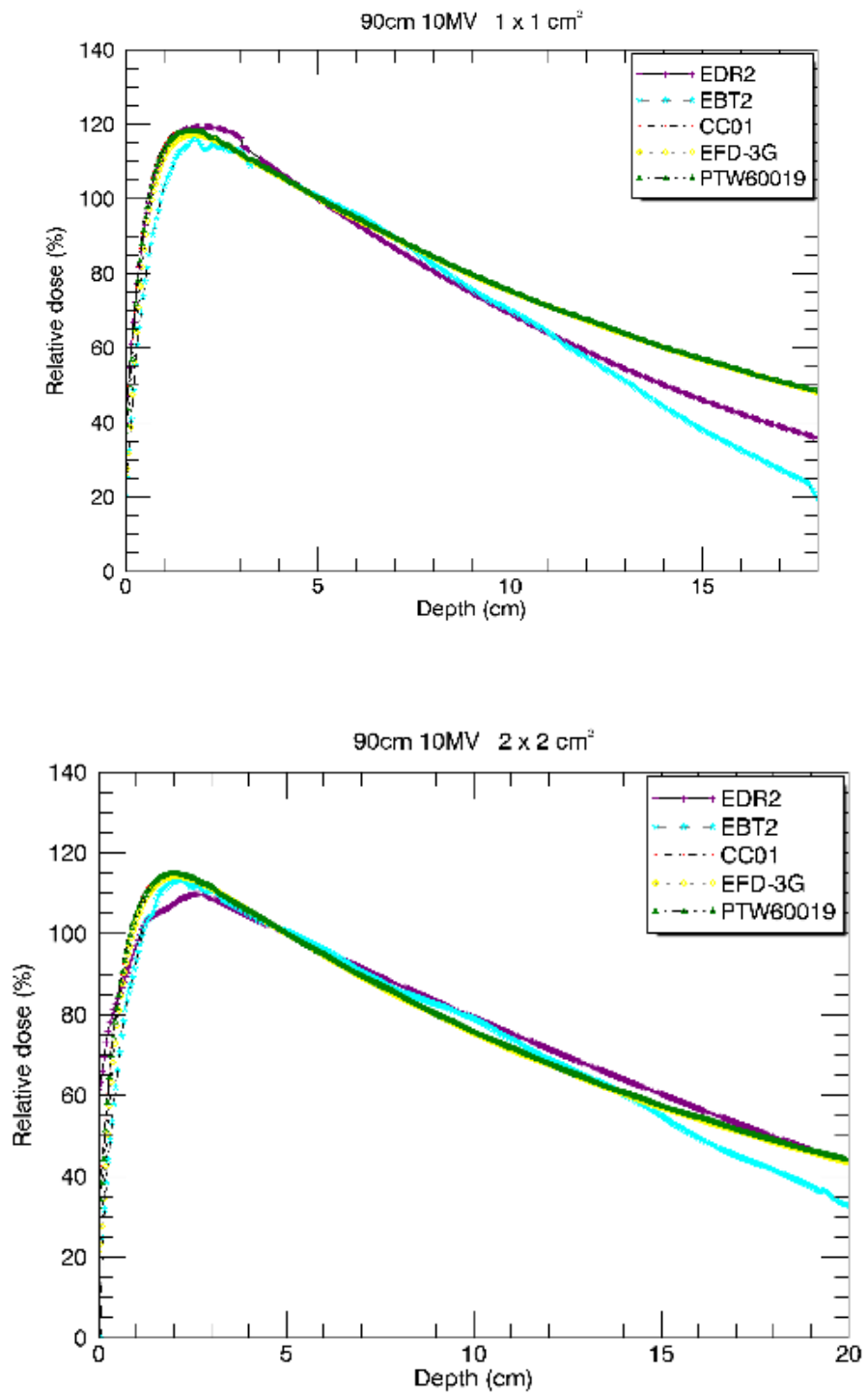


Figure 114. PDD curves for the different detectors measured at an SSD of 90 cm using a 10 MV photon beam for 1x1 cm² and 2x2 cm² field sizes

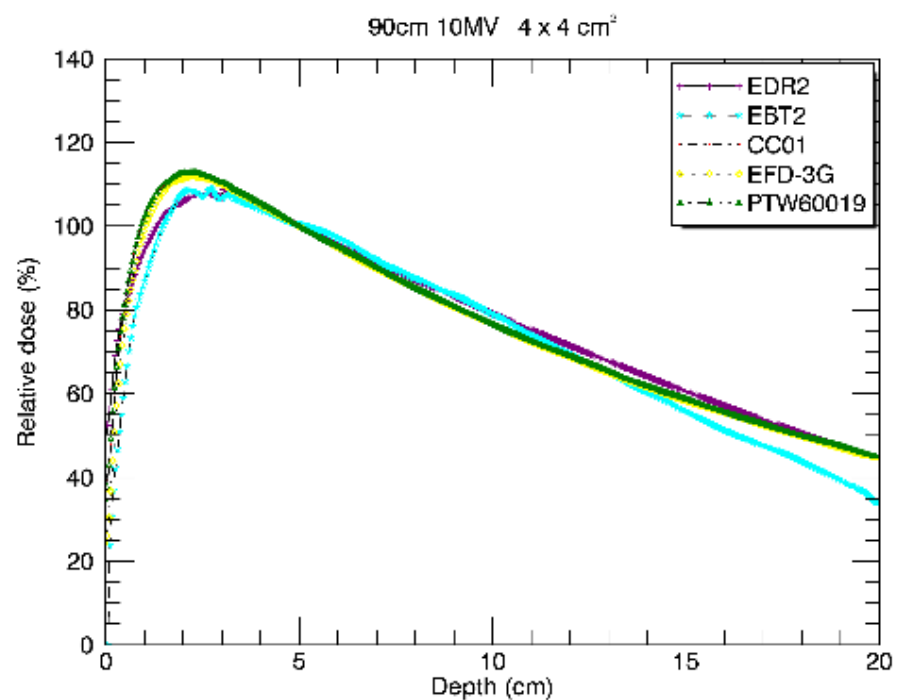
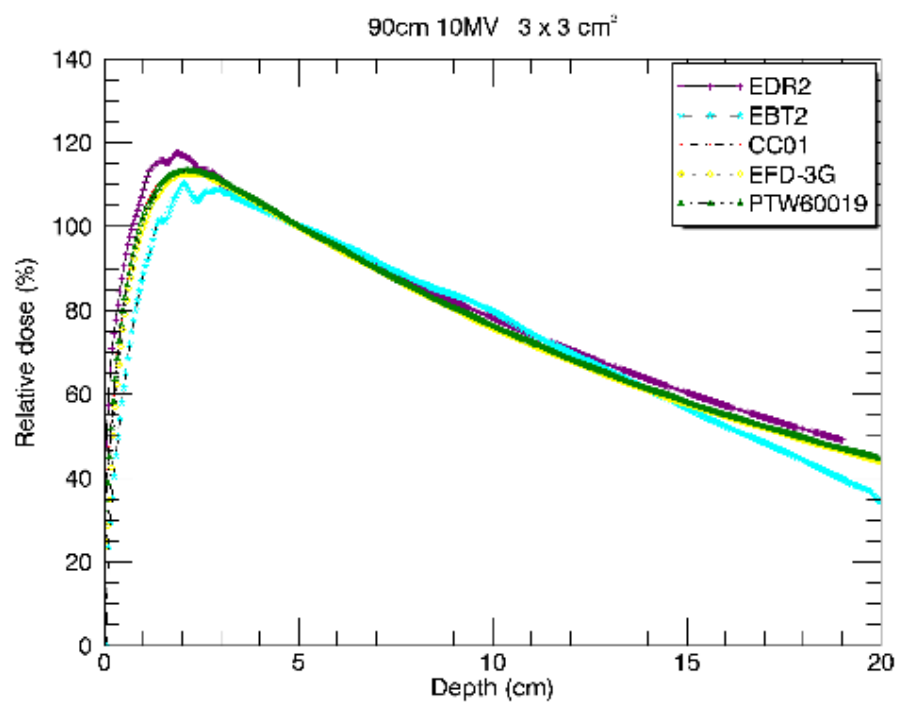


Figure 115. PDD curves for the different detectors measured at an SSD of 90 cm using a 10 MV photon beam for 3x3 cm² and 4x4 cm² field sizes

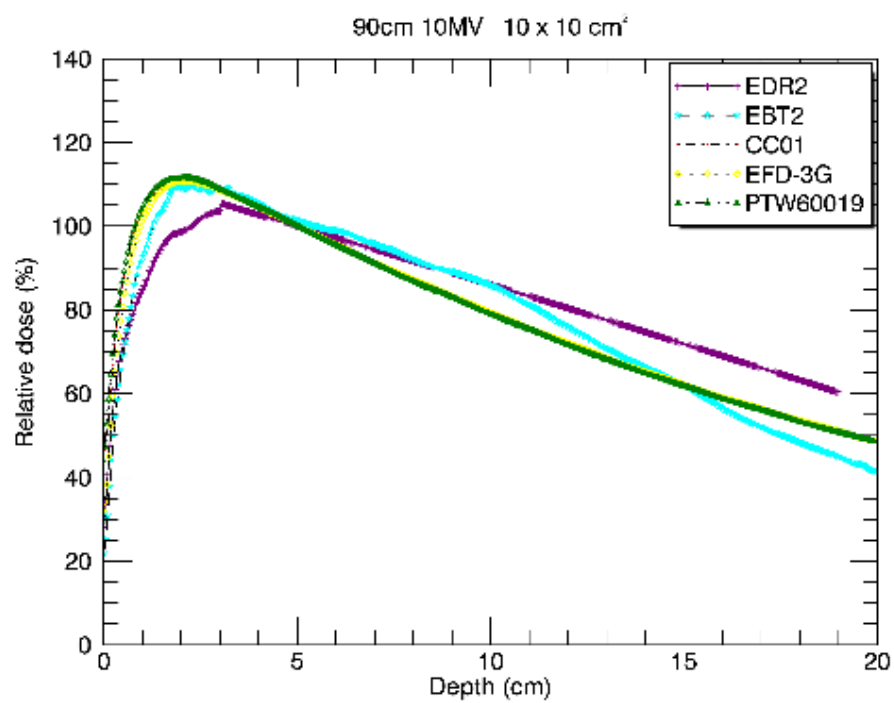
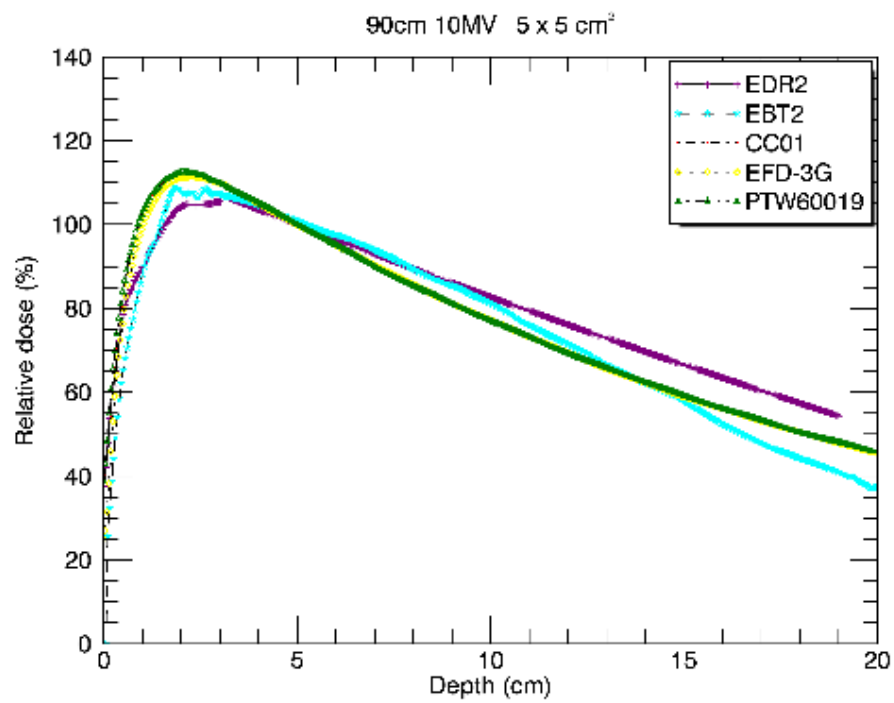


Figure 116. PDD curves for the different detectors measured at an SSD of 90 cm using a 10 MV photon beam for 5x5 cm² and 10x10 cm² field sizes

90 cm 15 MV PDD

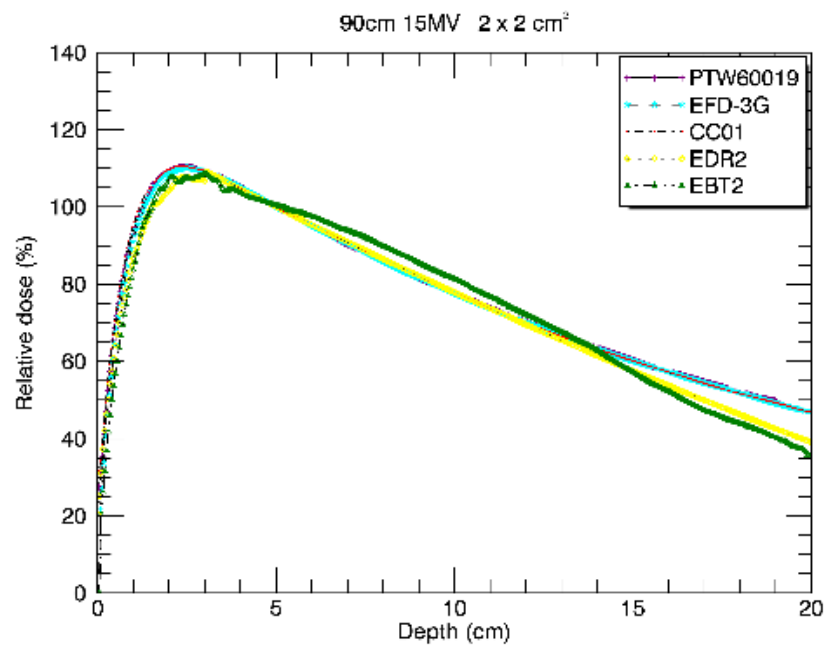
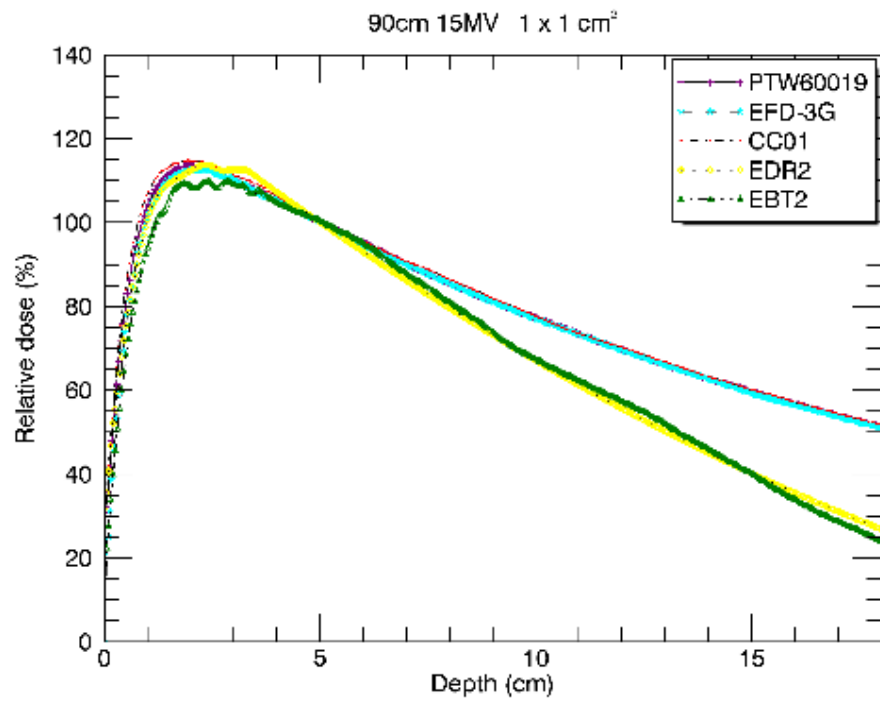


Figure 117. PDD curves for the different detectors measured at an SSD of 90 cm using a 15 MV photon beam for 1x1 cm² and 2x2 cm² field sizes

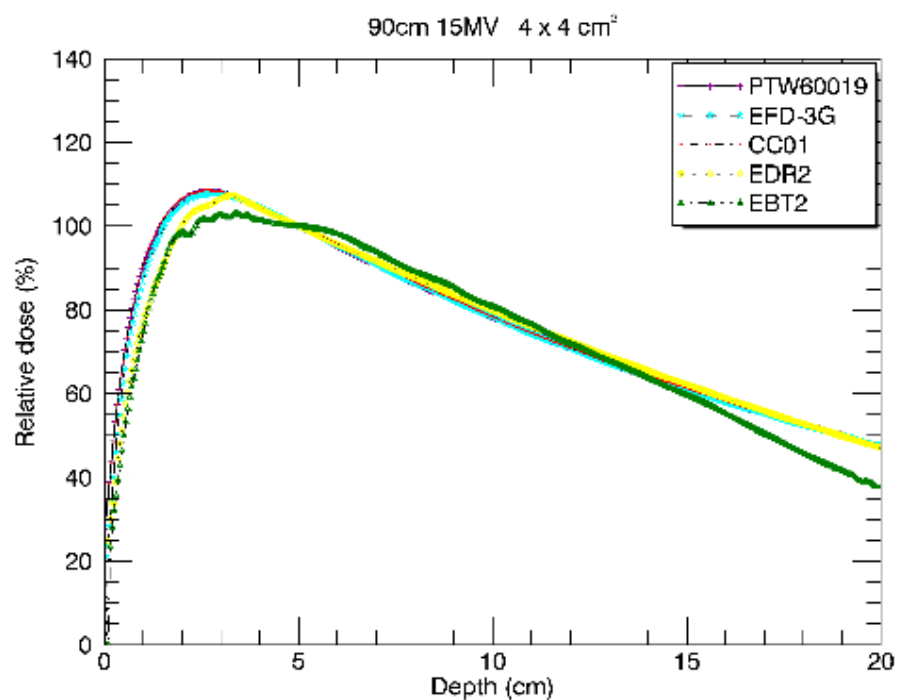
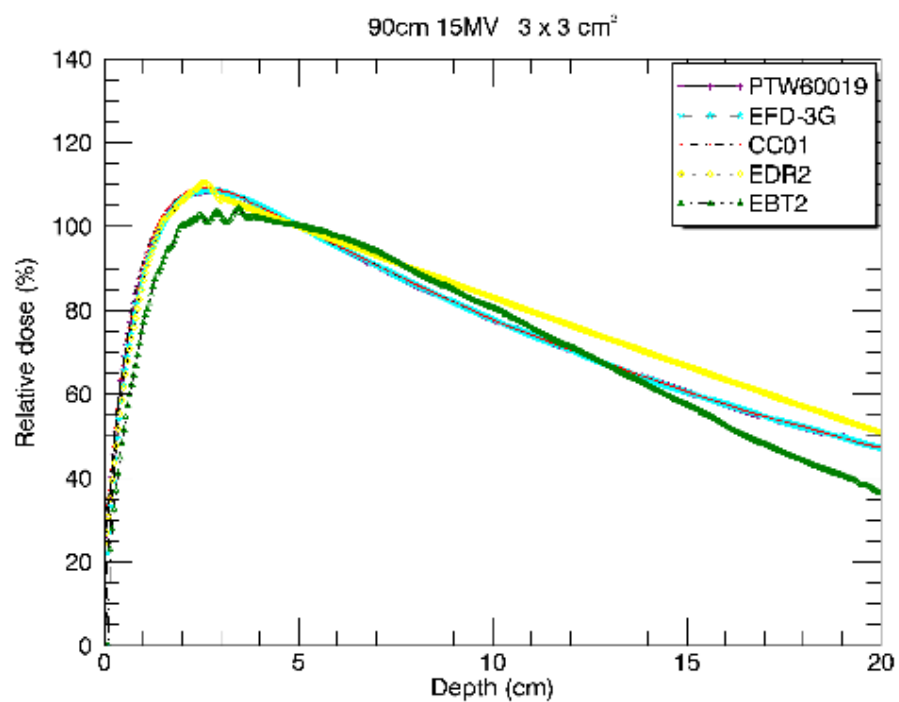


Figure 118. PDD curves for the different detectors measured at an SSD of 90 cm using a 15 MV photon beam for 3x3 cm² and 4x4 cm² field sizes

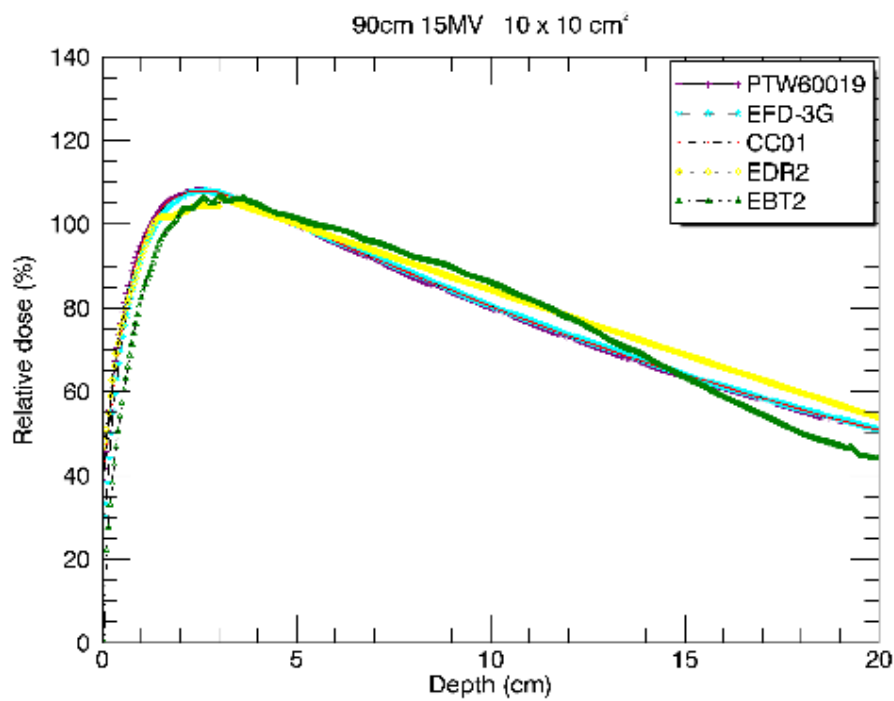
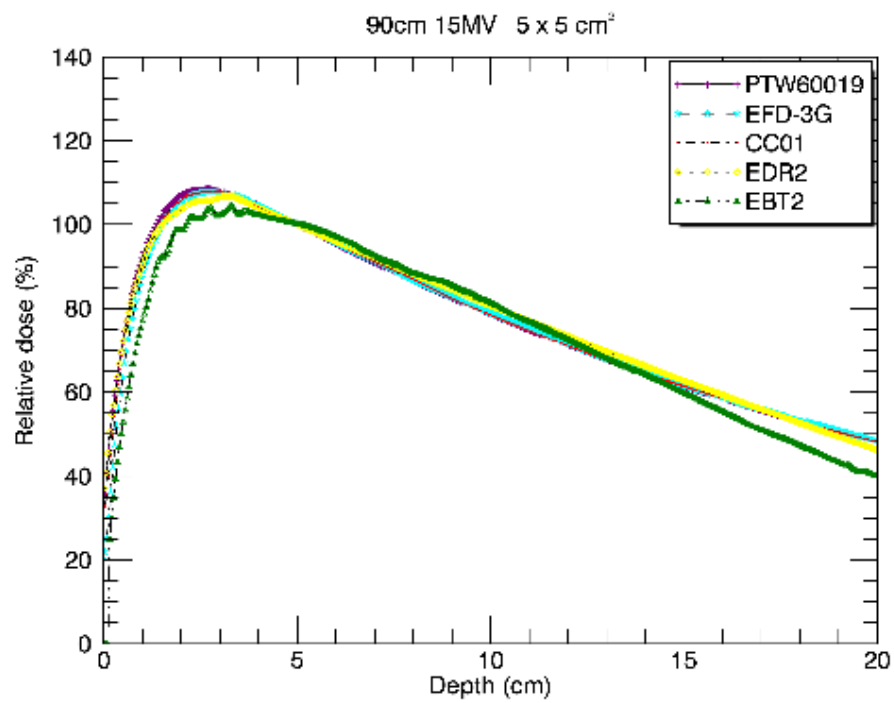


Figure 119. PDD curves for the different detectors measured at an SSD of 90 cm using a 15 MV photon beam for 5x5 cm² and 10x10 cm² field sizes

Table 7. Dmax positions for the different detectors measured at 90 cm SSD

Dmax							
90cm	6MV						
Field side length (cm)	Mean dmax (cm)	Stddev of Dmax	CC01 (cm)	EFD-3G (cm)	PTW60019 (cm)	EBT2 (cm)	EDR2 (cm)
1.00	1.39	0.11	1.24	1.38	1.35	1.54	1.46
2.00	1.62	0.12	1.54	1.56	1.52	1.80	1.70
3.00	1.65	0.13	1.54	1.60	1.54	1.74	1.82
4.00	1.64	0.11	1.56	1.62	1.54	1.70	1.80
5.00	1.72	0.25	1.54	1.60	1.50	1.84	2.10
10.00	1.54	0.09	1.50	1.58	1.46	1.68	1.50
Dmax							
90cm	10MV						
Field side length (cm)	Mean dmax (cm)	Stddev of Dmax	CC01 (cm)	EFD-3G (cm)	PTW60019 (cm)	EBT2 (cm)	EDR2 (cm)
1.00	1.84	0.26	1.59	1.80	1.71	1.84	2.28
2.00	2.18	0.25	2.00	2.10	2.02	2.16	2.60
3.00	2.27	0.38	2.14	2.24	2.16	2.92	1.90
4.00	2.30	0.17	2.12	2.28	2.20	2.30	2.58
5.00	2.39	0.48	2.19	2.28	2.14	2.08	3.24
10.00	2.38	0.57	2.12	2.14	2.03	2.20	3.40
Dmax							
90cm	15MV						
Field side length (cm)	Mean dmax (cm)	Stddev of Dmax	CC01 (cm)	EFD-3G (cm)	PTW60019 (cm)	EBT2 (cm)	EDR2 (cm)
1.00	2.29	0.31	1.98	2.34	2.04	2.76	2.34
2.00	2.56	0.19	2.40	2.56	2.46	2.88	2.52
3.00	2.81	0.38	2.61	2.70	2.74	3.48	2.54
4.00	2.95	0.31	2.70	2.80	2.70	3.34	3.22
5.00	2.83	0.28	2.76	2.76	2.68	3.32	2.64
10.00	2.70	0.21	2.52	2.64	2.58	3.06	2.68

Dmax is one of the factors that are used to describe the characteristics of a PDD. It is defined as the depth of maximum dose deposition. The dose deposited at this depth is composed of electrons released by the primary beam as well as electrons from the scattered radiation, it is dependent on the incoming photon energy as well as the field size.

The Dmax increases from 1×1 cm² to 2×2 cm² for the 6 MV and 10 MV, whilst the Dmax still increases up to 3×3 cm² for the 15 MV beam as shown in table 8. This can be explained by the lateral electronic disequilibrium, as suggested by Li et al. (Li et al., 1995), the minimum equivalent square field size required to maintain lateral equilibrium is 2.6×2.6 cm² (radius of 1.3), 3.4×3.4 cm² (radius of 1.7) and 3.8×3.8 cm² (radius of 1.9) in water for 6 MV, 10 MV and 15 MV respectively. At field sizes that are greater than the minimum field size required for LEE, Dmax starts to shift towards the surface due to the increase of electron scatter.

4.3.2 PDDs measured at an SSD of 95 cm

The figures 120 - 128 show the PDD curves obtained at an SSD of 95 cm, the curves were smoothed and normalized at 5 cm depth. The 1×1 cm² field size shows the same effect of gantry tilting as shown before. There is a decrease of the build-up region for the EDR2 film at the 2×2 cm², 3×3 cm² and 10×10 cm² field sizes for the 6 MV photon beam. The same effect is seen for the 10 MV photon beam at the 3×3 cm², 4×5 cm² and 10×10 cm² field sizes. A processor artefact is seen at the build-up region of the 5×5 cm² field size for the 10 MV photon beam.

The table 9 shows the variation of Dmax with different detectors at a certain field size for at an SSD of 95 cm. The EDR2 film shows deeper Dmax positions for each field size when compared to other detectors, but this can be attributed to the artefacts that were evident on the film. The resulting Dmax values similar to that seen in table 8.

95 cm 6 MV PDD

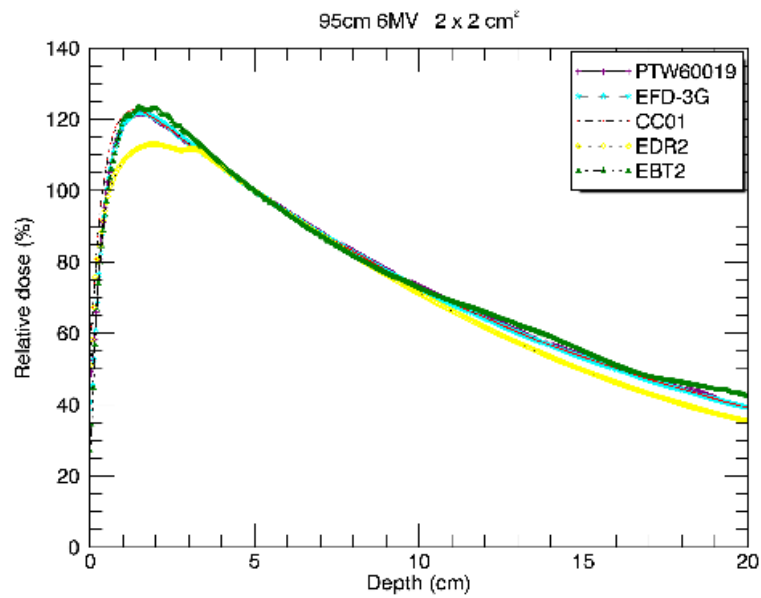
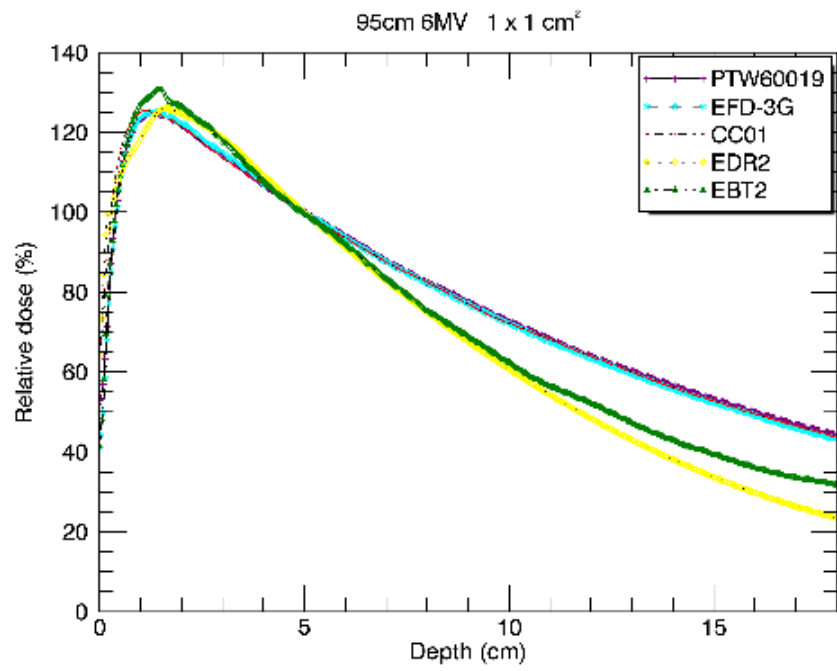


Figure 120. PDD curves for the different detectors measured at an SSD of 95 cm using a 6 MV photon beam for 1x1 cm² and 2x2 cm² field sizes

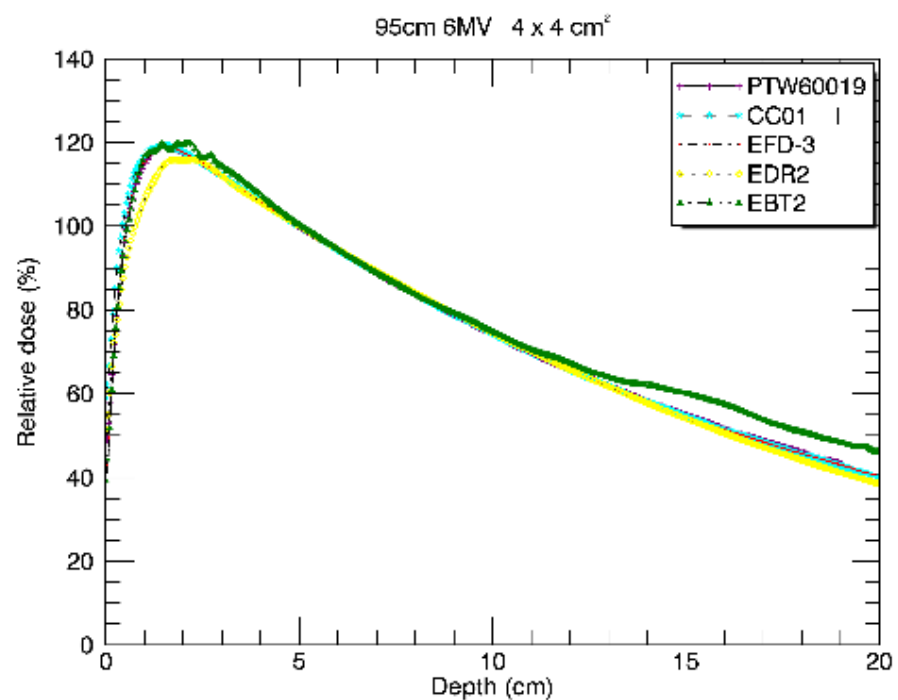
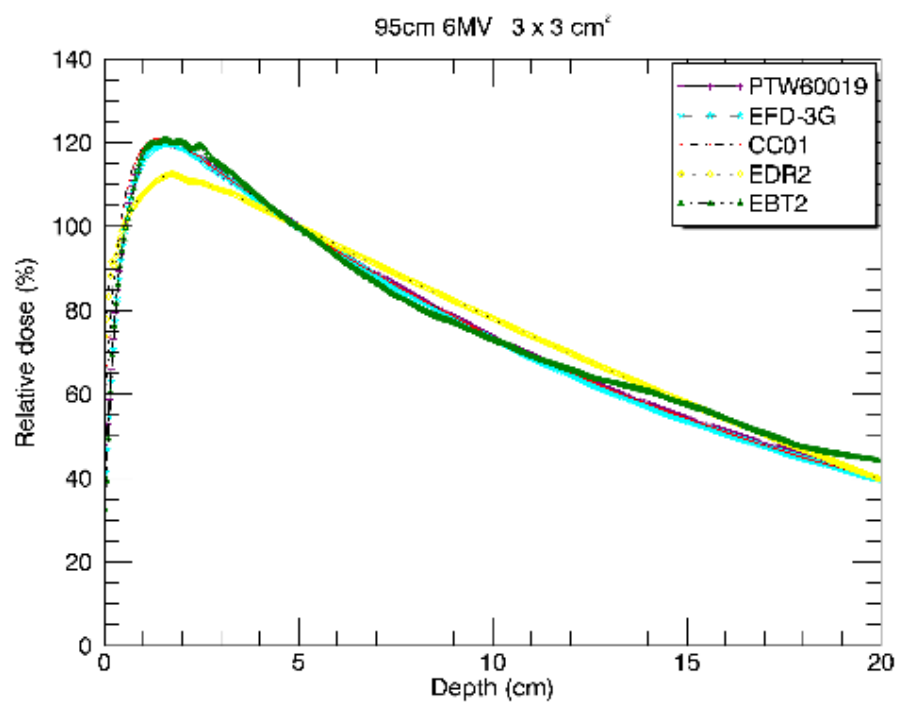


Figure 121. PDD curves for the different detectors measured at an SSD of 95 cm using a 6 MV photon beam for 3x3 cm² and 4x4 cm² field sizes

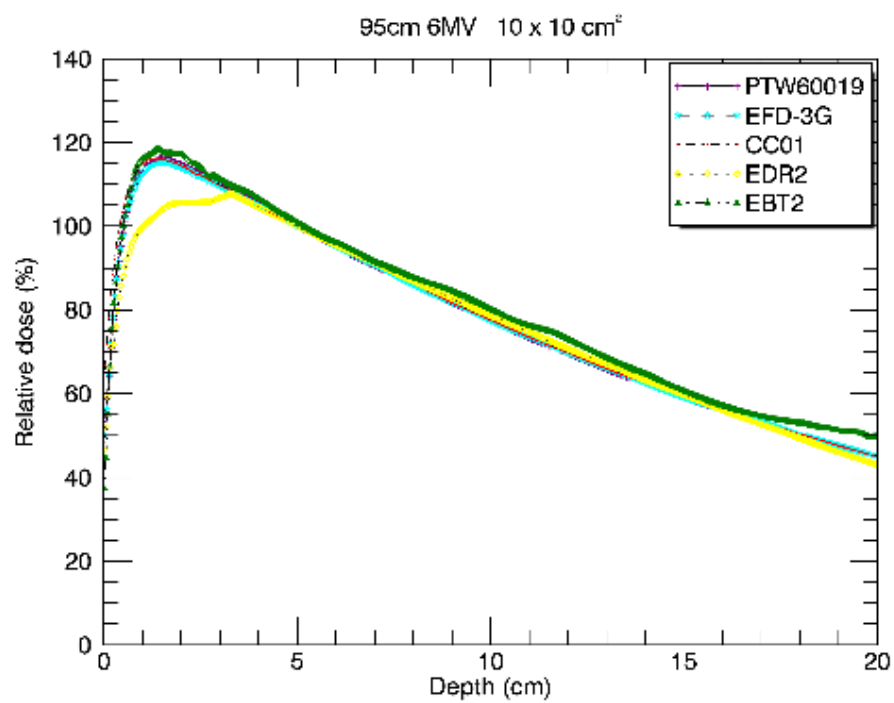
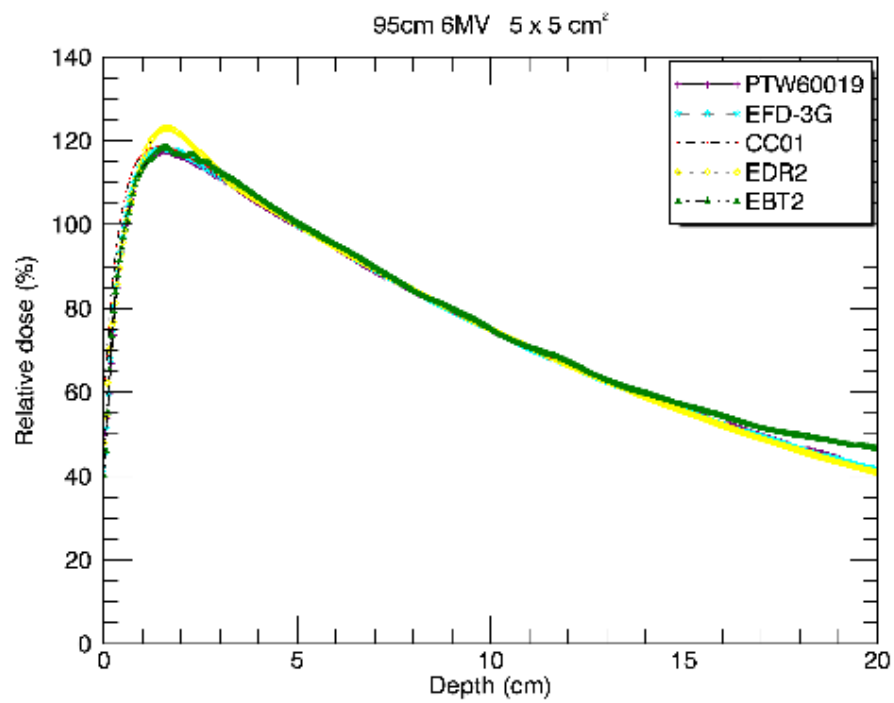


Figure 122. PDD curves for the different detectors measured at an SSD of 95 cm using a 6 MV photon beam for 5x5 cm² and 10x10 cm² field sizes

95 cm 10 MV PDD

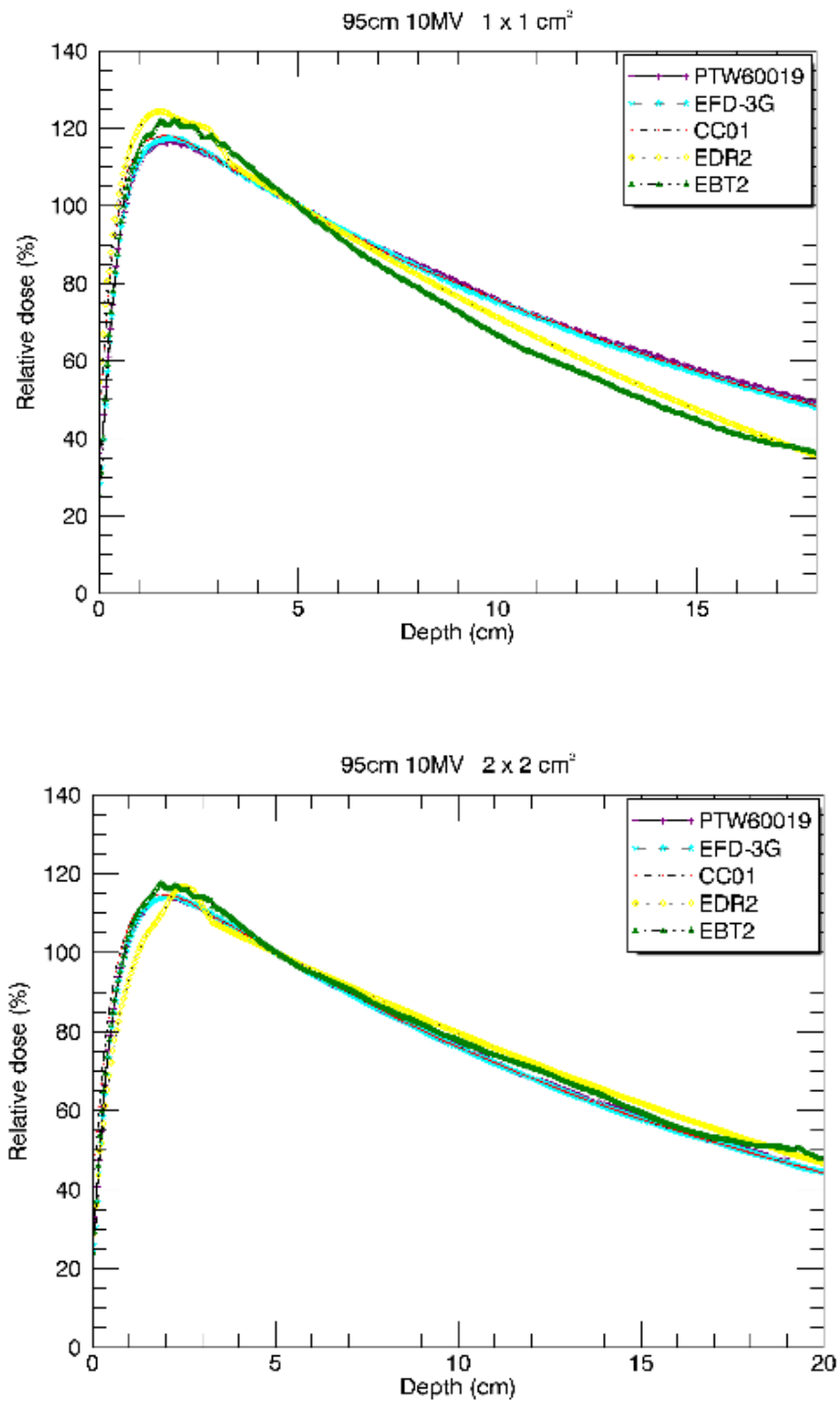


Figure 123. PDD curves for the different detectors measured at an SSD of 95 cm using a 10 MV photon beam for 1x1 cm² and 2x2 cm² field sizes.

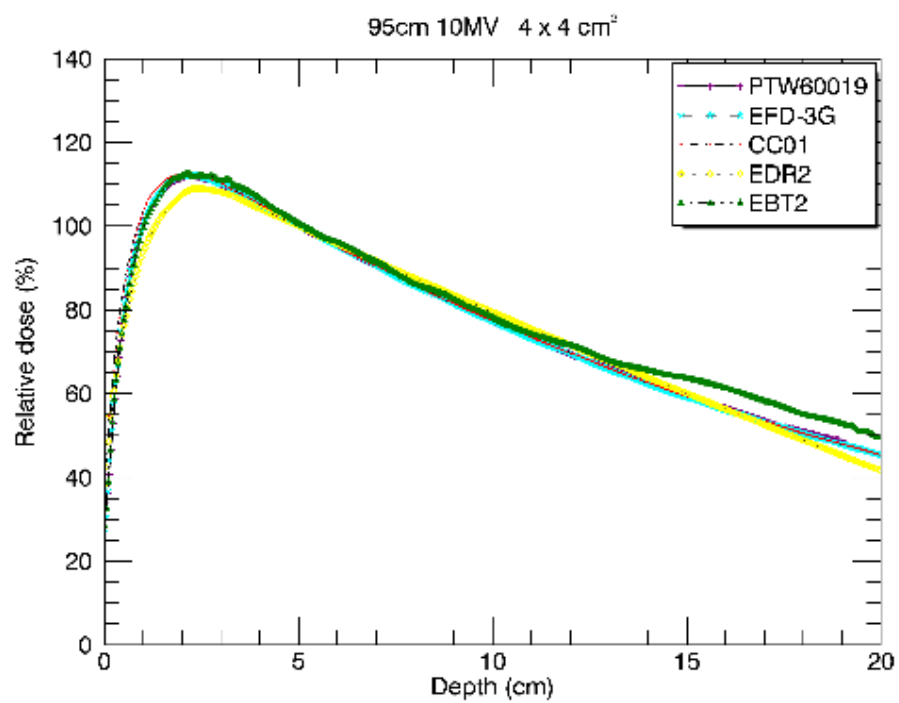
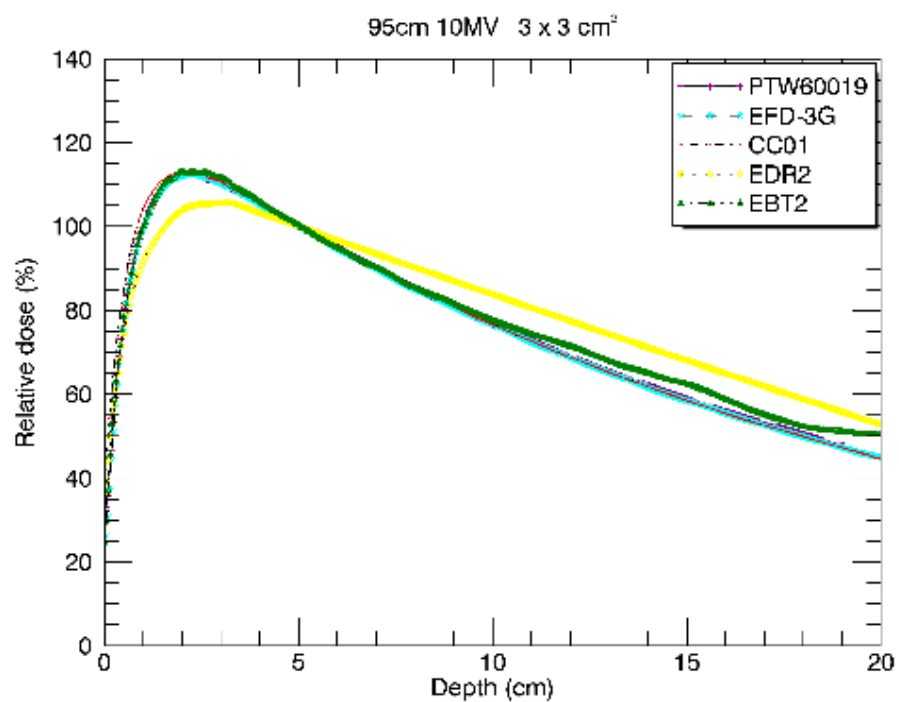


Figure 124. PDD curves for the different detectors measured at an SSD of 95 cm using a 10 MV photon beam for 3x3 cm² and 4x4 cm² field sizes

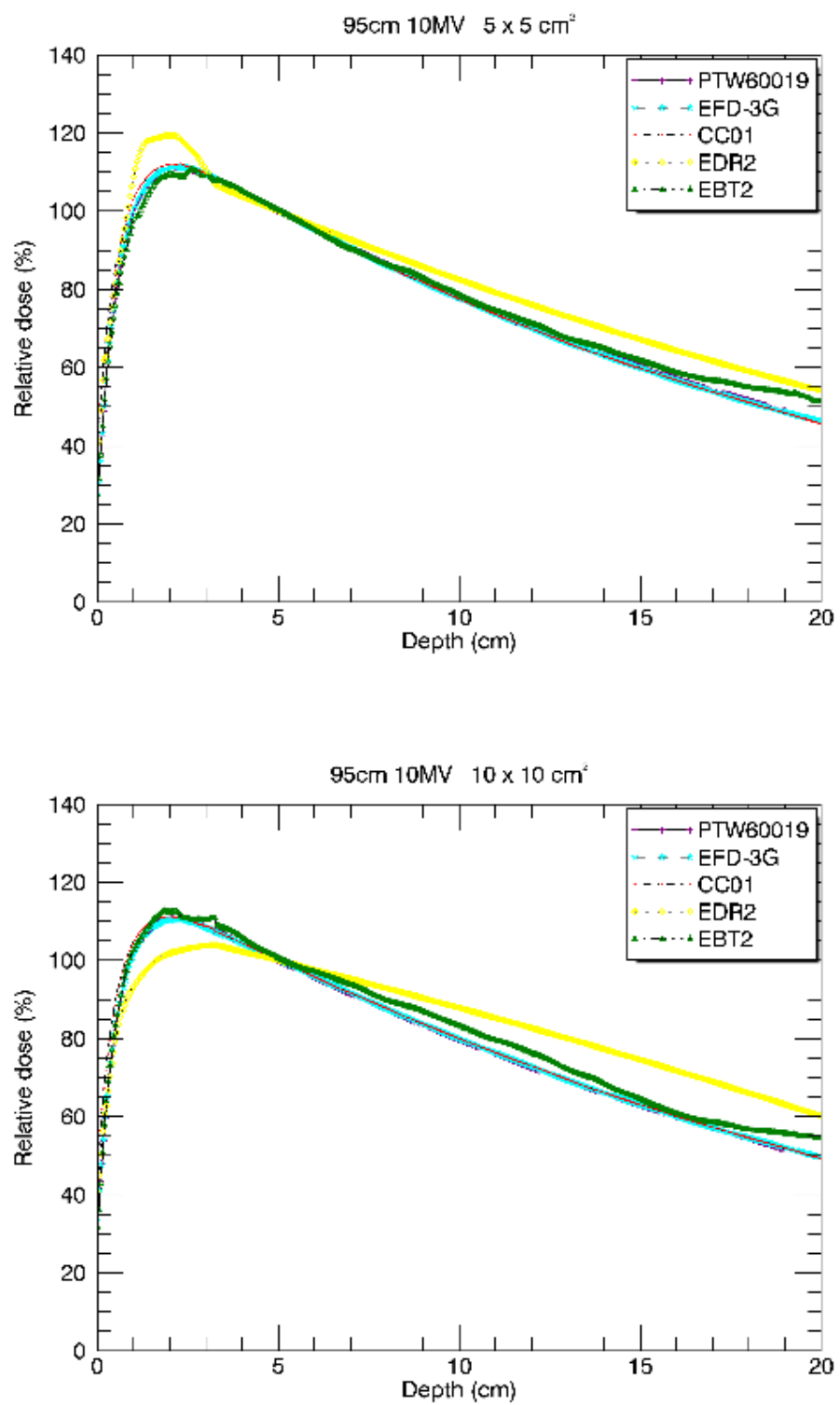


Figure 125. PDD curves for the different detectors measured at an SSD of 95 cm using a 10 MV photon beam for 5x5 cm² and 10x10 cm² field sizes

95 cm 15 MV PDD

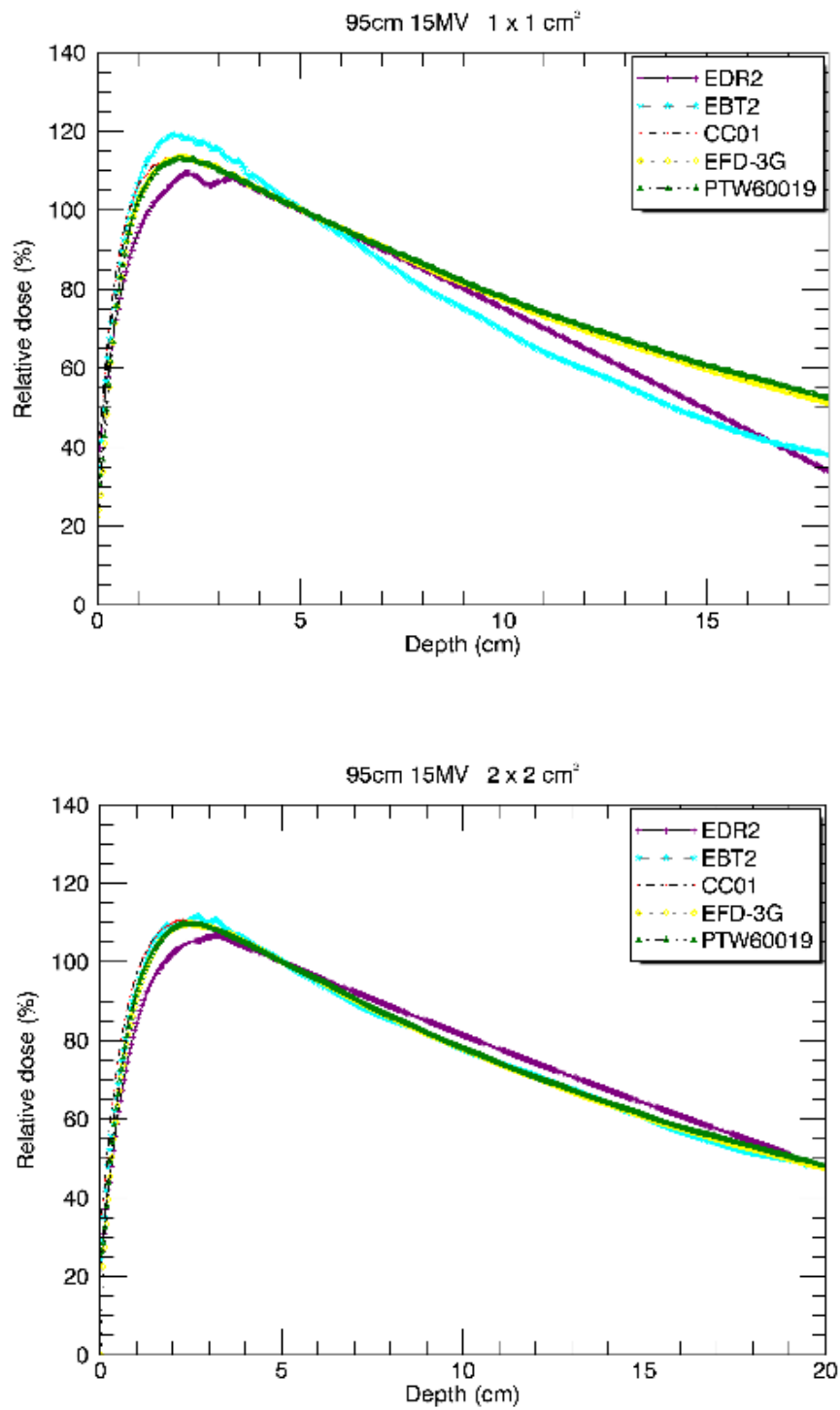


Figure 126. PDD curves for the different detectors measured at an SSD of 95 cm using a 15 MV photon beam for 1x1 cm² and 2x2 cm² field sizes

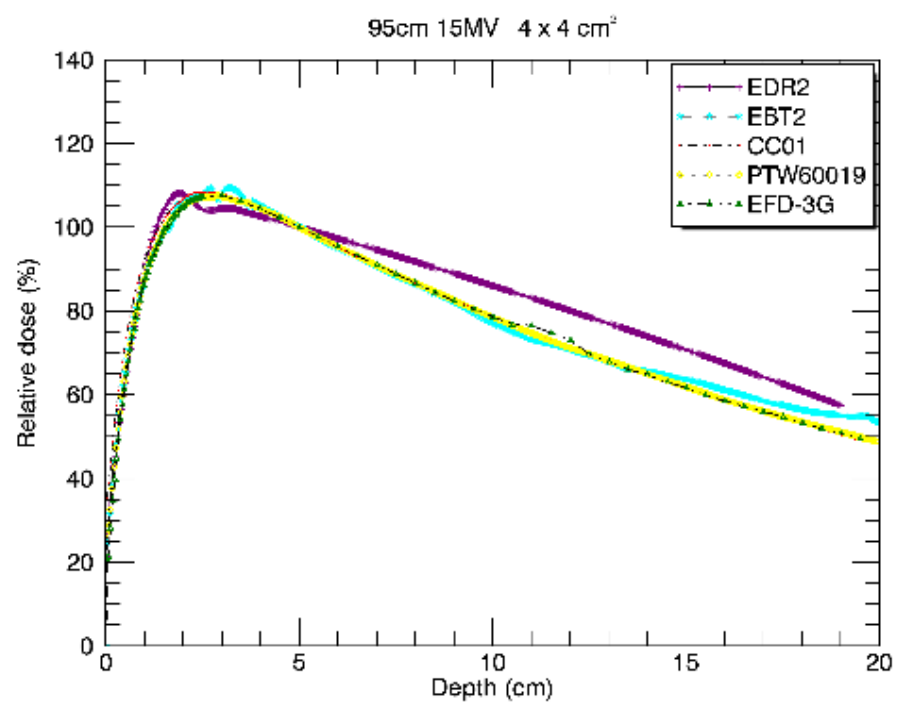
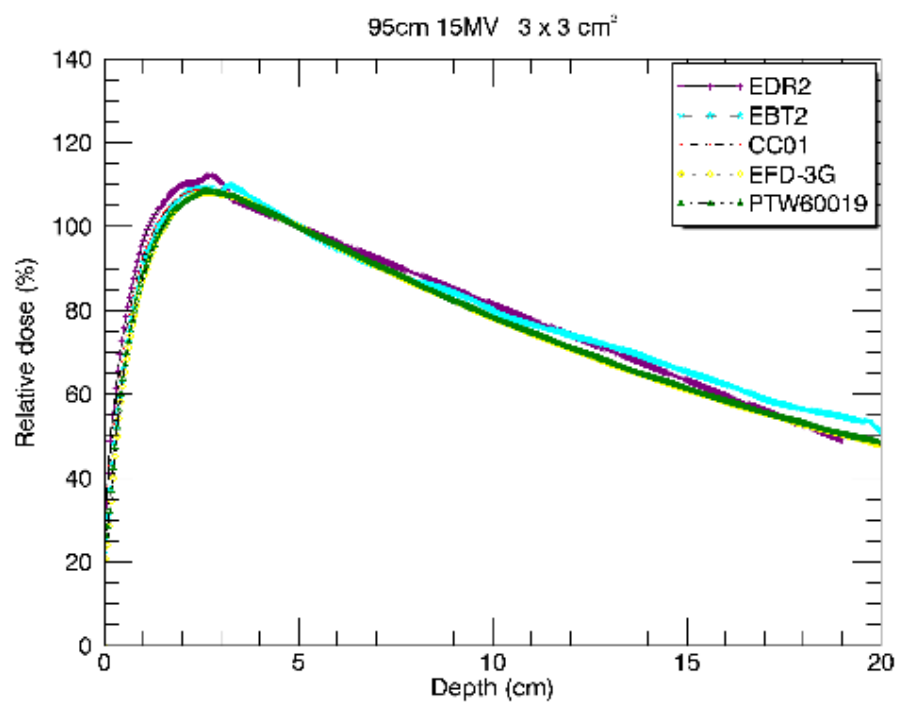


Figure 127. PDD curves for the different detectors measured at an SSD of 95 cm using a 15 MV photon beam for 3x3 cm² and 4x4 cm² field sizes

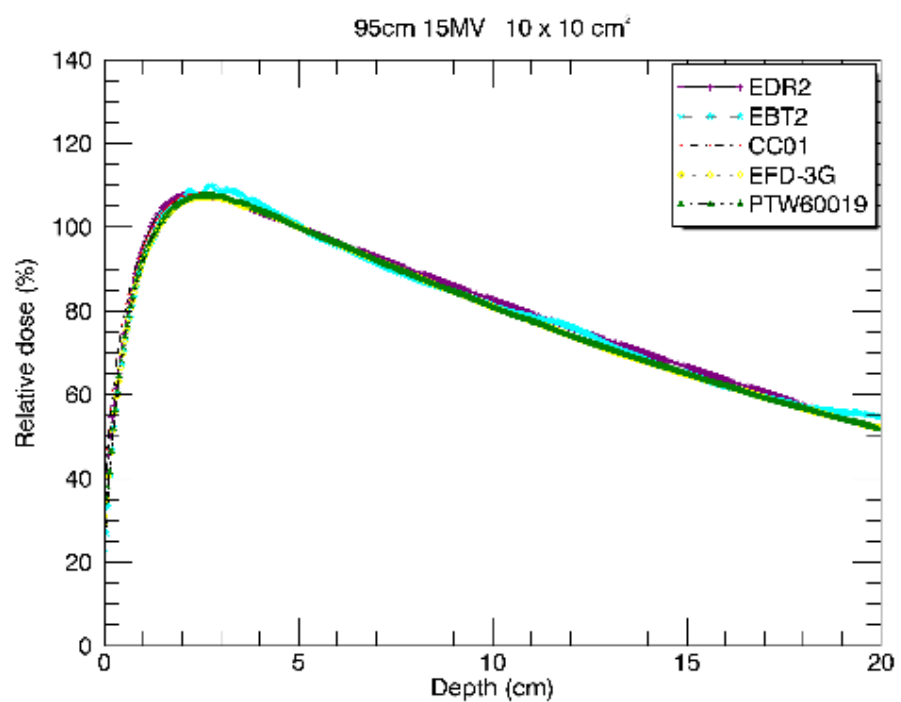
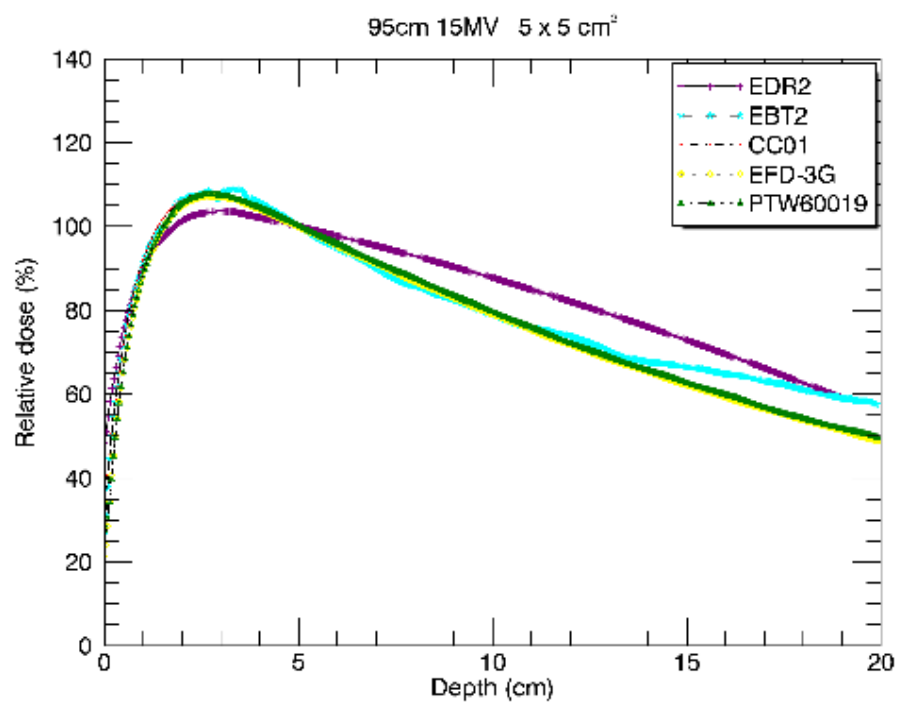


Figure 128. PDD curves for the different detectors measured at an SSD of 95 cm using a 15 MV photon beam for 5x5 cm² and 10x10 cm² field sizes

Table 8. Dmax positions for the different detectors measured at 95 cm SSD

Dmax							
95cm	6MV						
Field side length (cm)	Mean dmax (cm)	Stddev of Dmax	CC01 (cm)	EFD-3G (cm)	PTW60019 (cm)	EBT2 (cm)	EDR2 (cm)
1.05	1.40	0.17	1.20	1.36	1.36	1.42	1.66
2.10	1.65	0.21	1.40	1.57	1.56	1.74	1.96
3.15	1.60	0.10	1.48	1.64	1.56	1.60	1.74
4.20	1.71	0.20	1.58	1.52	1.59	1.94	1.90
5.25	1.59	0.06	1.48	1.59	1.60	1.62	1.64
10.05	1.75	0.55	1.42	1.58	1.52	1.50	2.72
Dmax							
95cm	10MV						
Field side length (cm)	Mean dmax (cm)	Stddev of Dmax	CC01 (cm)	EFD-3G (cm)	PTW60019 (cm)	EBT2 (cm)	EDR2 (cm)
1.05	1.73	0.12	1.66	1.81	1.78	1.84	1.54
2.10	2.30	0.35	1.94	2.12	2.10	2.80	2.52
3.15	2.33	0.24	2.10	2.28	2.22	2.30	2.74
4.20	2.29	0.13	2.12	2.26	2.25	2.40	2.44
5.25	2.24	0.24	2.16	2.24	2.20	2.64	1.98
10.00	2.24	0.24	2.16	2.24	2.20	2.64	1.98
Dmax							
95cm	15MV						
Field side length (cm)	Mean dmax (cm)	Stddev of Dmax	CC01 (cm)	EFD-3G (cm)	PTW60019 (cm)	EBT2 (cm)	EDR2 (cm)
1.05	2.07	0.11	1.98	2.08	2.13	2.22	1.96
2.10	2.59	0.20	2.38	2.51	2.52	2.90	2.64
3.15	2.84	0.23	2.62	2.76	2.72	2.88	3.22
4.20	2.66	0.46	2.60	2.81	2.79	1.92	3.16
5.25	2.86	0.25	2.62	2.78	2.78	2.82	3.29
10.00	2.58	0.25	2.49	2.69	2.64	2.20	2.86

4.3.3 PDDs measured at an SSD of 100 cm

The figures 129 - 137 show the PDD curves obtained at an SSD of 100 cm and normalized at 5 cm depth. The detectors show similar PDD measurements, especially above D_{max} for all the fields concerned, except for the $1 \times 1 \text{ cm}^2$ field size. Film measurements also present artefacts shown mostly below D_{max} . The bump which appeared on most of the PDDs measured at 90 cm and 95 cm with the EBT2 films is no longer apparent due to less scatter passing through the film gap.

Table 10 shows the D_{max} values for each detector at the different field sizes. In general, the films seem to have deeper D_{max} , but mostly the detectors have no significant differences between the measured D_{max} . This increase in D_{max} for the films is due to the artefacts that were shown.

100 cm 6 MV PDD

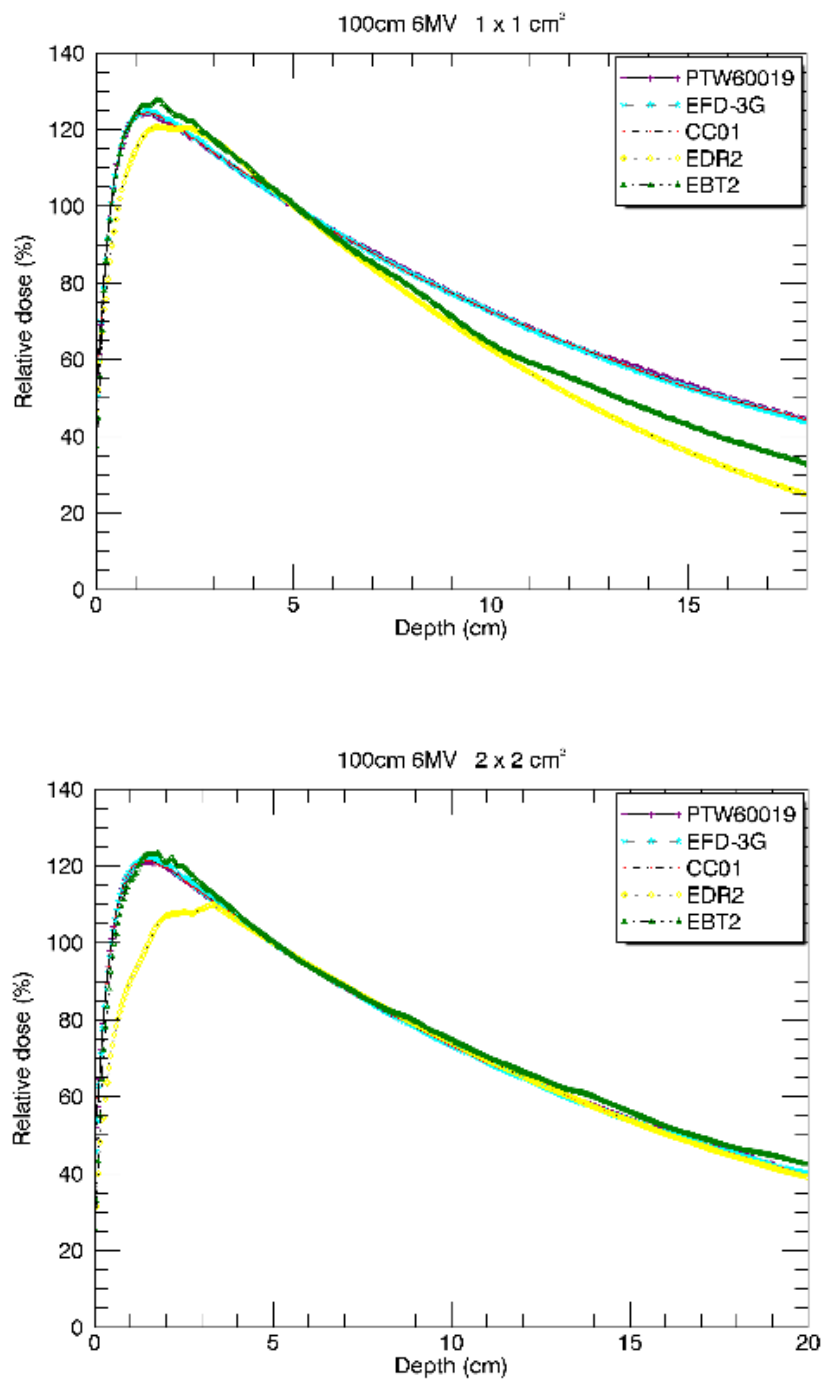


Figure 129. PDD curves for the different detectors measured at an SSD of 100 cm using a 6 MV photon beam for 1×1 cm² and 2×2 cm² field sizes

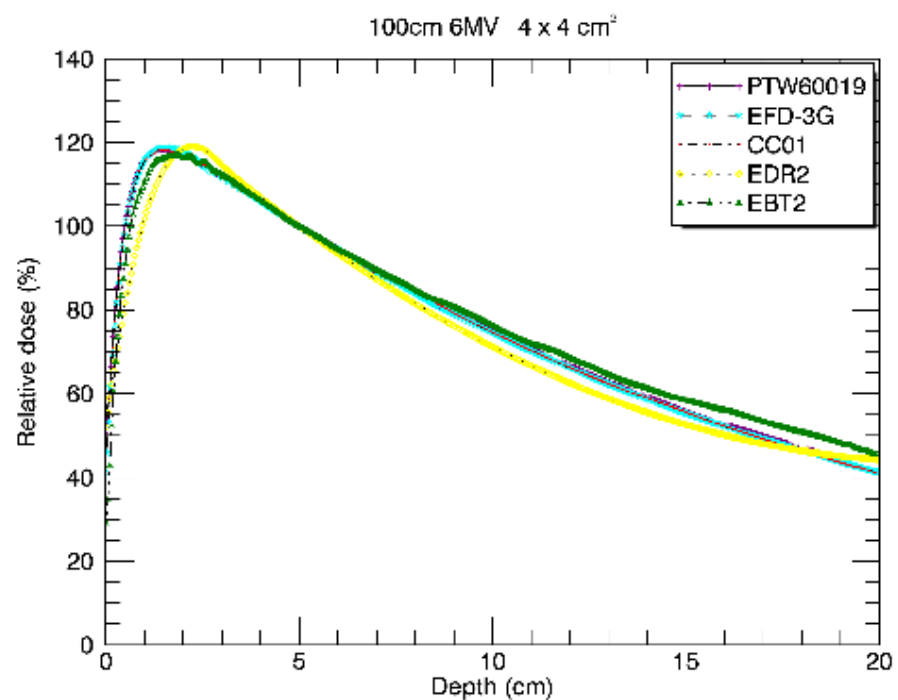
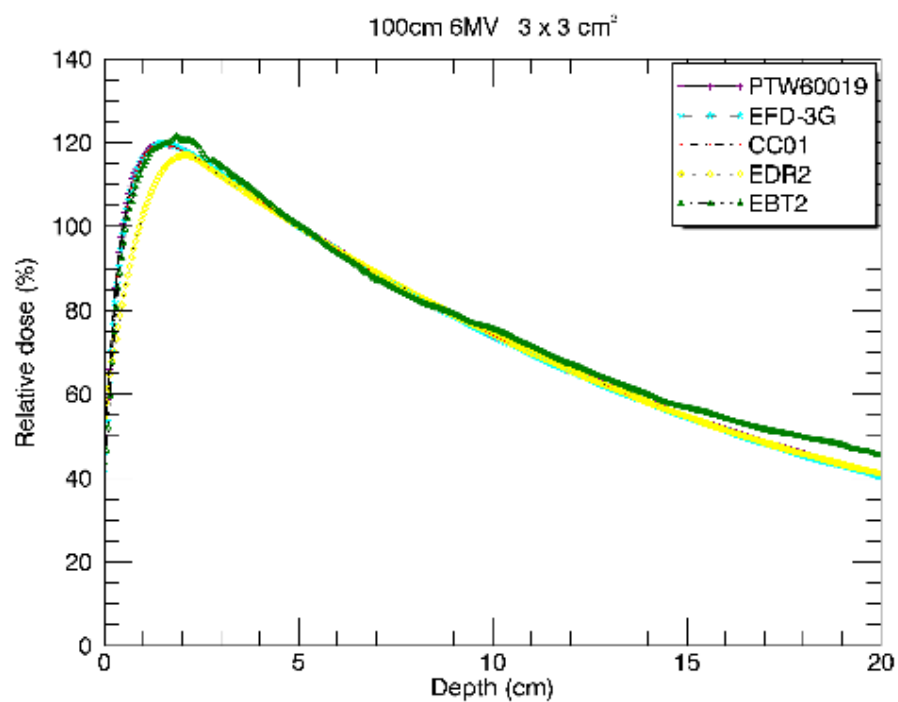


Figure 130. PDD curves for the different detectors measured at an SSD of 100 cm using a 6 MV photon beam for 3x3 cm² and 4x4 cm² field sizes

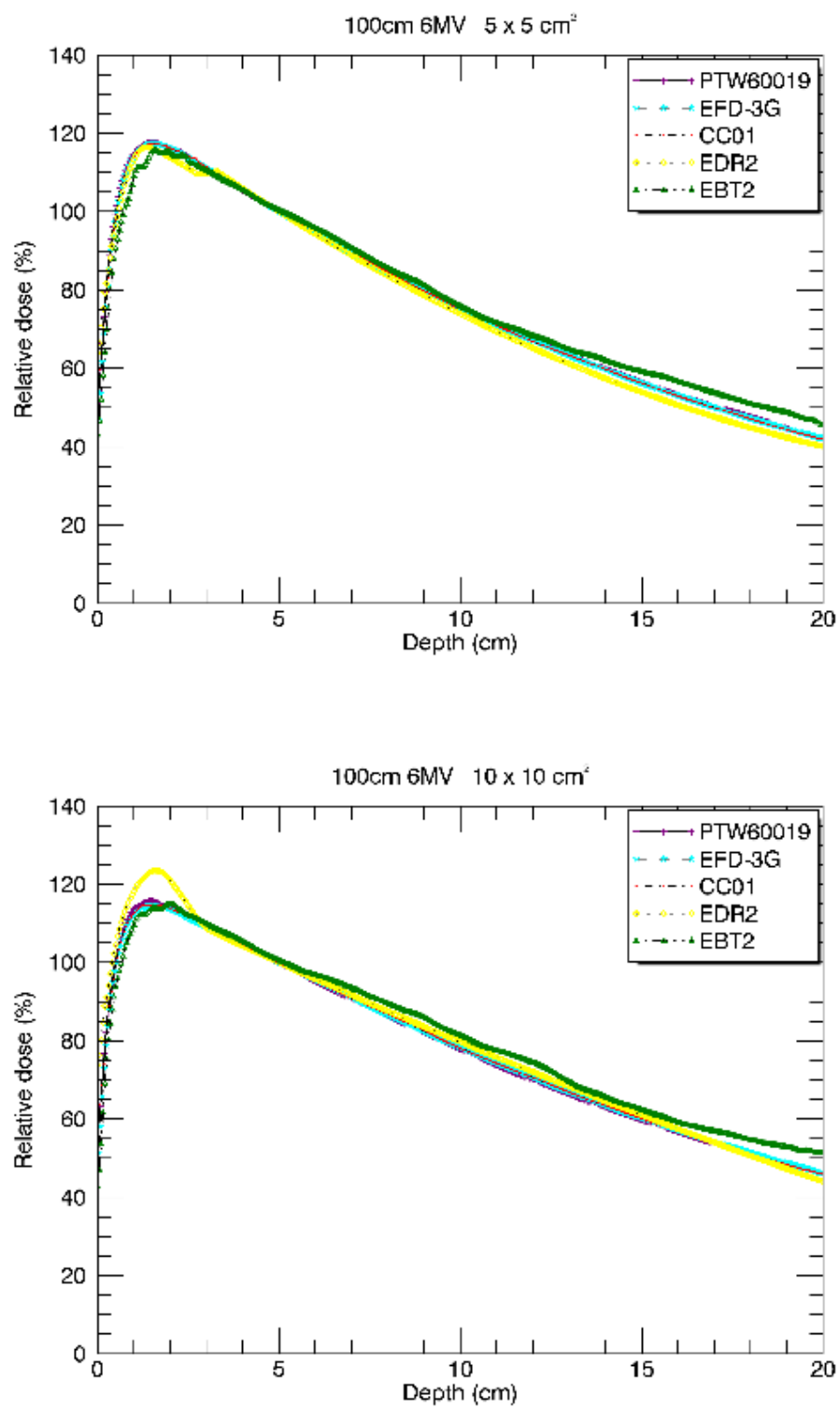


Figure 131. PDD curves for the different detectors measured at an SSD of 100 cm using a 6 MV photon beam for $5 \times 5 \text{ cm}^2$ and $10 \times 10 \text{ cm}^2$ field sizes

100 cm 10 MV PDD

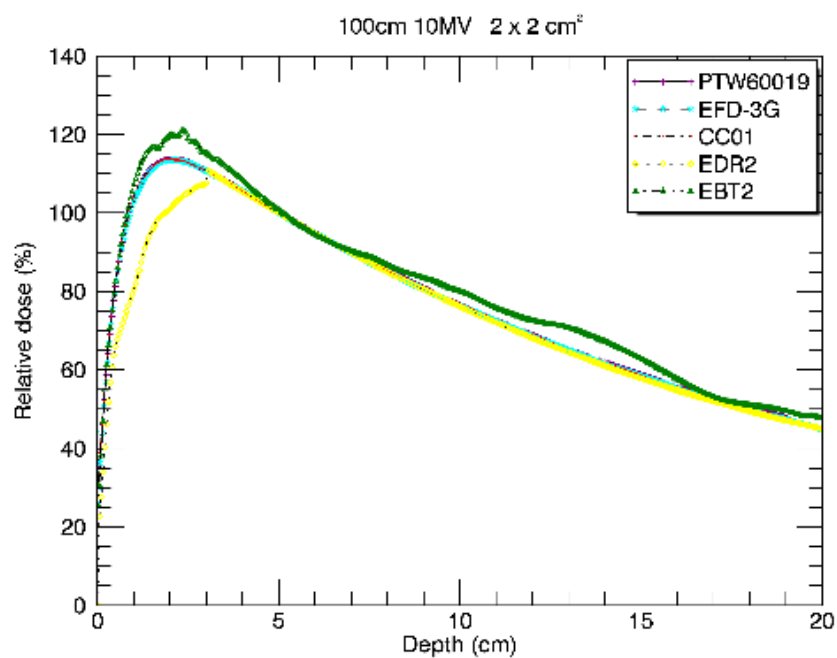
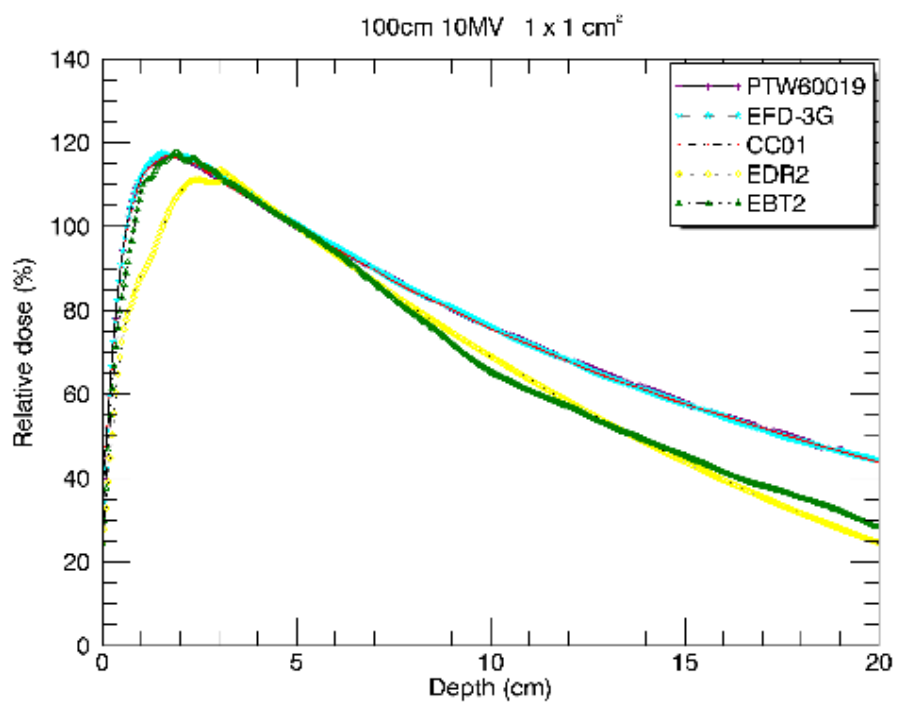


Figure 132. PDD curves for the different detectors measured at an SSD of 100 cm using a 10 MV photon beam for 1x1 cm² and 2x2 cm² field sizes

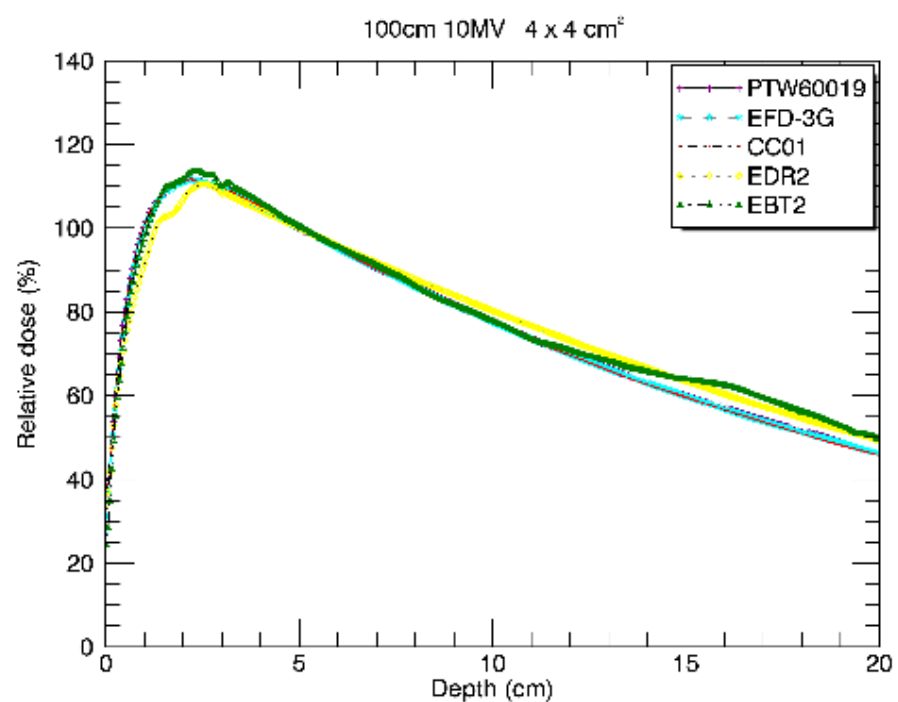
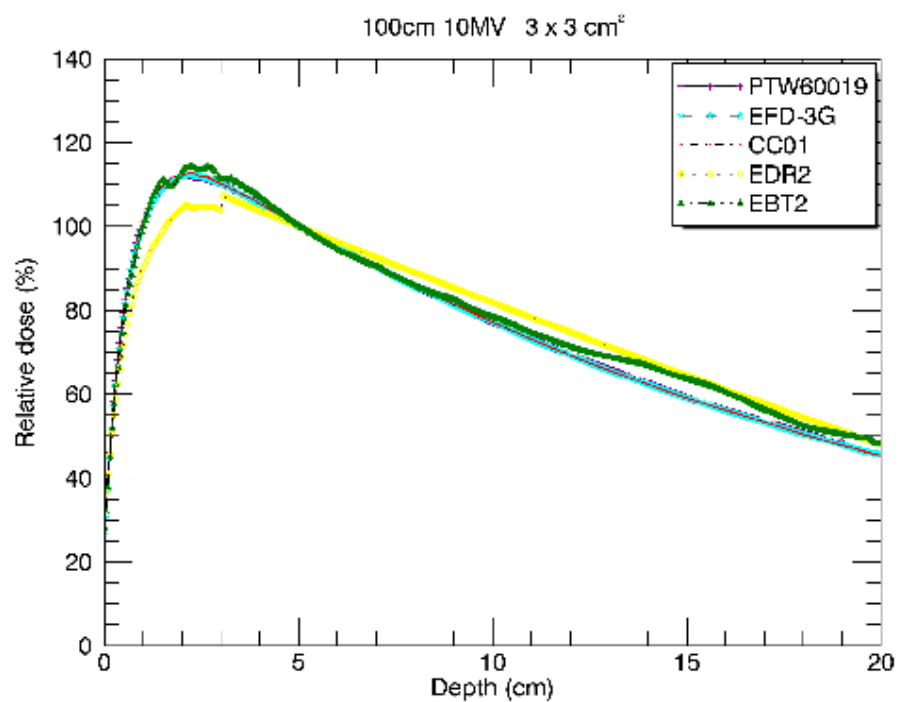


Figure 133. PDD curves for the different detectors measured at an SSD of 100 cm using a 10 MV photon beam for 3x3 cm² and 4x4 cm² field sizes

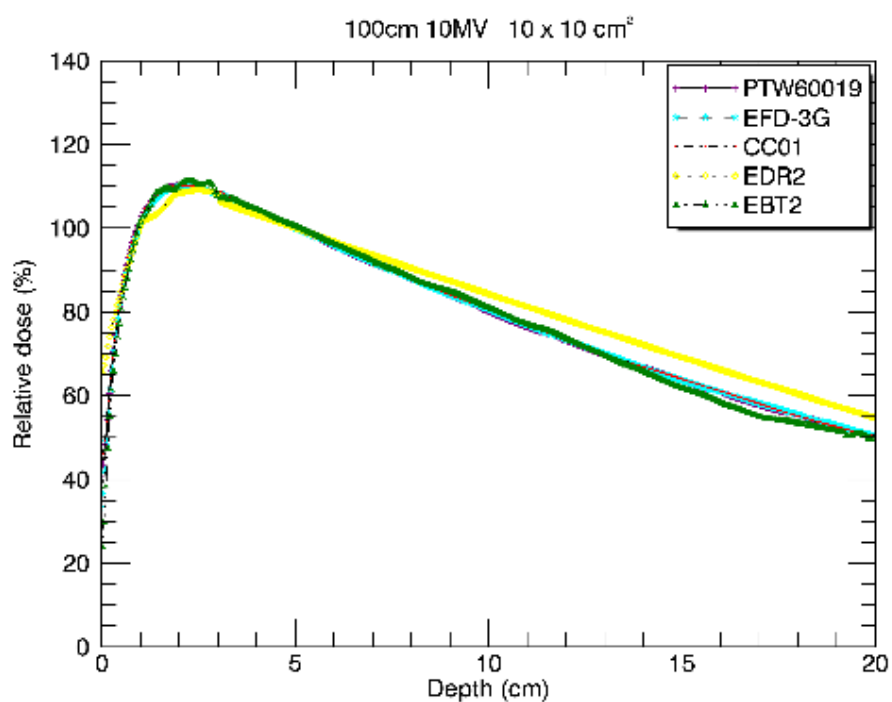
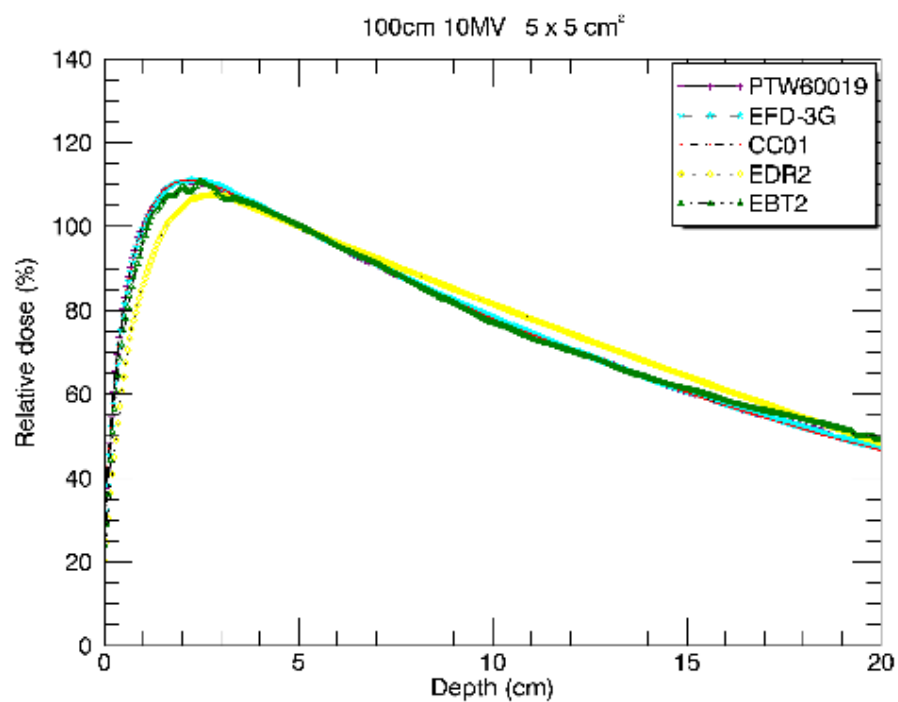


Figure 134. PDD curves for the different detectors measured at an SSD of 100 cm using a 10 MV photon beam for 5x5 cm² and 10x10 cm² field sizes

100 cm 15 MV PDD

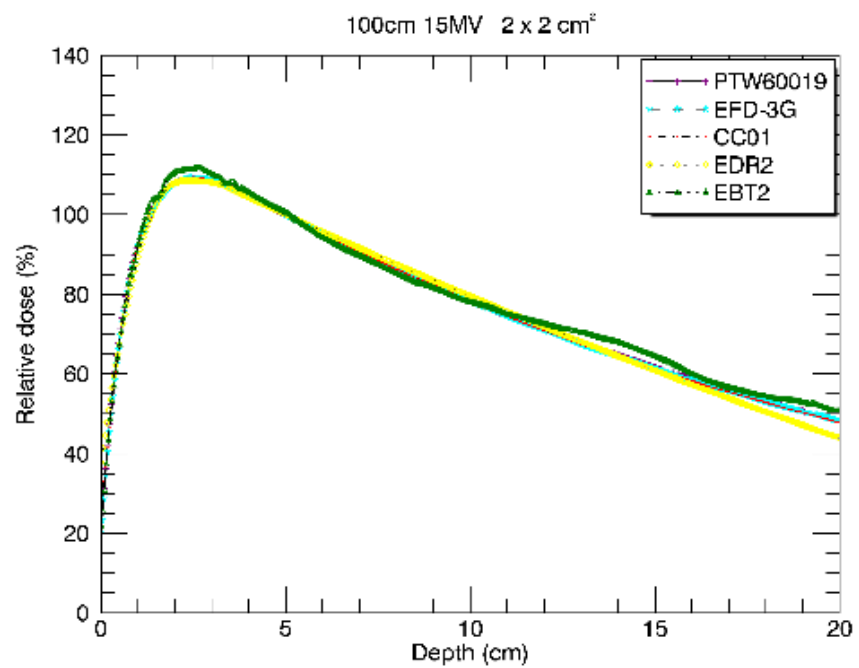
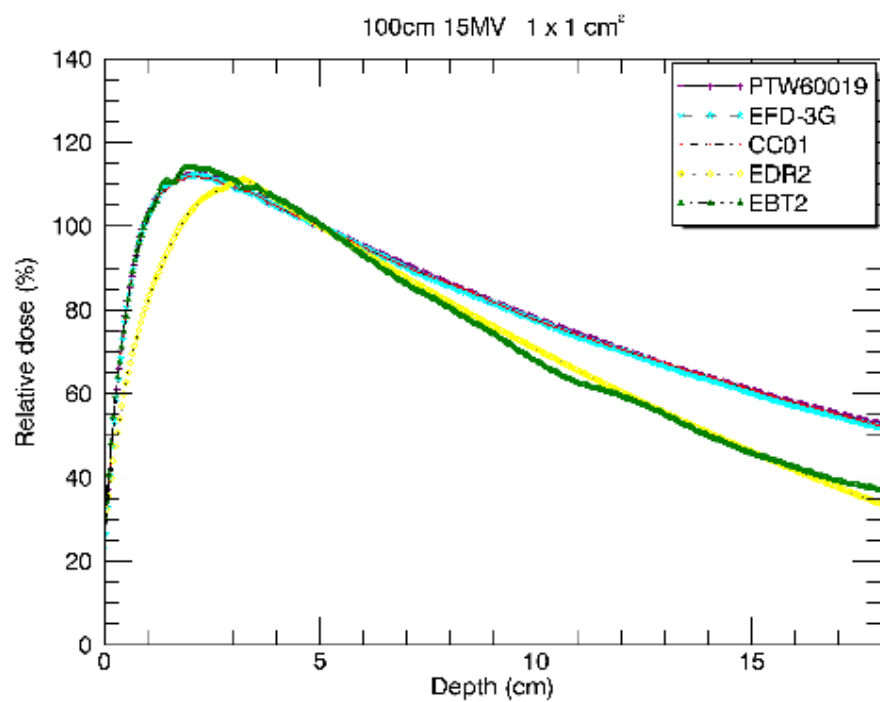


Figure 135. PDD curves for the different detectors measured at an SSD of 100 cm using a 15 MV photon beam for 1x1 cm² and 2x2 cm² field sizes

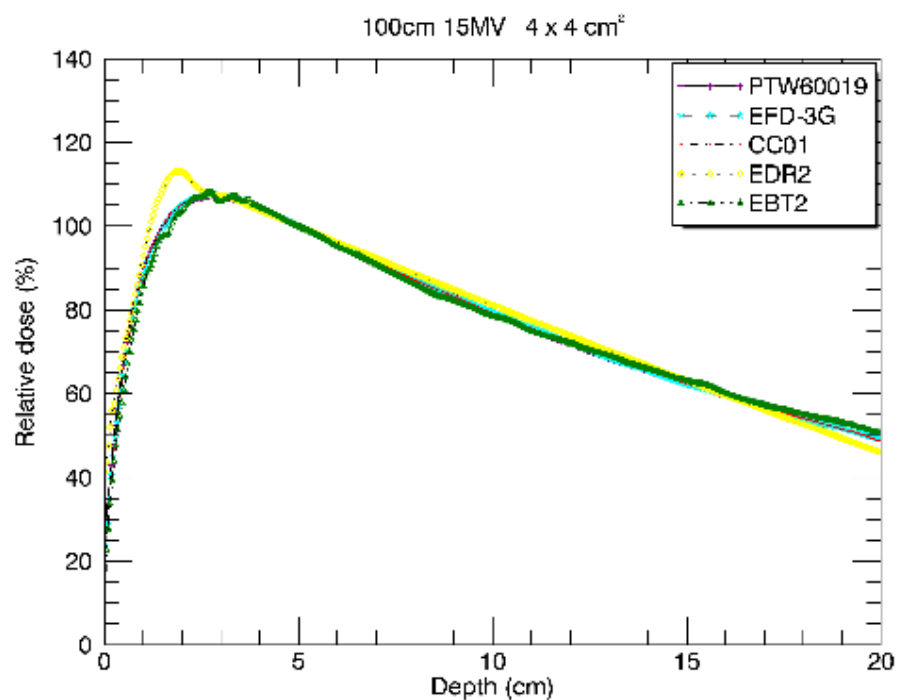
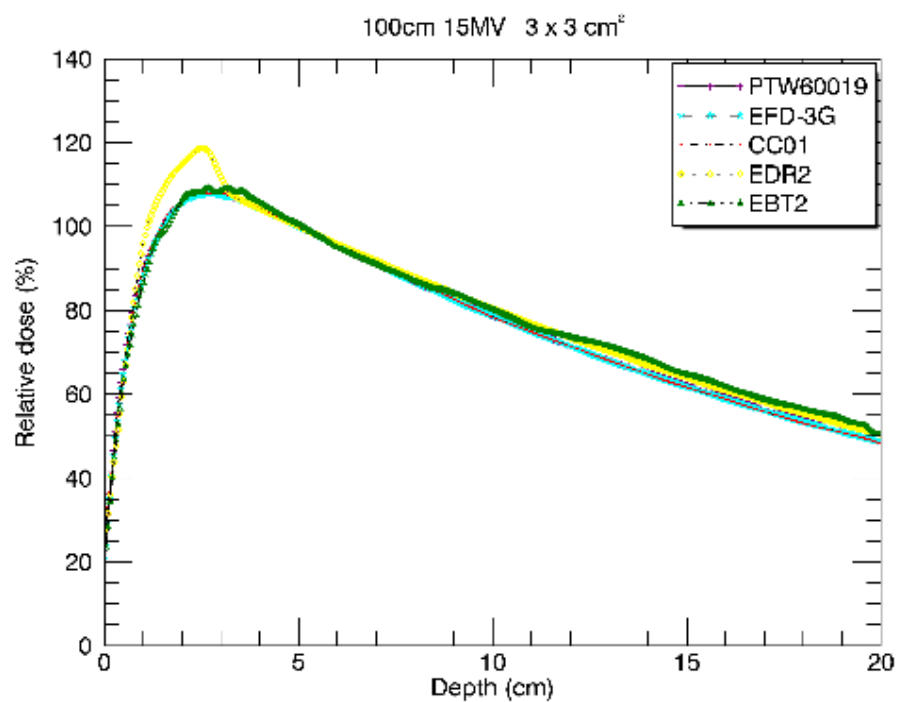


Figure 136. PDD curves for the different detectors measured at an SSD of 100 cm using a 15 MV photon beam for 3x3 cm² and 4x4 cm² field sizes

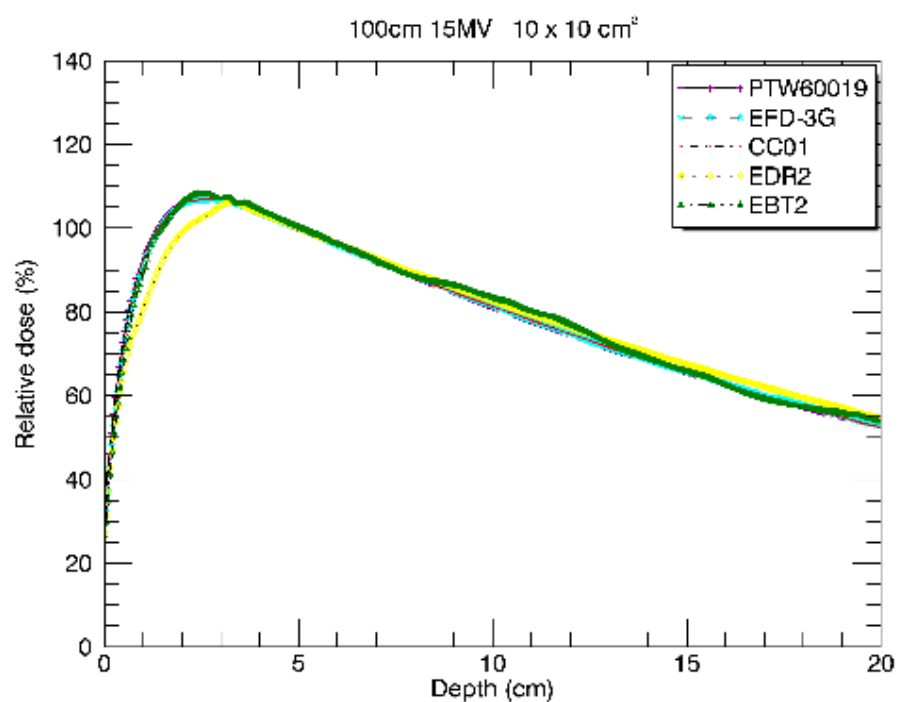
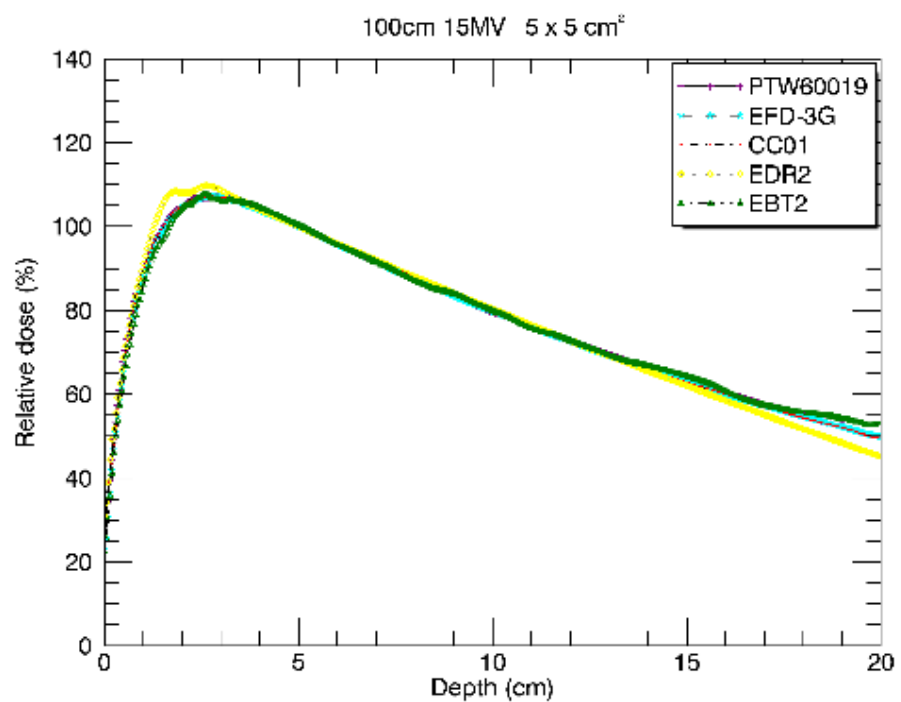


Figure 137. PDD curves for the different detectors measured at an SSD of 100 cm using a 15 MV photon beam for 5x5 cm² and 10x10 cm² field sizes

Table 9. Dmax positions for the different detectors measured at 100 cm SSD

Dmax							
100cm	6MV						
Field side length (cm)	Mean dmax (cm)	Stddev of Dmax	CC01 (cm)	EFD-3G (cm)	PTW60019 (cm)	EBT2 (cm)	EDR2 (cm)
1.10	1.42	0.15	1.32	1.34	1.30	1.50	1.64
2.20	1.79	0.53	1.50	1.53	1.52	1.66	2.72
3.30	1.77	0.35	1.52	1.57	1.54	1.92	2.32
4.40	1.65	0.13	1.56	1.59	1.56	1.86	1.70
5.50	1.59	0.14	1.60	1.59	1.56	1.78	1.40
11.00	1.64	0.18	1.54	1.58	1.50	1.94	1.62
Dmax							
100cm	10MV						
Field side length (cm)	Mean dmax (cm)	Stddev of Dmax	CC01 (cm)	EFD-3G (cm)	PTW60019 (cm)	EBT2 (cm)	EDR2 (cm)
1.00	1.96	0.37	1.76	1.72	1.76	1.94	2.60
2.20	2.39	0.56	2.06	2.13	2.12	2.26	3.38
3.30	2.29	0.13	2.20	2.24	2.16	2.42	2.44
4.40	2.33	0.14	2.26	2.24	2.20	2.40	2.54
5.50	2.40	0.25	2.21	2.28	2.22	2.50	2.80
11.00	2.26	0.17	2.12	2.19	2.12	2.36	2.50
Dmax							
100cm	15MV						
Field side length (cm)	Mean dmax (cm)	Stddev of Dmax	CC01 (cm)	EFD-3G (cm)	PTW60019 (cm)	EBT2 (cm)	EDR2 (cm)
1.00	2.36	0.54	2.12	2.09	2.16	2.12	3.32
2.20	2.37	0.40	2.52	2.53	2.56	2.56	1.66
3.30	2.73	0.19	2.70	2.72	2.70	3.04	2.50
4.40	2.60	0.38	2.80	2.81	2.80	2.68	1.92
5.50	2.75	0.07	2.76	2.80	2.82	2.66	2.70
11.00	2.83	0.38	2.74	2.70	2.68	2.54	3.50

4.3.4 PDDs measured at an SSD of 110 cm

The figures 138 – 146 below show the PDD curves obtained at an SSD of 110 cm normalized at 5 cm depth. Both films exhibit acceptable correlation except at the 1×1 cm² field size. The 5×5 cm² for the 10 MV photon beam, and the 4×4 cm² and 10×10 cm² fields for the 15 MV photon beam films (EDR2) demonstrate processor influence in the build-up region. The detectors show good correlation below D_{max} for the different field sizes.

Table 10 shows the D_{max} values for each detector at the different field sizes.

110 cm 6 MV PDD

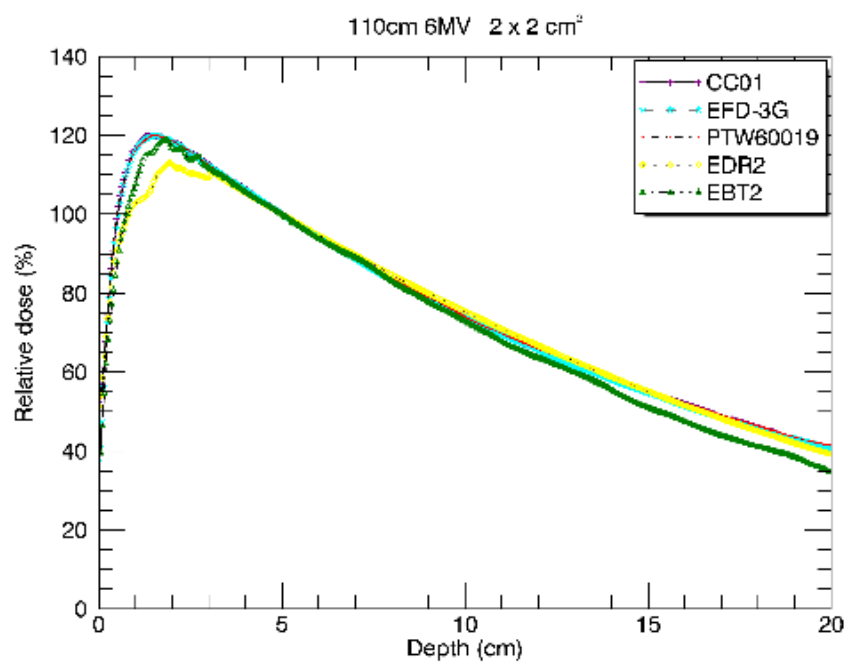
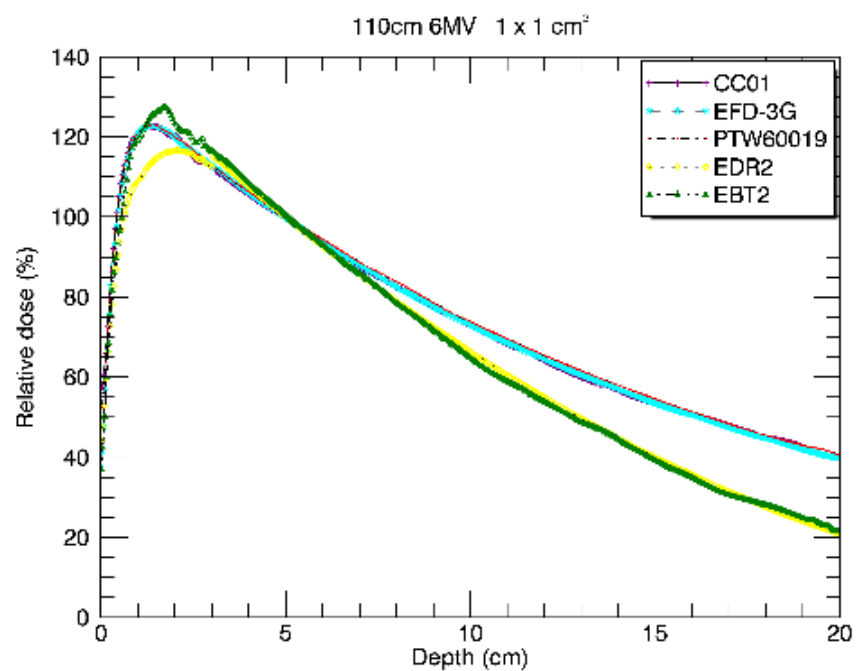


Figure 138. PDD curves for the different detectors measured at an SSD of 110 cm using a 6 MV photon beam for 1x1 cm² and 2x2 cm² field sizes

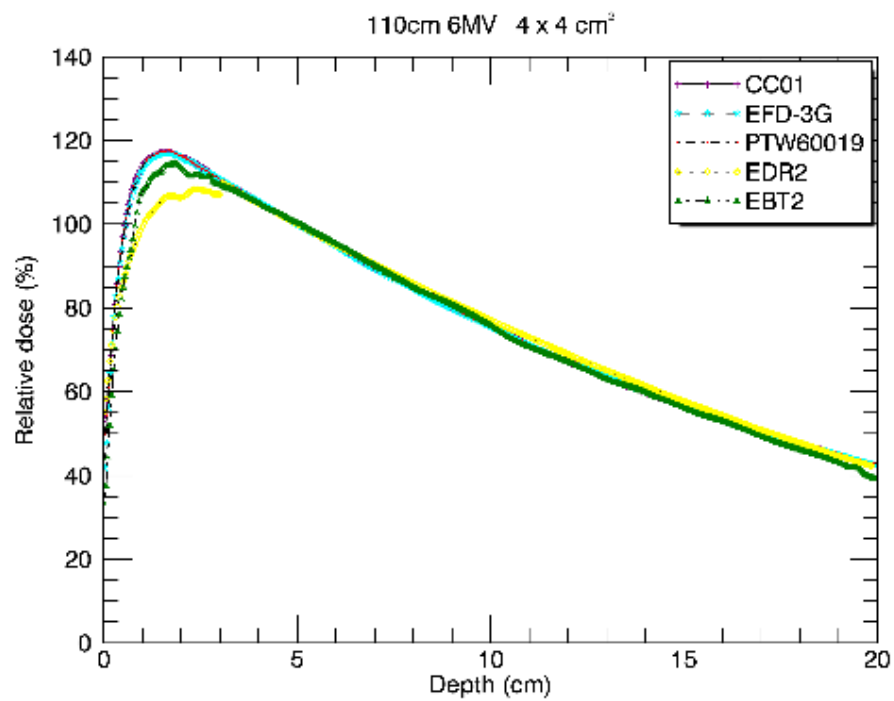
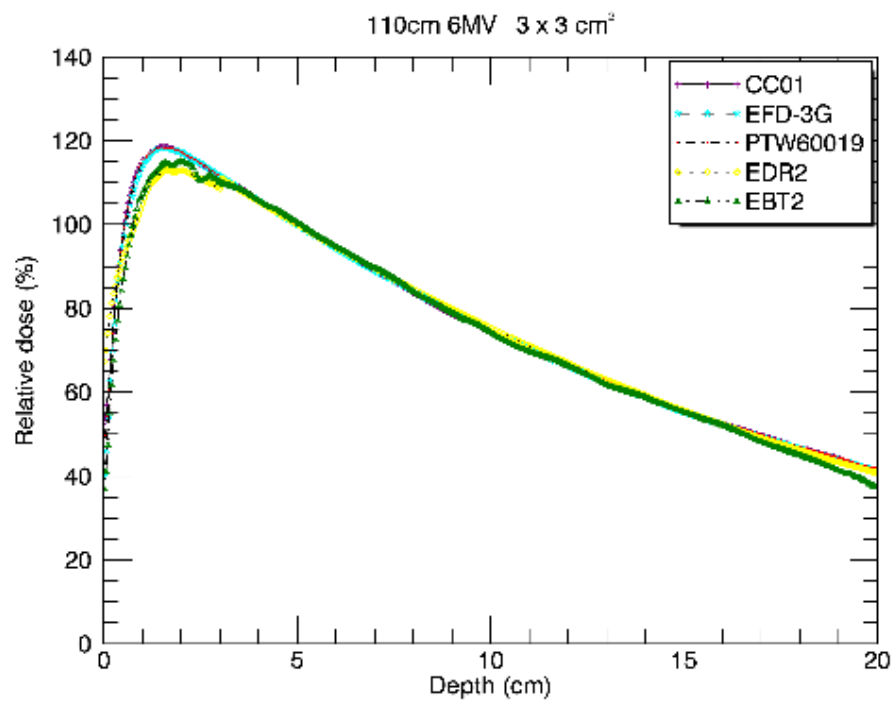


Figure 139. PDD curves for the different detectors measured at an SSD of 110 cm using a 6 MV photon beam for 3x3 cm² and 4x4 cm² field sizes

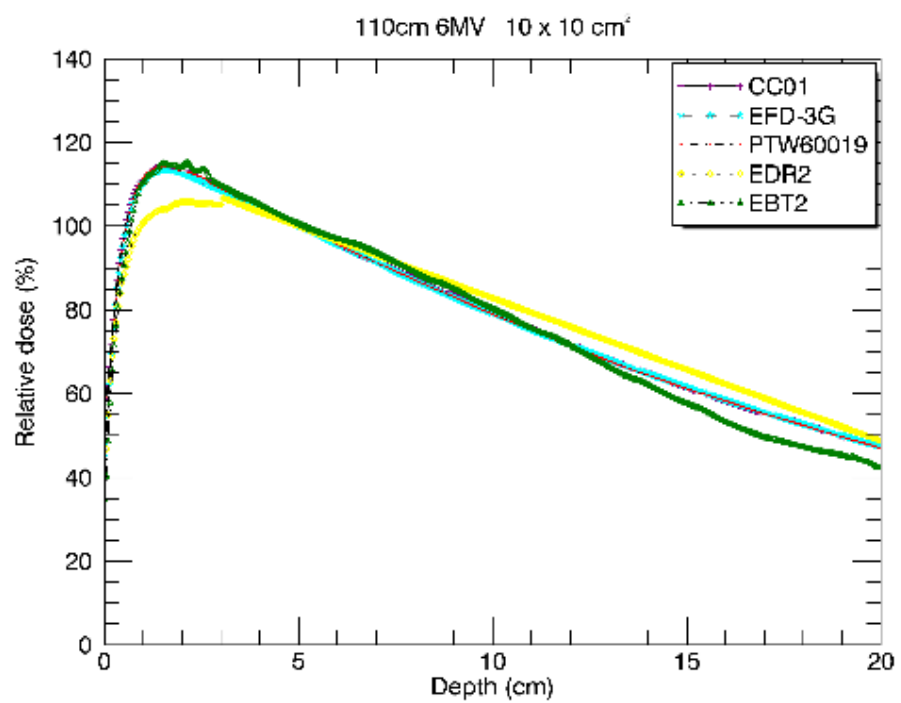
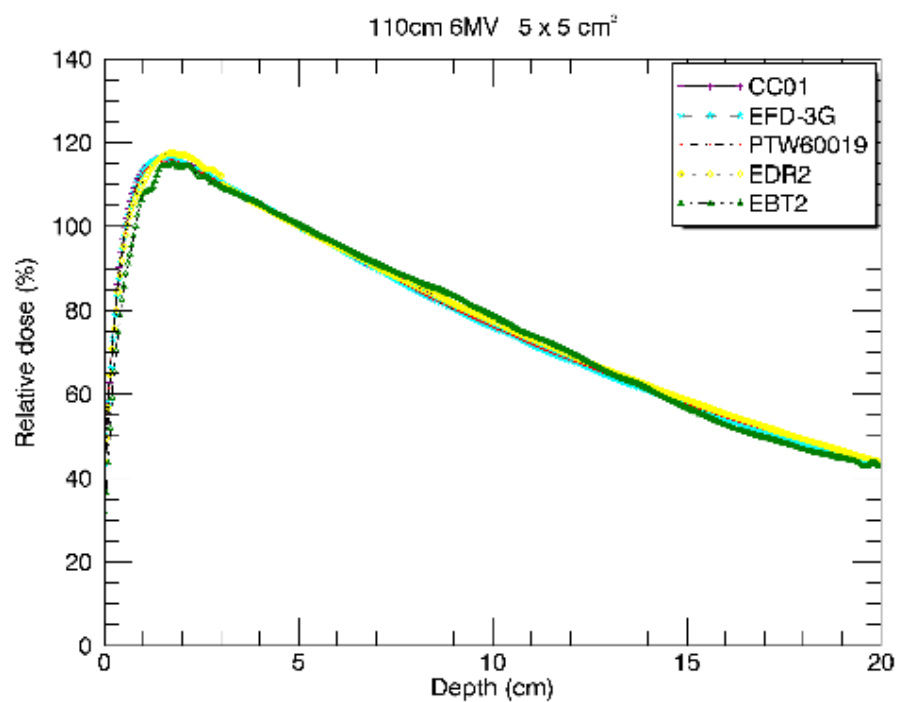


Figure 140. PDD curves for the different detectors measured at an SSD of 110 cm using a 6 MV photon beam for 5x5 cm² and 10x10 cm² field sizes

110 cm 10 MV PDD

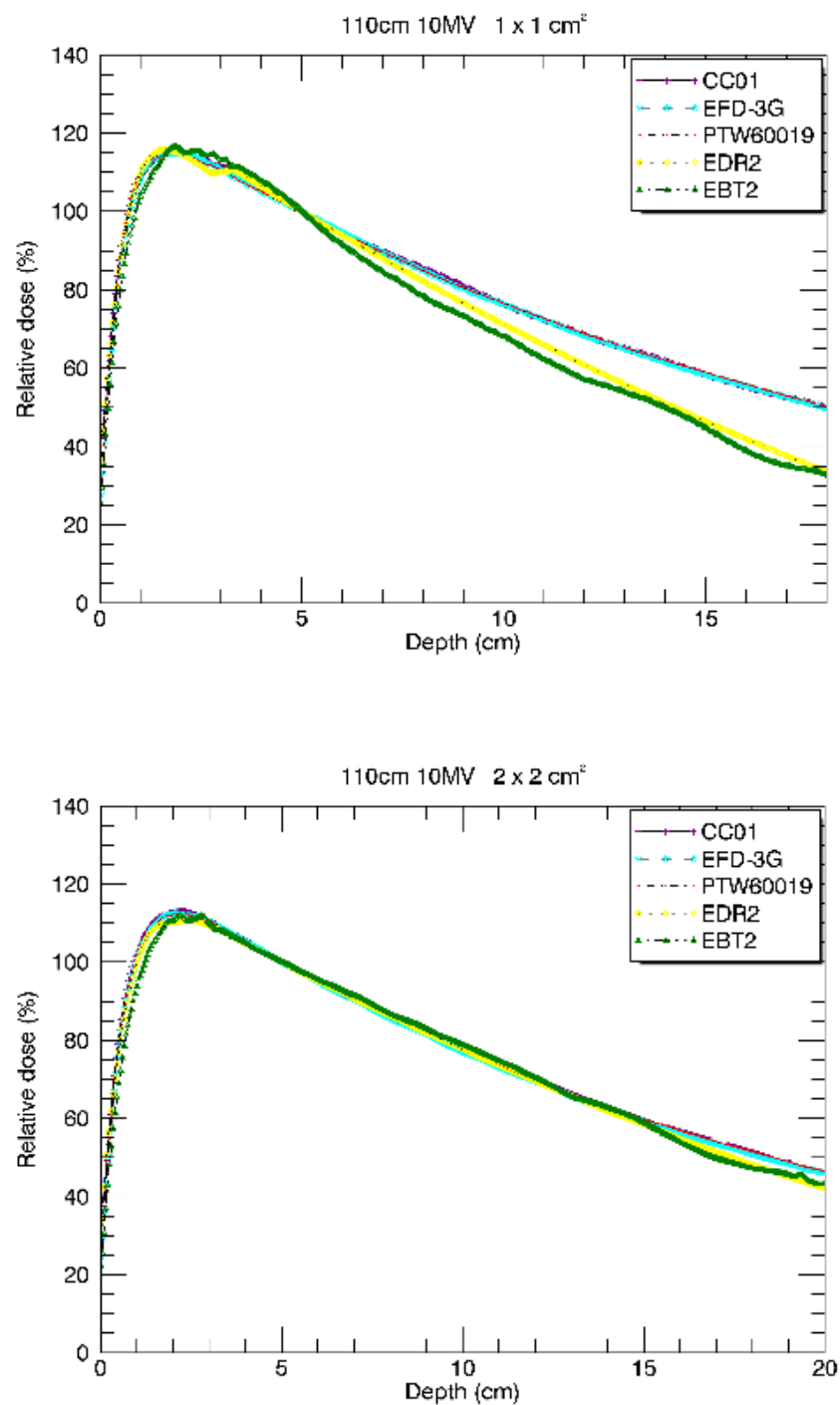


Figure 141. PDD curves for the different detectors measured at an SSD of 110 cm using a 10 MV photon beam for 1x1 cm² and 2x2 cm² field sizes

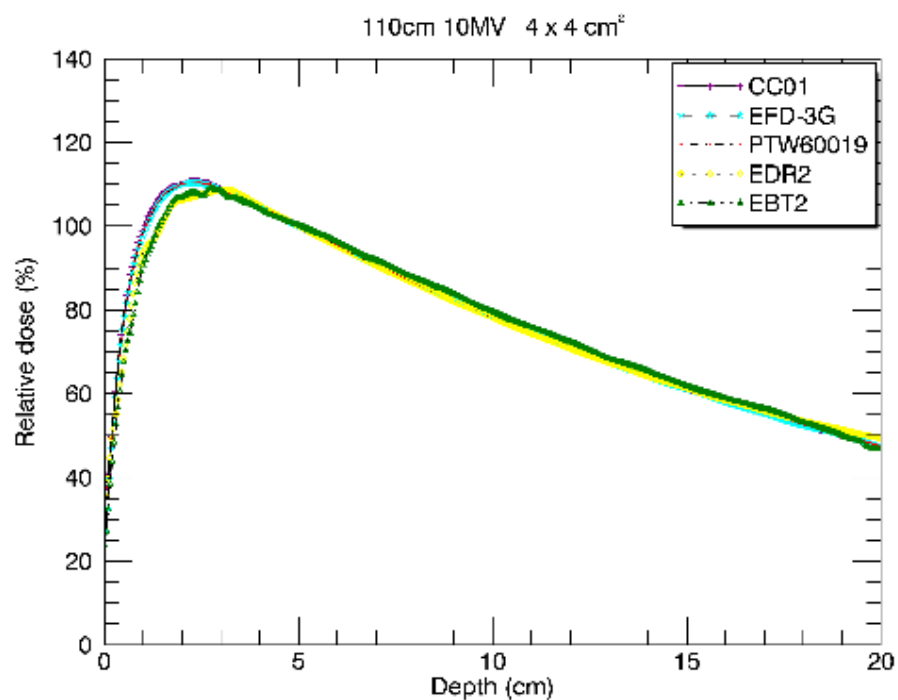
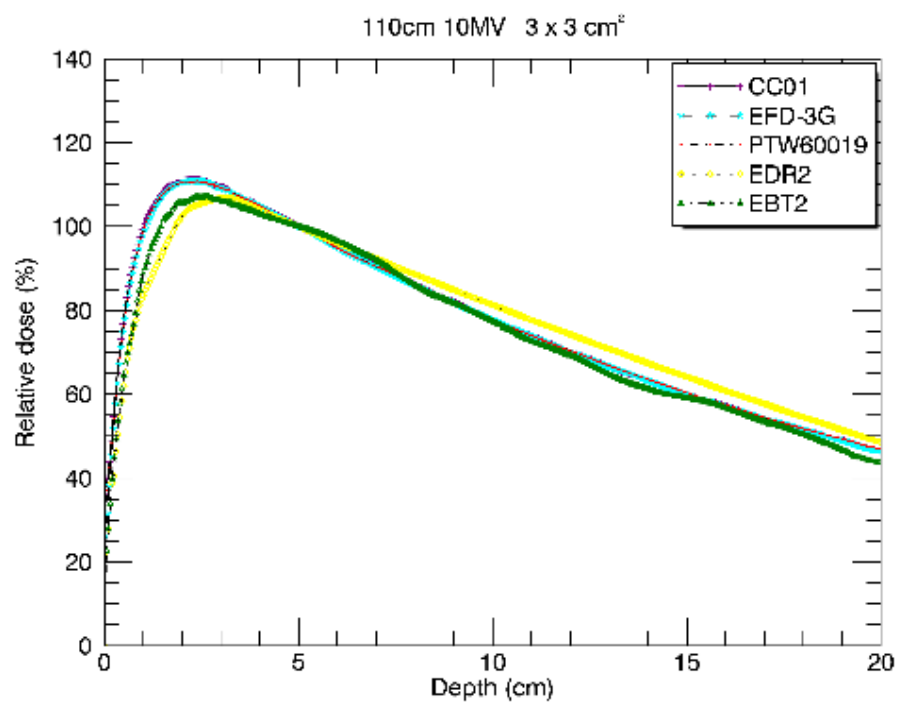


Figure 142. PDD curves for the different detectors measured at an SSD of 110 cm using a 106 MV photon beam for 3x3 cm² and 4x4 cm² field sizes

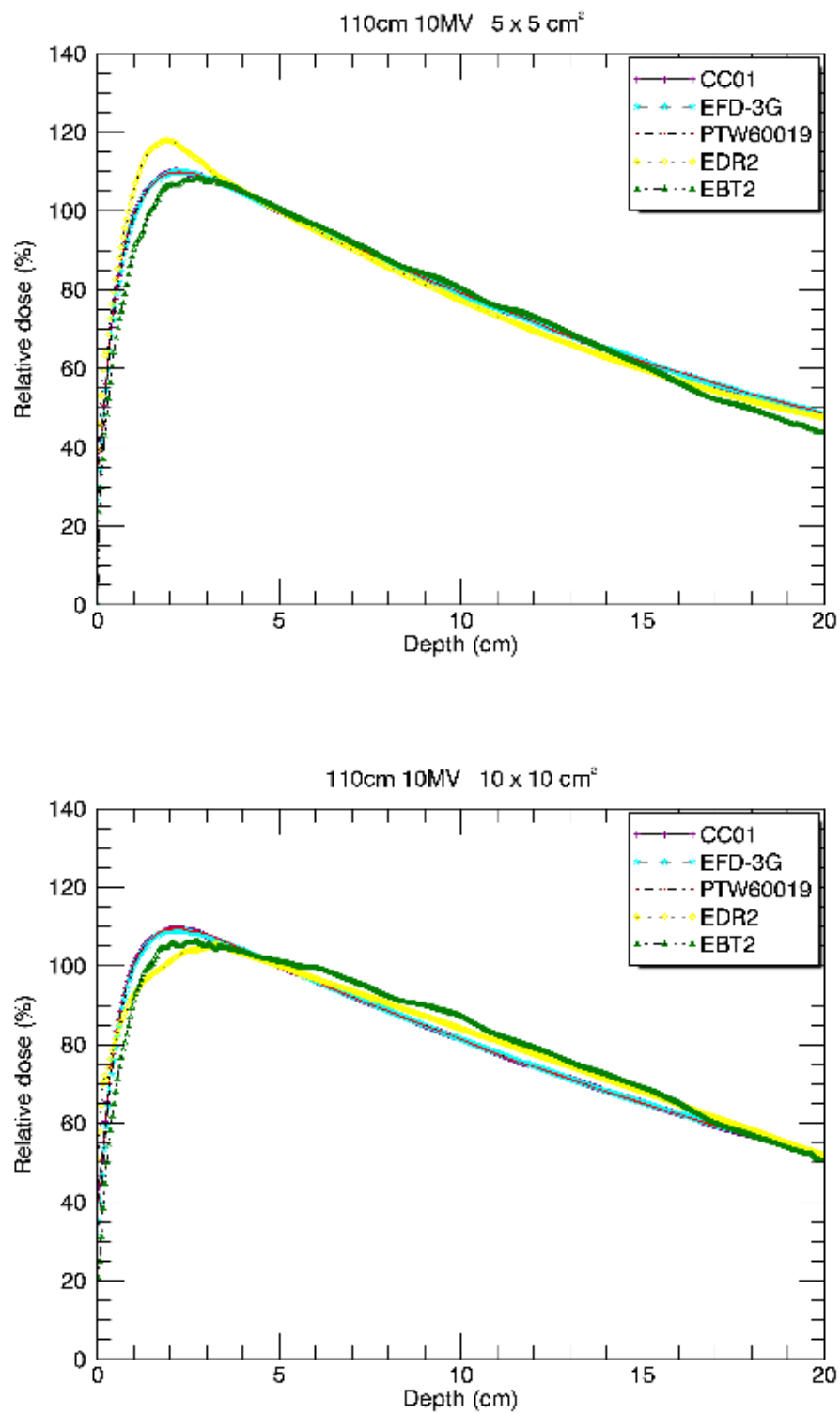


Figure 143. PDD curves for the different detectors measured at an SSD of 110 cm using a 10 MV photon beam for 5x5 cm² and 10x10 cm² field sizes

110 cm 15 MV PDD

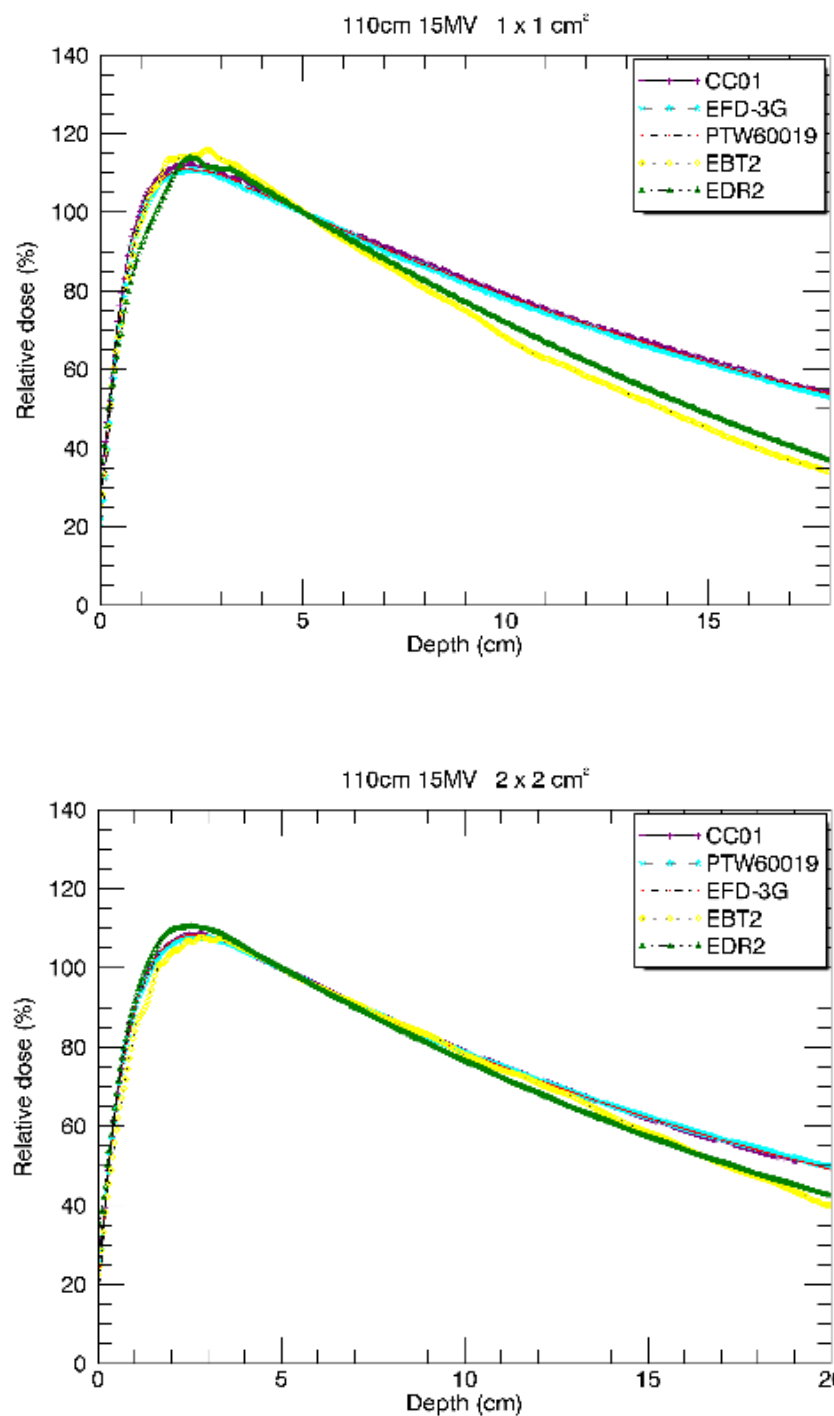


Figure 144. PDD curves for the different detectors measured at an SSD of 110 cm using a 15 MV photon beam for 1x1 cm² and 2x2 cm² field sizes

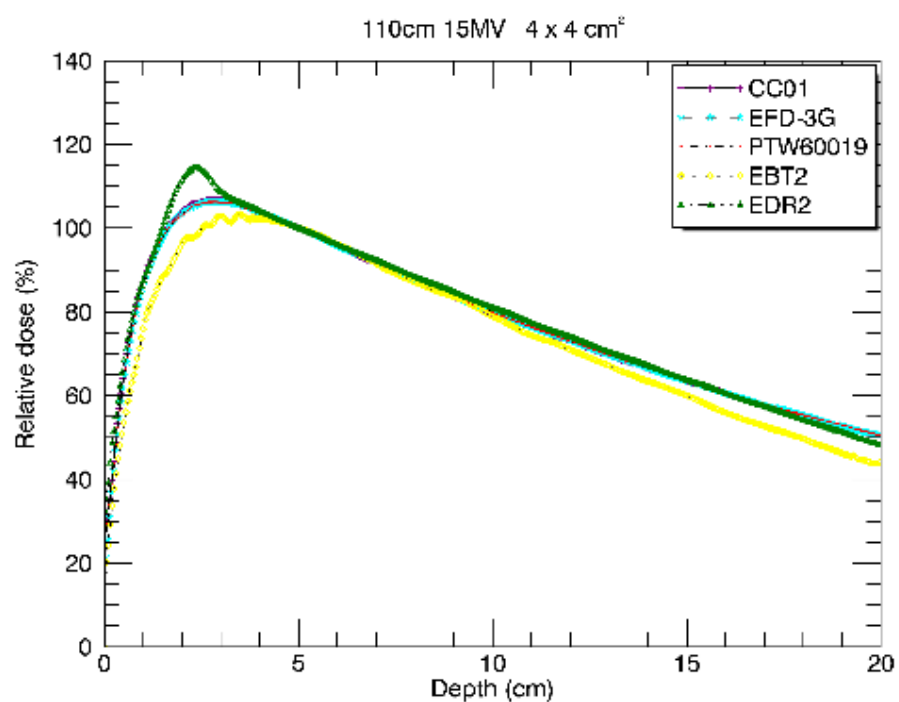
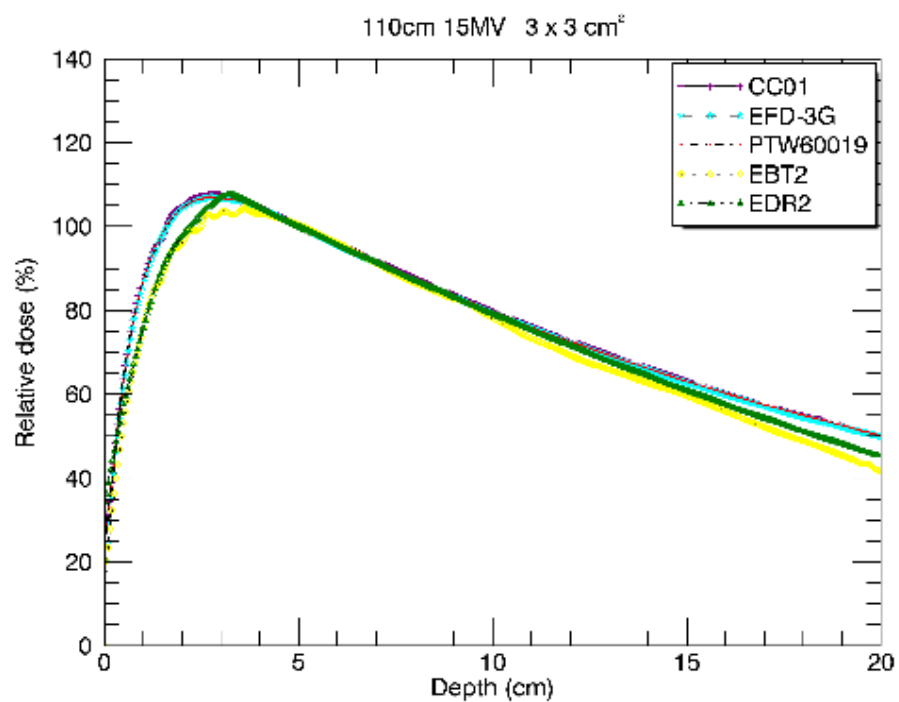


Figure 145. PDD curves for the different detectors measured at an SSD of 110 cm using a 15 MV photon beam for 3x3 cm² and 4x4 cm² field sizes

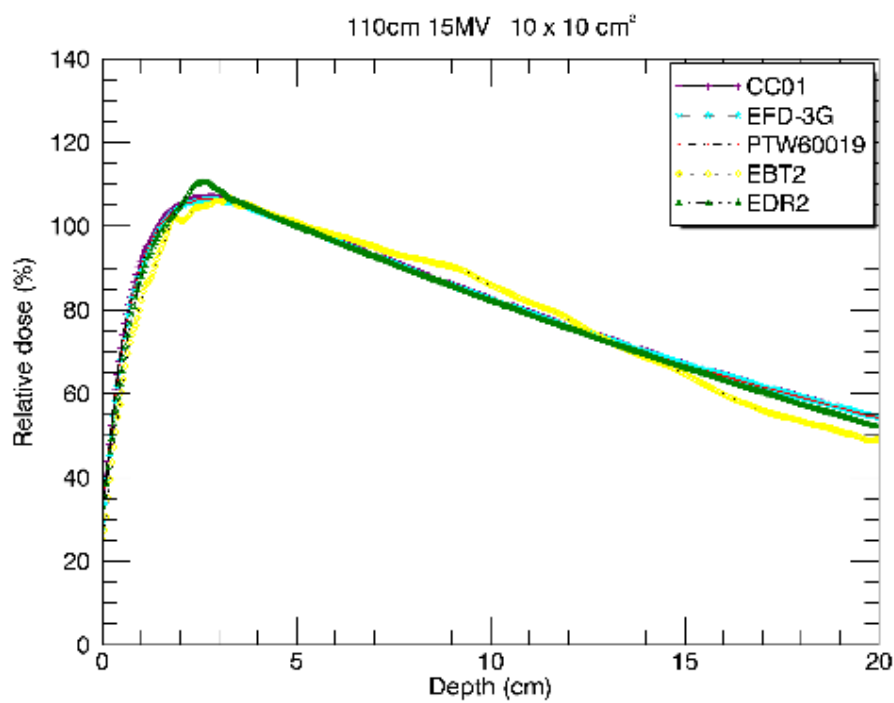
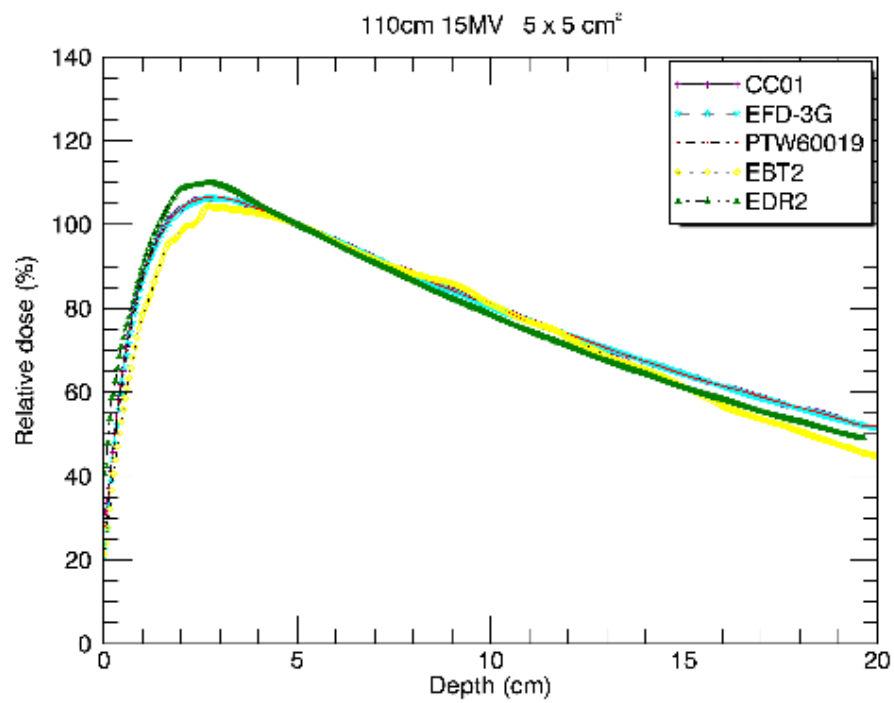


Figure 146. PDD curves for the different detectors measured at an SSD of 110 cm using a 15 MV photon beam for 5x5 cm² and 10x10 cm² field sizes

Table 10. Dmax positions for the different detectors measured at 110 cm SSD

Dmax							
110cm	6MV						
Field side length (cm)	Mean dmax (cm)	Stddev of Dmax	CC01 (cm)	EFD-3G (cm)	PTW60019 (cm)	EBT2 (cm)	EDR2 (cm)
1.20	1.59	0.30	1.40	1.41	1.40	1.66	2.08
2.40	1.71	0.19	1.56	1.58	1.59	1.82	2.00
3.60	1.72	0.16	1.58	1.63	1.60	1.92	1.86
4.80	1.83	0.39	1.60	1.65	1.62	1.78	2.52
6.00	1.68	0.13	1.56	1.57	1.62	1.82	1.82
12.00	1.74	0.28	1.56	1.58	1.56	1.80	2.20
Dmax							
110cm	10MV						
Field side length (cm)	Mean dmax (cm)	Stddev of Dmax	CC01 (cm)	EFD-3G (cm)	PTW60019 (cm)	EBT2 (cm)	EDR2 (cm)
1.20	1.86	0.08	1.80	1.88	1.84	1.98	1.78
2.40	2.29	0.19	2.14	2.15	2.18	2.58	2.38
3.60	2.51	0.36	2.26	2.30	2.30	2.58	3.12
4.80	2.50	0.26	2.30	2.32	2.32	2.76	2.82
6.00	2.31	0.30	2.22	2.30	2.30	2.78	1.94
12.00	2.39	0.27	2.21	2.20	2.18	2.66	2.70
Dmax							
110cm	15MV						
Field side length (cm)	Mean dmax (cm)	Stddev of Dmax	CC01 (cm)	EFD-3G (cm)	PTW60019 (cm)	EBT2 (cm)	EDR2 (cm)
1.20	2.30	0.17	2.20	2.20	2.28	2.60	2.24
2.40	2.73	0.21	2.66	2.64	2.74	3.08	2.54
3.60	3.05	0.38	2.80	2.80	2.82	3.68	3.14
4.80	2.99	0.56	2.86	2.90	2.88	3.92	2.38
6.00	2.88	0.13	2.96	2.84	2.90	3.00	2.68
12.00	2.82	0.20	2.76	2.74	2.78	3.18	2.66

4.4 Relative output factors

The relative output factor is defined as the ratio of the dose rate/MU measured at 10 cm depth for a particular field size to the dose rate/MU measured at the same depth for a reference field, in this case the 10×10 cm² field, at the same SSD. These factors were measured at different SSDs. The reason being to evaluate the change in the relative output factor as the detector moves away from the source, thereby decreasing source occlusion.

4.4.1 Output factors measured using a 6 MV photon beam at different SSDs

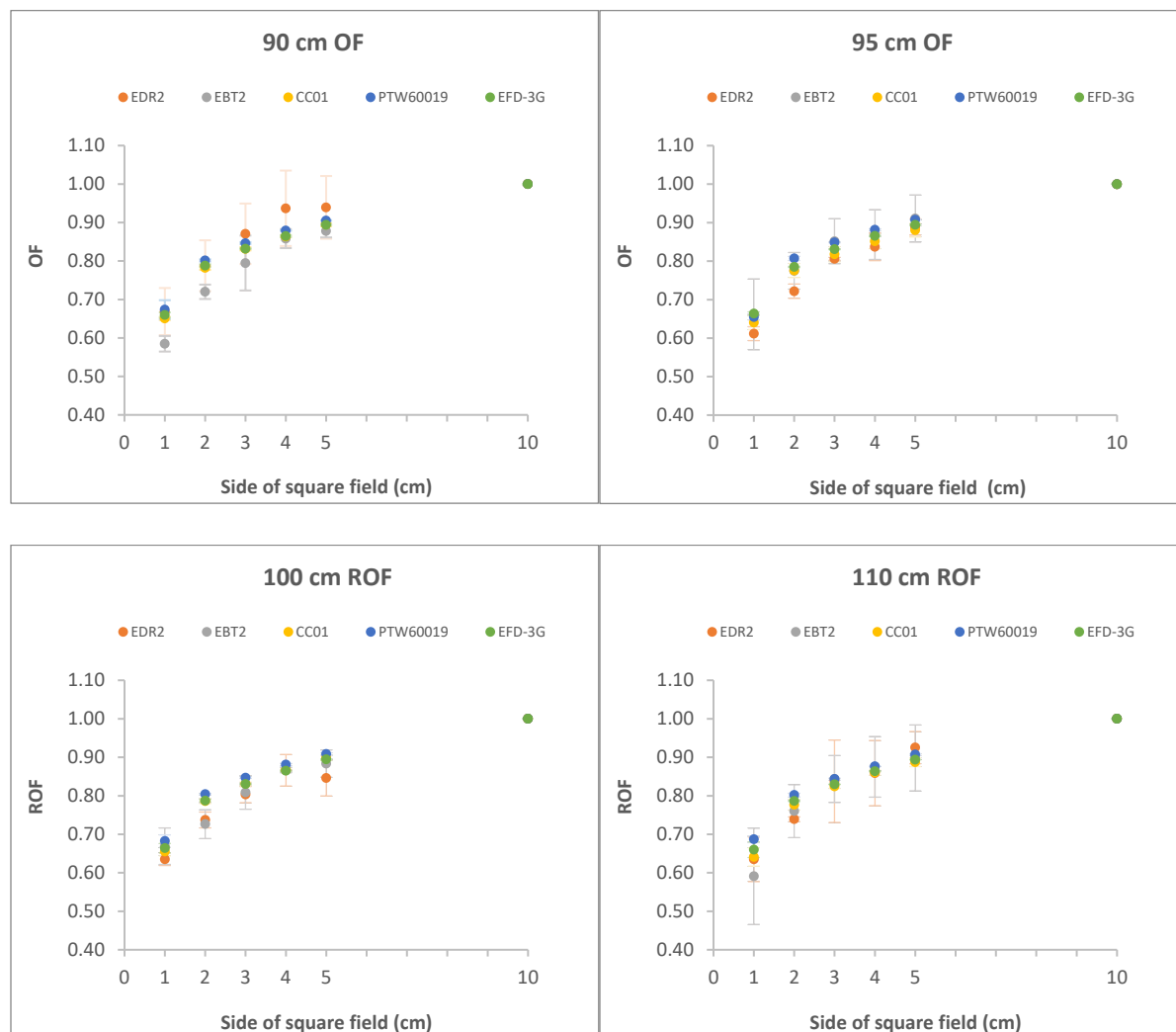


Figure 147. Output factors measured for the different detectors for a 6 MV photon energy beam (values are listed in appendix 2)

Figure 147 shows the ROF measured at different SSDs for the different detectors. These increases with increasing field sizes. The resulting output factors from the water based detectors are more stable compared to the two films that were used. The largest ROF variation is 3% for the CC01 (water based detector) at the 1×1 cm² field size. This field size is where most of the water tank detectors experienced the most variations even with the re-alignment measure put in place. The variation would have been higher if the detectors alignment was not checked. The films on the other hand, experience variations which ranged up to 10% in general (largest variation is 25% for the 1×1 cm² field size, these variations can be attributed to using different film lots in both types of films during the data acquisition process. The change in ROF from 1×1 cm² to 2×2 cm² field size

is higher compared the change between the $2 \times 2 \text{ cm}^2$ to $3 \times 3 \text{ cm}^2$. Literature (Li et al., 1995) showed that the minimum equivalent square field size is required to maintain the LEE for the 6 MV beam is $2.6 \times 2.6 \text{ cm}^2$, thus, the steep change of the output factor at field below this minimum field size. As explained the signal measured at a point is due to the influence of the primary beam and scatter. So, as the field size gradually decreases so does the influence of scatter at the central axis, or the point of measurement, resulting in a decrease of the signal measured thus a decrease in the output factor. Once the lateral electronic equilibrium minimum field size has been passed the decline in the measured signal is steeper resulting in a sharper drop of the relative output factor. This is shown in figure 147, there is a sharper drop in output factor for all the fields and as measured for the different detectors between the $1 \times 1 \text{ cm}^2$ and $2 \times 2 \text{ cm}^2$ field size.

The detectors that were used varied in density, with the high-density detector being expected to give a higher output factor at the field sizes in which the lateral equilibrium has broken down. The density effect is shown as the PTW60019 has slightly higher output factors compared to the low density CC01.

Figure 148, shows the different curve fitting formulas for the different SSDs. The curves are an average of the ROFs.

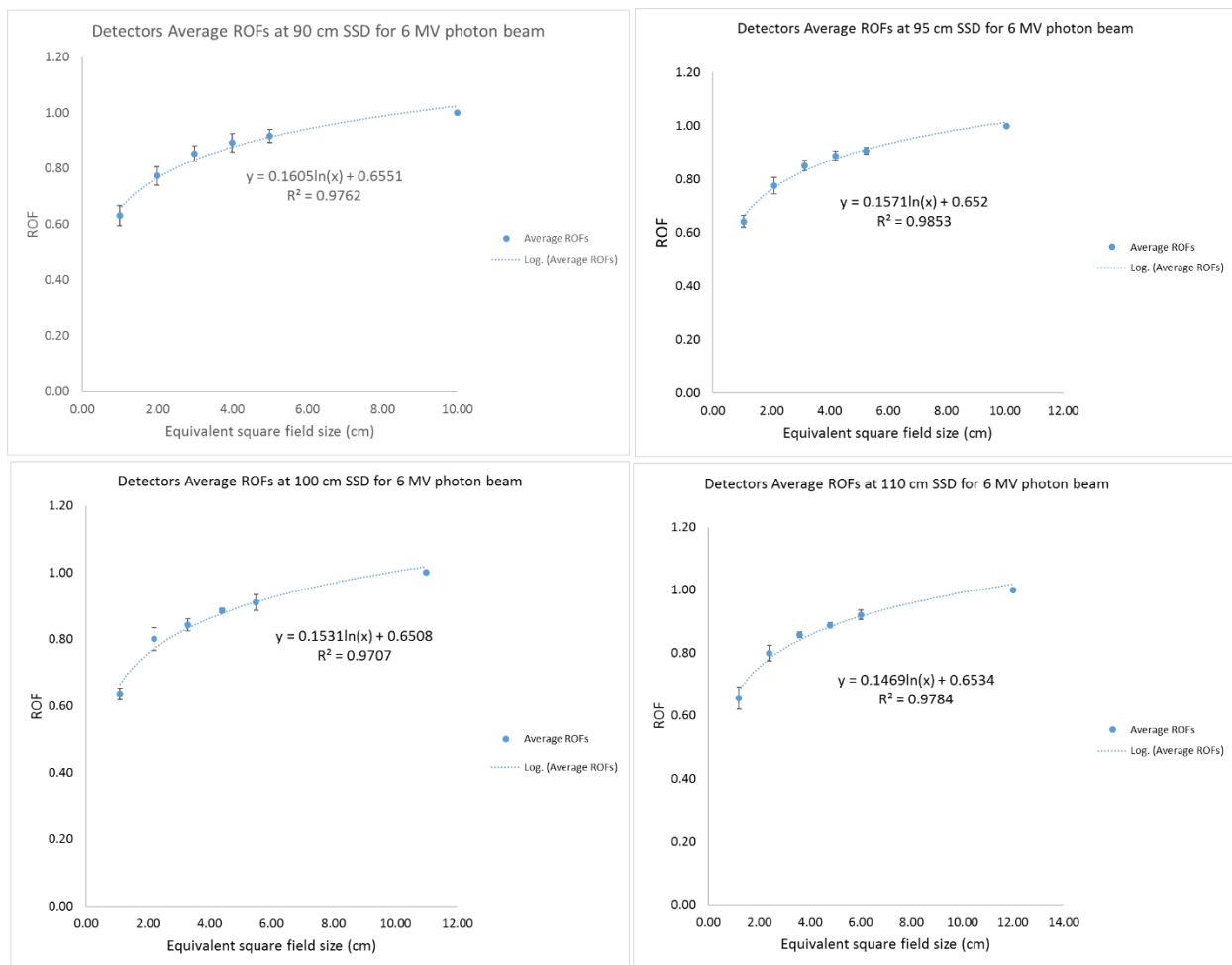


Figure 148. Curve fitting for the different ROFs

4.4.2 Output factors measured using a 10 MV photon beam at different SSDs

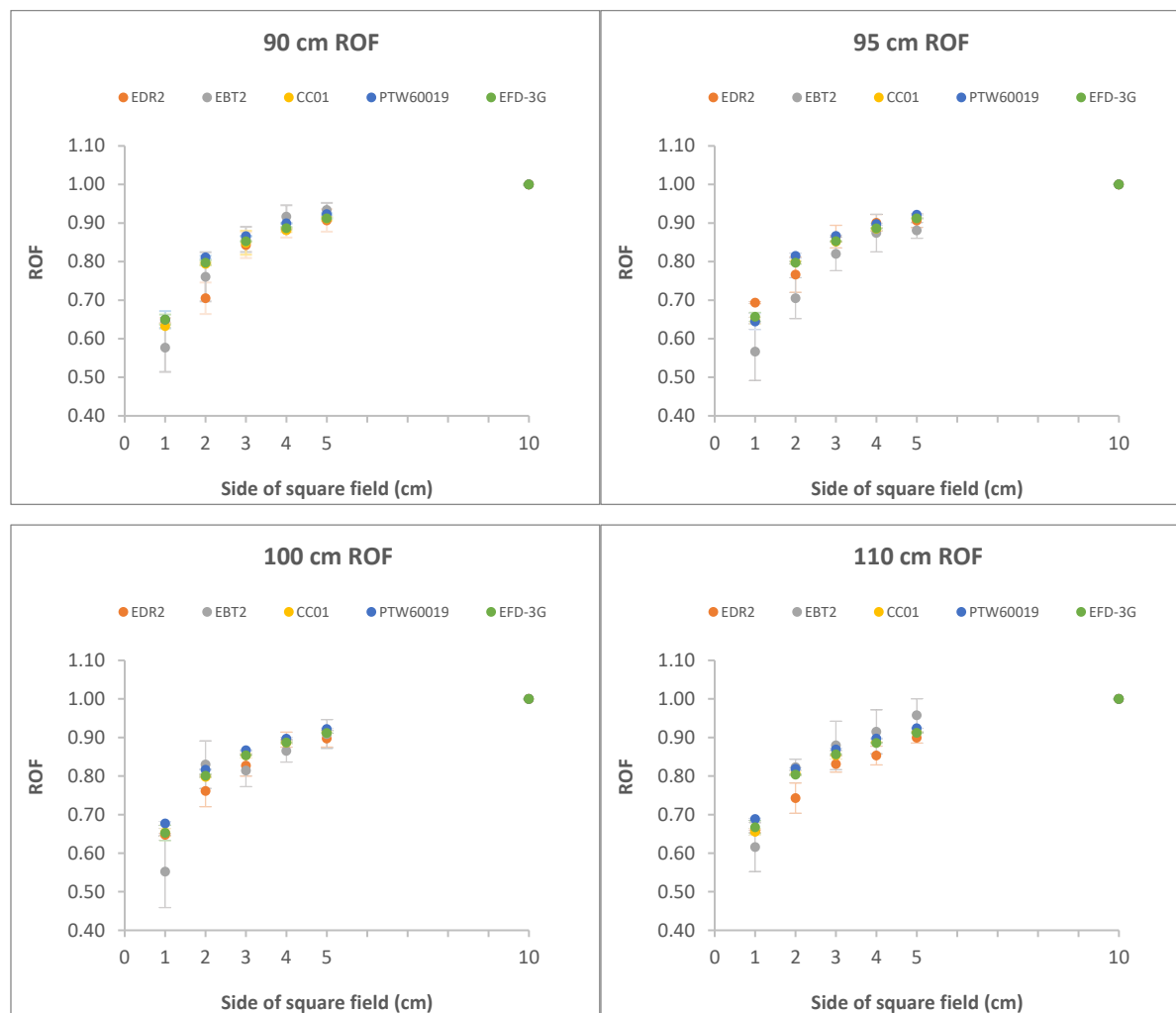


Figure 149. Output factors measured for the different detectors for a 10 MV photon energy beam (values are listed in appendix 2)

The ROFs were measured with a 10 MV photon beam at different SSDs as well as using different detectors, the results are shown in figure 149 and the average curve fits are shown in figure 150. As seen with the output factors measured increase as the field size is increased. Unlike the 6 MV photon beam, however the 10 MV photon beam has its minimum square field size required to maintain lateral electronic equilibrium at $3.4 \times 3.4 \text{ cm}^2$ field size. The drop in the ROF is seen only in the 1 cm and 2 cm fields as the 3 cm field is still within the LEE field.

The water based detectors displayed higher stability of the output factors compared to the films, with the highest standard deviation for these detectors being 3% for the EFD-3G diode at 100 cm

SSD with a 1 cm square field size set and the highest standard deviation for the films was 26% for the EBT2 film at 100 cm for a 1 cm square field size.

The increase in incident photon energy means more scatter will be in the forward direction, this will decrease the effect of artificial lateral electronic equilibrium due to the density of the detector. The measured output factors do indicate that the differences between the PTW60019 and the CC01 has decreased.

The water based detectors show a gradual increase of the 1 cm square field sizes as the SSD increases. This indicates that the signal detected increases slightly with SSD, the increase is solely due to the scatter component of the incident beam. The collected film data is too noisy at these levels to ascertain the output factor relation with the SSD.

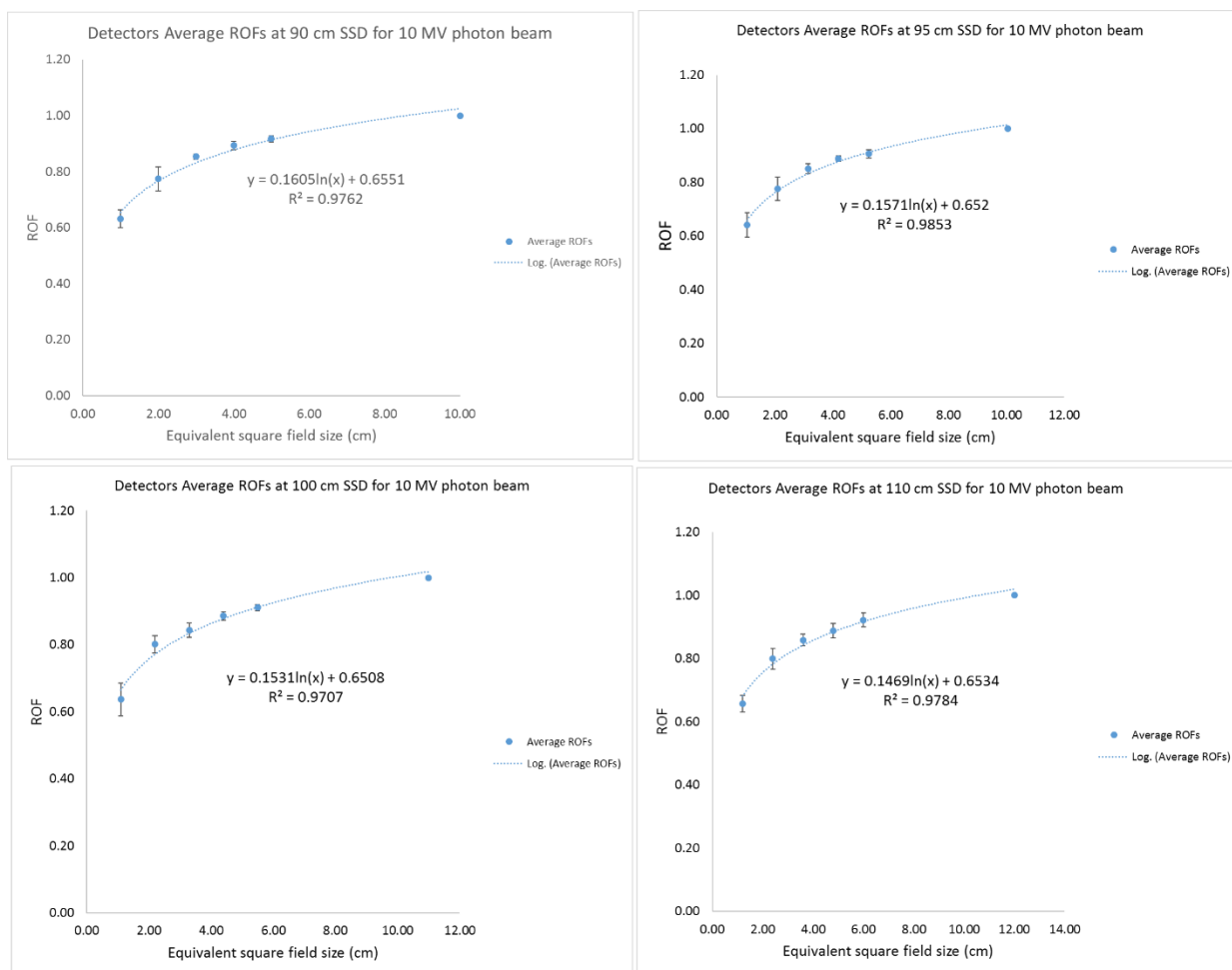


Figure 150. Curve fitting for the different ROFs

4.4.3 Output factors measured using a 15 MV photon beam at different SSDs

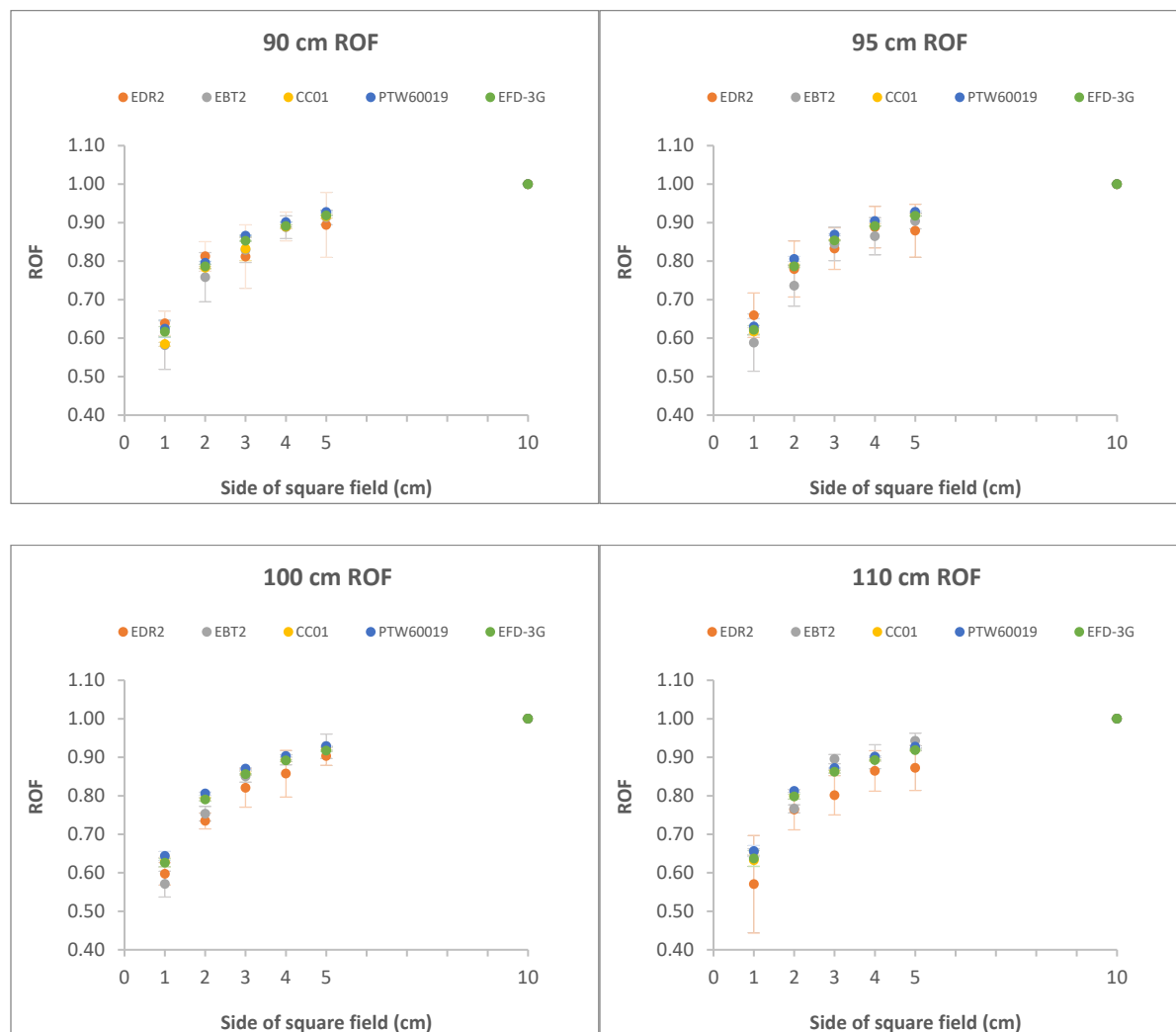


Figure 151. Output factors measured for the different detectors for a 15 MV photon energy beam (values are listed in appendix 2)

The 15 MV photon beam output factors also increase with field size with the minimum square field size for this energy to retain lateral electronic equilibrium increases to $3.8 \times 3.8 \text{ cm}^2$, as the scatter will travel further when compared to the two other energies. Thus, the output factor drop-off is expected to start at a field sizes below this minimum field, and this is clearly shown in figure 151 and the curve fits are shown in figure 152. There are sharp drops between the output factors measured at the 2 and 3 cm square field sizes compared to other energies, with the drop-off further increasing between the 1 cm and 2 cm square fields. The 15 MV has a higher output factor in fields larger than the required field size to maintain LEE, but these changes as soon as the field sizes are smaller and LEE cannot be maintained.

As mentioned earlier, with an increase in energy, scatter will be more in the forward direction and with higher energy, thus decreasing the ability of a denser material creates an artificial LEE. The denser detector, the PTW60019, still has larger ROFs but the differences are now smaller.

There is a gradual increase in the output factor as well here when comparing the different SSDs at the 1 cm square field size, but the order in increase is small.

The results have been collected using the stated detectors using the Synergy S LINAC. These results do show that there is variation among the detectors when it comes to measuring the beam profiles, PDDs and ROFs. This variation is shown to be dependent on the construction of the detector as was proposed.

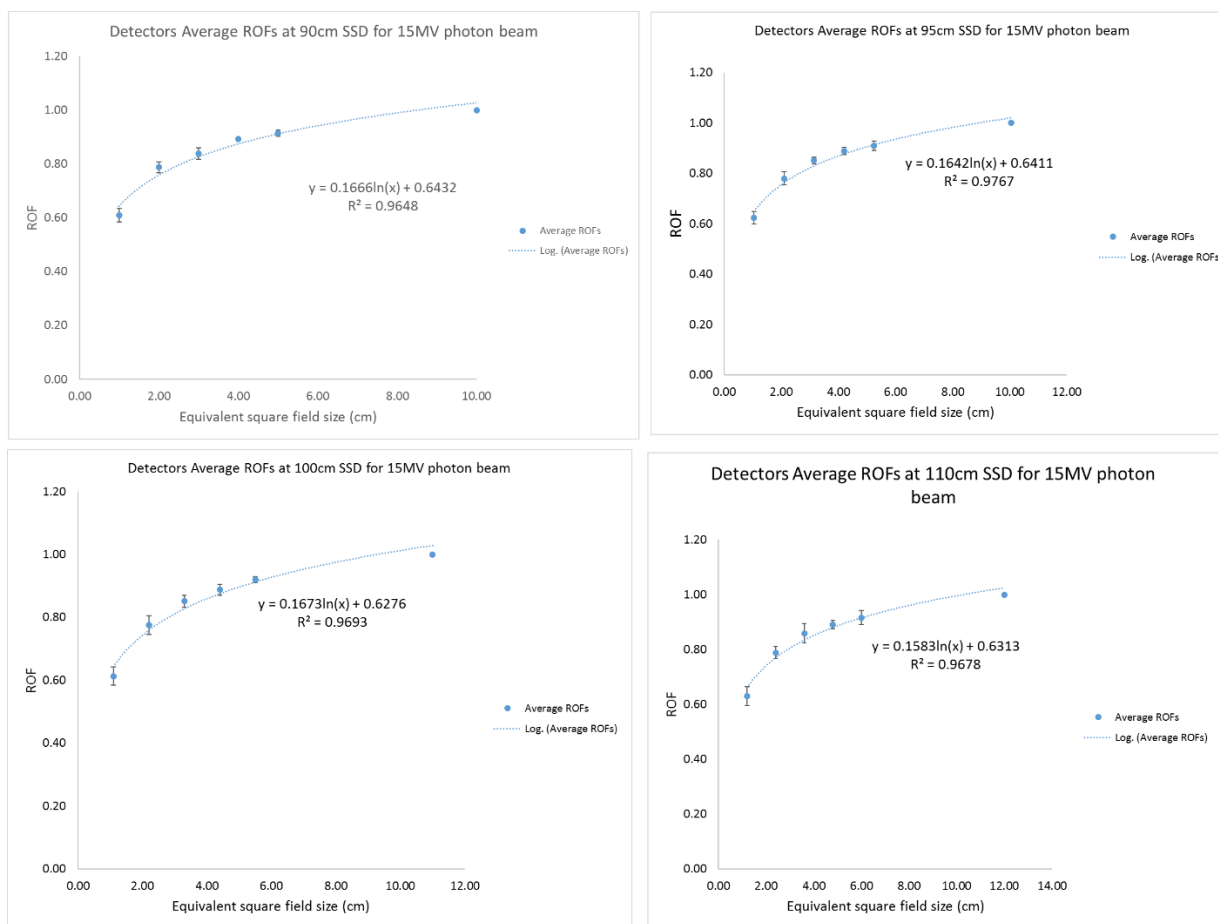


Figure 152. Curve fitting for the different ROFs

4.5 References

- Bucciolini, M., Buonamici, F. B., Mazzocchi, S., De Angelis, C., Onori, S., & Cirrone, G. A. P. (2003). Diamond detector versus silicon diode and ion chamber in photon beams of different energy and field size. *Medical Physics*, 30(8), 2149–54. <http://doi.org/10.1118/1.1591431>
- Cadman, P. F., McNutt, T., & Bzdusek, K. (2005, May 21). Validation of physics improvements for IMRT with a commercial treatment planning system. *Journal of Applied Clinical Medical Physics*. Retrieved from <http://www.jacmp.org/index.php/jacmp/article/view/2083/1209>
- Chetty, I. J., & Charland, P. M. (2002). Investigation of Kodak extended dose range (EDR) film for megavoltage photon beam dosimetry. *Physics in Medicine and Biology*, 47(20), 3629–3641. <http://doi.org/10.1088/0031-9155/47/20/305>
- Cheung, T., Butson, M. J., & Yu, P. K. N. (2006). Measurement of high energy x-ray beam penumbra with Gafchromic EBT radiochromic film. *Medical Physics*, 33(8), 2912–4. <http://doi.org/10.1118/1.2218318>
- Childress, N. L., & Rosen, I. I. (2004). Effect of processing time delay on the dose response of Kodak EDR2 film. *Medical Physics*, 31(8), 2284–2288. <http://doi.org/10.1118/1.1774111>
- Das, I. J., Cheng, C.-W., Watts, R. J., Ahnesjö, A., Gibbons, J., Li, X. A., ... Zhu, T. C. (2008). Accelerator beam data commissioning equipment and procedures: Report of the TG-106 of the Therapy Physics Committee of the AAPM. *Medical Physics*, 35(9), 4186–4215. <http://doi.org/10.1118/1.2969070>
- Hsu, S.-H., Kulasekere, R., & Roberson, P. L. (2010, August 5). Analysis of variation in calibration curves for Kodak XV radiographic film using model-based parameters. *Journal of Applied Clinical Medical Physics*. Retrieved from <http://www.jacmp.org/index.php/jacmp/article/view/3172/2039>
- Klein, E. E., Hanley, J., Bayouth, J., Yin, F.-F., Simon, W., Dresser, S., ... Holmes, T. (2009). Task Group 142 report: quality assurance of medical accelerators. *Medical Physics*, 36(9), 4197–212. <http://doi.org/10.1118/1.3190392>
- Lewis, D., & Devic, S. (2015). Correcting scan-to-scan response variability for a radiochromic film-based reference dosimetry system. *Medical Physics*, 42(10), 5692–701. <http://doi.org/10.1118/1.4929563>
- Lewis, D., Micke, A., Yu, X., & Chan, M. F. (2012). An efficient protocol for radiochromic film dosimetry combining calibration and measurement in a single scan. *Medical Physics*, 39(10), 6339. <http://doi.org/10.1118/1.4754797>

- Li, X. a, Soubra, M., Szanto, J., & Gerig, L. H. (1995). Lateral electron equilibrium and electron contamination in measurements of head-scatter factors using miniphantoms and brass caps. *Medical Physics*, 22(7), 1167–1170. <http://doi.org/10.1118/1.597508>
- Low, D. A., Moran, J. M., Dempsey, J. F., Dong, L., & Oldham, M. (2011). Dosimetry tools and techniques for IMRT. *Medical Physics*, 38(3), 1313–1338. <http://doi.org/10.1118/1.3514120>
- Micke, A., Lewis, D. F., & Yu, X. (2011). Multichannel film dosimetry with nonuniformity correction. *Medical Physics*, 38(5), 2523. <http://doi.org/10.1118/1.3576105>
- Pai, S., Das, I. J., Dempsey, J. F., Lam, K. L., Losasso, T. J., Olch, A. J., ... Wilcox, E. E. (2007). Radiographic film for megavoltage beam dosimetry. *Medical Physics*, 34(6), 2228–2258. <http://doi.org/10.1118/1.2736779>
- Roberson, P. L., Moran, J. M., & Kulasekere, R. (2008). Radiographic film dosimetry for IMRT fields in the near-surface buildup region. *Journal of Applied Clinical Medical Physics*, 9(4), 87–97. <http://doi.org/10.1120/jacmp.v9i4.2782>

Chapter 5 Conclusion

The characteristics of the small fields using different photon energies were measured with the different detectors at 90 cm, 95 cm, 100 cm and 110 cm SSDs.

The measurements were carried out using the water phantom as well as the RW3 phantom. These detectors took measurements in water. While, the EBT2 (radiochromic film) and the EDR2 (radiographic film) were used with the RW3 phantom.

The water phantom setup had a good reproducibility, due to use of a calibrated digital level, which allowed for more precise levelling of both the water phantom as well as the detector holders. This improved the water level, and also increased the accuracy with which the PDDs were collected especially in the small fields along the CAX. In addition, it was found that the centring of the detector was a major influence when measuring signals at smaller fields, therefore, it was necessary to re-centre the detector as soon as the field sizes reached $1 \times 1 \text{ cm}^2$ field size as the focal spot can move around when changing from one energy to the next. This will influence the measured ROF.

The EBT2 films were given a minimum of 24 hours to allow for full development prior to scanning. The film direction was indicated with a cut in the film, and a thin marker was used to indicate the relevant details. These were cleaned with alcohol to remove fingerprints and oils, however this resulted in smooth surfaces which caused Newton ring artefacts. The three-channel dosimetry was performed as this is able to correct for the fingerprints.

The EDR2 film presented problems when it came to developing the films. It was seen that the roller of the film developer was causing pressure artefacts. This issue was addressed digitally by smoothing the film data. The physical solution would be to develop the films by hand. This was not practical due to the amount of films that were developed.

The issue with both films was that different batches were utilized. The EBT2 film required a new calibration curve with change of different batch. The EDR2 calibration curves were carried out with each measurement session, to overcome the inter batch variations. The results showed that the EBT2 film calibration curves were more stable compared to the EDR2 curves as they showed

an RMSE below 2.5 for the different colour channels. The resulting calibration coefficients were used to convert the scanned pixel values to dose, and the resulting dose curves were smoothed prior to comparing the results with the water phantom detectors.

The resulting beam profiles in both the Inline and Crossline direction/axes indicated that the EBT2 film offered the best resolution of the penumbra and this was closely followed by the EFD-3G and PTW60019 detectors. The CC01 and the EDR2 film showed wider penumbrae, the CC01 penumbrae was widened due to the large active volume, whereas the EDR2 was widened due to its energy dependence. The field size measurements were insignificant as all detectors were able to measure the field size within the limit. It was noted from the measurements that the actual LINAC sets inconsistent field sizes in the Crossline direction. Hence, to measure the beam profiles, the PTW60019 would be the ideal detector as, its penumbra is not significantly different from the EBT2 film.

The PDD indicates the change in dose deposition with increasing depth. The measurements were performed at the CAX. The CAX function found in the Omnipro[®] software was used to re-evaluate the CAX positioning of the detector when the field size was changed to 1×1 cm². The differences between the Dmax values amongst the detectors were insignificant across the different energy ranges as well as the different SSDs. As the field size increases the DMAX increased, but this was only up to a certain field size. The 6 MV and 10 MV photon beam showed this change of Dmax from the 2 cm field, whereas the 15 MV showed this as early as the 3 cm field. The change Dmax for the 3 cm and 2 cm square fields is 10%, 7%, 5%, and 3% as the SSD increased from 90 cm to 95 cm, 100 cm and 110 cm respectively, for the 15 MV photon beam. The difference decreases as the field sizes increase.

The RW3 setup posed a problem when it came to measurement of the PDDs. The PDDs need the gantry to be set to 88° as the RW3 could not stand without proper support. The major errors in both films when measuring PDDs were in the 1×1 cm² field, this was due to the gantry tilt. The future measurements of PDD at the 1×1 cm² field size or lower should be performed at a tilt that is less than 2°, bearing in mind the electronic contamination. Any of these detectors can collect

PDD curves, nonetheless care should be taken when comparing the data within the build-up region especially for the films.

ROFs are shown to be dependent on the incoming photon beam energy and field size. As the field size is decreased there is an increase in the lateral electronic disequilibrium, therefore less dose is deposited on the CAX, consequently the measured ROFs values decrease as seen in the acquired data. The sharpness of the drop is energy dependent, i.e. the higher the energy the sharper the decline. The results show that the 15 MV photon beam has higher ROFs until 3 cm field size compared to the 6 MV and 10 MV, from there on the ROF dropped sharply to having the same or lower ROF at the 1 cm field size for all the photon energies.

The results do ascertain that the ROFs do not change with a change in SSD. This was the case for all the field sizes except the 1 cm field size. The CV of the ROFs at the different SSDs for the 6 MV photon beam were 3%, 7%, 1.1%, 2.1% and 0.4% for the EDR2, EBT2, CC01, PTW60019 and EFD-3G respectively. The CV of the ROFs at the different SSDs for the 10 MV photon beam were 3%, 4%, 1.6%, 3.2% and 1.2% for the EDR2, EBT2, CC01, PTW60019 and EFD-3G respectively. The CV of the ROFs at the different SSDs for the 15 MV photon beam were 6.5%, 6.2%, 3.5%, 2.2% and 1.4% for the EDR2, EBT2, CC01, PTW60019 and EFD-3G respectively. When the SSD is increased, there is more of the source that the detector can see thus there should be a slight increase in the signal detected, and this is shown in that the ROFs increase with the SSD. The 6 MV photon beam shows a smaller variation compared to the other energies, further research into the photon source width would shed more light onto this result.

The results from the detectors, PTW60019, EFD-3G, EDR2, EBT2, CC01, as listed in terms of decreasing physical density indicated that the PTW60019 measured a higher ROF especially in field sizes that had lateral electronic disequilibrium. The percentage differences between the PTW60019 and the CC01 were -3.5%, -2.2%, -4.4% and -6.6% at 90, 95, 100 and 110 cm respectively for the 6 MV photon beam at the field size. The percentage differences at the same SSDs for the 10 MV photon beams are -2.6%, 0.5%, -3.5% and -4.8%. And the 15 MV photon beam shows percentage differences of -6.4%, -2.1%, -2.5% and -3.6% between the two detectors.

The debate is still ongoing, as to which detector is best for use in small fields, but from this study, the data show that there is no significant difference between the ROF between the detectors. The film data showed a large variation in calculating the ROF, therefore multiple films should be used to calculate the ROF with acceptable accuracy.

Appendix A Penumbrae and Field sizes

Table 11. Beam profile details for the 1 - 3 square field sizes measured using the five different detectors at the different SSDs with a 6 MV photon beam. Penumbra on the left, PenL, penumbra on the right, PenR and field size, FS

90cm 6MV Inline						
1×1 cm ²	Detector	EDR2	EBT2	PTW60019	EFD-3G	CC01
	PenL	0.35	0.28	0.31	0.33	0.31
	PenR	0.39	0.28	0.34	0.34	0.32
	FS	1.04	1.00	1.01	1.01	1.05
95cm 6MV Inline						
1.05×1.05 cm ²	Detector	EDR2	EBT2	PTW60019	EFD-3G	CC01
	PenL	0.35	0.27	0.30	0.31	0.30
	PenR	0.35	0.27	0.32	0.32	0.30
	FS	1.08	1.07	1.01	1.10	1.03
100cm 6MV Inline						
1.1×1.1 cm ²	Detector	EDR2	EBT2	PTW60019	EFD-3G	CC01
	PenL	0.38	0.27	0.31	0.31	0.31
	PenR	0.40	0.27	0.33	0.31	0.34
	FS	1.11	1.09	1.06	1.07	1.09
110cm 6MV Inline						
1.2×1.2 cm ²	Detector	EDR2	EBT2	PTW60019	EFD-3G	CC01
	PenL	0.40	0.35	0.37	0.33	0.36
	PenR	0.40	0.36	0.37	0.33	0.36
	FS	1.23	1.20	1.17	1.16	1.18
90cm 6MV Inline						
2×2 cm ²	Detector	EDR2	EBT2	PTW60019	EFD-3G	CC01
	PenL	0.39	0.33	0.34	0.34	0.34
	PenR	0.40	0.34	0.33	0.34	0.32
	FS	2.06	1.96	1.97	1.97	1.99
95cm 6MV Inline						
2.1×2.1 cm ²	Detector	EDR2	EBT2	PTW60019	EFD-3G	CC01
	PenL	0.44	0.35	0.35	0.35	0.35
	PenR	0.44	0.35	0.36	0.34	0.35
	FS	2.09	2.11	2.05	2.05	2.07
100cm 6MV Inline						
2.2×2.2 cm ²	Detector	EDR2	EBT2	PTW60019	EFD-3G	CC01
	PenL	0.43	0.37	0.36	0.34	0.37
	PenR	0.44	0.34	0.39	0.34	0.37
	FS	2.20	2.20	2.16	2.19	2.17
110cm 6MV Inline						
2.4×2.4 cm ²	Detector	EDR2	EBT2	PTW60019	EFD-3G	CC01
	PenL	0.48	0.42	0.40	0.37	0.39
	PenR	0.48	0.42	0.42	0.28	0.41
	FS	2.41	2.41	2.36	2.36	2.36
90cm 6MV Inline						
3×3 cm ²	Detector	EDR2	EBT2	PTW60019	CC01	EFD-3G
	PenL	0.45	0.34	0.35	0.36	0.37
	PenR	0.45	0.34	0.36	0.37	0.37
	FS	3.03	3.00	2.97	2.99	3.01
95cm 6MV Inline						
3.15×3.15 cm ²	Detector	EDR2	EBT2	PTW60019	EFD-3G	CC01
	PenL	0.43	0.42	0.37	0.38	0.39
	PenR	0.43	0.42	0.38	0.38	0.39
	FS	3.12	3.13	3.11	3.12	3.13
100cm 6MV Inline						
3.3×3.3 cm ²	Detector	EDR2	EBT2	PTW60019	EFD-3G	CC01
	PenL	0.48	0.38	0.38	0.37	0.40
	PenR	0.48	0.39	0.39	0.39	0.41
	FS	3.28	3.31	3.27	3.30	3.27
110cm 6MV Inline						
3.6×3.6 cm ²	Detector	EDR2	EBT2	PTW60019	EFD-3G	CC01
	PenL	0.51	0.56	0.40	0.40	0.42
	PenR	0.51	0.56	0.41	0.40	0.41
	FS	3.64	3.54	3.54	3.55	3.57
90cm 6MV Crossline						
1×1 cm ²	Detector	EDR2	EBT2	PTW60019	EFD-3G	CC01
	PenL	0.46	0.37	0.44	0.46	0.46
	PenR	0.46	0.36	0.48	0.45	0.48
	FS	1.10	0.97	1.09	1.15	1.06
95cm 6MV Crossline						
1.05×1.05 cm ²	Detector	EDR2	EBT2	PTW60019	CC01	EFD-3G
	PenL	0.51	0.35	0.45	0.46	0.48
	PenR	0.49	0.34	0.51	0.47	0.48
	FS	1.14	1.06	1.24	1.24	1.18
100cm 6MV Crossline						
1.1×1.1 cm ²	Detector	EDR2	EBT2	PTW60019	EFD-3G	CC01
	PenL	0.52	0.39	0.50	0.51	0.49
	PenR	0.53	0.39	0.54	0.51	0.56
	FS	1.20	1.07	1.24	1.29	1.23
110cm 6MV Crossline						
1.2×1.2 cm ²	Detector	EDR2	EBT2	PTW60019	EFD-3G	CC01
	PenL	0.57	0.43	0.56	0.58	0.59
	PenR	0.57	0.42	0.56	0.58	0.59
	FS	1.35	1.16	1.47	1.42	1.29
90cm 6MV Crossline						
2×2 cm ²	Detector	EDR2	EBT2	PTW60019	EFD-3G	CC01
	PenL	0.57	0.48	0.55	0.58	0.55
	PenR	0.61	0.49	0.58	0.54	0.60
	FS	2.06	1.91	2.08	2.07	2.11
95cm 6MV Crossline						
2.1×2.1 cm ²	Detector	EDR2	EBT2	PTW60019	CC01	EFD-3G
	PenL	0.58	0.54	0.55	0.54	0.55
	PenR	0.59	0.53	0.59	0.57	0.59
	FS	2.16	2.05	2.14	2.24	2.13
100cm 6MV Crossline						
2.2×2.2 cm ²	Detector	EDR2	EBT2	PTW60019	EFD-3G	CC01
	PenL	0.63	0.58	0.56	0.56	0.59
	PenR	0.63	0.58	0.59	0.57	0.63
	FS	2.23	2.18	2.24	2.26	2.26
110cm 6MV Crossline						
2.4×2.4 cm ²	Detector	EDR2	EBT2	PTW60019	EFD-3G	CC01
	PenL	0.65	0.63	0.67	0.67	0.63
	PenR	0.61	0.63	0.63	0.64	0.68
	FS	2.38	2.32	2.52	2.37	2.49
90cm 6MV Crossline						
3×3 cm ²	Detector	EDR2	EBT2	PTW60019	EFD-3G	CC01
	PenL	0.64	0.55	0.56	0.53	
	PenR	0.64	0.55	0.56	0.55	0.58
	FS	3.06	2.95	3.07	3.10	3.06
95cm 6MV Crossline						
3.15×3.15 cm ²	Detector	EDR2	EBT2	PTW60019	CC01	EFD-3G
	PenL	0.61	0.58	0.60	0.56	0.60
	PenR	0.61	0.58	0.62	0.58	0.61
	FS	3.18	3.16	3.20	3.22	3.27
100cm 6MV Crossline						
3.3×3.3 cm ²	Detector	EDR2	EBT2	PTW60019	EFD-3G	CC01
	PenL	0.71	0.63	0.61	0.60	0.69
	PenR	0.71	0.63	0.61	0.59	0.69
	FS	3.26	3.33	3.37	3.41	3.37
110cm 6MV Crossline						
3.6×3.6 cm ²	Detector	EDR2	EBT2	PTW60019	EFD-3G	CC01
	PenL	0.77	0.66	0.71	0.74	0.75
	PenR	0.77	0.67	0.71	0.75	0.71
	FS	3.71	3.54	3.63	3.69	3.68

Table 12. Beam profile details for the 4 - 10 square field sizes measured using the five different detectors at the different SSDs with a 6 MV photon beam.

90cm 6MV Inline						
4x4 cm ²	Detector	EBT2	EDR2	CC01	PTW60019	EFD-3G
	PenL	0.41	0.60		0.40	0.38
	PenR	0.41	0.62		0.38	0.38
	FS	3.94	4.03		3.99	3.98
95cm 6MV Inline						
4.2x4.2 cm ²	Detector	EDR2	EBT2	PTW60019	EFD-3	CC01
	PenL	0.50	0.40		0.52	0.42
	PenR	0.50	0.40		0.52	0.40
	FS	4.26	4.23		4.30	4.18
100cm 6MV Inline						
4.4x4.4 cm ²	Detector	EDR2	EBT2	PTW60019	EFD-3G	CC01
	PenL	0.45	0.39		0.42	0.43
	PenR	0.47	0.42		0.39	0.41
	FS	4.38	4.42		4.35	4.38
110cm 6MV Inline						
4.8x4.8 cm ²	Detector	EDR2	EBT2	PTW60019	EFD-3G	CC01
	PenL	0.45	0.39		0.43	0.42
	PenR	0.47	0.42		0.39	0.41
	FS	4.38	4.42		4.35	4.38
90cm 6MV Inline						
5x5 cm ²	Detector	EDR2	EBT2	PTW60019	EFD-3G	CC01
	PenL	0.50	0.40		0.40	0.40
	PenR	0.50	0.39		0.39	0.40
	FS	5.04	4.97		5.04	5.02
95cm 6MV Inline						
5.25x5.25 cm ²	Detector	EDR2	EBT2	PTW60019	EFD-3G	CC01
	PenL	0.50	0.44		0.42	0.45
	PenR	0.50	0.44		0.43	0.43
	FS	5.28	5.23		5.26	5.28
100cm 6MV Inline						
5.5x5.5 cm ²	Detector	EDR2	EBT2	PTW60019	EFD-3G	CC01
	PenL	0.54	0.68		0.43	0.44
	PenR	0.54	0.68		0.42	0.45
	FS	5.51	5.50		5.55	5.53
110cm 6MV Inline						
6x6 cm ²	Detector	EDR2	EBT2	PTW60019	EFD-3G	CC01
	PenL	0.60	0.64		0.45	0.47
	PenR	0.62	0.64		0.45	0.47
	FS	6.08	6.06		6.01	6.04
90cm 6MV Inline						
10x10 cm ²	Detector	EDR2	EBT2	PTW60019	EFD-3G	CC01
	PenL	0.76	0.80		0.47	0.52
	PenR	0.76	0.80		0.46	0.53
	FS	10.12	9.93		9.99	10.04
95cm 6MV Inline						
10.5x10.5 cm ²	Detector	EDR2	EBT2	PTW60019	EFD-3G	CC01
	PenL	0.65	0.53		0.48	0.54
	PenR	0.65	0.53		0.49	0.53
	FS	10.84	10.52		10.48	10.49
100cm 6MV Inline						
11x11 cm ²	Detector	EDR2	EBT2	PTW60019	EFD-3G	CC01
	PenL	0.64	0.55		0.49	0.55
	PenR	0.64	0.55		0.51	0.57
	FS	11.11	11.05		10.97	11.01
110cm 6MV Inline						
12x12 cm ²	Detector	EDR2	EBT2	PTW60019	EFD-3G	CC01
	PenL	0.73	0.65		0.53	0.60
	PenR	0.73	0.65		0.54	0.60
	FS	12.08	12.05		11.98	12.01

90cm 6MV Crossline						
4x4 cm ²	Detector	EDR2	EBT2	PTW60019	EFD-3G	CC01
	PenL	0.70	0.55		0.56	0.61
	PenR	0.70	0.55		0.60	0.63
	FS	4.00	3.92		3.92	4.09
95cm 6MV Crossline						
4.2x4.2 cm ²	Detector	EDR2	EBT2	PTW60019	CC01	EFD-3G
	PenL	0.68	0.61		0.63	0.58
	PenR	0.68	0.61		0.63	0.70
	FS	4.21	4.16		4.27	4.38
100cm 6MV Crossline						
4.4x4.4 cm ²	Detector	EDR2	EBT2	PTW60019	EFD-3G	CC01
	PenL	0.69	0.68		0.68	0.61
	PenR	0.70	0.68		0.69	0.68
	FS	4.42	4.48		4.54	4.41
110cm 6MV Crossline						
4.8x4.8 cm ²	Detector	EDR2	EBT2	PTW60019	EFD-3G	CC01
	PenL	0.75	0.72		0.74	0.67
	PenR	0.75	0.72		0.73	0.66
	FS	4.91	4.80		4.71	4.86
90cm 6MV Crossline						
5	Detector	EDR2	EBT2	PTW60019	EFD-3G	CC01
	PenL	0.67	0.57		0.62	0.58
	PenR	0.67	0.57		0.62	0.65
	FS	5.06	4.90		5.08	5.09
95cm 6MV Crossline						
5.25x5.25 cm ²	Detector	EDR2	EBT2	PTW60019	CC01	EFD-3G
	PenL	0.69	0.62		0.66	0.66
	PenR	0.69	0.62		0.65	0.64
	FS	5.28	5.24		5.30	5.33
100cm 6MV Crossline						
5.5x5.5 cm ²	Detector	EDR2	EBT2	PTW60019	EFD-3G	CC01
	PenL	0.75	0.74		0.70	0.64
	PenR	0.75	0.74		0.69	0.71
	FS	5.45	5.56		5.56	5.59
110cm 6MV Crossline						
6x6 cm ²	Detector	EDR2	EBT2	PTW60019	EFD-3G	CC01
	PenL	0.75	0.81		0.74	0.77
	PenR	0.76	0.81		0.73	0.78
	FS	6.01	6.07		6.07	6.10
90cm 6MV Crossline						
10x10 cm ²	Detector	EDR2	EBT2	PTW60019	CC01	EFD-3G
	PenL	0.80	0.76		0.71	0.75
	PenR	0.80	0.76		0.69	0.71
	FS	10.00	9.84		10.01	10.01
95cm 6MV Crossline						
10.5x10.5 cm ²	Detector	EDR2	EBT2	PTW60019	CC01	EFD-3G
	PenL	0.75	0.83		0.70	0.77
	PenR	0.75	0.82		0.73	0.79
	FS	10.47	10.45		10.45	10.53
100cm 6MV Crossline						
11x11 cm ²	Detector	EDR2	EBT2	PTW60019	EFD-3G	CC01
	PenL	0.71	0.68		0.75	0.83
	PenR	0.71	0.68		0.76	0.83
	FS	11.03	11.02		10.92	11.03
110cm 6MV Crossline						
12x12 cm ²	Detector	EDR2	EBT2	PTW60019	EFD-3G	CC01
	PenL	0.95	0.91		0.84	0.91
	PenR	0.95	0.91		0.81	0.87
	FS	12.18	11.97		11.92	12.04

Table 13. Beam profile details for the 1 - 3 square field sizes measured using the five different detectors at the different SSDs with a 10 MV photon beam.

90cm 10MV Inline						
1×1 cm ²	Detector	EDR2	EBT2	PTW60019	EFD-3G	CC01
	PenL	0.40	0.35	0.36	0.42	0.34
	PenR	0.41	0.35	0.37	0.38	0.36
	FS	1.06	1.01	1.04	1.03	1.07
95cm 10MV Inline						
1.05×1.05 cm ²	Detector	EDR2	EBT2	PTW60019	EFD-3G	CC01
	PenL	0.39	0.32	0.35	0.32	0.35
	PenR	0.40	0.34	0.35	0.33	0.34
	FS	1.08	1.03	1.04	1.12	1.05
100cm 10MV Inline						
1.1×1.1 cm ²	Detector	EDR2	EBT2	PTW60019	EFD-3G	CC01
	PenL	0.41	0.30	0.36	0.36	0.36
	PenR	0.39	0.27	0.37	0.35	0.37
	FS	1.12	1.06	1.09	1.10	1.11
110cm 10MV Inline						
1.2×1.2 cm ²	Detector	EDR2	EBT2	PTW60019	EFD-3G	CC01
	PenL	0.43	0.33	0.38	0.39	0.39
	PenR	0.44	0.34	0.40	0.39	0.39
	FS	1.24	1.22	1.22	1.20	1.19
90cm 10MV Inline						
2×2 cm ²	Detector	EDR2	EBT2	PTW60019	EFD-3G	CC01
	PenL	0.53	0.39	0.41	0.41	0.42
	PenR	0.53	0.39	0.31	0.42	0.16
	FS	2.07	1.96	1.98	1.99	2.00
95cm 10MV Inline						
2.1×2.1 cm ²	Detector	EDR2	EBT2	PTW60019	EFD-3G	CC01
	PenL	0.44	0.40	0.39	0.40	0.40
	PenR	0.44	0.40	0.40	0.41	0.41
	FS	2.08	2.06	2.08	2.06	2.09
100cm 10MV Inline						
2.2×2.2 cm ²	Detector	EDR2	EBT2	PTW60019	EFD-3G	CC01
	PenL	0.44	0.41	0.42	0.41	0.43
	PenR	0.45	0.41	0.41	0.41	0.43
	FS	2.20	2.20	2.17	2.20	2.20
110cm 10MV Inline						
2.4×2.4 cm ²	Detector	EDR2	EBT2	PTW60019	EFD-3G	CC01
	PenL	0.53	0.40	0.45	0.45	0.47
	PenR	0.55	0.40	0.45	0.43	0.46
	FS	2.41	2.35	2.38	2.38	2.37
90cm 10MV Inline						
3×3 cm ²	Detector	EDR2	EBT2	PTW60019	EFD-3G	CC01
	PenL	0.53	0.41	0.46	0.47	0.46
	PenR	0.53	0.41	0.46	0.48	0.47
	FS	3.03	2.94	3.00	3.01	3.01
95cm 10MV Inline						
3.15×3.15 cm ²	Detector	EDR2	EBT2	PTW60019	EFD-3G	CC01
	PenL	0.52	0.49	0.42	0.43	0.45
	PenR	0.52	0.49	0.44	0.44	0.45
	FS	3.18	3.13	3.12	3.13	3.13
100cm 10MV Inline						
3.3×3.3 cm ²	Detector	EDR2	EBT2	PTW60019	EFD-3G	CC01
	PenL	0.53	0.49	0.43	0.43	0.45
	PenR	0.49	0.49	0.43	0.44	0.46
	FS	3.33	3.28	3.27	3.32	3.29
110cm 10MV Inline						
3.6×3.6 cm ²	Detector	EDR2	EBT2	PTW60019	EFD-3G	CC01
	PenL	0.54	0.49	0.50	0.50	0.46
	PenR	0.54	0.49	0.51	0.47	0.48
	FS	3.60	3.55	3.58	3.57	3.56
90cm 10MV Crossline						
1×1 cm ²	Detector	EDR2	EBT2	PTW60019	EFD-3G	CC01
	PenL	0.49	0.24	0.45	0.46	0.45
	PenR	0.48	0.28	0.46	0.46	0.45
	FS	1.11	0.99	1.12	1.15	1.03
95cm 10MV Crossline						
1.05×1.05 cm ²	Detector	EDR2	EBT2	PTW60019	EFD-3G	CC01
	PenL	0.52	0.30	0.44	0.48	0.46
	PenR	0.50	0.30	0.47	0.48	0.47
	FS	1.20	1.03	1.21	1.04	1.15
100cm 6MV Crossline						
1.1×1.1 cm ²	Detector	EDR2	EBT2	PTW60019	EFD-3G	CC01
	PenL	0.51	0.34	0.49	0.50	0.51
	PenR	0.51	0.38	0.49	0.52	0.52
	FS	1.21	1.06	1.26	1.30	1.28
110cm 6MV Crossline						
1.2×1.2 cm ²	Detector	EDR2	EBT2	PTW60019	EFD-3G	CC01
	PenL	0.55	0.41	0.55	0.56	0.55
	PenR	0.54	0.40	0.57	0.57	0.55
	FS	1.31	1.16	1.53	1.43	1.30
90cm 10MV Crossline						
2×2 cm ²	Detector	EDR2	EBT2	PTW60019	EFD-3G	CC01
	PenL	0.56	0.49	0.52	0.53	0.55
	PenR	0.57	0.47	0.56	0.55	0.60
	FS	2.02	1.93	2.07	2.09	2.15
95cm 10MV Crossline						
2.1×2.1 cm ²	Detector	EDR2	EBT2	PTW60019	EFD-3G	CC01
	PenL	0.61	0.52	0.54	0.55	0.52
	PenR	0.69	0.52	0.57	0.58	0.57
	FS	2.19	2.13	2.11	2.10	2.24
100cm 6MV Crossline						
2.2×2.2 cm ²	Detector	EDR2	EBT2	PTW60019	EFD-3G	CC01
	PenL	0.63	0.56	0.52	0.56	0.56
	PenR	0.63	0.58	0.60	0.58	0.61
	FS	2.27	2.24	2.21	2.27	2.21
110cm 6MV Crossline						
2.4×2.4 cm ²	Detector	EDR2	EBT2	PTW60019	EFD-3G	CC01
	PenL	0.66	0.58	0.58	0.63	0.56
	PenR	0.63	0.58	0.63	0.64	0.62
	FS	2.42	2.31	2.33	2.34	2.43
90cm 10MV Crossline						
3×3 cm ²	Detector	EDR2	EBT2	PTW60019	EFD-3G	CC01
	PenL	0.66	0.52	0.59	0.58	0.60
	PenR	0.65	0.53	0.58	0.58	0.61
	FS	3.06	2.92	3.06	3.11	3.09
95cm 10MV Crossline						
3.15×3.15 cm ²	Detector	EDR2	EBT2	PTW60019	EFD-3G	CC01
	PenL	0.65	0.59	0.57	0.58	0.58
	PenR	0.62	0.59	0.59	0.59	0.58
	FS	3.24	3.14	3.19	3.24	3.22
100cm 6MV Crossline						
3.3×3.3 cm ²	Detector	EDR2	EBT2	PTW60019	EFD-3G	CC01
	PenL	0.65	0.62	0.63	0.59	0.61
	PenR	0.65	0.62	0.62	0.60	0.64
	FS	3.32	3.29	3.35	3.41	3.35
110cm 6MV Crossline						
3.6×3.6 cm ²	Detector	EDR2	EBT2	PTW60019	EFD-3G	CC01
	PenL	0.69	0.60	0.68	0.67	0.65
	PenR	0.69	0.60	0.67	0.65	0.72
	FS	3.63	3.52	3.64	3.72	3.67

Table 14. Beam profile details for the 4 – 10 square field sizes measured using the five different detectors at the different SSDs with a 10 MV photon beam.

90cm 10MV Inline						
4x4 cm ²	Detector	EDR2	EBT2	PTW60019	EFD-3G	CC01
	PenL	0.57	0.56	0.44	0.45	0.45
	PenR	0.57	0.56	0.44	0.47	0.45
	FS	4.06	3.89	3.97	4.00	3.98
95cm 10MV Inline						
4.2x4.2 cm ²	Detector	EDR2	EBT2	PTW60019	EFD-3G	CC01
	PenL	0.52	0.49	0.46	0.49	0.46
	PenR	0.52	0.49	0.49	0.47	0.49
	FS	4.28	4.19	4.18	4.31	4.19
100cm 10MV Inline						
4.4x4.4 cm ²	Detector	EDR2	EBT2	PTW60019	EFD-3G	CC01
	PenL	0.53	0.54	0.47	0.46	0.48
	PenR	0.54	0.54	0.47	0.46	0.49
	FS	4.42	4.49	4.37	4.37	4.39
110cm 10MV Inline						
4.8x4.8 cm ²	Detector	EDR2	EBT2	PTW60019	EFD-3G	CC01
	PenL	0.61	0.50	0.51	0.50	0.50
	PenR	0.61	0.50	0.51	0.52	0.48
	FS	4.80	4.81	4.78	4.77	4.76
90cm 10MV Inline						
5	Detector	EDR2	EBT2	PTW60019	EFD-3G	CC01
	PenL	0.55	0.58	0.50	0.51	0.50
	PenR	0.55	0.58	0.50	0.51	0.51
	FS	5.00	4.90	5.05	5.03	5.04
95cm 10MV Inline						
5.25x5.25 cm ²	Detector	EDR2	EBT2	PTW60019	EFD-3G	CC01
	PenL	0.54	0.49	0.48	0.48	0.48
	PenR	0.54	0.49	0.47	0.48	0.49
	FS	5.23	5.24	5.30	5.29	5.28
100cm 10MV Inline						
5.5x5.5 cm ²	Detector	EDR2	EBT2	PTW60019	EFD-3G	CC01
	PenL	0.60	0.59	0.60	0.51	0.52
	PenR	0.60	0.59	0.49	0.52	0.53
	FS	5.55	5.51	5.57	5.53	5.54
110cm 10MV Inline						
6x6 cm ²	Detector	EDR2	EBT2	PTW60019	EFD-3G	CC01
	PenL	0.63	0.51	0.52	0.54	0.51
	PenR	0.63	0.51	0.53	0.54	0.52
	FS	5.96	6.01	6.03	6.06	6.05
90cm 10MV Inline						
10x10 cm ²	Detector	EDR2	EBT2	PTW60019	EFD-3G	CC01
	PenL	0.74	0.81	0.53	0.56	0.54
	PenR	0.74	0.81	0.52	0.55	0.53
	FS	10.09	9.81	10.01	10.05	10.01
95cm 10MV Inline						
10.5x10.5 cm ²	Detector	EDR2	EBT2	PTW60019	EFD-3G	CC01
	PenL	0.63	0.56	0.53	0.58	0.58
	PenR	0.63	0.56	0.54	0.56	0.55
	FS	10.58	10.40	10.51	10.50	10.50
100cm 10MV Inline						
11x11 cm ²	Detector	EDR2	EBT2	PTW60019	EFD-3G	CC01
	PenL	0.62	0.55	0.54	0.56	0.59
	PenR	0.62	0.55	0.55	0.57	0.60
	FS	11.02	11.06	11.00	11.00	11.02
110cm 10MV Inline						
12x12 cm ²	Detector	EDR2	EBT2	PTW60019	EFD-3G	CC01
	PenL	0.76	0.62	0.65	0.61	0.59
	PenR	0.76	0.62	0.64	0.61	0.59
	FS	12.04	11.99	12.02	12.02	12.00
90cm 10MV Crossline						
4x4 cm ²	Detector	EDR2	EBT2	PTW60019	EFD-3G	CC01
	PenL	0.62	0.58	0.57	0.58	0.62
	PenR	0.62	0.58	0.63	0.58	0.68
	FS	4.06	3.93	3.88	4.10	4.12
95cm 10MV Crossline						
4.2x4.2 cm ²	Detector	EDR2	EBT2	PTW60019	EFD-3G	CC01
	PenL	0.64	0.65	0.60	0.60	0.59
	PenR	0.67	0.65	0.61	0.60	0.61
	FS	4.30	4.25	4.24	4.24	4.11
100cm 6MV Crossline						
4.4x4.4 cm ²	Detector	EDR2	EBT2	PTW60019	EFD-3G	CC01
	PenL	0.63	0.66	0.63	0.61	0.64
	PenR	0.63	0.66	0.64	0.60	0.66
	FS	4.45	4.40	4.60	4.45	4.39
110cm 6MV Crossline						
4.8x4.8 cm ²	Detector	EDR2	EBT2	PTW60019	EFD-3G	CC01
	PenL	0.77	0.63	0.68	0.64	0.71
	PenR	0.77	0.63	0.70	0.64	0.71
	FS	4.86	4.75	4.78	4.92	4.82
90cm 10MV Crossline						
5	Detector	EDR2	EBT2	PTW60019	EFD-3G	CC01
	PenL	0.64	0.57	0.61	0.58	0.63
	PenR	0.64	0.57	0.60	0.57	0.64
	FS	5.04	4.91	5.09	5.08	5.06
95cm 10MV Crossline						
5.25x5.25 cm ²	Detector	EDR2	EBT2	PTW60019	EFD-3G	CC01
	PenL	0.69	0.50	0.64	0.64	0.63
	PenR	0.69	0.50	0.64	0.61	0.63
	FS	5.37	5.24	5.29	5.31	5.34
100cm 6MV Crossline						
5.5x5.5 cm ²	Detector	EDR2	EBT2	PTW60019	EFD-3G	CC01
	PenL	0.71	0.65	0.67	0.63	0.67
	PenR	0.71	0.65	0.66	0.63	0.68
	FS	5.55	5.54	5.54	5.55	5.60
110cm 6MV Crossline						
6x6 cm ²	Detector	EDR2	EBT2	PTW60019	EFD-3G	CC01
	PenL	0.84	0.71	0.72	0.73	0.78
	PenR	0.84	0.71	0.73	0.70	0.72
	FS	5.96	5.98	6.03	6.05	6.10
90cm 10MV Crossline						
10x10 cm ²	Detector	EDR2	EBT2	PTW60019	EFD-3G	CC01
	PenL	0.89	0.71	0.70	0.73	0.74
	PenR	0.89	0.70	0.70	0.73	0.76
	FS	10.00	9.91	10.00	10.03	10.01
95cm 10MV Crossline						
10.5x10.5 cm ²	Detector	EDR2	EBT2	PTW60019	EFD-3G	CC01
	PenL	0.76	0.60	0.70	0.72	0.72
	PenR	0.76	0.60	0.72	0.73	0.72
	FS	10.49	10.48	10.45	10.52	10.52
100cm 6MV Crossline						
11x11 cm ²	Detector	EDR2	EBT2	PTW60019	EFD-3G	CC01
	PenL	0.99	0.75	0.70	0.74	0.75
	PenR	0.99	0.75	0.74	0.75	0.78
	FS	11.10	11.04	10.93	11.03	11.04
110cm 6MV Crossline						
12x12 cm ²	Detector	EDR2	EBT2	PTW60019	EFD-3G	CC01
	PenL	0.93	0.85	0.76	0.81	0.81
	PenR	0.93	0.85	0.80	0.83	0.84
	FS	11.93	12.05	11.92	12.02	12.00

Table 15. Beam profile details for the 1 - 3 square field sizes measured using the five different detectors at the different SSDs with a 15 MV photon beam.

90cm 15MV Inline						
1×1 cm ²	Detector	EDR2	EBT2	PTW60019	EFD-3G	CC01
	PenL	0.39	0.27	0.35	0.35	0.34
	PenR	0.40	0.26	0.36	0.35	0.35
	FS	1.03	1.00	1.02	1.06	1.02
95cm 15MV Inline						
1.05×1.05 cm ²	Detector	EDR2	EBT2	PTW60019	EFD-3G	CC01
	PenL	0.45	0.25	0.36	0.35	0.36
	PenR	0.42	0.26	0.34	0.38	0.36
	FS	1.12	1.04	1.12	1.05	1.06
100cm 15MV Inline						
1.1×1.1 cm ²	Detector	EDR2	EBT2	PTW60019	EFD-3G	CC01
	PenL	0.41	0.23	0.38	0.37	0.38
	PenR	0.40	0.27	0.38	0.35	0.41
	FS	1.14	1.07	1.10	1.10	1.12
110cm 15MV Inline						
1.2×1.2 cm ²	Detector	EDR2	EBT2	PTW60019	EFD-3G	CC01
	PenL	0.46	0.31	0.40	0.39	0.39
	PenR	0.48	0.32	0.41	0.40	0.41
	FS	1.22	1.08	1.21	1.20	1.22
90cm 15MV Inline						
2×2 cm ²	Detector	EDR2	EBT2	PTW60019	EFD-3G	CC01
	PenL	0.49	0.48	0.44	0.46	0.44
	PenR	0.50	0.08	0.36	0.29	0.37
	FS	1.99	1.96	1.98	2.00	1.98
95cm 15MV Inline						
2.1×2.1 cm ²	Detector	EDR2	EBT2	PTW60019	EFD-3G	CC01
	PenL	0.51	0.55	0.44	0.44	0.43
	PenR	0.50	0.55	0.44	0.45	0.44
	FS	2.15	2.06	2.07	2.07	2.09
100cm 15MV Inline						
2.2×2.2 cm ²	Detector	EDR2	EBT2	PTW60019	EFD-3G	CC01
	PenL	0.51	0.38	0.45	0.45	0.47
	PenR	0.52	0.39	0.45	0.44	0.45
	FS	2.20	2.15	2.17	2.22	2.19
110cm 15MV Inline						
2.4×2.4 cm ²	Detector	EDR2	EBT2	PTW60019	EFD-3G	CC01
	PenL	0.53	0.46	0.50	0.47	0.51
	PenR	0.53	0.46	0.50	0.46	0.47
	FS	2.36	2.36	2.38	2.39	2.39
90cm 15MV Inline						
3×3 cm ²	Detector	EDR2	EBT2	PTW60019	EFD-3G	CC01
	PenL	0.53	0.46	0.46	0.47	0.48
	PenR	0.54	0.46	0.49	0.47	0.48
	FS	2.97	2.97	2.98	2.99	2.99
95cm 15MV Inline						
3.15×3.15 cm ²	Detector	EDR2	EBT2	PTW60019	EFD-3G	CC01
	PenL	0.62	0.60	0.51	0.47	0.49
	PenR	0.60	0.60	0.49	0.48	0.49
	FS	3.19	3.11	3.12	3.12	3.14
100cm 15MV Inline						
3.3×3.3 cm ²	Detector	EDR2	EBT2	PTW60019	EFD-3G	CC01
	PenL	0.52	0.45	0.49	0.51	0.50
	PenR	0.54	0.43	0.48	0.49	0.50
	FS	3.30	3.27	3.28	3.31	3.27
110cm 15MV Inline						
3.6×3.6 cm ²	Detector	EBT2	EDR2	PTW60019	EFD-3G	CC01
	PenL	0.52	0.54	0.50	0.51	0.51
	PenR	0.52	0.54	0.51	0.51	0.52
	FS	3.55	3.56	3.55	3.57	3.58
90cm 15MV Crossline						
1×1 cm ²	Detector	EDR2	EBT2	PTW60019	EFD-3G	CC01
	PenL	0.51	0.39	0.45	0.48	0.47
	PenR	0.51	0.39	0.48	0.47	0.47
	FS	1.12	1.02	1.17	1.19	1.07
95cm 15MV Crossline						
1.05×1.05 cm ²	Detector	EDR2	EBT2	PTW60019	EFD-3G	CC01
	PenL	0.52	0.35	0.50	0.51	0.49
	PenR	0.53	0.35	0.50	0.50	0.48
	FS	1.20	1.03	1.25	1.15	1.20
100cm 15MV Crossline						
1.1×1.1 cm ²	Detector	EDR2	EBT2	PTW60019	EFD-3G	CC01
	PenL	0.54	0.33	0.54	0.52	0.53
	PenR	0.52	0.33	0.51	0.54	0.54
	FS	1.23	0.99	1.25	1.30	1.36
110cm 15MV Crossline						
1.2×1.2 cm ²	Detector	EDR2	EBT2	PTW60019	EFD-3G	CC01
	PenL	0.54	0.42	0.53	0.55	0.57
	PenR	0.54	0.42	0.55	0.56	0.57
	FS	1.27	1.21	1.30	1.37	1.30
90cm 15MV Crossline						
2×2 cm ²	Detector	EDR2	EBT2	PTW60019	EFD-3G	CC01
	PenL	0.63	0.50	0.58	0.57	0.58
	PenR	0.63	0.52	0.59	0.63	0.60
	FS	2.01	1.92	2.01	2.09	2.11
95cm 15MV Crossline						
2.1×2.1 cm ²	Detector	EDR2	EBT2	PTW60019	EFD-3G	CC01
	PenL	0.62	0.40	0.56	0.58	0.55
	PenR	0.62	0.40	0.63	0.62	0.60
	FS	2.20	2.10	2.11	2.13	2.25
100cm 15MV Crossline						
2.2×2.2 cm ²	Detector	EDR2	EBT2	PTW60019	EFD-3G	CC01
	PenL	0.65	0.56	0.61	0.59	0.59
	PenR	0.65	0.56	0.63	0.60	0.65
	FS	2.22	2.15	2.30	2.30	2.36
110cm 15MV Crossline						
2.4×2.4 cm ²	Detector	EDR2	EBT2	PTW60019	CC01	EFD-3G
	PenL	0.71	0.60	0.60	0.59	0.65
	PenR	0.71	0.60	0.66	0.65	0.68
	FS	2.38	2.32	2.38	2.41	2.41
90cm 15MV Crossline						
3×3 cm ²	Detector	EDR2	EBT2	PTW60019	EFD-3G	CC01
	PenL	0.65	0.59	0.60	0.60	0.62
	PenR	0.67	0.59	0.60	0.60	0.65
	FS	2.99	2.93	3.07	3.10	3.05
95cm 15MV Crossline						
3.15×3.15 cm ²	Detector	EDR2	EBT2	PTW60019	EFD-3G	CC01
	PenL	0.74	0.51	0.62	0.64	0.60
	PenR	0.69	0.51	0.66	0.64	0.63
	FS	3.23	3.14	3.20	3.25	3.22
100cm 15MV Crossline						
3.3×3.3 cm ²	Detector	EDR2	EBT2	PTW60019	EFD-3G	CC01
	PenL	0.68	0.66	0.66	0.64	0.66
	PenR	0.68	0.66	0.67	0.65	0.68
	FS	3.32	3.23	3.34	3.42	3.37
110cm 15MV Crossline						
3.6×3.6 cm ²	Detector	EDR2	EBT2	PTW60019	EFD-3G	CC01
	PenL	0.82	0.68	0.73	0.72	0.73
	PenR	0.82	0.67	0.73	0.72	0.74
	FS	3.50	3.50	3.63	3.68	3.65

Table 16. Beam profile details for the 4 – 10 square field sizes measured using the five different detectors at the different SSDs with a 15 MV photon beam.

90cm 15MV Inline						
4x4 cm ²	Detector	EDR2	EBT2	PTW60019	EFD-3G	CC01
	PenL	0.64	0.48	0.49	0.48	0.52
	PenR	0.57	0.48	0.49	0.48	0.51
	FS	3.96	3.96	3.97	3.97	3.99
95cm 15MV Inline						
4.2x4.2 cm ²	Detector	EDR2	EBT2	PTW60019	EFD-3G	CC01
	PenL	0.67	0.65	0.39	0.50	0.52
	PenR	0.67	0.65	0.41	0.51	0.52
	FS	4.23	4.16	4.30	4.16	4.18
100cm 15MV Inline						
4.4x4.4 cm ²	Detector	EDR2	EBT2	PTW60019	EFD-3G	CC01
	PenL	0.61	0.49	0.50	0.51	0.53
	PenR	0.61	0.49	0.51	0.52	0.54
	FS	4.42	4.40	4.35	4.36	4.37
110cm 15MV Inline						
4.8x4.8 cm ²	Detector	EDR2	EBT2	PTW60019	EFD-3G	CC01
	PenL	0.63	0.61	0.54	0.54	0.54
	PenR	0.65	0.61	0.54	0.55	0.54
	FS	4.75	4.79	4.75	4.75	4.77
90cm 15MV Inline						
5	Detector	EDR2	EBT2	PTW60019	EFD-3G	CC01
	PenL	0.58	0.51	0.56	0.53	0.57
	PenR	0.58	0.52	0.54	0.53	0.52
	FS	4.96	4.95	5.04	5.02	5.01
95cm 15MV Inline						
5.25x5.25 cm ²	Detector	EDR2	EBT2	PTW60019	EFD-3G	CC01
	PenL	0.60	0.68	0.55	0.54	0.55
	PenR	0.60	0.68	0.55	0.52	0.53
	FS	5.29	5.23	5.28	5.29	5.27
100cm 15MV Inline						
5.5x5.5 cm ²	Detector	EDR2	EBT2	PTW60019	EFD-3G	CC01
	PenL	0.63	0.52	0.53	0.54	0.55
	PenR	0.63	0.52	0.53	0.54	0.57
	FS	5.54	5.53	5.54	5.52	5.52
110cm 15MV Inline						
6x6 cm ²	Detector	EBT2	EDR2	PTW60019	EFD-3G	CC01
	PenL	0.64	0.65	0.54	0.57	0.59
	PenR	0.64	0.65	0.57	0.60	0.58
	FS	6.07	5.90	6.01	6.03	6.04
90cm 15MV Inline						
10x10 cm ²	Detector	EDR2	EBT2	PTW60019	EFD-3G	CC01
	PenL	0.71	0.63	0.61	0.59	0.61
	PenR	0.71	0.63	0.60	0.59	0.62
	FS	9.94	9.96	10.00	10.02	10.03
95cm 15MV Inline						
10.5x10.5 cm ²	Detector	EDR2	EBT2	PTW60019	EFD-3G	CC01
	PenL	0.79	0.81	0.63	0.59	0.63
	PenR	0.81	0.81	0.63	0.61	0.61
	FS	10.68	10.57	10.48	10.48	10.48
100cm 15MV Inline						
11x11 cm ²	Detector	EDR2	EBT2	PTW60019	EFD-3G	CC01
	PenL	0.88	0.64	0.59	0.62	0.64
	PenR	0.87	0.64	0.61	0.63	0.65
	FS	11.00	11.00	10.97	10.98	11.00
110cm 15MV Inline						
12x12 cm ²	Detector	EDR2	EBT2	PTW60019	EFD-3G	CC01
	PenL	0.79	0.85	0.63	0.64	0.67
	PenR	0.79	0.85	0.67	0.66	0.72
	FS	11.95	12.07	11.98	12.00	12.00
90cm 15MV Crossline						
4x4 cm ²	Detector	EDR2	EBT2	PTW60019	EFD-3G	CC01
	PenL	0.69	0.62	0.64	0.62	0.68
	PenR	0.69	0.62	0.65	0.63	0.68
	FS	3.95	3.93	3.89	4.11	4.16
95cm 15MV Crossline						
4.2x4.2 cm ²	Detector	EDR2	EBT2	PTW60019	EFD-3G	CC01
	PenL	0.70	0.54	0.69	0.62	0.64
	PenR	0.70	0.54	0.68	0.63	0.66
	FS	4.27	4.19	4.20	4.16	4.10
100cm 15MV Crossline						
4.4x4.4 cm ²	Detector	EDR2	EBT2	PTW60019	EFD-3G	CC01
	PenL	0.72	0.67	0.65	0.66	0.73
	PenR	0.72	0.67	0.67	0.66	0.73
	FS	4.44	4.35	4.43	4.48	4.42
110cm 15MV Crossline						
4.8x4.8 cm ²	Detector	EDR2	EBT2	PTW60019	EFD-3G	CC01
	PenL	0.75	0.77	0.77	0.70	0.76
	PenR	0.75	0.77	0.76	0.70	0.77
	FS	4.69	4.73	4.70	4.87	4.70
90cm 15MV Crossline						
5	Detector	EDR2	EBT2	PTW60019	EFD-3G	CC01
	PenL	0.71	0.63	0.68	0.64	0.69
	PenR	0.71	0.63	0.67	0.63	0.68
	FS	4.96	4.93	5.06	5.07	5.07
95cm 15MV Crossline						
5.25x5.25 cm ²	Detector	EDR2	EBT2	PTW60019	EFD-3G	CC01
	PenL	0.75	0.56	0.74	0.71	0.70
	PenR	0.75	0.56	0.71	0.68	0.70
	FS	5.30	5.27	5.27	5.31	5.31
100cm 15MV Crossline						
5.5x5.5 cm ²	Detector	EDR2	EBT2	PTW60019	EFD-3G	CC01
	PenL	0.78	0.69	0.74	0.68	0.76
	PenR	0.77	0.69	0.73	0.69	0.75
	FS	5.44	5.47	5.53	5.55	5.55
110cm 15MV Crossline						
6x6 cm ²	Detector	EDR2	EBT2	PTW60019	EFD-3G	CC01
	PenL	0.70	0.81	0.78	0.78	0.81
	PenR	0.70	0.81	0.77	0.76	0.79
	FS	5.85	6.01	6.03	6.04	6.08
90cm 15MV Crossline						
10x10 cm ²	Detector	EDR2	EBT2	PTW60019	EFD-3G	CC01
	PenL	0.83	0.77	0.74	0.77	0.78
	PenR	0.83	0.77	0.77	0.74	0.78
	FS	9.88	9.86	10.01	10.03	10.02
95cm 15MV Crossline						
10.5x10.5 cm ²	Detector	EDR2	EBT2	PTW60019	EFD-3G	CC01
	PenL	0.80	0.67	0.75	0.80	0.75
	PenR	0.80	0.67	0.78	0.80	0.78
	FS	10.51	10.46	10.44	10.50	10.53
100cm 15MV Crossline						
11x11 cm ²	Detector	EDR2	EBT2	PTW60019	EFD-3G	CC01
	PenL	0.92	0.82	0.76	0.78	0.82
	PenR	0.92	0.82	0.78	0.78	0.84
	FS	11.02	11.00	10.93	11.05	11.01
110cm 15MV Crossline						
12x12 cm ²	Detector	EDR2	EBT2	PTW60019	EFD-3G	CC01
	PenL	0.89	1.11	0.86	0.87	0.85
	PenR	0.89	1.13	0.87	0.88	0.89
	FS	11.86	12.01	11.91	12.02	11.98

Appendix B Relative output factors

Relative output factor values are listed in the following tables for the different detectors that were used to measure these factors.

Table 17. ROF values using a 6 MV photon beam for the different detectors as measured at various SSDs

6MV										
90cm										
Field side length (cm)	EDR2		EBT2		CC01		PTW60019		EFD-3G	
	Avg	Std	Avg	Std	Avg	Std	Avg	Std	Avg	Std
1.00	0.67	0.06	0.58	0.02	0.65	0.00	0.67	0.02	0.66	0.01
2.00	0.79	0.07	0.72	0.02	0.78	0.01	0.80	0.00	0.79	0.00
3.00	0.87	0.08	0.79	0.07	0.83	0.00	0.85	0.00	0.83	0.00
4.00	0.94	0.10	0.86	0.02	0.86	0.00	0.88	0.00	0.86	0.00
5.00	0.94	0.08	0.88	0.02	0.89	0.00	0.91	0.00	0.89	0.00
10.00	1.00	0.00	1.00	0.00	1.00	0.00	1.00	0.00	1.00	0.00
95cm										
Field side length (cm)	EDR2		EBT2		CC01		PTW60019		EFD-3G	
	Avg	Std	Avg	Std	Avg	Std	Avg	Std	Avg	Std
1.05	0.61	0.02	0.66	0.09	0.64	0.02	0.65	0.01	0.66	0.00
2.10	0.72	0.02	0.77	0.05	0.78	0.02	0.81	0.01	0.78	0.00
3.15	0.81	0.00	0.85	0.06	0.82	0.02	0.85	0.00	0.83	0.00
4.20	0.84	0.04	0.87	0.06	0.85	0.02	0.88	0.00	0.87	0.00
5.25	0.89	0.02	0.91	0.06	0.88	0.02	0.91	0.00	0.89	0.00
10.50	1.00	0.00	1.00	0.00	1.00	0.00	1.00	0.00	1.00	0.00
100cm										
Field side length (cm)	EDR2		EBT2		CC01		PTW60019		EFD-3G	
	Avg	Std	Avg	Std	Avg	Std	Avg	Std	Avg	Std
1.10	0.64	0.02	0.67	0.05	0.65	0.01	0.68	0.02	0.66	0.01
2.20	0.74	0.02	0.73	0.04	0.79	0.01	0.80	0.00	0.79	0.00
3.30	0.80	0.02	0.81	0.04	0.83	0.00	0.85	0.00	0.83	0.00
4.40	0.87	0.04	0.87	0.01	0.87	0.00	0.88	0.00	0.86	0.00
5.50	0.85	0.05	0.88	0.04	0.90	0.01	0.91	0.00	0.89	0.00
11.00	1.00	0.00	1.00	0.00	1.00	0.00	1.00	0.00	1.00	0.00
110cm										
Field side length (cm)	EDR2		EBT2		CC01		PTW60019		EFD-3G	
	Avg	Std	Avg	Std	Avg	Std	Avg	Std	Avg	Std
1.20	0.63	0.06	0.59	0.12	0.64	0.02	0.69	0.01	0.66	0.02
2.40	0.74	0.01	0.76	0.07	0.78	0.01	0.80	0.00	0.79	0.00
3.60	0.84	0.11	0.84	0.06	0.82	0.01	0.84	0.00	0.83	0.00
4.80	0.86	0.08	0.88	0.08	0.86	0.01	0.88	0.00	0.86	0.00
6.00	0.93	0.04	0.90	0.09	0.89	0.01	0.91	0.00	0.89	0.00
12.00	1.00	0.00	1.00	0.00	1.00	0.00	1.00	0.00	1.00	0.00

Table 18. ROF values using a 10 MV photon beam for the different detectors as measured at various SSDs

10MV										
90cm										
Field side length (cm)	EDR2		EBT2		CC01		PTW60019		EFD-3G	
	Avg	Std	Avg	Std	Avg	Std	Avg	Std	Avg	Std
1.00	0.65	0.01	0.58	0.05	0.63	0.01	0.65	0.01	0.65	0.01
2.00	0.70	0.04	0.76	0.06	0.79	0.00	0.81	0.00	0.80	0.00
3.00	0.84	0.03	0.86	0.06	0.85	0.00	0.87	0.00	0.85	0.00
4.00	0.88	0.02	0.92	0.07	0.88	0.00	0.90	0.00	0.89	0.00
5.00	0.91	0.03	0.93	0.07	0.91	0.00	0.92	0.00	0.91	0.00
10.00	1.00	0.00	1.00	0.00	1.00	0.00	1.00	0.00	1.00	0.00
95cm										
Field side length (cm)	EDR2		EBT2		CC01		PTW60019		EFD-3G	
	Avg	Std	Avg	Std	Avg	Std	Avg	Std	Avg	Std
1.05	0.69	0.00	0.57	0.15	0.65	0.01	0.64	0.00	0.66	0.00
2.10	0.77	0.05	0.71	0.11	0.80	0.00	0.81	0.00	0.80	0.00
3.15	0.86	0.03	0.82	0.08	0.85	0.00	0.87	0.00	0.85	0.00
4.20	0.90	0.02	0.87	0.05	0.89	0.00	0.90	0.00	0.89	0.00
5.25	0.91	0.02	0.88	0.09	0.91	0.00	0.92	0.00	0.91	0.00
10.50	1.00	0.00	1.00	0.00	1.00	0.00	1.00	0.00	1.00	0.00
100cm										
Field side length (cm)	EDR2		EBT2		CC01		PTW60019		EFD-3G	
	Avg	Std	Avg	Std	Avg	Std	Avg	Std	Avg	Std
1.10	0.65	0.00	0.55	0.09	0.65	0.01	0.68	0.00	0.65	0.02
2.20	0.76	0.04	0.83	0.06	0.80	0.00	0.82	0.00	0.80	0.00
3.30	0.83	0.03	0.81	0.04	0.85	0.01	0.87	0.00	0.85	0.00
4.40	0.89	0.02	0.87	0.03	0.89	0.00	0.90	0.00	0.89	0.00
5.50	0.90	0.02	0.91	0.04	0.91	0.00	0.92	0.00	0.91	0.00
11.00	1.00	0.00	1.00	0.00	1.00	0.00	1.00	0.00	1.00	0.00
110cm										
Field side length (cm)	EDR2		EBT2		CC01		PTW60019		EFD-3G	
	Avg	Std	Avg	Std	Avg	Std	Avg	Std	Avg	Std
1.20	0.66	0.00	0.62	0.06	0.66	0.01	0.69	0.00	0.67	0.02
2.40	0.74	0.04	0.82	0.02	0.81	0.01	0.82	0.00	0.80	0.00
3.60	0.83	0.02	0.88	0.06	0.85	0.01	0.87	0.00	0.86	0.00
4.80	0.85	0.02	0.91	0.06	0.89	0.00	0.90	0.00	0.89	0.00
6.00	0.90	0.01	0.96	0.04	0.91	0.00	0.92	0.00	0.91	0.00
12.00	1.00	0.00	1.00	0.00	1.00	0.00	1.00	0.00	1.00	0.00

Table 19. ROF values using a 15 MV photon beam for the different detectors as measured at various SSDs

15MV										
90cm										
Field side length (cm)	EDR2		EBT2		CC01		PTW60019		EFD-3G	
	Avg	Std	Avg	Std	Avg	Std	Avg	Std	Avg	Std
1.00	0.64	0.03	0.58	0.06	0.58	0.01	0.62	0.02	0.62	0.01
2.00	0.81	0.04	0.76	0.06	0.78	0.00	0.80	0.00	0.79	0.01
3.00	0.81	0.08	0.83	0.03	0.83	0.03	0.87	0.00	0.85	0.00
4.00	0.89	0.04	0.89	0.03	0.89	0.00	0.90	0.00	0.89	0.00
5.00	0.89	0.08	0.91	0.02	0.92	0.00	0.93	0.00	0.92	0.00
10.00	1.00	0.00	1.00	0.00	1.00	0.00	1.00	0.00	1.00	0.00
95cm										
Field side length (cm)	EDR2		EBT2		CC01		PTW60019		EFD-3G	
	Avg	Std	Avg	Std	Avg	Std	Avg	Std	Avg	Std
1.05	0.66	0.06	0.59	0.07	0.62	0.01	0.63	0.02	0.62	0.01
2.10	0.78	0.07	0.74	0.05	0.79	0.00	0.81	0.01	0.79	0.00
3.15	0.83	0.05	0.84	0.04	0.86	0.00	0.87	0.00	0.85	0.00
4.20	0.89	0.05	0.86	0.05	0.89	0.00	0.90	0.00	0.89	0.00
5.25	0.88	0.07	0.90	0.02	0.92	0.00	0.93	0.00	0.92	0.00
10.50	1.00	0.00	1.00	0.00	1.00	0.00	1.00	0.00	1.00	0.00
100cm										
Field side length (cm)	EDR2		EBT2		CC01		PTW60019		EFD-3G	
	Avg	Std	Avg	Std	Avg	Std	Avg	Std	Avg	Std
1.10	0.60	0.03	0.57	0.03	0.63	0.01	0.64	0.01	0.63	0.01
2.20	0.73	0.02	0.75	0.02	0.79	0.00	0.81	0.00	0.79	0.00
3.30	0.82	0.05	0.85	0.01	0.86	0.01	0.87	0.00	0.86	0.00
4.40	0.86	0.06	0.89	0.01	0.89	0.01	0.90	0.00	0.89	0.00
5.50	0.90	0.02	0.93	0.03	0.92	0.00	0.93	0.00	0.92	0.00
11.00	1.00	0.00	1.00	0.00	1.00	0.00	1.00	0.00	1.00	0.00
110cm										
Field side length (cm)	EDR2		EBT2		CC01		PTW60019		EFD-3G	
	Avg	Std	Avg	Std	Avg	Std	Avg	Std	Avg	Std
1.20	0.57	0.13	0.65	0.01	0.63	0.01	0.66	0.01	0.64	0.02
2.40	0.76	0.05	0.77	0.01	0.80	0.01	0.81	0.00	0.80	0.01
3.60	0.80	0.05	0.90	0.01	0.86	0.00	0.87	0.00	0.86	0.00
4.80	0.86	0.05	0.90	0.03	0.89	0.00	0.90	0.00	0.89	0.00
6.00	0.87	0.06	0.94	0.02	0.92	0.00	0.93	0.00	0.92	0.00
12.00	1.00	0.00	1.00	0.00	1.00	0.00	1.00	0.00	1.00	0.00